University of Strathclyde

Department of Mechanical and Aerospace Engineering

Investigation of erosion-corrosion behaviour of pump materials

Lampros-Gerasimos Giourntas

A thesis submitted for the degree of Doctor of Philosophy

2016

Dedicated to my grandparents; Grigoris and Aggeliki, and my godfather Dimosthenis who taught me how to catch my dreams.

Acknowledgements

Firstly, I would like to express my sincere gratitude to my supervisors Dr. Trevor Hodgkiess and Dr. Alexander M. Galloway for their continuous support of my Ph.D study, for their patience, motivation, and immense knowledge. Their guidance helped me in all the time of research and writing of this thesis. I could not have imagined having a better supervisors and mentors for my Ph.D study.

Besides my advisors, I would like to thank my Weir Project champions; Dr. Edward Humphries (R&D Director, Weir Minerals Australia) and Dr. Alastair Pearson (Chief Metallurgist, Weir Engineering Services, Glasgow) for their insightful comments and encouragement.

My sincere thanks also goes to James Kelly, who provided me continuous advice and support on his metallography laboratory, Liza Hall, who familiarised me with the surface topography and Dr. Fiona Sillars, who helped me with the SEM and XRD investigations. Without their precious support, it would not be possible to conduct this research.

I thank my fellow labmates; N. Andrews, R. McDermott, E.I. Chrysochoos, G. Karafyllias, F. Brownlie, R. Stevenson, R. Logan, I. Palmeira and O. Odutayo for the stimulating discussions, for the sleepless nights we were working together before deadlines, and for all the fun we have had in the last four years.

My sincere gratitude goes also to my lovely friends, with special thanks to A.T. Alexakis, A. Toumpis and A. Anagnostakis, who supported me throughout this project by showing me the bright side of the Ph.D. life.

Last but not the least, I would like to thank my family: my parents and my brother for supporting me spiritually throughout writing this thesis and my life in general.

Abstract

A novel erosion-corrosion approach, that expands the assessment of damage occurring on engineering materials subjected to a submerged impingement jet, has been developed. This new analytical method yields quantitative data that facilitates a substantially improved understanding of the material degradation mechanisms that take place in different regions of the surface of a material when exposed to aqueous saline solutions and solid particles. The validation of this methodology involved a medium carbon steel and an austenitic stainless steel, where the stainless steel exhibited almost two-fold erosion-corrosion resistance. The application of this new evaluation technique was extended to white cast irons to enhance the understanding of interaction of the chromium carbides and the metallic matrix on the erosion-corrosion behaviour of these multi-phase materials. For this reason, two stainless steels that mimic the ferrous matrix were also investigated. The free erosion-corrosion results showed that there is no difference among the two cast irons and the stainless steels but the cathodic protection unravelled the advantages of the martensitic based alloys compared with austenitic based alloys. Sintered and HVOF coatings WC-based cermets of similar chemical composition were studied to elucidate the influence of the manufacturing process on their erosion-corrosion response of the cermets. The manufacturing process effect resulted to be significant as the sintered cermets displayed greater erosion-corrosion performance than the HVOF coatings due to the lack of process defects. By incorporating both WC-Co and WC-Ni cermets in this testing phase, the role of the binder type on the erosion-corrosion behaviour of cermets was also examined, showing the superiority of the Ni binder compared to the Co binder. The research findings enabled the formation of a material matrix, where the relative erosion-corrosion performance of the materials is evaluated, and it comprises a substantial contribution on the material selection process for critical pump components.

Table of Contents

Chapter 3: Experimental Methods

Chapter 6: Manufacturing process effect on the erosion-corrosion behaviour of cermets

Chapter 7: Concluding remarks and recommendations for further work

Apendix

List of Abbreviations

AFM	Atomic force microscopy
C	Corrosion
CP	Cathodic protection
CRA	Corrosion resistant alloys
CVF	Carbide volume fraction
DIZ	Direct impinged zone
E	Erosion
FEC	Free erosion-corrosion
FGM	Functionally graded material
HE	Hydrogen Embrittlement
HK	Knoop hardness
HRC	Rockwell C hardness
HV	Hardness Vickers
HVOF	High velocity oxy fuel
OA	Outer area
OCP	Open circuit potential
PREN	Pitting resistance equivalent number
S	Synergy
SCC	Stress corrosion cracking
SCE	Saturated calomel reference electrode
SEM	Scanning Electron Microscope
SRB	Sulphate reducing bacteria
TML	Total mass loss
TVL	Total volume loss
VF	Volume fraction
VL	Volume loss
WARC	Weir Advanced Research Centre
WDS	Wavelength dispersive X-Ray spectroscopy
XRD	X-Ray diffraction
ΔC	Enhanced corrosion by erosion
ΔE	Enhanced erosion by corrosion

List of Symbols

$\%Cr_{cast\ iron}$	Percentage of chromium in cast iron
$\%Cr_{matrix}$	Percentage of chromium in the matrix
%wt	Weight percentage of content
$(OH)^-$	Hydroxide
"n"	Factor of velocity depend on slurry conditions
A	Surface area
A_a	Surface area of anode
A_c	Surface area of cathode
Ag/AgCl	Silver/Silver Chloride
Al_2O_3	Alumina particles
b_a	Anodic Tafel slope
b_c	Cathodic Tafel slope
c_m	Concentration of metal
c_{mn}	Metal concentration in the aqueous environment
E	Potential
e^-	Electron
E_{corr}	Corrosion potential
E_o	Equilibrium potential
E_o^o	Standard equilibrium potential at "standard states"
F	Faradays constant
H_2	Hydrogen
H_2O	Water
H_p	Hardness of the particles
H_t	Hardness of the target
I	Current
i_a	Anodic current density
i_c	Cathodic current density
i_{corr}	Corrosion current density
I_{retW}	Index of tungsten carbide retention
I_W	Intensity of tungsten
I_{W2C}	Intensity of W_2C brittle tungsten carbide phase
I_{WC}	Intensity of WC
$logC_{H^+}$	Logarithmic concentration of hydrogen anions
m	Particle size exponent
M	Metal
M	Molar mass
N	Number of electrons
NaCl	Sodium chloride
O_2	Oxygen
Q^*	Flow rate per 30secs
R	General gas constant
r	Radius
R_a	Arithmetic average of the roughness profile
R_p	Polarisation resistance
SiC	Silicon carbide

T	Temperature
V	Velocity
W_{Cr}	Weight of chromium
W_{Mo}	Weight of molybdenum
W_{N}	Weight of nitrogen
W_{W}	Weight of tungsten
z	Valency
η	Collision efficiency
μ	Viscosity
ρ	Density

Chapter 1

Thesis Introduction

1.1 Thesis introduction

Material selection, as an engineering process, requires consideration of various factors which will control the performance of an engineering component and/or system. During the first design stage, each engineering component is assessed as a single element that will exhibit certain mechanical properties, such as strength, toughness, ductility associated with its application. Therefore, the engineering component is evaluated as part of a system which interacts with the environment that it is exposed to. When the operating conditions involve aqueous slurries, which consist of various aqueous solutions, including saline and different size of solid particles, erosion-corrosion performance of the material is crucial for the efficient and safe functionality of the system. The detrimental effects of erosion-corrosion are apparent in numerous industrial sectors.

The Oil and Gas sector experiences erosion-corrosion failures associated with erosion by small particles and damage caused by corrosive agents, such as carbon dioxide, present in the aqueous solution. In fact, the hydraulic fracturing industry, which is a well-developed practice of extracting gas, lays down the challenge of preventing severe erosion-corrosion problems due to the injected pressurised aqueous solution which contains a range of chemicals and hydraulic fracturing sand. As a result of the conditions encountered in oil and gas industry, numerous complex and interactive degradation processes, such as erosion [1.1], corrosion [1.2,1.3] and cavitation [1.4,1.5], take place.

The mining sector also suffers from substantial erosion-corrosion damage due to the severity of the transported slurry, which often contains large suspended particles [1.6,1.7]. The mining operation is comprised of three major stages; extraction, transportation and processing. Each of the above phases encounters severe erosion damage, due to the oversize rocks that are transported. The typical life of a slurry pump is in the range of 1500h-4000h and material wear rates can be over 2mm/year, and for this reason some pump components can be over 100mm thick [1.6]. An additional deterioration is provoked by the effect of corrosion as the slurries are usually saline aqueous solutions which sometimes can be highly acidic. The minerals processing commonly involves neutral slurries, but about 20% of the operations are taking place in acidic environments [1.8].

The Power sector is affected the least, compared to the two above sectors, since the operating conditions are not as aggressive as the above circumstances. Hydroelectric

turbines are robust since they operate on river water of low salinity and low solid concentration. For instance, the Niagara Falls hydroelectric turbines exhibit 50 years' service life due to the mild erosion-corrosion environment. However, there are some current situations where the hydro turbine life expectancies have been reduced from 50 years to 1-2 years on account of upstream factories pumping their waste water into the rivers without filtering it properly [1.9].

Weir Group PLC is a global engineering leader in providing expert engineering services for oil and gas, minerals, and power markets. Weir Group PLC established the Weir Advanced Research Centre (WARC) within Strathclyde University to optimise their capabilities in terms of research and development. There is an on-going requirement to characterise and control the erosion-corrosion processes experienced in a range of Weir Group products that function in hostile environments. In such cases, it is widely accepted that there is a need to mitigate these degradation mechanisms by the application of high performance coatings or by substitution of materials, prone to erosion-corrosion, by materials that are likely to demonstrate an increase in performance. The objective of this research programme was to;

a) Broaden the understanding of the main erosion-corrosion mechanisms that occur in range of Weir products.
b) Assess the potential impact of electrochemical intervention in terms of cathodic protection application in engineering components.
c) Develop a material selection solution to improve the life expectancy of components prone to erosion-corrosion to a more acceptable level.

This thesis shapes a distinct contribution to the knowledge of the erosion-corrosion phenomena by developing a novel quantitative approach that merges the up-to-date assessments procedures with advanced surface topography. The advantage of this enhanced technique is the quantification of the direct impingement erosion-corrosion damage along with the corrosive sliding abrasion during a normal impact impingement test. The application of cathodic protection facilitated the isolation of the mechanical deterioration mechanisms that take place under the jet; direct erosion and adjacent to it; sliding abrasion. The use of segmented specimen enabled also the electrochemical monitoring of the tested material within the two different flowing conditions. An additional benefit of this work, described herein, is the wide application of this novel practice to a number of materials (e.g. stainless

steels, high chromium cast irons, cermets), which represent the currently used materials in Weir Group sectors.

The layout of the thesis is summarised as follows. Chapter 2 includes a detailed review of the fundamentals of erosion-corrosion and it is followed by a chapter that describes the experimental methodologies utilised in this study (Chapter 3).

Chapter 4 describes a novel approach that expands the assessment of damage occurring as a result of solid/liquid impingement at normal incidence. This new analytical method yields quantitative data that facilitates a substantially improved understanding of the material degradation mechanisms (i.e. erosion, sliding abrasion, corrosion and interactive effects) that take place on different regions of the component subjected to slurry conditions. This newly developed technique involved a validation exercise on a medium carbon steel and an austenitic stainless steel.

Subsequent chapters illustrate the application of the above described practice on the erosion-corrosion behaviour of two white cast irons and four WC-based cermet materials. In Chapter 5, the two high chromium white cast irons' erosion-corrosion resistance was compared with two stainless steels that represent the metallic matrix of each cast iron. The objective of this study was to understand the consequences of the introduction of carbides in a stainless steel matrix. Chapter 6 demonstrates the relative performance of two sintered WC-based composites along with two high velocity oxy fuel (HVOF) sprayed coatings of similar composition under solid/liquid impingement. The effectiveness of the coatings in protecting the austenitic stainless steel substrate was also assessed, as the substrate material was also included in this testing phase.

Taking into account the diversity of the topics discussed in this study, the materials' assessment chapters is organised in terms of a literature review, followed by experimental results, extensive discussion, concluding remarks and chapter's references.

The final chapter includes an exercise in which the research findings are integrated into materials selection tool for relevant equipment with the aim of enhancing the material selection process.

1.2 References

[1.1] O. Hundseid, E. Duesten, O. Lauridsen, Investigation report on hydrocarbon leak occurred on Oseberg A platform, Statoil, 2013.

[1.2] B. Yu, D.Y. Li, A. Grondin, Effects of the dissolved oxygen and slurry velocity on erosion–corrosion of carbon steel in aqueous slurries with carbon dioxide and silica sand, Wear. 302 (2013) 1609–1614.

[1.3] D. Zheng, D. Che, Y. Liu, Experimental investigation on gas-liquid two-phase slug flow enhanced carbon dioxide corrosion in vertical upward pipeline, Corros. Sci. 50 (2008) 3005–3020.

[1.4] A. Iannetti, M.T. Stickland, W.M. Dempster, An advanced CFD model to study the effect of non-condensable gas on cavitation in positive displacement pumps, 11th Int. Symp. Compress. Turbine Flow Syst. Theory Appl. Areas SYMKOM 2014 IMP2 (2014).

[1.5] S.M. Price, D.R. Smith, J.D. Tison, The effects of valve dynamics on recirpocating pump reliability, in: Proc. 12th Int. Pump Users Symp.

[1.6] C.I. Walker, P. Robbie, Comparison of some laboratory wear tests and field wear in slurry pumps, Wear. 302 (2013) 1026–1034.

[1.7] H.H. Tian, G.R. Addie, K. V. Pagalthivarthi, Determination of wear coefficients for erosive wear prediction through Coriolis wear testing, Wear. 259 (2005) 160–170.

[1.8] Private communication with Tony Lawson, Managing Director, Weir Minerals Europe Limited, Todmorden, UK, (2014).

[1.9] Private communication with Gerry Russel, Vice President of Engineering & Field Service,Weir American Hydro, York, Pennsylvania, USA, (2015).

Chapter 2
Fundamentals of Erosion-Corrosion

2.1 Introduction

This chapter focuses on summarising the fundamentals of erosion-corrosion phenomenon in order to establish the basis of this research work.

2.2 Erosion-Corrosion Phenomenon

Erosion-corrosion is a surface degradation mechanism caused by flowing fluid, with or without solid particles. The phenomenon of erosion-corrosion is complex, since it involves mechanical damage (erosion), electrochemical damage (corrosion) and the interaction of the two individual processes. Many researchers [2.1–2.3] often use Equation 2.1 below to describe the mechanisms attributed with the material loss due to erosion-corrosion:

$$TML = E + C + \Delta E + \Delta C \qquad \textbf{Equation 2.1}$$

where, TML is the total material loss, E is the mechanical degradation, C is the electrochemical corrosion in static conditions, ΔE is enhanced erosion by the corrosion process, and ΔC is the enhanced corrosion by the erosion processes.

In this thesis, the erosion-corrosion phenomenon will be described using the Equation 2.2 shown below, which is a simplification of the Equation 2.1:

$$TML = E + C + S \qquad \textbf{Equation 2.2}$$

where, C demonstrates the (C+ΔC) component of the Equation 2.1 as it was measured in situ during erosion-corrosion tests and it is therefore the total electrochemical (corrosion) mass loss, and S is the synergy term which represents the enhanced erosion by the corrosion processes (i.e. ΔE in Equation 2.1).

Erosion-corrosion receives great attention as the operating conditions become more severe in most of the industrial sectors due to higher demands of energy through oil and gas extraction, minerals processing and power industries. For example, the more severe operating conditions are typically translated to higher rotational speeds in the slurry pumps and more flowing conditions in oil and gas pipelines; conditions that subsequently accelerate erosion-corrosion. These higher production rates also lead to the development of new materials that are able to withstand the increasingly hostile environments that are generated. Understanding the erosion-corrosion mechanisms and the key parameters that

govern their severity is essential for the optimum material selection. Hence, the following sections describe each degradation process that occurs during erosion-corrosion; a) erosion, b) corrosion and c) synergy.

2.3 Erosion

Erosion is the mechanical removal of material from a metal surface by the action of air with solid particles (dry erosion) or aqueous fluid with or without suspended particles (aqueous erosion). With the presence of solid particles the erosion becomes more severe and it takes place by different deterioration mechanisms. De Haller [2.4] found that, in the erosion of metals, two types of erosion are involved; high impingement angle erosion and small impact angle erosion. At high impact angles, the solid particles plastically deform the surface of the sample, which may form a rim of highly strained material that would be removed by further impacts [2.4–2.6]. The process of penetration of a rigid particle into the plane surface of a plastically deforming material at normal incidence is called indentation by Hutchings [2.5]. The erosion mechanisms at low impact angles (i.e. 30^{o}) are associated with the type of the solid particle. Rounded particles deform the surface by ploughing, displacing the particle to the side and in front of the particle (Fig 2.1 a). Angular particles, on the other hand, cause two slightly different types of cutting depending on the rolling direction of the particle (i.e. forward or backward), as illustrated in Figure 2.1 (b) & (c).

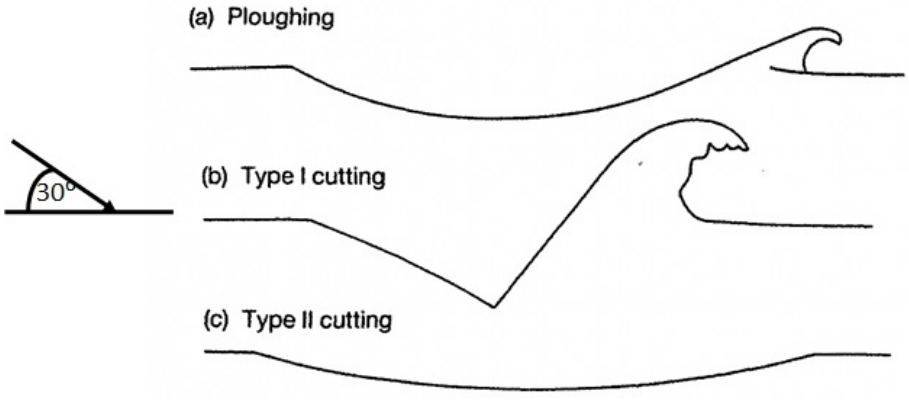

Figure 2.1 Sections through impact sites formed by hard particles on a ductile metal, showing typical shapes. The impact direction was from left to right. a) Ploughing deformation by a sphere, b) Type I cutting where the particle rotates forward during the impact; c) Type II cutting where the particle rotates backward during impact. [2.5]

2.3.1 Key influential parameters for erosion

A series of factors, such as flow field, solid particle characteristics and target material properties, affect the erosion resistance of a material experiencing solid particle erosion, according to Hutchings [2.7] and Clark [2.8]. Table 2.1 illustrates the groups of these parameters in more detail.

Table 2.1 Three major groups of factors influencing erosion

Flow Field	Particles	Target material
Slurry velocity	Concentration	Hardness
Angle of impact	Size	Fracture toughness
Viscosity	Shape	Microstructure
Particle rebounding	Hardness	Work hardening

The various features of Table 2.1 interact with each other and it is difficult to study them independently as Clark [2.9] reported. Hence, erosion models in conjunction with laboratory work should be developed to overcome the lack of control of each single variable. The following sections analyse some of the most important elements of Table 2.1.

2.3.1.1 Flow field

Figure 2.2 illustrates the various forces acting on the particle that comes into contact with a horizontal surface [2.7]. The gravitational force is apparent in the centre of the particle due to its mass. Inter-particle contact forces may also appear in cases where other particles hit the particle of interest. The flowing fluid initiates the drag forces due to the relative motion of the fluid and the particle. The wall contact force between the particle and the surface, also named as reaction force, is the most important force as it is responsible for the deformation of the surface.

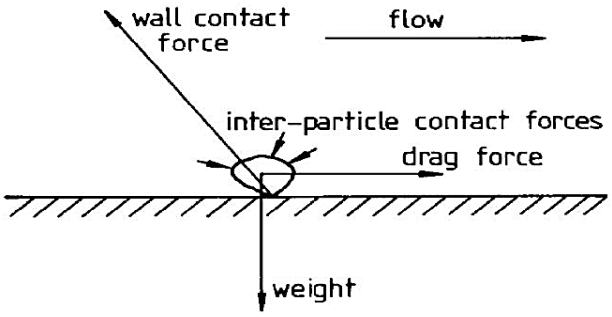

Figure 2.2 Schematic diagram of forces acting on a particle at a solid boundary. [2.7]

2.3.1.2 Viscosity

Any increase of the liquid viscosity accentuates the drag force on particles. Hence, a high viscosity liquid will prevent particle collisions with the specimen surface, reducing the collision efficiency, and subsequently the erosion rate, as demonstrated by Clark in Figure 2.3 [2.10]. Levy [2.11] has observed similar features in his research, where the erosion rate of mild steel under exposure on 23%wt 250µm SiC in solvent refined coal (SRC) process (viscosity = 52 $x10^{-3}$ N s m^{-2}) was decreased by 16 times compared with solids/tap water slurry (0.89 $x10^{-3}$ N s m^{-2}).

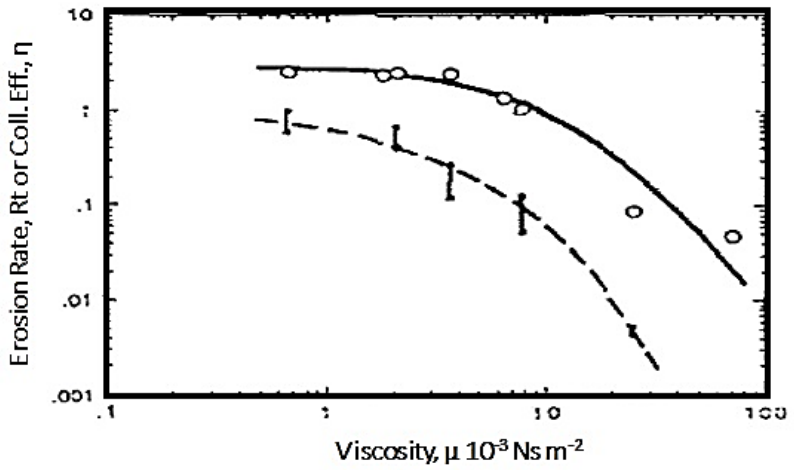

Figure 2.3 Variation in erosion rate and collision efficiency of cylindrical steel targets 4.76 mm in diameter as a function of viscosity for 3 wt% 75-106µm Al_2O_3 suspensions in a slurry pot tester at 18.7 m/s. [2.10]

2.3.1.3 Velocity

Finnie [2.12] showed a relationship between material removal and the square of velocity in air blast erosion. The erosion is correlated to the change in velocity using an exponent, n, as shown in Equation 2.3 below:

$$Erosion\_\text{rate} \propto V^{n} \qquad \textbf{Equation 2.3}$$

The "n" factor varies according to the slurry conditions (e.g. from 0.34 to 4.83) but for low solid concentration (less than 5 wt%) and ductile target materials, the exponent n is around 2.5 according to Clark [2.13].

Since the impingement velocity interacts with other environmental parameters, the investigation of its effect on erosion is not straight forward. Levy et al [2.14], studied the

effect of velocity on erosion damage of carburised UNS G86200 in solid liquid impingement with sand concentration of 0.24g/cm^3. At low velocity (12m/s) impingement resulted in 1.93 x10^{-7}g/g erosion rate of the carburised steel, whereas the same material exhibited four times higher erosion rate (8.39x10^{-7}g/g) when the impingement velocity was almost doubled (23m/s). Further velocity increase (from 23m/s to 30m/s) almost doubled the erosion rate of the carburised steel (14.26x10^{-7}g/g). As demonstrated by the researchers, the type of material can also play a significant role on the impact of velocity on erosion rates, as the hard carburised layer was eroded quicker at high flow velocities allowing the soft substrate steel to erode in shorter time compared with the low velocity (12m/s).

According to Levy and Hickey [2.15], the "n" factor of velocity also depends on the sand concentration, as the erosion/velocity slope with 20%wt sand concentration was quite different from that with 50%wt sand concentration for both UNS G10180 carbon steel and the UNS S30400 stainless steel. Hence, sand concentration interplays with the velocity which makes the erosion prediction more complicated. The severity of the velocity is also influenced by the impact angle of the solid particles as reported by Singh et al [2.16], who investigated the effect of velocity on the relative air blast erosion of two austenitic stainless steels (UNS S30400, UNS S31600) and a martensitic stainless steel (UNS S41000) under three different impingement angles (90^o, 60^o, 30^o). The impact of the velocity was less predominant on 90^o rather than on 30^o angle of impingement.

2.3.1.4 Sand characteristics

2.3.1.4.1 Sand Size

By increasing the particle size, the erosion rate will be accentuated [2.13]. The particle size can be related to erosion rate by Equation 2.4:

$$Erosion\_\text{Rate} \propto (\text{Particle\_Size})^m \qquad \textbf{Equation 2.4}$$

where "m" is the particle size exponent.

The particle size exponent "m" has been reported to vary in the range 0.3-2 [2.17]. This variation is attributed to the differences in the material properties, experimental conditions, particle size, and size distributions according to Clark [2.13]. Lynn et al [2.18], demonstrated that and increase in the particle size (from 20μm το 500μm) results in higher erosion rates of grade P110 oil well casing pipe steel in 1.2wt% suspensions of SiC powder in

diesel oil at 18.7m/s nominal speed due to the higher collision efficiency. Similar trends were found by Tian et al [2.19], who reported that an increase of the particle size led to intensified wear rates on the high chromium cast irons in a Corriolis tester.

The prediction of the particle size effect is not simple and for this reason there is on-going research on characterisation of the particles to understand their effect on erosion [2.20,2.21]. Clark and Hartwich [2.22] also reports that change of the erodent particle size can cause changes in the slurry flow conditions and particle impact behaviour which means that the experimental results with different particle sizes would hardly be directly comparable even though they have been conducted at the same nominal tests conditions. Clark's statement about the complications that arise on studies that focus on the particle size effect was evident in the work of Neville and Reza [2.23] on high chromium cast irons. The relative performance of the three white cast irons and the reference austenitic stainless steel (UNS S31603) was found to change with the change of the erodent size, showing clearly that the erosion resistance depends on the slurry conditions.

2.3.1.4.2 Sand shape

The sand shape should be considered along with the feed rate and the sand size to derive a relationship between the sand properties and abrasion, as reported by Woldman et al [2.24]. The particle shape dictates the form of the plastic deformation and the quantity of the displaced material by its collision. Palasamudram and Bahadur [2.25], conducted erosion tests in a fluidised bed tester and they reported that the round silica sand particles resulted in a smoother eroded surface of the UNS G10200 steel than the angular SiC and alumina particles which penetrated the steel's surface deeper producing a rugged topography. It is noteworthy that the three sand types used in their study depicted extremely higher hardness than the target material, and hence the mechanisms described above were derived only by the sand shape. Desale et al [2.26], concluded similar outcomes in their study on the effect of shape of erodent particles on the erosion wear of ductile materials. In fact, they discovered that angular sand particles produce deep craters and generates higher average surface roughness compared to that of the rounded particles.

2.3.1.4.3 Sand concentration

As the solid concentration increases, the number of impacting particles in solid liquid mixture increases, causing higher erosion rates. Levy et al [2.14], demonstrated that the erosion rate

of carburised UNS G86200 steel doubles when the sand concentration is raised from 0.12g/cm^3 to 0.24 g/cm^3 at 23m/s sand water slurry impingement velocity. Neville and Hu [2.27], have also studied the effect of sand concentration on pure erosion resistance of three stainless steels (UNS S31245, UNS S32654, UNS S32750) under impingement. Their findings indicated that the mass loss of the stainless steels due to erosion was increased by a factor of two when the solid loading was raised from 150-200mg/l to 600-640mg/l.

However, Steinour [2.28] suggested that above 5wt% sand concentration, significant interaction between particles is observed. Spencer and Sagues [2.29] investigated the erosion rate of UNS S30400 stainless steel under air jet impingement at 40m/s velocity at normal incidence and found that over the range of 1.4-8wt.% silica sand the erosion rate was reduced by 40%, in terms of mass loss per mass of the impinging particles. Similar particle-particle interactions can also be obtained during slurry erosion, and a good example is reported by Turenne et al [2.30] work, in which the erosion rate of pure aluminium was increased as the sand concentration was increased on the slurry jet impingement apparatus. They showed that the influence of the sand concentration on erosion rate decreases as the sand concentration increases. The collision of the particles leads to loss of the kinetic energy of the particle that would subsequently cause lower impact energies on the target material. It is believed that an instantaneous stratified sand bed is formed at the target surface by the particles, which have insufficient energy to rebound off the target, and subsequently acts as a barrier to the incoming particles. This usually happens in circumstances, where the flow velocity is low.

An additional view about the effect of sand concentration was derived by Zitoun et al [2.31], whose research focused on the investigation of the solids velocity, solid motion and orientation in solid liquid flow by using particle tracking velocimetry. They found that despite the solids interaction in high solid concentration, there is also a reduction of the free space for free motion that result in further reduction of erosion rates.

2.3.1.5 Impingement angle

The erosion rate of materials is strongly related to the impingement angle of the particles on the target surface. Finnie [2.32] showed that the maximum erosion damage of ductile type materials is observed between 10^o and 20^o. On the other hand, the mass loss of brittle

materials increases linearly by moving from glancing angles towards high impact angles (90°). Figure 2.4 demonstrates the wear trends of ductile and brittle materials.

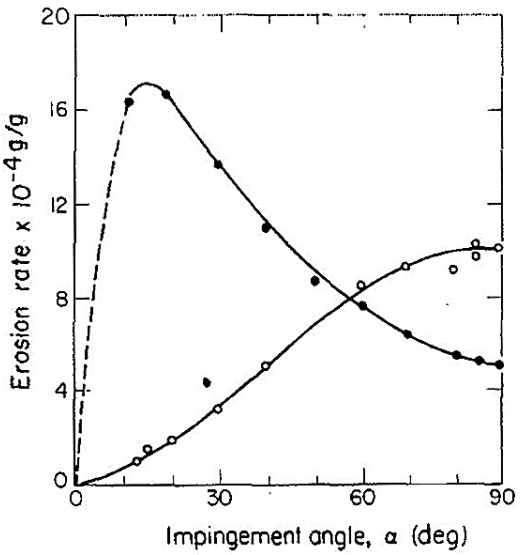

Figure 2.4 Impingement angle effects on a typical ductile (●) and brittle (○) material. [2.32]

Finnie's work [2.32] has shown that ductile materials are more susceptible at oblique angles as "cutting" mechanism takes place at those angles. He showed that the particles strike on the surface causing strain of the metal surface and initiating lips that would be detached after multiple cycles of plastic deformation. The brittle materials do not undergo such plastic strain processes and hence they show superior erosion performance at low angles.

Burstein and Sasaki [2.33], showed that the austenitic stainless steel UNS S30400 exhibited its maximum erosion rate at 43°, which agrees with Finnie's findings as the UNS S30400 is a common ductile material. Feng and Ball [2.34], investigated the performance of WC-7Co hardmetal and a stainless steel UNS S30400 under air blast erosion. The WC-7Co hardmetal experienced a brittle response to erosion as the maximum erosion was obtained at 90°, whereas the UNS S30400 stainless steel exhibited a more ductile response since its maximum mass loss was obtained at 20°.

Indication that the influence of angle of impingement can be similar in erosion-corrosion situations come from the two following studies. Andrews et al [2.35], reported similar behaviour of the UNS S31600 stainless steel which displayed its highest erosion

damage on 45^{o} under solid/liquid impingement. Stellite 6 exhibited its maximum erosion damage at 60^{o}. The brittle Co carbides of the Stellite 6 were assumed to be the reason for this behaviour. Clark and Wong [2.36], also compared a brittle material (pyrex glass) with the ductile hot rolled UNS G10200 carbon steel in a slurry pot tester. Their outcomes showed similar features as Figure 2.4, where the brittle material undergoes high erosion rates on normal impacts but the maximum damage of the carbon steel was between 30^{o} and 35^{o} angle of attack.

2.3.1.6 Relationship between the target material and the abrasive particle characteristics

Further investigation of the microstructure of the target material and the sand particle properties is required to define the erosion resistance of material. Shipway and Hutchings [2.37] proposed the hardness ratio of the particles and the target material (Hp/Ht) to model the air blast erosion damage. If the particles were harder than the target, erosion by an indentation-induced fracture mechanism would occur, whereas when the particles are softer than the target, a small scale chipping mechanism would take place. Desale et al [2.38], showed that the hardness ratio can also be applied on erosion of ductile materials (UNS A96063 and UNS S30400) under 90^{o} impingement with alumina particles in a slurry pot test. The lower the Hp/Ht ratio resulted in lower erosion rates of the tested materials. Desale et al [2.26] and Ninham [2.39] also studied the effect of hardness of the erodent on the erosion rate of various materials and they found that, no matter of the mechanical properties of the target, the higher the hardness of the abrasive the greater material loss would occur.

The target hardness, though, cannot be considered as a single factor for erosion resistance prediction as other mechanical properties such as ductility, toughness and elastic modulus also play a significant role on the erosion behaviour of the target. Neville and Hu [2.27] have reported that macrohardness of the material is not the controlling factor of the pure erosion under slurry conditions as the UNS S42750 superduplex stainless steels (318HV) exhibited better erosion resistance than the two harder (335HV) superaustenitic stainless steels (UNS S31254 and UNS S32654) emphasising the role of microstructure. Giourntas et al [2.40], also reported that the simple correlation of the pure slurry erosion behaviour with the material hardness is questionable, as the UNS S32760 superduplex stainless (257HV) showed superior erosion resistance to impingement compared to the UNS S17400 martensitic stainless steel (358HV).

Hardness can be more indicative of the erosion resistance of the material when it is correlated with the elastic modulus, which is another important mechanical property. High values of the ratio of hardness to elastic modulus are always desirable to absorb high levels of elastic energy as well as having high resilience and toughness [2.41,2.42]. Some researchers are favoured to use the hardness in conjunction with fracture toughness [2.43]. Foley and Levy [2.44], studied the erosion behaviour of a UNS S30400 stainless steel on its annealed and as-wrought form on an air blast erosion tester. They found that the greater ductility of the annealed UNS S30400 provided an advantage against erosion compared with the as rolled form. In fact, the ability of the annealed UNS S30400 stainless steel to plastically deform during the repeated impact of the sand particles resulted to an increased yield strength which reduced the erosion rate.

The complications about the hardness and the erosion rates are mostly evident on the impingement and not on the sliding abrasion, which is in essence a form of low impact angle erosion. This remark can be related to Finnie's research outcomes [2.32] where the ductile materials, commonly soft metals, experience high erosion rates on the oblique angles whereas the brittle materials, mainly hard metals, are not affected at all. Richardson [2.45] proposed the necessity of the surface hardness to exceed the hardness of the erodent, particularly under abrasion conditions. Thus, the hardness facilitates a good estimation of the low impact angle erosion resistance of a material.

It is clear that there is always an objective to quantitatively correlate the erosion damage to the mechanical properties of the target material. However, the use of the conventional mechanical properties is more likely to be unsuccessful according to Sundararajan [2.46], who suggested that the laboratory results would be more relevant, if researchers would incorporate mechanical properties determined under high-strain-rate conditions into pure erosion damage models.

2.4 Corrosion Background [2.47–2.49]

Most metals have a tendency to corrode in an aqueous environment as they are converted from their relatively unstable condition (alloy) to a more stable state (ore). In more detail, the tendency of corrosion to occur can be expressed via the thermodynamic property, free energy. Chemical thermodynamic principles demonstrate that a spontaneous reaction is

associated with a reduction in free energy of the system. In other words, when metal converts to corrosion product, the free energy change is negative. This transformation comprises two electrochemical reactions; anodic and cathodic. For example, the metal M corrodes as follows:

$$M \Rightarrow M^{z+} + ze^{-} \qquad \textbf{Equation 2.5}$$

Where, "z" varies according to the valency state of the metal.

In neutral and alkaline aqueous solutions, the cathodic reaction is usually the following, also called as "oxygen-reduction":

$$O_2 + 2H_2O + 4e^{-} \Rightarrow 4\left(OH^{-}\right) \qquad \textbf{Equation 2.6}$$

It is evident that the corrosion rate is controlled by the availability of oxygen at the corroding metal surface.

In acidic environments, however, the following cathodic reactions are more likely to occur:

$2H^{+} + 2e^{-} \Rightarrow H_2$ (In the absence of oxygen) **Equation 2.7**

$4H^{+} + O_2 + 4e^{-} \Rightarrow 2H_2O$ (In the presence of oxygen) **Equation 2.8**

$2H_2O + 2e^{-} \Rightarrow 2\left(OH^{-}\right) + H_2$ ("Water reduction reaction") **Equation 2.9**

2.4.1 Electrode potential

As shown in Equations 2.5-2.9, there is a charge transfer across the metal surface at anodic and cathodic sites. This charge transfer is associated with a potential difference which is called "the electrode potential" and it yields useful information about corroding metals. The measurement involves connection of the metal to a reference electrode via a high-impedance voltmeter. The voltmeter would indicate the electrode potential measured using a stated reference electrode (e.g. saturated calomel reference electrode (SCE) or a silver/silver chloride reference electrode (Ag/AgCl)).

2.4.2 Equilibrium electrode potential

For any given electrode reaction and specific circumstances, there is a certain value of electrode potential, E_o, called equilibrium electrode potential, at which the electrode reaction is at equilibrium. The value of E_o depends upon the temperature and the concentration of the chemical substances that take part in the reaction. For example, these relationships for the metal-dissolution reaction can be described with the following Equation 2.10:

$$E_o = E_o^{\,o} + \frac{\left[R \times T \times \ln\left(\frac{C_{m^n}}{C_m} \right) \right]}{n \times F} \qquad \textbf{Equation 2.10}$$

where, C_{mn} and C_m respectively represent the concentration of the metal in the aqueous environment and in the metal itself.

R is the general gas constant

T is the temperature,

F is the Faraday's constant

n is the number of electrons involved in the reaction.

E_o° is the standard equilibrium potential that represents a particular value of the equilibrium electrode potential when the substances are in the "standard states".

If the electrode potential is more positive than the equilibrium electrode potential, E_o, the electrode reaction is driven in the anodic direction (i.e. $M \rightarrow M^{n+}+ne^-$) and eventually the corrosion of the metal is initiated. The rate of the electrode reaction at any electrode potential is governed by the polarisation phenomenon.

2.4.3 Polarisation

Since electrode reactions involve transfer of charge, their rates can be expressed in term of current flow. The magnitude of the current flow is dependent upon the electrode potential but also by so-called "polarisation phenomena". The term "polarisation" relates to event at, or near, the metal surface controls the rate of the electrode reactions. The effects of polarisation are illustrated on "polarisation diagrams" that are plots of electrode potential

versus some function of current. Figure 2.5 shows the schematic diagrams of the anodic polarisations of two different electrodes.

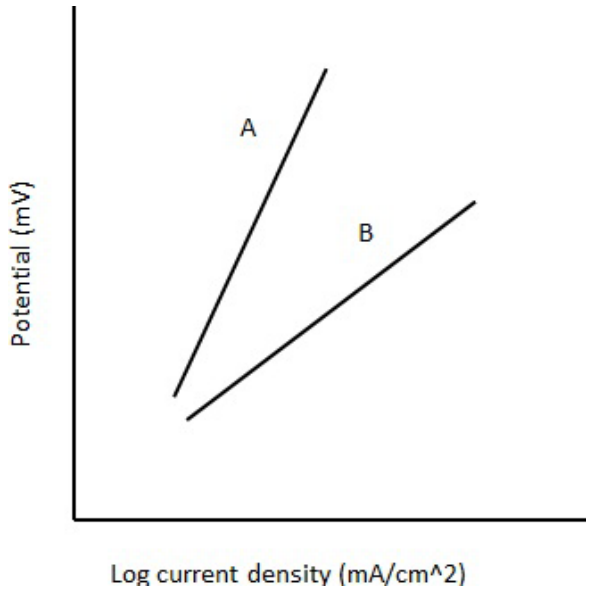

Figure 2.5 Anodic polarisation scans of two different electrodes (A & B).

In flowing or turbulent conditions, the relationship between electrode potential and current is given by the Tafel relation (Equation 2.11), which for anodic reactions is

$$E - E_o = b_a \log_{10}\left(\frac{i_a}{i_o}\right)$$

Equation 2.11

where,

b_a is known as the anodic Tafel slope, i_a is the anodic current density and the i_o "exchange current density".

And for cathodic reactions

$$E - E_o = b_c \log_{10}\left(\frac{i_c}{i_o}\right)$$ **Equation 2.12**

where, the $E\text{-}E_o$ has a negative value since the E would be less negative than the E_o, the i_c is the cathodic current density (i.e. rate of charge transfer across cathode interface), i_o is the exchange current density for the particular cathodic reaction and b_c is the Tafel constant.

2.4.4 Passivity

Passivity refers to the loss of chemical reactivity of the metal surface under particular environmental conditions. Some metallic alloys form thin, non-porous and adherent oxide films which protect the underlying metal from corrosive attack. Good examples of this type of behaviour are the stainless steels, other groups of chromium-rich alloys as Inconels (Ni-base) and Stellites (Co-base), titanium. This group of materials is often called corrosion resistant alloys (CRA).

2.4.5 Types of corrosion

Corrosion is apparent in different types and these are divided into two major groups; general corrosion and localised corrosion. The general corrosion involves distributed attack over the surface of the material, and it leads to a generally uniform thickness loss. There are many different types of localised corrosion, some of which are discussed in the following sections.

2.4.5.1 Galvanic Corrosion

Galvanic corrosion occurs when two different metals are exposed to an aqueous solution and are in contact by bolting or welding or connected through an electrical conductor. An example of this galvanic cell is shown in Figure 2.6. The electrode potential of each metal dictates the corrosion tendency, and hence, the more electronegative of the two metals (i.e. the metal which has the more negative electrode potential) becomes the anode and the other metal becomes the cathode. As a result, the less noble metal suffers more corrosion whereas the more noble metal suffers less corrosion than if they were immersed in the same environment separately. The flowing current between these two components represents the additional corrosion damage exhibited by the anode. The driving force for galvanic corrosion is the difference in electrode potentials of the two components when exposed separately in the same environment.

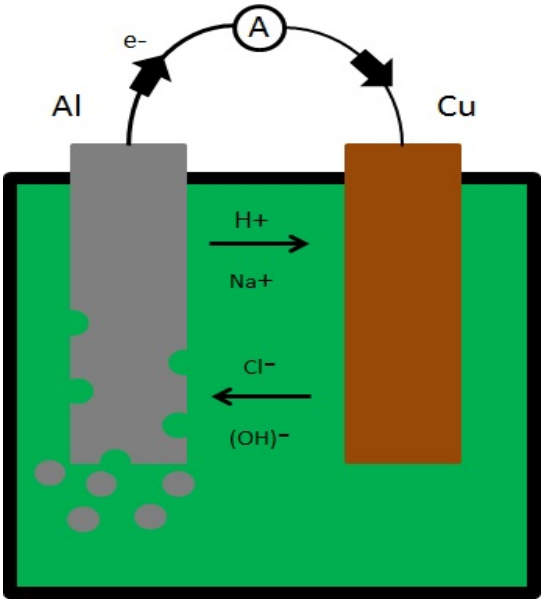

Figure 2.6 Galvanic cell between aluminium (Al) and copper (Cu).

The relative areas of the two metals are also important. Large areas of cathode, and small areas of anode will accelerate the attack on the anode, resulting in deleterious failure of the engineering system. The total rate of production of electrons (i.e. anodic current, i_a) must be equal to the total rate of consumption of electrons (i.e. cathodic current, i_c).

$$i_a \times A_a = i_c \times A_c \qquad \textbf{Equation 2.13}$$

where

i is the current density (A/cm^2) and A is the surface area of the component

If $A_a << A_c$ i.e. small anode with large cathode

$i_a >> i_c$ high dissolution of the anode.

2.4.5.2 Pitting and Crevice corrosion

Pitting corrosion is a local attack that occurs due to the fact that some regions of the material surface have higher corrosion rates from others, either due to the absence of passive film or because of higher sensitivity to various environmental effects. As a result, both types occur on materials which have the ability to form passive films. Figure 2.7, shows the surface pits on the surface of an austenitic stainless steel under liquid impingement.

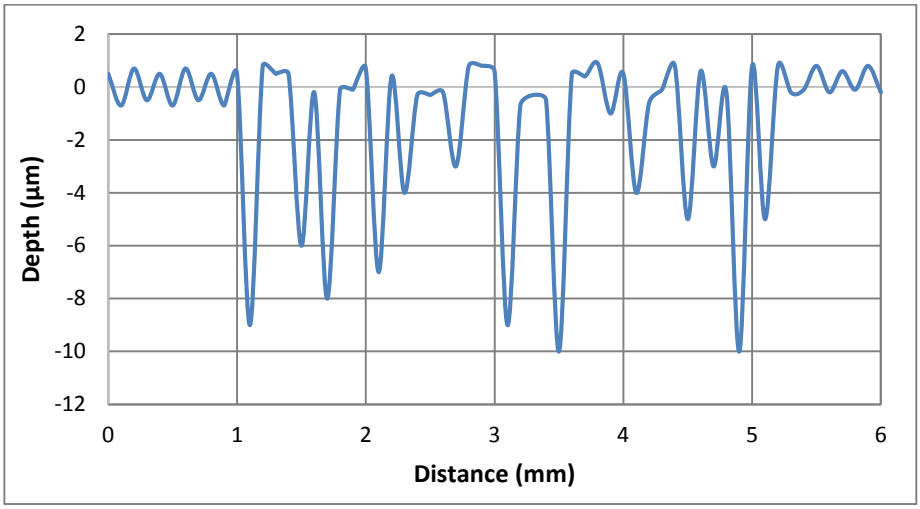

Figure 2.7 Example of pitting corrosion.

The major difference between the pitting and crevice corrosion is that the former usually takes place on the free surface of a material whereas the latter develops under a deposit on the surface or at joints of an assembly. The pitting resistance equivalent number (PREN) [2.50] shown in Equation 2.14, determines the resistance of the stainless steels to pitting corrosion but it can be applied also to crevice corrosion too.

$$PREN = w_{Cr} + 3.3\,w_{Mo} + 1.65\,w_{W} + 16\,w_{N} \qquad \textbf{Equation 2.14}$$

where,

W_{cr} is the weight percentage of chromium in the alloy,

W_{Mo} is the weight percentage of molybdenum in the alloy

W_{w} is the weight percentage of tungsten in the alloy

W_{N} is the weight percentage of nitrogen in the alloy

Figure 2.8 demonstrates the low crevice corrosion resistance of the martensitic stainless steel UNS S42000, which confirms that the PREN number can also be applied for the crevice corrosion resistance. The martensitic stainless steel UNS S42000 exhibits a PREN of 13, almost half the value of the austenitic stainless steel UNS S31600 (PREN = 27).

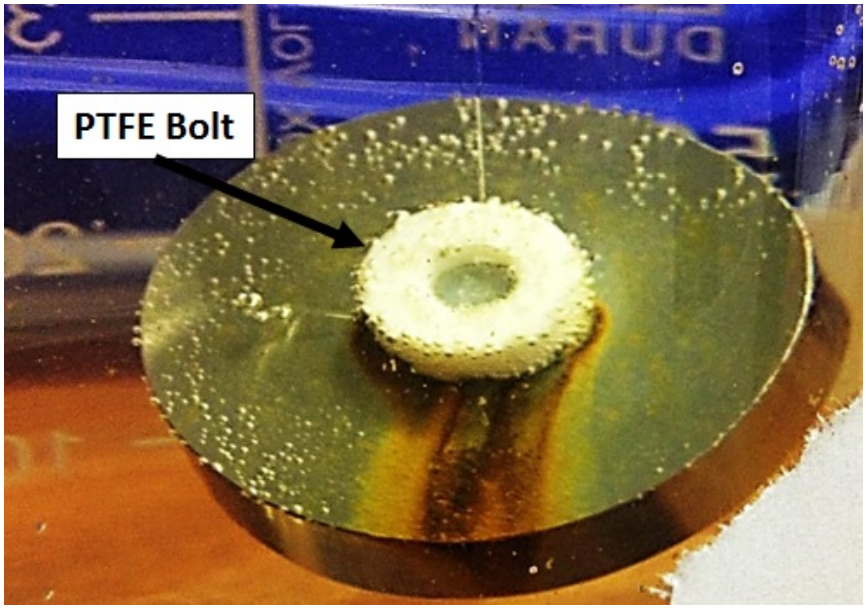

Figure 2.8 Corrosion attack on a UNS S42000 martensitic stainless steel under a 24h crevice corrosion test.

2.4.5.3 Intergranular corrosion

Intergranular corrosion takes place at grain boundaries with significant deterioration effects. The corrosion attack propagates into the material, which makes it one of the most dangerous forms of corrosion, as surface grains become detached from the component. The main cause of intergranular corrosion is the precipitation at/or adjacent to the grain boundaries of phases vulnerable to corrosion or depletion of an element that in crucial for the corrosion resistance of the material (e.g. chromium in stainless steels).

2.4.5.4 Stress corrosion cracking and corrosion fatigue

Both stress corrosion cracking (SCC) and corrosion fatigue involve failure of a component by crack propagation during service. SCC occurs in the presence of a steady applied or residual tensile stress. The environmental conditions are playing significant role on SCC initiation on each material, as they have to be extremely specific; e.g. low pH range or a certain temperature. During the SCC process, one or more cracks initiate on the surface of the component surface and a slow crack propagation occurs which is followed with component fracture or leak. Most SCC failures are originated from residual stresses, which makes the SCC prediction extremely difficult. On the other hand, corrosion fatigue involves deterioration under fluctuating stress loading that can occur in any environment. Material flaws, like inclusions, and corrosive environments accelerate the fatigue deterioration process of the component.

2.4.5.5 Hydrogen embrittlement

Hydrogen embrittlement (HE) occurs by the ingress of hydrogen into the material surface, which leads to decrease of ductility and load bearing capacity. One example of HE is when a cathodic protection system is subjected to poor control. HE can also occur in heat affected zone (HAZ) of welded components or in hardened steels when they are exposed to hydrogen injection conditions.

2.4.6 Environmental factors

The severity of the corrosion is associated with the environmental factors that the alloy is exposed to. The effects of these environmental factors are discussed below:

2.4.6.1 pH

The pH is the measure of the hydrogen cations (H^+) concentration in the aqueous solution, which is defined as pH = $-\log_{10} C_{H+}$. Figure 2.9 demonstrates the logarithmic pH scale (at temperature 25 ^oC) with the red side representing the acidic solutions and the blue side representing alkaline (basic) water.

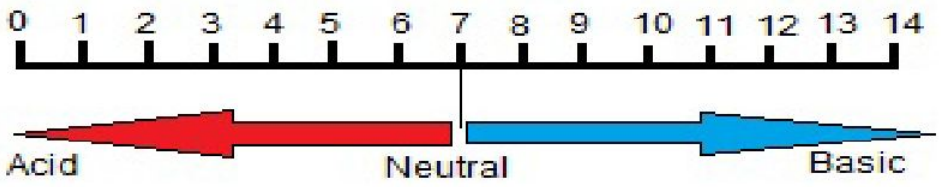

Figure 2.9 pH scale

The fact that is logarithmic indicates that any change from one decade to the other, the H^+ concentration should be either raised or decreased by ten times. The majority of the water in earth is around neutral state. However, some oil and gas operations and more frequently in mining processing involve either acidic or alkaline water. Also, pollution of the sea water can alter the pH from its normal pH of around 8.

When pH becomes more acidic, the passive oxide film of the corrosion resistant alloys is likely to destabilise, which tends to cause accelerated corrosion on their metal surface. Exposure of materials, with absence of passive film, into low pH media would provoke hydrogen-reduction cathodic reaction rather than oxygen reduction. In multi-phase alloys, like high chromium white irons, the effect of pH causes complex phenomena. In neutral and acidic environments, local galvanic cells can be set up with the metallic matrix

acting as an anode, and the noble carbides the cathode [2.51]. In alkaline environments, though, it has been observed that the alkalinity transforms the carbides into anodic regions and the matrix as cathode [2.52].

2.4.6.2 Flow velocity

It is well known that any increase of the flow velocity will result in an increase of the oxygen reduction reaction rate as the dissolved oxygen concentration at the metal surface will be enhanced. Figure 2.10 illustrates the difference in cathodic reactions when the fluid is in static and turbulent flow. The less steep cathodic polarisation indicates a higher rate of the cathodic reaction and, and thereby an increase of corrosion rate (shown by the interpretation of the anodic and cathodic polarisation curves).

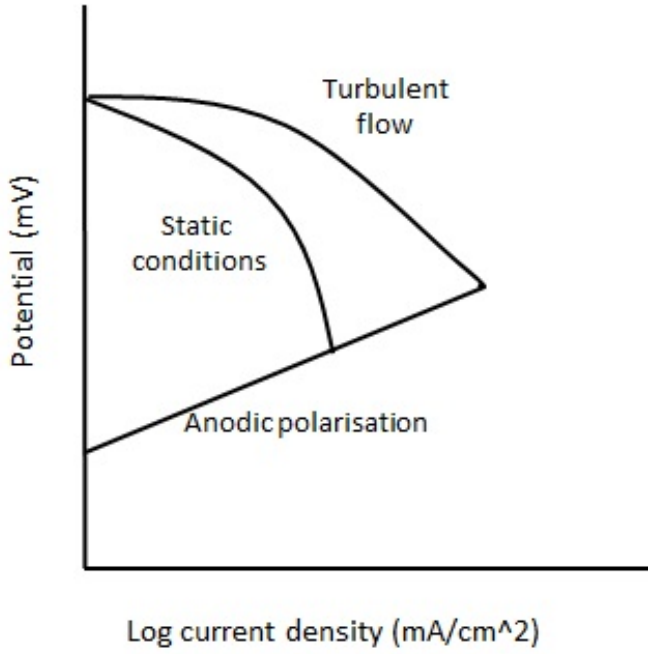

Figure 2.10 Corrosion rates in static conditions and turbulent flows**.**

Thus, the flow velocity is a significant corrosion factor in neutral and alkaline solutions, where the oxygen reduction takes place. As stated earlier, in acidic conditions when the hydrogen reduction cathodic reaction occurs, the flow velocity is less important, until the flow velocity magnitude reaches a point where the mechanical damage arises.

2.4.6.3 Temperature

Since corrosion comprises electrochemical reactions, temperature acts as a catalyst. In other words, the raise of the temperature will tend to increase the corrosivity of the aqueous solution. Figure 2.11 describes schematically the effect of the temperature in corrosion rates.

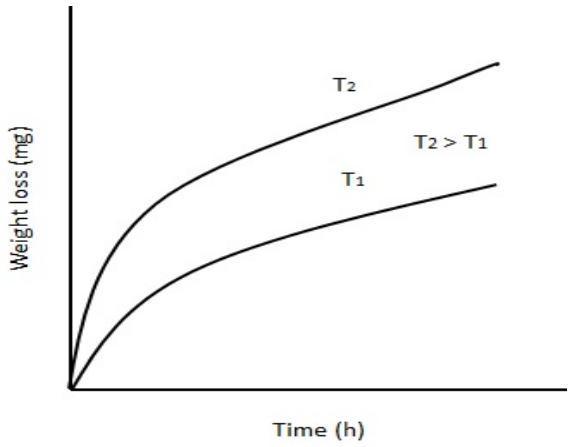

Figure 2.11 Temperature effect on the weight loss of materials

The accelerating effect of temperature can be stabilised by considering that the solubility of corrosive gases in water would be decreased when the temperature is considerably increased.

Meng et al [2.1], studied the temperature effect on their evaluation of a superduplex stainless steel and austenitic stainless steel under solid/liquid impingement. The superduplex stainless steel wasn't affected by the temperature rise from 18 ^{o}C to 50 ^{o}C as much as the austenitic stainless steel. The superior corrosion resistance of the superduplex stainless steel on Meng et al work was associated with the higher chromium content compared to austenitic stainless steel. Mesa et al [2.53], also reported that the specific mass loss was increased linearly with the testing temperature. Aiming et al [2.54], highlighted the testing temperature as corrosion factor as the mass losses of the stainless steels were raised in all impingement angles. Hu and Neville [2.55], also stated that the rise of temperature in conjunction with the higher solid loading can become deleterious on stainless steels.

2.4.6.4 Dissolved salts

The presence of sodium chloride in an aqueous solution intensifies the corrosion processes. The charged ions increase the electrical conductivity of the fluid solution. Hence, the current within the corrosion cells flows in higher magnitudes. In general, 99% of the dissolved solids

constitute of chloride (55.04%), sodium (30.61%), sulphate (7.68%), magnesium (3.69%), calcium (1.16%) and potassium (1.10%). These salts are playing a significant role to the corrosion action of the sea water.

Addition of 3% NaCl into the acidic aqueous solution (pH=2) resulted in higher corrosion rates of white cast irons in Tian and Taylor's [2.56] work. Al-Malahy and Hodgkiess [2.57] reported that even the rise of 3.5% to 5.5% (maximum salinity percentage observed in sea water) can reduce the breakdown potential substantially, which indicates that the corrosion severity is increased. Guanghong et al [2.58], has also studied the effect of NaCl on SS316L and a 13Cr-23Mn-0.44N erosion-corrosion performance and they concluded that their mass loss ratios can be increased up to 50% in a slurry pot tester.

2.4.6.5 Dissolved gases

Dissolved gases often play a key role in stimulating corrosion. Oxygen, carbon dioxide and hydrogen sulphide are the most important dissolved gases in sea water.

Oxygen is the basic element in the corrosion process occurring in most neutral and alkaline environments, as it is the key reactant of the oxygen reduction cathodic reaction. The concentration of oxygen at the metal surface depends on temperature, time, flow velocity and the biological activities that take place. De-aerated waters (absence of oxygen), tend to be less corrosive than the aerated. Parent and Li [2.59] have shown that the mass loss of the X65 and dual phase stainless steel erosion-corrosion damage is decreased to half when the dissolved oxygen is depleted.

The carbon dioxide is contributing to the cathodic reaction rate by reducing the H_2CO_3 or dissociating the H_2CO_3 that can result in higher source of H^+ ions, forming a weak acid, called carbonic acid. Yu et al [2.60] stated that the mass loss of X65 steel is increased by 50% by the dissolved CO_2 at a slurry velocity of 3.5m/s, whereas the difference between the aerated slurry and aerated slurry and CO_2 would be decreased when the slurry velocity would increase.

Hydrogen sulphide is also apparent in sea water solutions as a product of metabolism reactions of the sulphate reducing bacteria (SRB). The concentration of hydrogen sulphide usually amplifies the corrosion of ferrous and non-ferrous materials.

2.4.7 Electrochemical monitoring systems

2.4.7.1 DC - Linear polarisation

Stern-Geary [2.61] simplified the kinetic expression to provide an approximation to the charge-transfer-controlled reaction kinetics given by Equations 2.11 and 2.12 for the case of small over potentials with respect to E_{corr}. If the equations will be linearised by taking its series expansion and neglecting higher terms, the equation will form as described below:

$$R_p = \frac{b_a \times b_c}{2.3 \times (b_a + b_c) \times i_{corr}} \qquad \textbf{Equation 2.15}$$

where,

R_p is the polarisation resistance measured through the gradient of the polarisation plot (E/I) at small overpotentials (dE/dI).

The Equation 2.15 can be rearranged in respect to i_{corr}:

$$i_{corr} = \frac{b_a \times b_c}{2.3 \times (b_a + b_c) \times R_p} \qquad \textbf{Equation 2.16}$$

Since the measured current is approximately linear within a potential range of ±20mV from E_{corr}, this technique is called linear polarisation. Linear polarisation monitoring is mainly used to provide reasonable estimates of changes in corrosion rate without altering the surface condition of the specimen. Calculations of accurate values of corrosion rate crucially depend on using the reliable values of the anodic and cathodic Tafel slopes (b_a and b_c). In cases where the Tafel slopes are not known, the R_p can still provide a qualitative indication of the corrosion current density.

2.4.7.2 DC - Tafel plots

The Tafel plots are not limited to scans of small potential ranges around E_{corr} but they utilise a broader DC potential spectrum (at least 200mV away from E_{corr}). Figure 2.12 demonstrates the E/I plot, where the current is plotted on a logarithmic scale, and the coloured lines represent the Tafel plots for the anodic (red) and cathodic (blue). Extrapolation of the linear parts of the scans back to E_{corr} yields the corrosion current density.

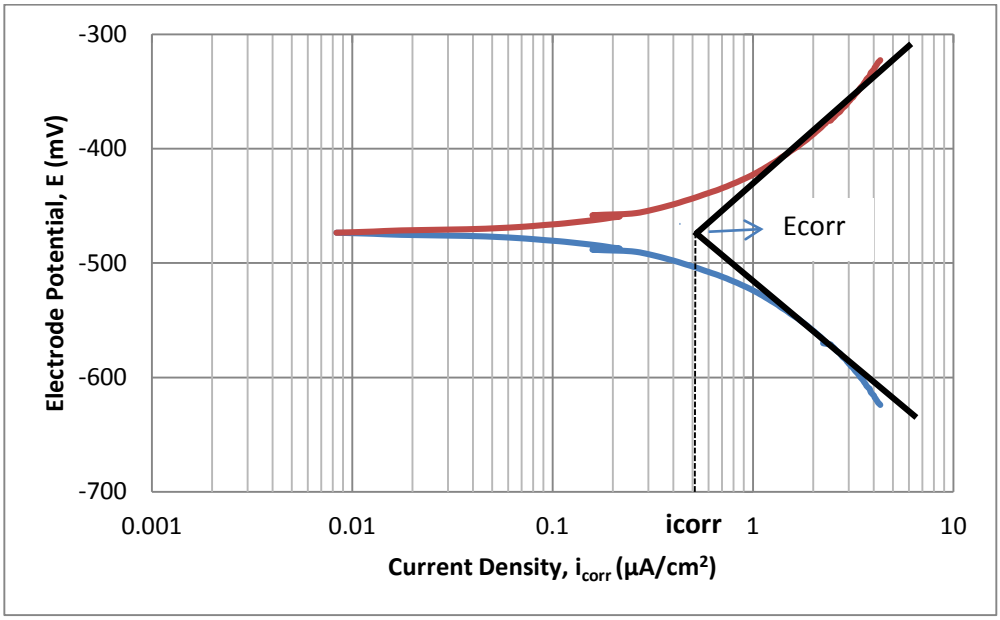

Figure 2.12 Schematic diagram of an anodic and cathodic polarisation along with the Tafel extrapolation lines.

Faraday's law can be applied to determine the mass and thickness loss due to corrosion, from the corrosion current density. Faraday's law declares that the mass loss of a substance during an electrode reaction is directly proportional to the quantity of electricity transferred at that electrode in relation to the anodic reaction $M = M^{z+} + ne^-$.

$$Mass\_Loss \propto i_{corr} \qquad \textbf{Equation 2.17}$$

Faraday law also states that for a given quantity of electric charge, the mass loss of a metal is directly proportional to the element's equivalent weight. Thus, the synopsis of Faraday's law can be described by the Equation 2.18 below:

$$Mass\_Loss = \frac{i \times M}{n \times F} \qquad \textbf{Equation 2.18}$$

where,

i is the corrosion current, M is the molar mass of the alloy, n is the valency of the metal and F is the Faraday constant.

The thickness loss, also referred as penetration rate, is also useful factor for the industry and it is expressed in mm/year using the Equation 2.19 below:

$$Thickness\_Loss = \frac{i \times M}{n \times F \times \rho \times A} \times 60 \times 60 \times 24 \times 365 \qquad \textbf{Equation 2.19}$$

where,

ρ is the material's density and A is the exposed surface area.

This technique can be used to provide information on the corrosion behaviour in three ways:

1) Corrosion rate through Tafel extrapolations.
2) The values of the Tafel slopes of anodic (b_a) and cathodic (b_c) curves, which are required for the i_{corr} calculation in linear polarisation exercises.
3) The breakdown potential, which is an indication of the localised corrosion resistance of a material, can be measured by undertaking a wider anodic scan than that required for the Tafel extrapolation.

2.4.8 Mitigation of corrosion

Corrosion can be mitigated through various protection techniques that are listed below:

1. Application of inhibitors
2. Material selection that involves CRA's and coatings
3. Application of cathodic protection methods

2.4.8.1 Application of inhibitors

Inhibitors are widely used as corrosion control strategy, especially in oil and gas pipelines. The inhibitor mechanism is consisted by its adsorption on the metal surface forming a compact protective thin layer. This protective film enables suppression of either anodic or cathodic reactions or both. The effects of organic inhibitors have received some attention in relation to erosion-corrosion. Neville and Wang [2.2] reported that the erosion-corrosion resistance can be substantially increased, up to two times, by adding inhibitors which are minimising the corrosion component to zero.

The effect of inhibitor concentration was also assessed by the same group of researchers, discovering that the higher inhibitor concentration results in additional corrosion resistance even in erosion-corrosion conditions [2.62]. Hu et al [2.63], have examined the effect of the corrosion inhibitors used on real elbows' pipework to determine the degradation mechanisms, and they found that the concentration and the type of the

inhibitor used in the flowing system influences substantially the corrosion protection of the elbows.

2.4.8.2 Material selection

Carbon steels are widely employed in many engineering sectors due to their low cost and their attractive mechanical properties. However, their drawback is their relatively poor corrosion resistance. There are two main strategies to counteract their poor performance under corrosive slurries; application of corrosion resistant coatings or their replacement with corrosion resistant alloys. The corrosion resistant coatings function as barriers to the exposure of the substrate to the environment.

Fusion bonded epoxy coatings are widely selected for the corrosion protection of offshore pipelines [2.64]. HVOF spray WC-based coatings comprise another group of corrosion resistant coatings, which can double the service life of a component, according to Hodgkiess et al [2.65]. The application of CRAs into engineering components as potential candidates of replacement of carbon steels is also a possible corrosion mitigation route [2.66]. Giourntas et al [2.40], showed that stainless steels exhibit up to eight times greater corrosion resistance than carbon steel under solid/liquid impingement. Karafyllias et al [2.67], has also reported the substantial difference in corrosion behaviour when the pH is more acidic (pH = 4) and the superduplex stainless steel shows about 110 times lower corrosion rate (i_{corr}) than the carbon steel under solid/liquid impingement.

2.4.8.3 Cathodic protection

The basis of cathodic protection is to drive the electrode potential (E_{corr}) of the freely corroding component down to more negative values. This shift of the electrode potential stimulates cathodic reactions and reduces the rate of the anodic reactions which are completely suppressed when the electrode potential reaches the value of the equilibrium electrode potential for the anodic reaction. The electrode potential shift can be achieved by either application of a direct current from an external DC generator or as a result of electrically coupling the component to a less noble metal.

2.5 Synergy

As mentioned in section 2.1, the synergy is not a totally separate deterioration process but the interaction between the electrochemical and mechanical mechanisms. This type of

material degradation can be a result of a series of corrosion effects that enhance the mechanical damage. Wood et al [2.68], reported that the transformation of the austenite to martensite, as work hardening process occurs during the impact of solid particles to the target material, creates a hardened layer which is more vulnerable to corrosion and to instantaneous removal resulting in exposure of the softer metal surface that will enhance the erosion.

Intergranular corrosion can also increase the erosion rate, as entire grains flake off the metallic structure as a result of lack of mechanical support. Figure 2.13 represents a photomicrograph of a grey cast iron specimen that had been subject to erosion corrosion with an impinging jet [2.69]. Corrosion has occurred along the graphite/metal interface and this has accelerated the removal of material by erosive action.

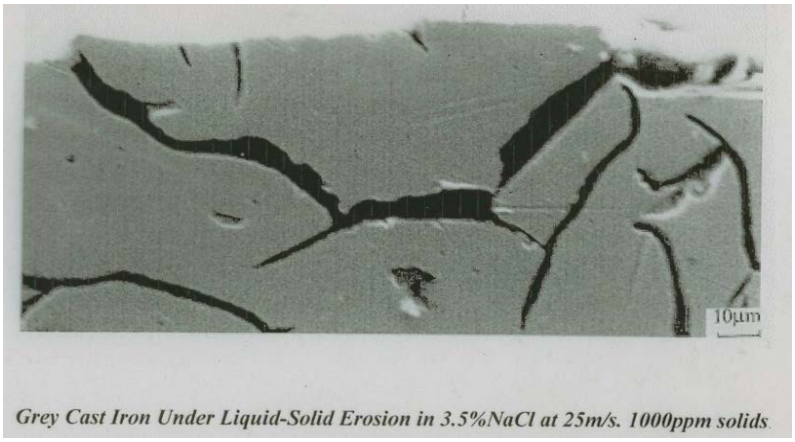

Figure 2.13 Example of the synergy mechanism during erosion-corrosion of grey cast iron in saline solution**.** [2.69]

The galvanic interactions in multiphase materials, like Co-based alloys or high chromium cast irons, can also result in accelerated erosion. It is evident from Neville and Hodgkiess [2.70] study on superduplex stainless steel, Stellite 6 and Inconel 625, where the superduplex stainless exhibited the least synergy (12%) where the multiphase alloys' synergy percentage was double to 22% and 24% for Stellite 6 and Inconel 625, respectively. Another example which indicates the role of the microstructure on the synergistical effect is apparent from the work of Jones and Llewellyn [2.71], where the hypereutectic cast iron synergy was higher than the austenitic stainless steel UNS S31600 under the same testing conditions.

It is generally accepted, though, that the synergy of materials depends on their characteristics and also on the exposure environment. Figure 2.14 illustrates the view of

Neville [2.72], who reported that the synergy is mainly apparent on erosion-corrosion conditions, and the synergy component is decreasing when the environment becomes erosion or corrosion dominated.

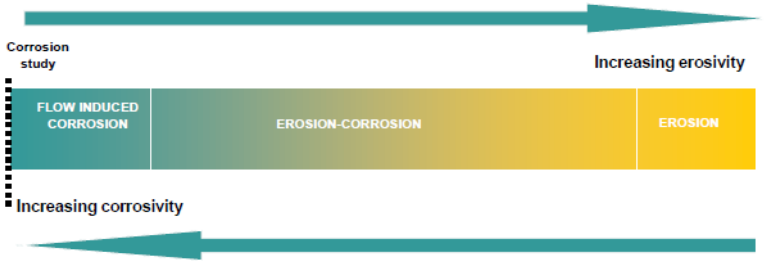

Figure 2.14 Regimes in erosion-corrosion**.** [2.72]

2.6 References

[2.1] H. Meng, X. Hu, A. Neville, A systematic erosion-corrosion study of two stainless steels in marine conditions via experimental design, Wear. 263 (2007) 355–362.

[2.2] A. Neville, C. Wang, Erosion–corrosion of engineering steels—Can it be managed by use of chemicals?, Wear. 267 (2009) 2018–2026.

[2.3] M.M. Stack, J.S. James, Q. Lu, Erosion–corrosion of chromium steel in a rotating cylinder electrode system: some comments on particle size effects, Wear. 256 (2004) 557–564.

[2.4] P. De Haller, Erosion and Kavitations-erosion, in Handbuch der Werkstoffprüfung, Vol.2, edited by E. Siebel, Springer Verlag, (1939) 471-488.

[2.5] I.M. Hutchings, Tribology: Friction and Wear of Engineering Materials . 1992, London.

[2.6] J.G.A. Bitter, A study of erosion phenomena Part I, Wear. 6 (1963) 169–190.

[2.7] I. Hutchings, Wear by particulates, Chem. Eng. Sci. 42 (1987) 869–878.

[2.8] H.M. Clark, Particle velocity and size effects in laboratory slurry erosion measurements OR… do you know what your particles are doing?, Tribol. Int. 35 (2002)

617–624.

[2.9] H.M. Clark, On the impact rate and impact energy of particles in a slurry pot erosion tester, Wear. 147 (1991) 165–183.

[2.10] H.M. Clark, The effect of carrier liquid viscosity on the erosion rate of steel by solid/liquid suspensions and the nature of the wear debris produced, in: 5th Int. Congr. Tribol. EUROTRIB'87, Finnish Soc. Tribol., 1989.

[2.11] A.V. Levy, Erosion / Corrosion of metals in coal-liquefaction environments, Mater. Perform. 19 (1980) 45–51.

[2.12] I. Finnie, Erosion of surfaces by solid particles, Wear. 3 (1960) 87–103.

[2.13] H.M. Clark, The influence of the flow field in slurry erosion, Wear. 152 (1992) 223–240.

[2.14] A.V. Levy, J. Yan, V.D. Arora, Sand-water slurry erosion of carburized AISI 8620 steel, Wear. 1 (1985) 117–126.

[2.15] A. Levy, G. Hickey, Erosion of corrosion-resistant alloy steels, Wear. 108 (1986) 61–79.

[2.16] T. Singh, S.N. Tiwari, G. Sundararajan, Room temperature erosion behaviour of 304, 316 and 410 stainless steels, Wear. 145 (1991) 77–100.

[2.17] A. Abouel-Kasem, Particle Size Effects on Slurry Erosion of 5117 steels, J. Tribol. 133 (2011).

[2.18] R.S. Lynn, K.K. Wong, H.M. Clark, On the particle size effect in slurry erosion, Wear. 149 (1991) 55–71.

[2.19] H.H. Tian, G.R. Addie, K. V. Pagalthivarthi, Determination of wear coefficients for erosive wear prediction through Coriolis wear testing, Wear. 259 (2005) 160–170.

[2.20] C.I. Walker, M. Hambe, Influence of particle shape on slurry wear of white iron, Wear. 332-333 (2015) 1021–1027.

[2.21] Z.G. Liu, S. Wan, V.B. Nguyen, Y.W. Zhang, A numerical study on the effect of particle shape on the erosion of ductile materials, Wear. 313 (2014) 135–142.

[2.22] H.M. Clark, R.B. Hartwich, A re-examination of the "particle size effect" in slurry erosion, Wear. 248 (2001) 147–161.

[2.23] A. Neville, F. Reza, Erosion-corrosion of cast white irons for application in the oilsand industry, in: Nace Int. Corros. 2007 Conf. Expo, 2007: pp. 1–13.

[2.24] M. Woldman, E. Van Der Heide, D.J. Schipper, T. Tinga, M.A. Masen, Investigating the influence of sand particle properties on abrasive wear behaviour, Wear. 294-295 (2012) 419–426.

[2.25] S.L. Palasamudram, S. Bahadur, Particle characterization for angularity and the effects of particle size and angularity on erosion in a fluidized bed environment, Wear. 203-204 (1997) 455–463.

[2.26] G.R. Desale, B.K. Gandhi, S.C. Jain, Effect of erodent properties on erosion wear of ductile type materials, Wear. 261 (2006) 914–921.

[2.27] A. Neville, X. Hu, Mechanical and electrochemical interactions during liquid–solid impingement on high-alloy stainless steels, Wear. 251 (2001) 1284–1294.

[2.28] H.H. Steinour, Rate of Sedimentation, Ind. Eng. Chem. 36 (1944) 840–847.

[2.29] D.K. Spencer, A.A. Sagues, Erosion by sand and coal slurries, in: Corros. Eros. Wear Mater. Elev. Temp., 1986: pp. 27–29.

[2.30] S. Turenne, M. Fiset, J. Masounave, The effect of sand concentration on the erosion of materials by a slurry jet, Wear. 133 (1989) 95–106.

[2.31] K.B. Zitoun, S.K. Sastry, Y. Guezennec, Investigation of three dimensional interstitial

velocity, solids motion, and orientation in solid-liquid flow using particle tracking velocimetry, Int. J. Multiph. Flow. 27 (2001) 1397–1414.

[2.32] I. Finnie, The mechanism of erosion of ductile metals, in: Proced. 3rd U.S. Congr. Appl. Mechnanics., 1958.

[2.33] G.T. Burstein, K. Sasaki, Effect of impact angle on the slurry erosion–corrosion of 304L stainless steel, Wear. 240 (2000) 80–94.

[2.34] Z. Feng, A. Ball, The erosion of four materials using seven erodents - towards an understanding, Wear. 233-235 (1999) 674–684.

[2.35] N. Andrews, L. Giourntas, A.M. Galloway, A. Pearson, Effect of impact angle on the slurry erosion-corrosion of Stellite 6 and SS316, Wear. 320 (2014) 143–151.

[2.36] H.M. Clark, K.K. Wong, Impact angle, particle energy and mass loss in erosion by dilute slurries, Wear. 186-187 (1995) 454–464.

[2.37] P.H. Shipway, I.M. Hutchings, The rôle of particle properties in the erosion of brittle materials, Wear. 193 (1996) 105–113.

[2.38] G.R. Desale, B.K. Gandhi, S.C. Jain, Slurry erosion of ductile materials under normal impact condition, Wear. 264 (2008) 322–330.

[2.39] A. Ninham, The effect of mechanical properties on erosion*, Wear. 121 (1988) 307–324.

[2.40] L. Giourntas, T. Hodgkiess, A.M. Galloway, Comparative study of erosion–corrosion performance on a range of stainless steels, Wear. 332-333 (2015) 1051–1058.

[2.41] A. Matthews, A. Leyland, Materials related aspects of nanostructured tribological coatings, 51st SVC TechCon. (2008).

[2.42] R.J.K. Wood, Erosion–corrosion interactions and their effect on marine and offshore materials, Wear. 261 (2006) 1012–1023.

[2.43] P. Kulu, I. Hussainova, R. Veinthal, Solid particle erosion of thermal sprayed coatings, Wear. 258 (2005) 488–496.

[2.44] T. Foley, A. Levy, The erosion of heat-treated steels, Wear. 91 (1983) 45–64.

[2.45] R.C.D. Richardson, The wear of metals by relatively soft abrasives, Wear. 11 (1968) 245–275.

[2.46] G. Sundararajan, The solid particle erosion of metallic materials: The rationalization of the influence of material variables, Wear. 186-187 (1995) 129–144.

[2.47] E. Bardal, Corrosion and Protection, 2004.

[2.48] L.L. Shreir, R.A. Jarman, G.T. Burstein, Corrosion & Corrosion Control, 1994.

[2.49] R. Heidersbach, Metallurgy and Corrosion Control in Oil and Gas Production, 2011.

[2.50] NACE MR0175/ISO 15156-3. Petroleum and natural gas industries- Materials for use in H2S containing environments in oil and gas production-Part 3: Cracking-resistant CRAs.

[2.51] A.F. Zhang, J.D. Xing, L. Fang, J.Y. Su, Inter-phase corrosion of chromium white cast irons in dynamic state, Wear. 257 (2004) 198–204.

[2.52] M. Salasi, G.B. Stachowiak, G.W. Stachowiak, Three-body tribocorrosion of high-chromium cast irons in neutral and alkaline environments, Wear. 271 (2011) 1385–1396.

[2.53] D.H. Mesa, A. Toro, A. Sinatora, a. P. Tschiptschin, The effect of testing temperature on corrosion - erosion resistance of martensitic stainless steels, Wear. 255 (2003) 139–145.

[2.54] F. Aiming, J. Jinming, T. Ziyun, An investigation of the corrosive wear of stainless steels in aqueous slurries, Wear. (1995) 73–77.

[2.55] X. Hu, A. Neville, The electrochemical response of stainless steels in liquid-solid impingement, Wear. 258 (2005) 641–648.

[2.56] H.H. Tian, P.A. Taylor, Corrosion study on high alloyed white cast irons in acidic and chloride containing solutions, in: Nace Int. Corros. 2011 Conf. Expo, 2011: pp. 1–14.

[2.57] K.S.E. Al-Malahy, T. Hodgkiess, Comparative studies of the seawater corrosion behaviour of a range of materials, Desalination. 158 (2003) 35–42.

[2.58] Z. Guanghong, D. Hongyan, Z. Yue, L. Nianlian, Corrosion–erosion wear behaviors of 13Cr24Mn0.44N stainless steel in saline–sand slurry, Tribol. Int. 43 (2010) 891–896.

[2.59] L.L. Parent, D.Y. Li, Wear of hydrotransport lines in Athabasca oil sands, Wear. 301 (2013) 477–482.

[2.60] B. Yu, D.Y. Li, A. Grondin, Effects of the dissolved oxygen and slurry velocity on erosion–corrosion of carbon steel in aqueous slurries with carbon dioxide and silica sand, Wear. 302 (2013) 1609–1614.

[2.61] M. Stern, A method for determining corrosion rates from linear polarization data, Corrosion. 14 (1958) 60-64.

[2.62] A. Neville, C. Wang, Erosion–corrosion mitigation by corrosion inhibitors—An assessment of mechanisms, Wear. 267 (2009) 195–203.

[2.63] X. Hu, R. Barker, A. Neville, A. Gnanavelu, Case study on erosion–corrosion degradation of pipework located on an offshore oil and gas facility, Wear. 271 (2011) 1295–1301.

[2.64] J. Britton, “Integrity through corrosion control, materials and design”, Corrosion Matters NACE Workshop, London, (2015).

[2.65] T. Hodgkiess, A. Neville, S. Shrestha, Electrochemical and mechanical interactions during erosion-corrosion of a high-velocity oxy-fuel coating and a stainless steel, Wear. 233-235 (1999) 623–634.

[2.66] C. Britton, Corrosion Control in Oil & Gas Industry Course, Amsterdam, Holland, (2013).

[2.67] G. Karafyllias, T. Hodgkiess, A. Galloway, The Influence of Acidic Conditions in Erosion-Corrosion Behavior of Medium Carbon Steel (UNS G10400) and Superduplex Stainless Steel (UNS S32760), in: Dep. Def. -Allied Nations Tech. Corros. Conf. Pittsburgh, 2015.

[2.68] R.J.K. Wood, J.C. Walker, T.J. Harvey, S. Wang, S.S. Rajahram, Influence of microstructure on the erosion and erosion-corrosion characteristics of 316 stainless steel, Wear. 306 (2013) 254–262.

[2.69] T. Hodkgiess, A. Neville, Unpublished work

[2.70] A. Neville, T. Hodgkiess, Characterisation of high-grade alloy behaviour in severe erosion-corrosion conditions, Wear. 233-235 (1999) 596–607.

[2.71] M. Jones, R.J. Llewellyn, Erosion-corrosion assessment of materials for use in the resources industry, Wear. 267 (2009) 2003–2009.

[2.72] A. Neville, “Erosion-corrosion; Management of material damage”, Corrosion Matters NACE Workshop, London, (2015).

Chapter 3

Experimental Methods

3.1 Introduction

In this chapter, the experimental methods that have been commonly used throughout this study are described. The methods have been divided as follows; pre-test methodologies, erosion-corrosion testing procedures and post-test analysis techniques.

3.2 Pre-test Methodologies

3.2.1 Source of materials

A total of five metallic alloys, two High Velocity Oxy-Fuel (HVOF) cermet coatings and two sintered cermets were subjected to erosion-corrosion testing. Table 3.1 shows the range of materials tested in addition to the corresponding chapters of this thesis, in which test results and conclusions are reported in detail.

Table 3.1 List of supply materials and corresponding chapters

Materials	Corresponding chapters
UNS G10400	Chapter 4
UNS S31600	Chapter 4, 5 and 6
UNS S42000	Chapter 5
27%Cr cast iron	Chapter 5
37%Cr cast iron	Chapter 5
Sin WC-11Co	Chapter 6
Sin WC-6Ni	Chapter 6
HVOF WC-12Co	Chapter 6
HVOF WC-10Ni	Chapter 6

The commercially available medium carbon steel (UNS G10400) and the two stainless steels (UNS S31600 & UNS S42000) were supplied as round bars and these were sectioned into 17mm thick cylindrical specimens of 35mm diameter and 38mm diameter for the medium carbon steel and the stainless steels, respectively. The white cast irons (27%Cr & 37%Cr) specimens were electro-discharge machined (EDM) from industrial quality frame plate liner inserts (Figures 3.1 & 3.2) supplied by Weir Minerals, Australia foundry. The finished dimensions following EDM were 38mm diameter and 17mm thickness.

Figure 3.1 27%Cr cast iron frame plate liner insert (diameter: 240mm, thickness: 30mm)

Figure 3.2 37%Cr cast iron frame plate liner insert (diemeter: 430mm, thickness: 35mm)

The sintered WC-based cermets (Sin WC-11Co & Sin WC-6Ni) were provided as cylindrical test coupons of 38mm diameter and 7mm thickness. The HVOF cermet coatings (WC-12Co & WC-10Ni) were sprayed on top of the cylindrical specimens of the austenitic stainless steel (UNS S31600) substrate and the coatings were deposited by an external provider in accordance with industrial standards.

3.2.2 Surface preparation of the test coupons

The surface preparation of the test coupons involved grinding with 220, 500, 800 and 1200 grit papers which developed a surface finish of 0.07μm Ra. The cermet materials were tested in their as-received condition (surface finish of Ra = 0.2-0.4μm) in order to evaluate the industrially relevant surface finishes.

3.2.3 Metallographic preparation

Each test material was evaluated with the aid of standard metallographic preparation methods. This consisted of mechanical sectioning by a Struers Discotom-2 abrasive cutting machine, hot mounting on a Struers PromtoPress-10 mounting machine and final grinding and polishing on a Struers RotoPol-21 using a 1μm diamond paste. For the metallic materials a subsequent etch (Table 3.2) highlighted their microstructure prior to their examination under an Olympus GX-51 light microscope.

Table 3.2 Assigned etching agents for the materials studied.

Test Materials	Etching Agents
UNS G10400	2%Nital
UNS S31600 & 37%Cr cast iron	10% Oxalic acid (electrolytic 1V DC)
UNS S42000 & 27%Cr cast iron	Kallings reagent swab etched

3.2.4 Material characterisation

3.2.4.1 Wavelength-dispersive X-ray Spectroscopy (WDS)

A HITACHI SU-6600 high resolution analytical variable pressure field emission scanning electron microscope was employed for the wavelength-dispersive X-ray spectroscopy (WDS) analysis, along with imaging of the microstructures in their pre-test and post-test states. The WDS enabled the quantitative analysis of the chromium content in cast irons and the metallic binder (i.e. Co and Ni) of the cermets. The 45 faradays cup universal block layout with certified reference material standards was used to compare the X-ray intensity count rates of chromium in the detector at 20kV.

3.2.4.2 X-ray Diffraction (XRD)

A Bruker D8 Advance with Davinci X-ray diffractrometer (XRD) with Göbel Mirror type of optics was also used to determine the metallic and ceramic phases of the cermet materials. A Cu tube was utilised with the two theta range from 30^{o} to 130^{o}, step size of 0.025^{o} and step time 0.3s at 40kV and 40mA.

3.2.5 Hardness measurements

Macrohardness measurements were obtained for all the test materials by using a calibrated Vickers hardness tester. The load used for the metallic alloys and cermets were 5kgf and 20kgf, respectively. Consideration was given to the fact that the depth of the indentation corresponded to lower than 0.1 of the cermet coatings' thickness [3.1]. The error of the macrohardness tester was found to be ±15HV and this was determined by taking 10 measurements on a calibration test block. Micro-hardness measurements were determined via the Mitutoyo MVK-G1 micro-hardness tester with a load of 200gf for the hardness measurements of phases and 50gf for the hardness assessment of the chromium carbides of the white cast irons and the primary metallic phases (austenite and martensite).

3.2.6 Volume fraction measurements

The volume fraction measurements involved etching of the cross sections to distinguish the different phases of the high chromium cast irons. Through the Image J software package, the average area fraction of the phases, which in essence represents the volume fraction, was obtained. In this way the volume fraction of carbides and the metallic matrix were measured quantitatively. It is noteworthy that the austenitic based cast iron (37%Cr cast iron) was etched with 40% Potassium Hydroxide (electrolytic 1V DC) to highlight the different phases and metallographic features. The optimum magnification for the volume fraction of carbides and ferrous matrix was x100 and, for the determination of the eutectic matrix balance, x500 was utilised.

3.2.7 Surface roughness measurements

Surface roughness measurements were performed on a Mutotoyo SurfTest machine in accordance with the BS EN ISO 4288 [3.2] , which suggests at least 4mm travel distance of the stylus pin for accurate measurements. Table 3.3 illustrates the conditions of the Stylus during the surface roughness measurement.

Table 3.3 Surface roughness measurements conditions

Measurement length	5.6mm
Range	800µm
Speed	1m/s
Pitch	1.0µm
Number of points	5,600

3.2.8 Sand characterisation

Two types of silica sand particles were employed for the solid/liquid impingement tests herein. The hydraulic fracturing sand is commonly used in hydraulic fracturing operations and it possesses 7 mohs hardness, which is about 1,160HV. Figure 3.3 shows the spherical shape of this particle along with its size. The main difference with the second batch of silica sand is the shape of the particle, as the average size is quite similar. The second silica sand exhibited a sub-angular shape, as shown in Figure 3.4. Figure 3.5 demonstrates the size distribution of both sand types as measured through standard sieves with sizes from 710µm - 600µm - 500µm - 410µm - 325µm - 250µm - 180µm.

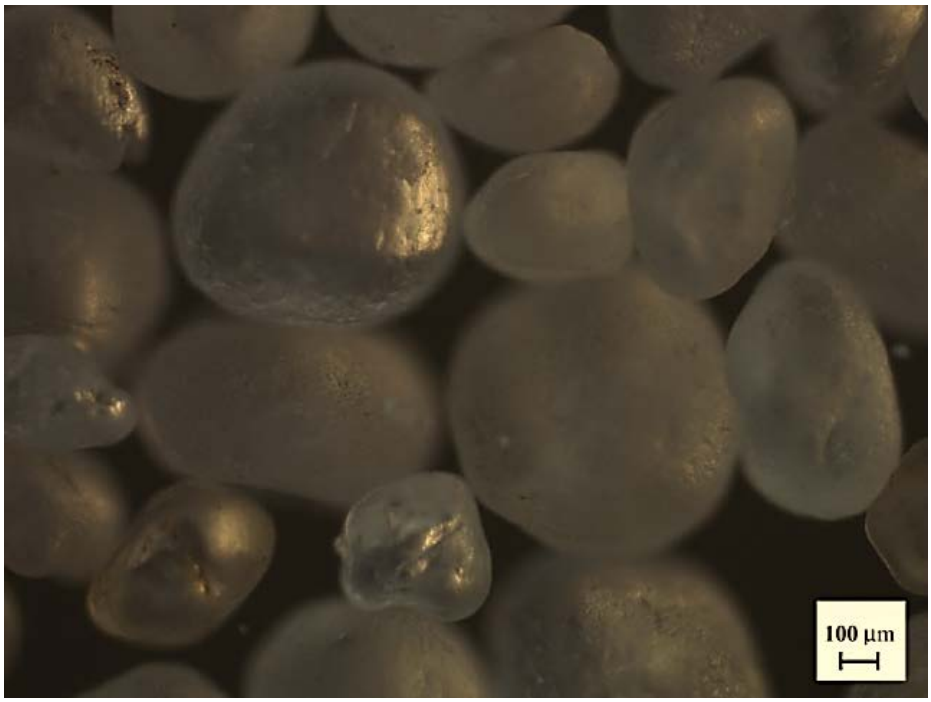

Figure 3.3 Hydraulic fracturing sand particles of 500µm average size.

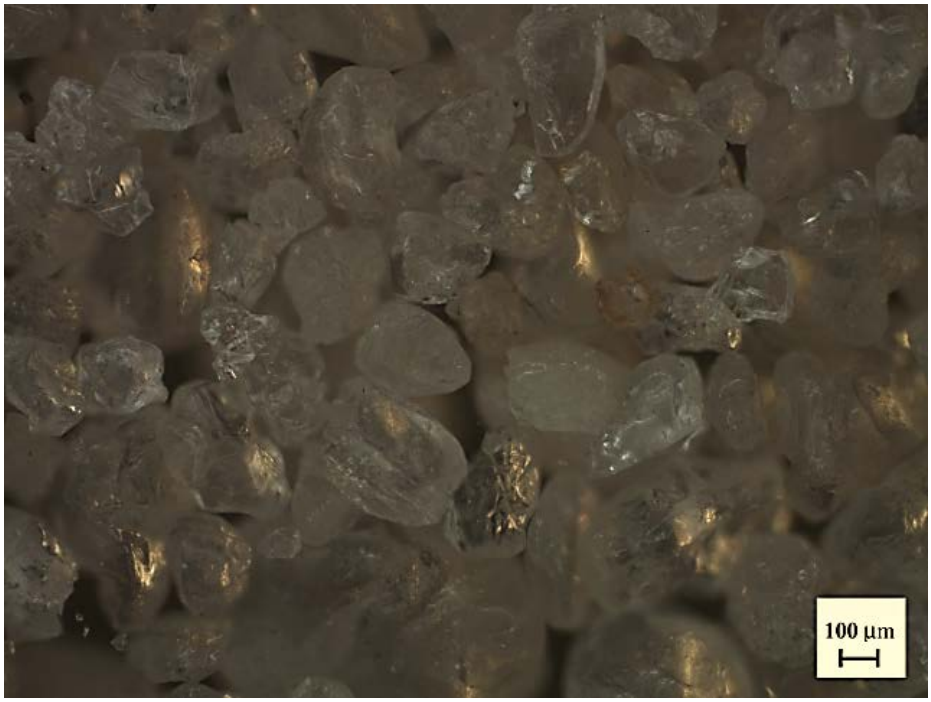

Figure 3.4 Silica sand particles of a wide range of 355µm-500µm size range of particles.

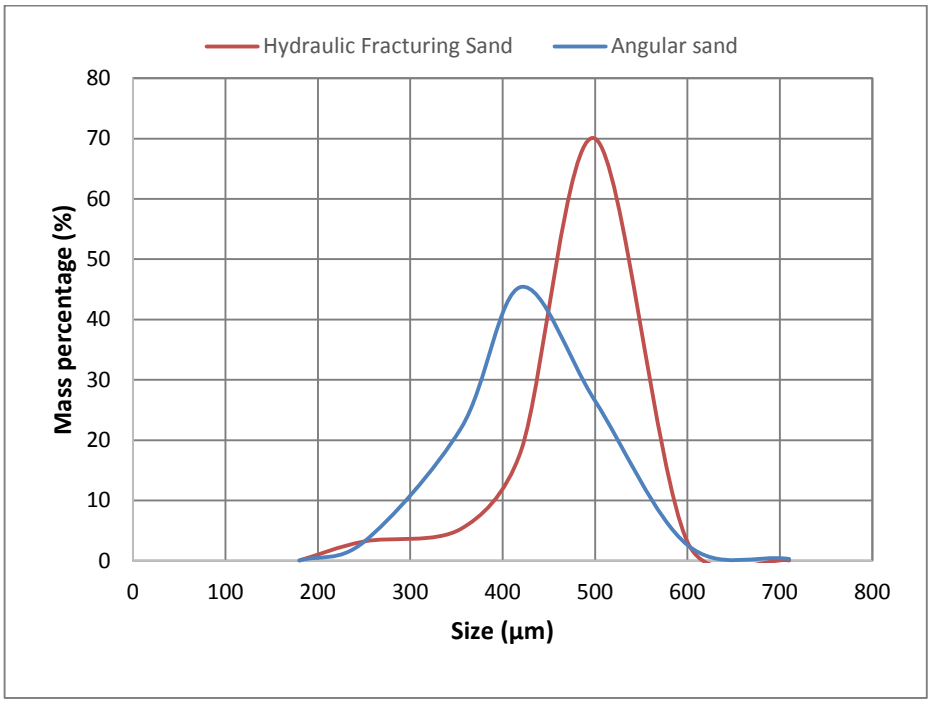

Figure 3.5 Average size distributions of the two silica sand types used in this thesis.

3.3 Erosion-corrosion testing procedures

3.3.1 Testing protocol

The initial step of the testing procedure was the surface preparation of the specimens, as described in Section 3.2.2, followed by cleaning with methanol and then weighing at least five times on a mass balance with 0.1mg accuracy. The erosion-corrosion impingement tests were conducted on a submerged jet impingement rig, as shown in Figure 3.6. The rig was filled with 33L of pre-heated water in order to avoid any temperature change during the impingement tests. Sodium chloride (NaCl) of 1,150g content was dissolved into the pre-heated water to simulate the chemistry of sea water of 3.5%NaCl. A HANNA HI9033 multi-range portable conductivity meter was used to verify that the salinity of the aqueous solution was the same (50mS/cm^2) for each experiment.

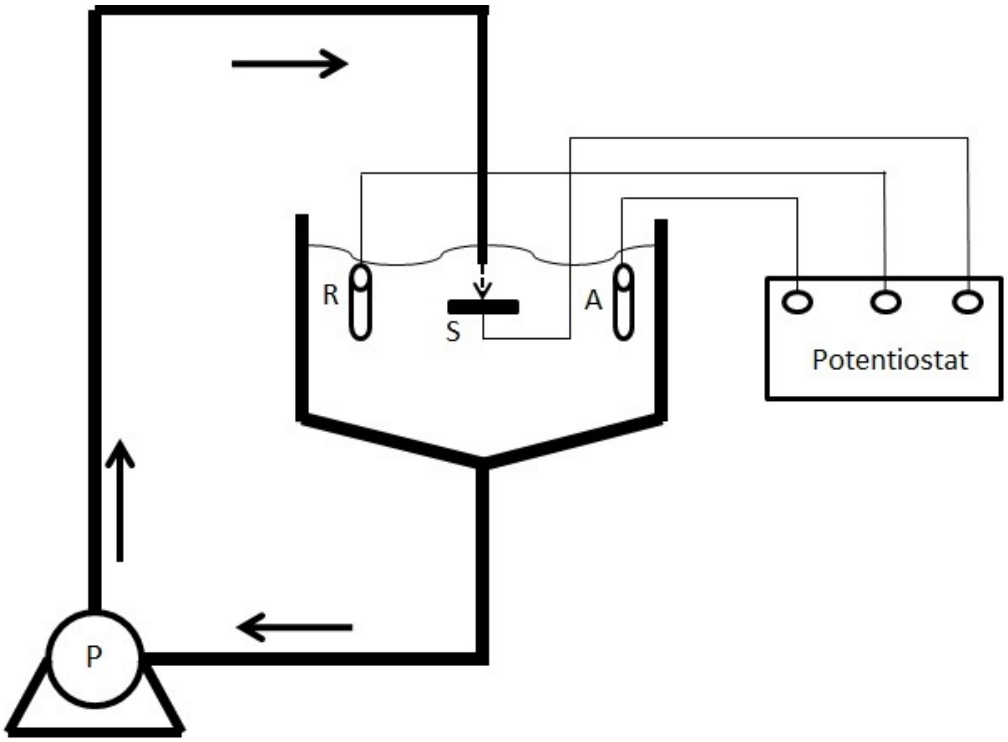

Figure 3.6 Schematic diagram of the submerged jet impingement rig showing also the electrochemical monitoring system (A- Auxiliary Electrode, R- Reference Electrode and S – Specimens or Working electrode)

The test coupon was located in the centre of the specimen holder inside an extruded blind hole of 40mm diameter and 17mm thickness, as shown in Figure 3.7. The distance between the nozzle and the specimen was held constant at 5mm with the aid of a 5mm thick disc. The impingement angle was constant at 90^{o}. The specimen holder was assembled with the impingement rig and the specimen was submerged 10cm below the water level. The sand was loaded into the aqueous solution gradually within the first seconds of experiment. The duration of the tests varied. Initially, the duration was 1h (Chapter 4) but thereafter, it was decided that better discrimination of the comparative materials would be obtained by higher overall mass losses. Hence, the testing duration was increased to 2h (Chapters 5 & 6). The post-test coupon was cleaned with methanol and dried with pressurized air prior to the final mass measurement. After each test, the impingement rig was drained; cleaned and new slurry (aqueous solution and sand) was used for each test.

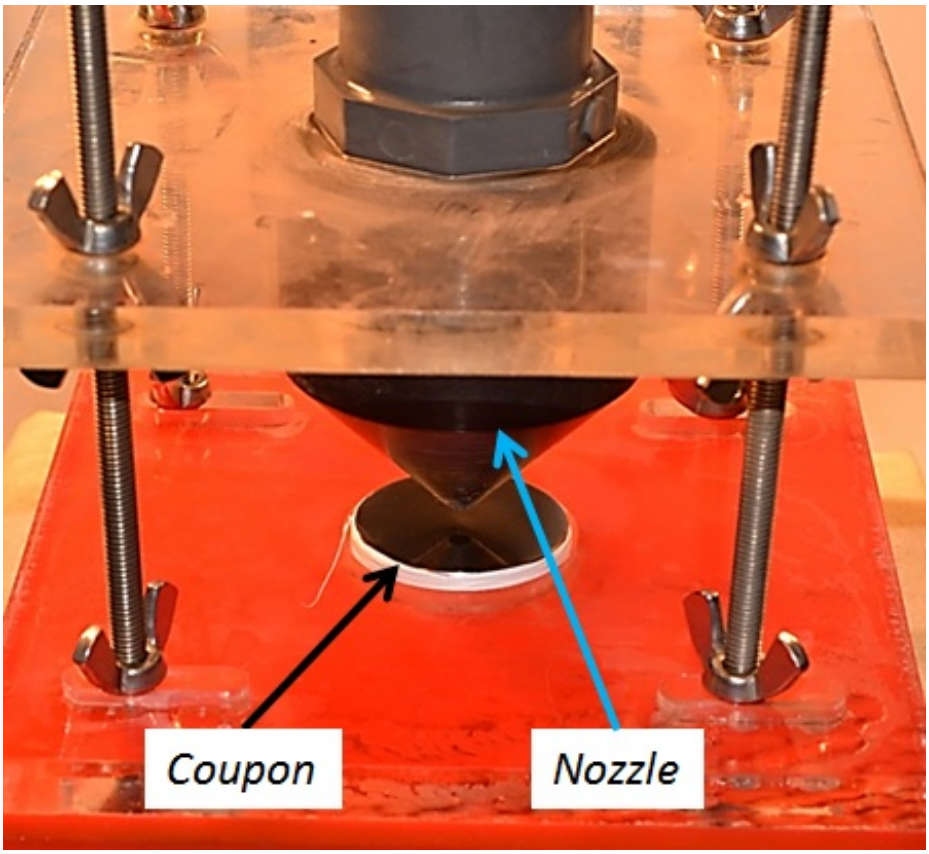

Figure 3.7 Coupon holder with the test coupon in place.

3.3.2 Flow velocity/sand concentration measurements

The flow velocity and the sand concentration were measured by filling the impingement rig with the 33L water and solid loading equal to that of the impingement tests. After 15mins of operation of the pump a plastic hose was placed underneath the submerged nozzle exit and the flowing water solution was collected on a 10L beaker. The beaker had a 250µm sieve fitted to accumulate the sand particles. The collection duration was 30 seconds. The jet velocity was calculated using the Equation 3.1 below:

$$V = \frac{Q^*}{30 \times \pi R_n^{\ 2}} \qquad \textbf{Equation 3.1}$$

where,

V is the flow velocity

Q^* is the flow rate per 30 seconds

R_n is the nozzle radius

The sieve was dried in a pre-heated oven (220^{o}C) and the sand sample was weighed on a balance of 0.1mg accuracy. The sand concentration was obtained through the flow rate in mg/L. The velocity and sand concentration tests were performed every five impingement tests to confirm the repeatability and reproducibility of the tests. It should be noted that no variation of the flow velocity and sand concentration was observed throughout each testing phase.

3.3.3 Segmentation of the test specimens

To determine the corrosion rates on the zone under the jet and the region adjacent to it, the 38mm Dia test coupon was segmented into two separate specimens; one with 0.2cm^2 (5mm Dia) surface area, which represents the direct impinged zone (DIZ) and the other with 11.0 cm^2 surface area, which represents the outer area (OA). The metallic alloys and the HVOF coatings were segmented using a Maxiem abrasive waterjet 1515 by setting up a circular cutting path of 5mm diameter right in the centre of the specimen, as shown in Figure 3.8. The solid sintered cermets were segmented using the electro-discharge machining (EDM) into the two separate components.

The two sections of the segmented specimens were spot welded or soldered to electrical wires to form electrodes. The small specimen was inserted in the centre of the remainder of the specimen surrounded by a heat shrink tube of 0.8mm thickness to provide the electrical insulation between the two specimens. They were encapsulated in 40mm diameter cold mounting moulds, which also offered an additional electrical exchange barrier between the two specimens. Figure 3.8 illustrates an example of the segmentation and encapsulation of the medium carbon steel (UNS G10400). Figure 3.9 shows the fresh water test to ensure that the slurry would impinge directly on the central segment of the specimen prior to any electrochemical monitoring test.

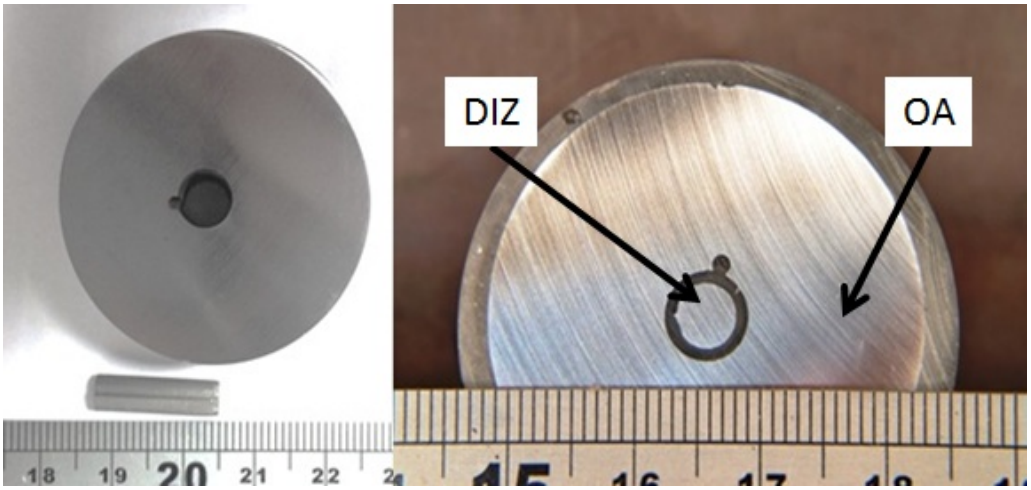

Figure 3.8 The two segments of the 35mm UNS G10400 steel specimen (left) and the encapsulated segmented UNS G10400 steel (right).

Figure 3.9 Fresh water test on the segmented WC-6Ni sintered cermet specimen.

3.3.4 Linear and Potentiodynamic polarisation scans

Linear polarisation scans were utilised to indirectly monitor the corrosion rate of the specimens (full and segmented) during the impingement test. The linear polarisation scans as well as the full potentiodynamic polarisation scans employed a standard three-electrode cell (Ag/AgCl reference electrode, platinum auxiliary electrode and the working electrode (test piece)) using Gill AC electrochemical equipment. The linear polarisations comprised a 40mV scan, starting from 20mV more negative from E_{corr} to 20mV more positive to E_{corr} whilst recording the cell current. The sweep rate was 14mV/min. The linear polarisation technique involves plotting electrode potential versus cell current and the determination of the gradient of the E/I plot yields the "polarisation resistance" (R_p), which, by reference to electrochemical theory, can be considered to be inversely proportional to the specimen's corrosion current density. The time intervals of the linear polarisation scans were the first 5 mins, 30mins, 60mins and 90mins, respectively.

After the linear polarisation scan (90min), the full DC anodic potentiodynamic polarisation scan started by shifting the potential of the testing piece from 20mV more negative to E_{corr}, to more positive potentials (about 300mV above E_{corr}) at a fixed sweep rate of 14mV/min. The potential range of each polarisation was sufficient to facilitate corrosion current determination via Tafel extrapolation.

3.3.5 Application of cathodic protection

The standard three-electrode cell (Ag/AgCl reference electrode, platinum auxiliary electrode and the working electrode (test piece)) using Gill AC electrochemical equipment was also used for the Impressed Current Cathodic Protection (ICCP) tests. The National Association of Corrosion Engineers (NACE) suggests that the level of cathodic protection in soils and water is accepted for carbon-manganese at potentials of -850 mV (Ag/AgCl). Cathodic potentials more negative than -850mV should be avoided as water reduction reaction (Eq. 2.9) will take place, as illustrated in Figure 3.10, and hydrogen embrittlement would be likely to occur.

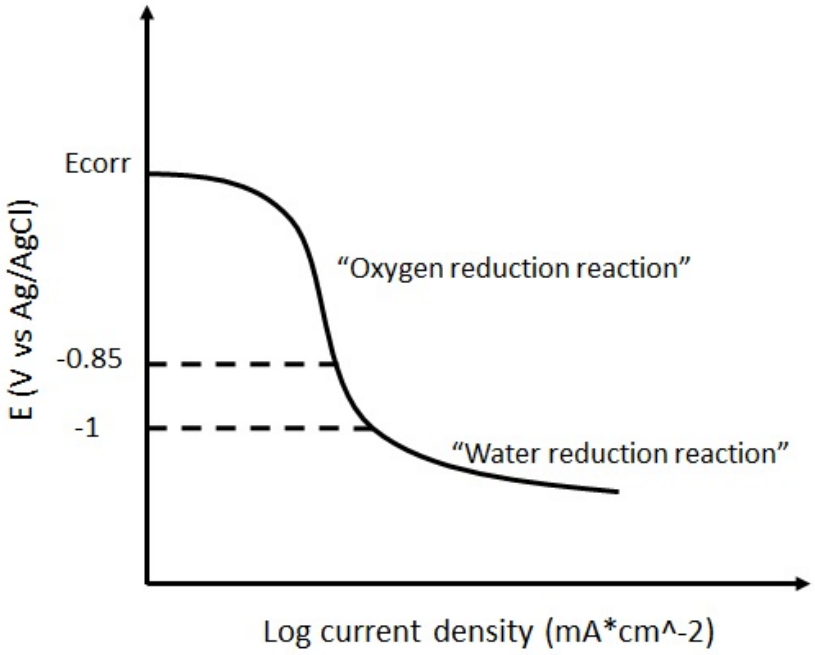

Figure 3.10 Cathodic reactions that occur in different cathodic protection potentials.

Therefore, the potentiostatic tests performed herein facilitated mitigation of any electrochemical processes on the testing sample by keeping the electrode potential at -850mV (Ag/AgCl reference electrode). The selection of the electrode potential was also a result of the back extrapolation of the linear Tafel region of each material which showed that the residual anodic current densities at -850mV were representing a negligibly low percentage of the corrosion rate of the specimen. Figure 3.11 shows, in more detail, a representation of the back extrapolation on the anodic polarisation chart.

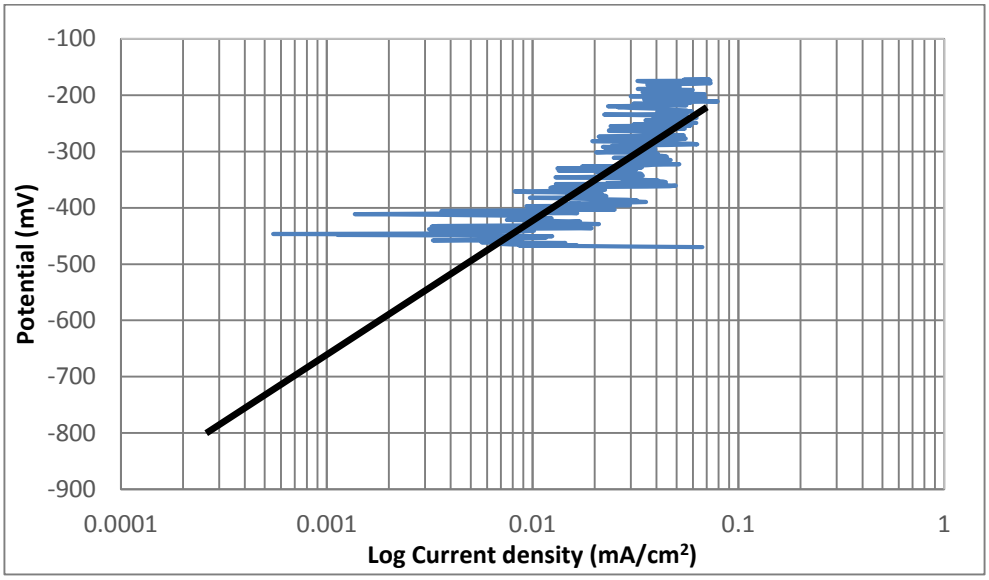

Figure 3.11 Example of the back extrapolation to distinguish the residual current densities at -850mV cathodic protection potential.

Table 3.4 shows the measured corrosion current densities along with the residual anodic current densities of the materials assessed in the following chapters to determine the effect of the selected cathodic protection potential (-850mV) on the suppression of the electrochemical reactions. It should be noted that the current densities of the metallic materials have been estimated through the surface area of the specimens (11.34 cm^2), whereas the cermets' current densities have been considered with the surface area of the binder.

Table 3.4 Residual current densities of the test materials at -850mV cathodic protection potential.

Material	Corrosion Current Density (μA/cm^2)	Residual Current density (μA/cm^2)	Corrosion rate reduction with -850mV cathodic potential
UNS G10400	350	2.8	99.2 %
UNS S31600	7	0.2	97.2 %
UNS S31600	7	0.1	98.6 %
UNS S42000	26	0.8	96.9 %
27%Cr cast iron	35	0.1	99.7 %
37%Cr cast iron	4	0.1	97.5%
UNS S31600	9.7	0.4	95.9 %
Sin WC-11Co	500	0.5	99.9 %
Sin WC-6Ni	30	0.8	97.3 %
HVOF WC-12Co	440	1.6	99.6 %
HVOF WC-10Ni	400	1.8	99.6 %

3.4 Post-test analysis techniques

3.4.1 Macro and micro examination

Macro-examination of the post-test surface of each material is an initial step to understand the features of the deterioration mechanisms that occur during the solid/liquid impingement tests. Thus, images of the post-test surfaces of each material specimen were captured by using a standard digital SLR camera.

3.4.2 Surface topography

The post-test surface was assessed using an Alicona Infinite Focus Optical Microscope. The Alicona software enabled the definition of the X, Y and Z coordinates to scan the area of interest, which in this case is the area directly under the impinging jet, or in other words, wear scar. Each test coupon was scanned with an optical magnification of 5x, in which the vertical resolution ranged from 26.5μm to 200nm. To achieve precision through this surface topography assessment, the vertical resolution was set at 800nm. Hence, the 3-D model of the surface exhibits ±1μm error in surface texture and 0.02mm^3 in volumetric analysis, which can effectively be ignored.

The surface texture analysis mimics the conventional methodology of a Stylus, by initiating a line scan on the wear scar. However, multiple scans are created simultaneously to distinguish the deepest wear scar profile. By utilising the colour bands of the 3D scan, higher precision profile scans, with respect to the depth size and geometry, were achieved. The wear scar depths are essential to understand the deterioration mechanisms that occur within this area. However, volumetric analysis of the wear scar, adds value on the overall surface topography as it becomes a more effective quantitative tool. The programme yielded the formation of a polygon that comprised the area of interest and then a calculation of the volume below the surface was executed.

Calibration tests were performed on the Alicona machine prior to the volumetric analysis of the post-test materials to certify the accuracy of the equipment. To facilitate this, a blind hole of 5mm diameter and 90μm depth was drilled on a 38mm diameter UNS S17400 specimen using a CNC machine. Figure 3.12 illustrates the UNS S17400 stainless steel with the 90μm blind hole at its centre and Figure 3.13 shows the profile scan of the cylindrical scar as obtained by the Alicona machine. Therefore, the volume of the holes

(mimicking a cylinder) were scanned by the Alicona Infinite Focus and they were verified by comparing it with the mathematically measured volume, since the diameter and the depth were known. Table 3.5 summarises the calibration measurement along with the mathematical calculation of the cylinder. The Alicona volume loss measurement depicted 7% difference (error) with the mathematically volume calculation due to the fact that the latter considers the volume of a perfect cylinder.

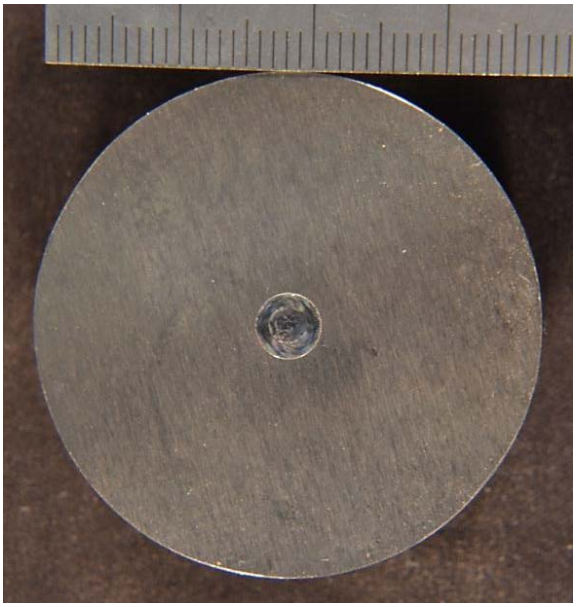

Figure 3.12 UNS S17400 specimen with a 5mm diameter and 90µm depth blind hole at the centre.

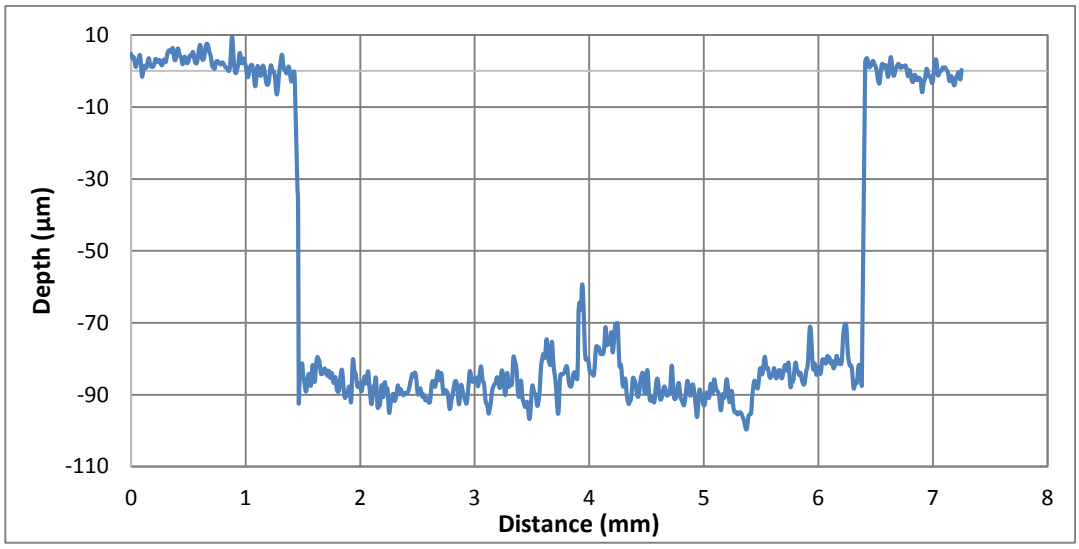

Figure 3.13 A profile scan of the 90µm blind hole on the UNS S17400 specimen.

Table 3.5 Summary of the calibration activities.

Measurement method	Volume of the blind hole (mm^3)
Mathematical	1.76
Alicona	1.63

Figure 3.14 shows any potential errors on the top surface axis due to thickness loss by sliding abrasion, corrosion or synergy. They are estimated to be negligible. Table 3.6 shows the estimations of the errors on the volumetric analysis by considering the average wear scar depths and thickness loss in the outer region of the materials studied in the following chapters. The maximum errors of the profilometry measurements is 2.44% on the HVOF WC-12Co coating, and 2.18% on the sintered WC-11Co cermet. All the other comparative materials are falling into less than 1% error. The error at the cathodic protection specimens was generally reduced as sliding abrasion was the single degradation mechanism of the outer region.

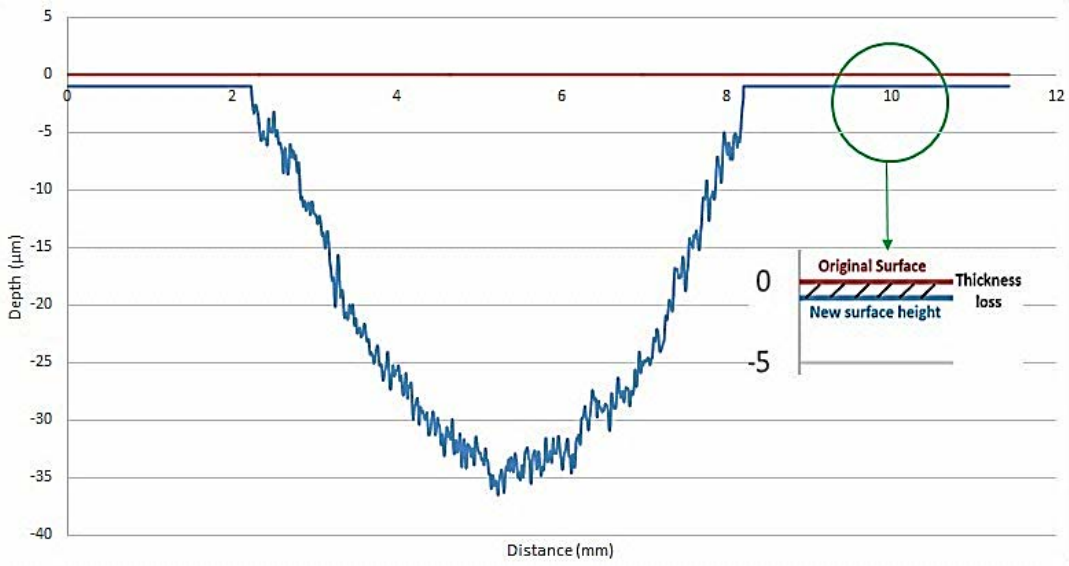

Figure 3.14 Typical 2D profile scan with the thickness loss due to sliding abrasion and corrosion related component.

Table 3.6 Volume loss measurement error estimation according to wear scar and thickness loss in free erosion-corrosion (FEC) and cathodic protection (CP) conditions**.**

Material	Wear scar depth (μm)		Thickness loss outside the wear scar (μm)		Error (%)	
	FEC	CP	FEC	CP	FEC	CP
UNS G10400	122	126	0.92	0.31	0.75	0.25
UNS S31600	110	100	0.31	0.18	0.28	0.18
UNS S31600	99	95	0.49	0.45	0.49	0.47
UNS S42000	107	83	0.50	0.41	0.47	0.49
27%Cr cast iron	85	73	0.47	0.15	0.55	0.21
37%Cr cast iron	130	99	0.46	0.46	0.35	0.46
UNS S31600	87	86	0.52	0.52	0.60	0.60
Sin WC-11Co	33	13	0.72	0.07	2.18	0.54
Sin WC-6Ni	16	17	0.08	0.07	0.50	0.41
HVOF WC-12Co	57	30	1.39	0.02	2.44	0.07
HVOF WC-10Ni	89	53	0.33	0.03	0.37	0.06

3.4.3 Post-test Hardness measurements

A Zwick ZHVI Knoop hardness tester was employed to determine potential subsurface hardening effects on the post-test surface of the austenitic stainless steel. The small thickness of the indentations, shown in Figure 3.15, facilitated the determination of the 30um thick layer's micro-hardness with average 5μm distance from the interface of the specimen with the Bakelite which could potentially affect the results. The load used on each indentation was 500gf. The distance between the indentations was kept higher than 270μm, as shown on Figure 3.16, to avoid any loss of accuracy by the plastically deformed surface due to the indentation load. The calibration specimen demonstrated that the accuracy of each measurement was ±4HK.

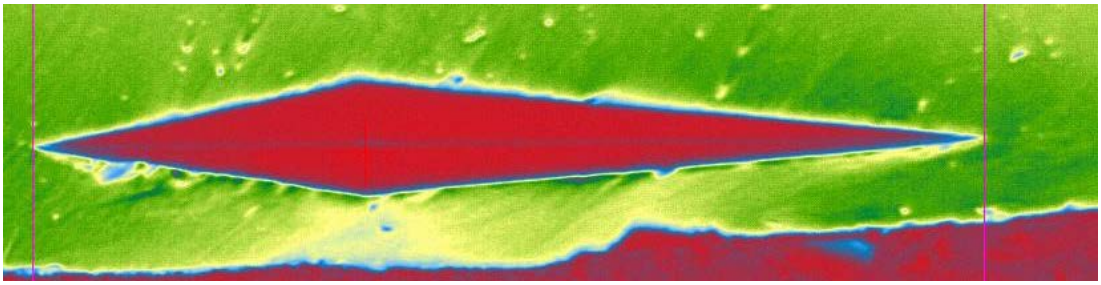

Figure 3.15 Typical example of the Knoop hardness indentation morphology.

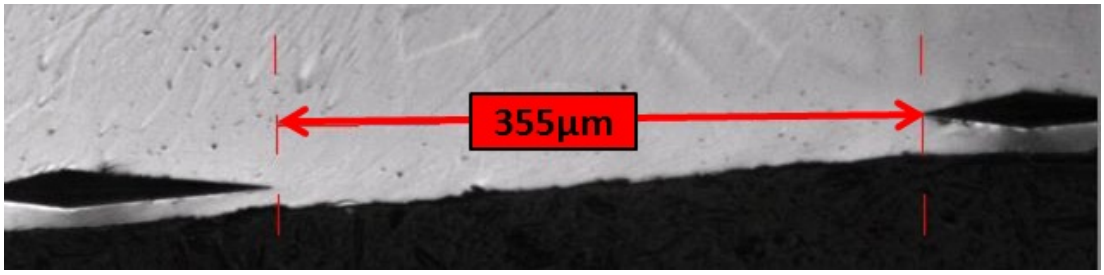

Figure 3.16 Example of the intermediate distance between the Knoop hardness indentations.

3.5 References

[3.1] ISO 14577-4 (2007): Metallic materials – Instrumented indentation test for hardness and materials parameters – Part 4: Test method for metallic and non-metallic coatings, 4 (2007) 14577.

[3.2] BS EN ISO 4288:1998 British Standard for Geometric Specification and Surface Texture, (1998).

Chapter 4

Development of a novel erosion-corrosion assessment technique

4.1 Introduction

The main focus of this chapter is to describe a method of investigating erosion-corrosion behaviour of materials using the submerged jet apparatus with a novel, expanded assessment of the post-test surface damage. This yields an evaluation of the mechanical processes, electrochemical responses and the synergistical effects that occur simultaneously on the target material surface during solid/liquid impingement.

The organisation of this chapter commences with a review of the erosion-corrosion assessment methods, and the role of surface topography in the development of this enhanced experimental approach. The new technique was validated by means of erosion-corrosion experiments on a carbon steel and an austenitic stainless steel, hence a literature review of the behaviour of these two materials was undertaken. This section is then followed by a detailed presentation of the experimental results, data analysis and discussion of the findings.

4.2 Summary of erosion-corrosion assessment methods

A number of experimental techniques have been adopted for studying the complexities of the erosion-corrosion phenomena. These include slurry pot [4.1–4.4], rotating cylinder [4.5–4.7] and Corriolis tester [4.8–4.10]. These approaches have their limitations, as they enable examination of low impingement angles and not the complete spectrum of angles (from 0^o to 90^o) to which most industrial components are subjected. In fact, Tian et al [8] attempted to extend the range of impingement angles in a Corriolis tester but this approach does not appear to have been followed up.

On the other hand, the submerged jet impingement is a commonly used erosion-corrosion technique because it facilitates assessments within a wide range of impingement angles [4.11,4.12]. In such experiments, an aqueous stream, with or without solid particles, is directed onto a specimen whose surface area is greater than the diameter of the jet. The current study has focused on the 90^o angle of impingement, as most use of this technique has involved normal incidence (90^o) [4.13–4.18], recognising though, that there is an opportunity to investigate simultaneously the effects of low angle of impingement that also take place on the testing coupon. Figure 4.1 shows an example of the post-test surface of the UNS S31600 after solid/liquid impingement, which comprises two discrete regions:

- The directly impinged zone in which a distinct wear scar is produced by solid particles impinging at angles that vary from 85^{o} in the centre of the wear scar to 45^{o} at the edge of the wear scar [4.19,4.20], and
- the outer zone adjacent to the wear scar where the fluid is producing an essentially abrasive action which is illustrated by sliding abrasion marks which diminish in intensity from the wear scar towards the edge of the specimen.

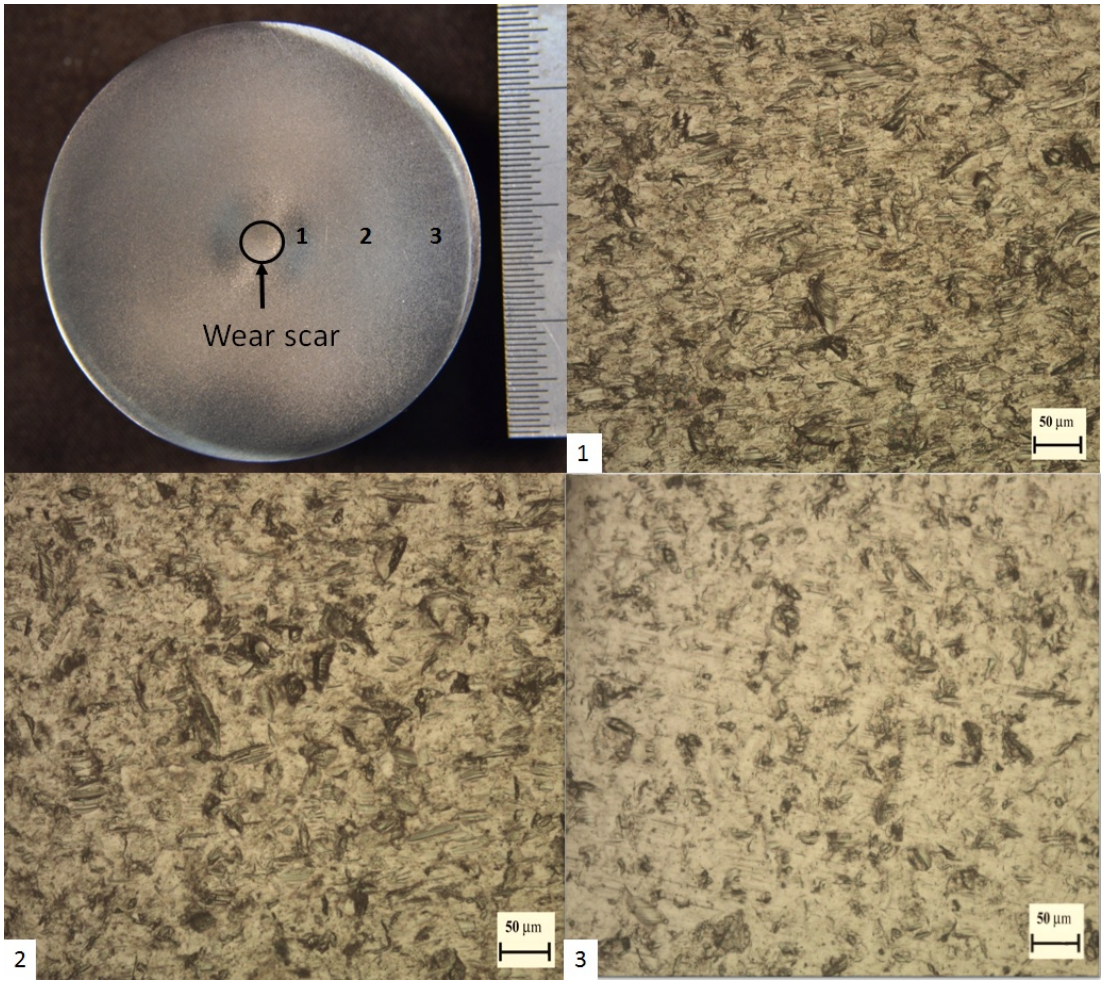

Figure 4.1 Post-test surface of the 38mm diameter UNS S31600 stainless steel specimen after solid/liquid impingement with evidence of sliding abrasion marks outside the wear scar (1) adjacent to the wear scar, (2) outermost area, (3) near the edge.

4.3 Role of surface topography in enhancement of the erosion-corrosion assessment

A basic feature of the erosion-corrosion tests is that they involve the mass loss measurement of the testing coupon and such information has proved extremely valuable in exercises that compare different materials and/or test conditions. In a typical submerged jet test, the total mass loss of a specimen is composed of the damage occurred in the directly impinged zone and the outer area. Despite the fact that the localised damage is more severe in the directly impinged zone, the material loss is unlikely to be negligible in the area outside the wear scar. Moreover, a change in target material, or impinging fluid characteristics, may result in different relative magnitudes of damage in those two regions.

The submerged jet investigations would be enhanced by post-test surface evaluation, which would discriminate the total mass loss into these two distinct areas. This strategy enables a deeper interpretation of fundamental mechanisms of erosion-corrosion and expanded data for industrial use. This is a tactic that, to the author's knowledge, does not appear to have been employed hitherto. The key evaluation method that contributes to this objective makes use of advanced surface topography.

There are several ways of undertaking topographical investigations; atomic force microscopy (AFM) [4.21–4.23], interferometry [4.24–4.26], stylus [4.27–4.31], and non-contact optical profilometry [4.10,4.32–4.35]. Surface profile scanning is the most common post-test surface examination method as they yield a two dimension profile of the worn area from a simple line scan across the specimen surface. Surface profile scanning is a non-destructive method that determines the effect of erosive media on the target surface and avoids cross sections of the tested coupons, especially on coated specimens. Hawthorne et al [4.29] have also reported that an estimation of wear scar volume is feasible by employing solid geometry to measure values of wear scar depth and diameter on HVOF sprayed coatings after slurry jet impingement. Similar attempts have been made by Matzavinos [4.36] on commercially-pure titanium alloy specimens under solid/liquid impingement.

Volumetric analysis, through non-contact optical profilometry, enhances the value of the surface topography and it holds great advantages in many engineering applications. Cook et al [4.37] have recently developed a volumetric assessment of material loss from retrieved cemented metal hip replacement stems. Volume loss estimations have also

assisted impact studies, where the behaviour of wear resistant steels under deformation is important [4.38]. Sliding wear studies have implemented volumetric analysis of the sliding wear tracks to compare the performance of coatings [4.39–4.41]. One piece of work did measure the wear scar volumes of API X42 steel which had been subjected to dry sand erosion [4.42]. Within the context of corrosion inhibitor performance, Barker [4.43] presented some wear scar depth data and he discussed, without further investigation, the issue of comparing mass losses within the wear scar with the overall mass loss.

Hence, it is evident that evaluation of erosion-corrosion experimental data, where direct volume loss measurement of the wear scar is included, would extend the interpretation of the erosion-corrosion damage.

4.4 Literature review of comparative studies of stainless steels with carbon steels.

Many studies have shown the superiority of the stainless steels compared with carbon steels in erosion-corrosion environments due to the greater corrosion resistance. A clear distinction in erosion-corrosion performance of two stainless steels (UNS S41000 martensitic and UNS S32760 superduplex) and the carbon steel (UNS K03014) was evident in the work of Neville and Wang [4.44]. The carbon steel depicted almost four times higher mass loss than the two stainless steels under solid/liquid impingement at normal incidence with 500ppm sand concentration. Also, the corrosion related component of the carbon steel displayed 40% contribution on the overall mass loss, whereas the martensitic stainless steel exhibited just 14% corrosion and synergy, which shows the great corrosion resistance of the stainless steels.

The poor erosion-corrosion and corrosion resistance of the carbon steels was also apparent in the study by Karafyllias et al [4.45], which demonstrated that the UNS G10400 medium carbon steel exhibited substantially higher mass loss in liquid impingement with 3.5% NaCl solution compared to the negligible mass loss of the UNS S32760 superduplex stainless steel. With the addition of solids (250mg/L), the medium carbon steel displayed seven times higher mass loss than the superduplex stainless steel.

Rajahram et al [4.4], investigated the low-angle impingement erosion-corrosion resistance of the UNS G10200 carbon steel and the UNS S31603 austenitic stainless steel in

a slurry pot. Their solid/liquid erosion-corrosion tests with distilled water and 1%wt sand showed that the mass losses of the carbon steel were similar to the austenitic stainless steel. However, the addition of 3.5% NaCl differentiated the two comparative steels by clarifying the superiority of the stainless steel. This study showed the similarities of the carbon steel with the stainless steel in mechanical resistance and the vulnerability of carbon steels in erosion-corrosion environments. Quite contradictory traits were shown by Levy and Hickey [4.46], who studied the low-angle erosion resistance of UNS G101800 carbon steel and a UNS S31600 stainless steel in a slurry pot with kerosene and 30wt% of coal, in which the authors considered that corrosion effects were negligible. The erosion performance of the stainless steel was greater than the carbon steel.

Figure 4.2 illustrates the average weight loss of the comparative study from Uhbi and Hodgkiess [4.18]. It is evident that the solid/liquid impingement resistance of the UNS S31603 austenitic stainless steel was greater than that of the UNS G41300 low alloy steel. The corrosion and synergy dominated the low alloy steel deterioration, whereas erosion component was the primary factor of the material loss of the stainless steel. In terms of erosion behaviour, though, the austenitic stainless steel exhibited quite similar behaviour with the low alloy steel.

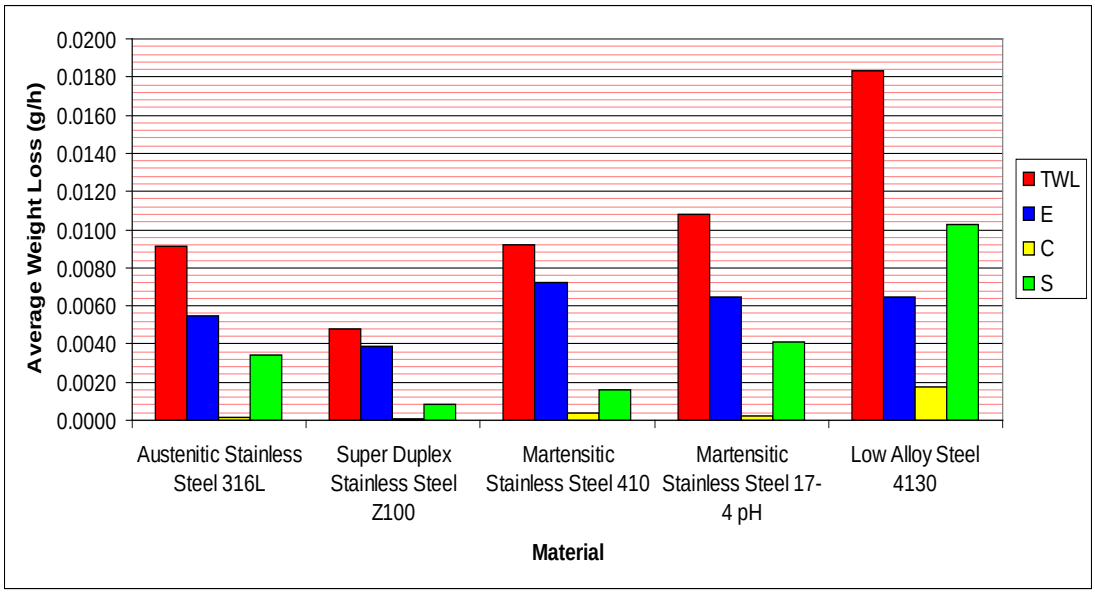

Figure 4.2 Material loss for a range of engineering steels after solid/liquid impingement at 90° angle of impingement in aerated 3.5%NaCl at 32°C, 15m/s and 2 g/l solid loading. The Z100 stands for the UNS S32760. [4.18]

Similar trends were observed in the work of Giourntas et al [4.47], which assessed the erosion-corrosion response of the austenitic stainless steel (UNS S31600) and the medium carbon steel (UNS G10400) under solid/liquid impingement. The mass loss of the medium carbon steel was two times higher than that of the austenitic stainless steel under erosion-corrosion conditions. In pure mechanical conditions, however, the carbon steel exhibited only 1.3 times higher mass loss than the stainless steel. This attribute was associated with the high proportion of corrosion and synergy effect on the overall material degradation of the carbon steel. The anodic polarisation scans also indicated the relatively poor corrosion resistance of the carbon steel, since the mass loss due to corrosion was around 16 times higher than that of the UNS S31600 stainless steel.

Comparable performance outcomes of the stainless steels and the carbon steels were found in the study of Neville et al [4.48], where a C-Mn steel and UNS S31603 austenitic stainless steel were evaluated under solid/liquid impingement conditions. The erosion-corrosion resistance of the austenitic stainless steel was almost two times better than the C-Mn steel. The contribution of corrosion to the overall mass loss of the stainless steel was only 2.3%, in comparison with that of carbon steel which was 7%. It should be noted, though, that the pure mechanical damage of the carbon steel (29mg) was quite close to the stainless steel (22mg). The poor corrosion resistance of the carbon steels manifests the key factor of their discrimination with stainless steels.

In summary, whilst the superior erosion-corrosion performance of stainless steels compared to carbon steels is evident, this generality masks some comparative features involved in the detailed contributors to erosion-corrosion damage. These factors have been unravelled in the experimental work described herein.

4.5 Experimental work objectives

The objective of this work has been to merge the conventional erosion-corrosion assessment methodologies with the non-optical profilometry capabilities to segregate the different degradation mechanisms that occur in a material that is subjected to a submerged solid/liquid impingement. This expanded scope of the submerged jet impingement was evaluated on two steel alloys (a stainless steel and a carbon steel) that exhibit different erosion-corrosion behaviour under impingement. It is well known, that the austenitic

stainless steel (UNS S31600) falls under the corrosion resistant alloys (CRAs) group in which the alloys exhibit superior resistance to flowing/impinging conditions in solid free saline solutions. In solid/liquid impingement conditions, however, the durability of the austenitic stainless steel is significantly impaired [4.16,4.49]. On the other hand, the medium carbon steels possess extremely poor corrosion resistance in aqueous environments and this aspect is also manifested in erosion-corrosion conditions.

4.6 Methodology

The materials that were selected for this study are listed below:

- Austenitic stainless steel (UNS S31600), which exhibits good corrosion resistance in various corrosive environments.
- A medium carbon steel (UNS G10400), which has poor corrosion performance in most aqueous conditions.

The nominal compositions of the two alloys are shown in Table 4.1. The measured hardness values of UNS S31600 and UNS G10400 are 200HV and 240HV, respectively. The density values of the alloys are 8.00 g/cm^3 and 7.85 g/cm^3 for the austenitic stainless steel and the medium carbon steel, respectively.

Table 4.1 Nominal composition (wt%) of the stainless steel and the carbon steel.

Material	C	Cr	Ni	Mo	S	Mn	Si	N	P	Fe
UNS S31600	≤0.08	16-18	10-14	2.0-3.0	≤ 0.03	≤2.0	≤0.75	≤ 0.10	0.045	Bal.
UNS G10400	0.37-0.44				≤ 0.05	0.6-0.9			≤0.04	Bal.

The erosion-corrosion experiments were carried out using a submerged jet impingement rig described in Section 3.3.1. The duration of the impingement tests was 1 h. The nozzle diameter was 3 mm and the slurry, which consisted of 3.5% NaCl and sand particles, impinged at 19 m/s velocity perpendicular to the specimen surface. Hydraulic fracturing sand was used in this study, which exhibits hardness of 1160HV and has spherical shape, as shown in Section 3.2.8. The sand concentration was 150 mg/L. The testing

temperature range was 30°C - 36°C. After the free erosion-corrosion experiments, the medium carbon steel specimens were immersed briefly in an inhibited acid solution (Clark's solution) before weighing to remove the extensive corrosion on their surface.

4.7 Results

4.7.1 Mass loss measurements

Figure 4.3 demonstrates the average mass loss measurements with error bars showing the scatter from the three replicates under free erosion-corrosion and cathodic protection (CP) conditions. The erosion-corrosion performance of the UNS S31600 was superior compared with the carbon steel UNS G10400. The discrimination of these two steels was evident in both conditions as the UNS S31600 maintained its superior resistance even when the cathodic protection was applied. It is also apparent that the UNS G10400 suffers severely by the corrosion factor, as its mass loss is almost half when electrochemical reactions were negligible (i.e. CP).

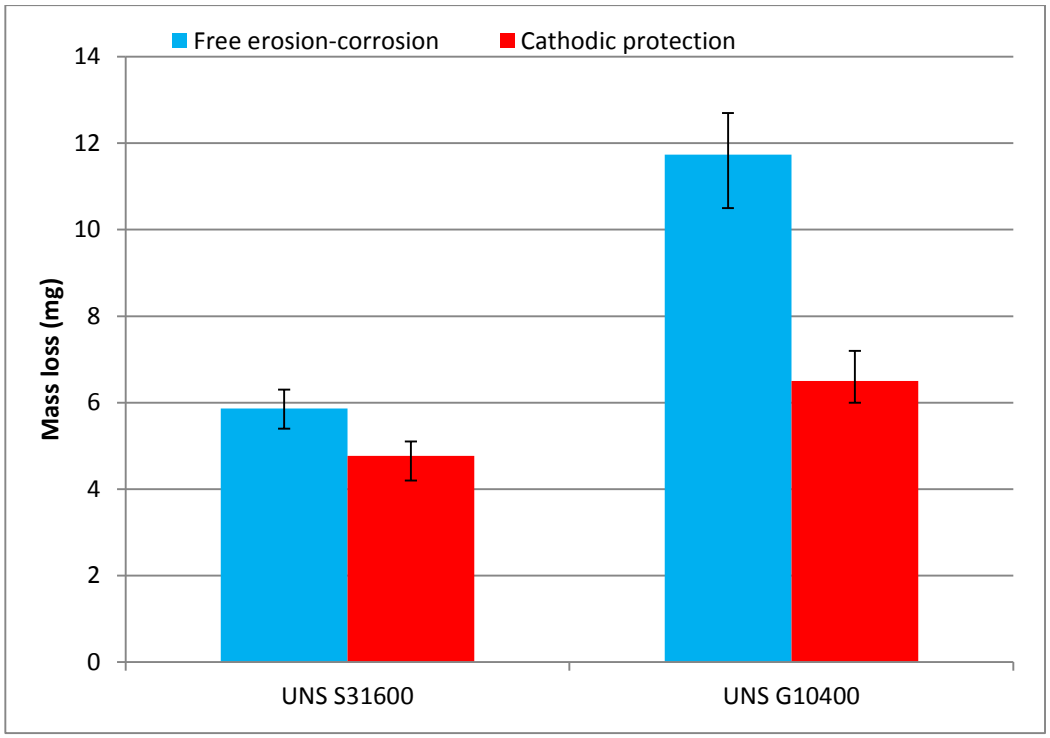

Figure 4.3 Mass losses of the steels in solid/liquid impingement with and without cathodic protection.

4.7.2 Potentiodynamic scans

Figures 4.4 and 4.5 illustrate the results of the anodic polarisation scans that were conducted on the segmented specimens of the stainless steel and carbon steel, respectively. These scans were conducted using the anodic polarisation scanning methodology described in Section 3.3.3. It should be noted that the potentiodynamic scans were commenced after the stabilisation of the free corrosion potential (E_{corr}), which occurred after the first 30 minutes, as described in Section 3.3.4. The normalised electrode potential represents the electrode potential at least 25mV more negative to E_{corr} and it has been employed for better comparison, since the E_{corr} values were different between the two regions. The current density of stainless steel in the direct impinged zone (DIZ) is greater than in the outer area (OA) because of the aggressive erosion-corrosion conditions that pertain within the wear scar. Due to the high concentration of solids in the direct impinged zone, the stainless steel exhibited higher rates of periodic passivation/de-passivation events (i.e fluctuations of the current density) compared to the outer area. On the other hand, the carbon steel was active in both regions.

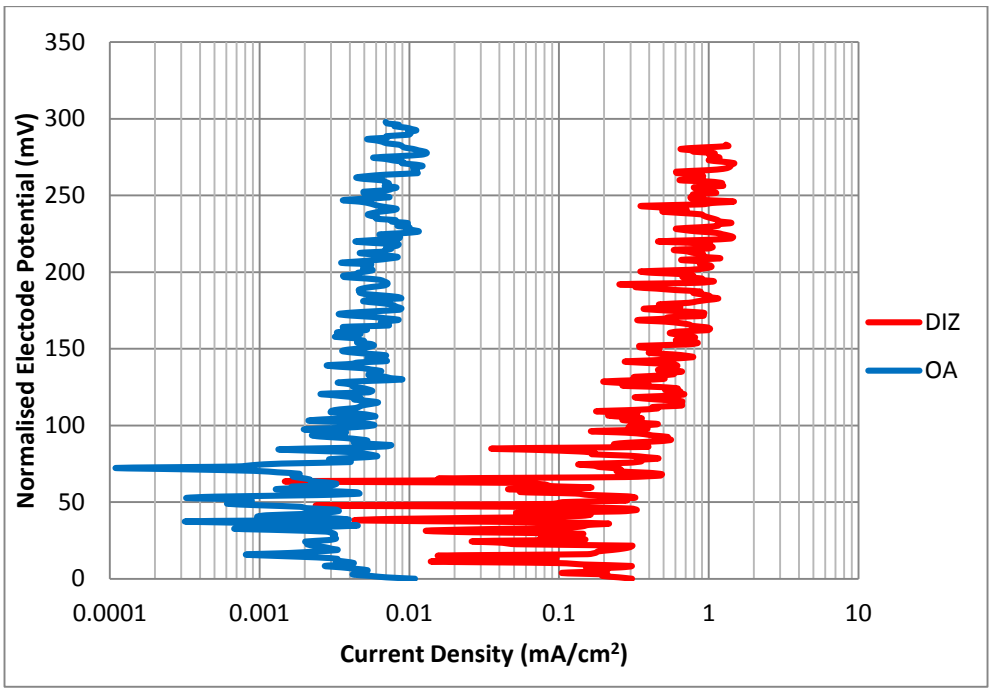

Figure 4.4 Anodic polarisation scans of the segmented specimen of stainless steel UNS S31600 under solid/liquid impingement

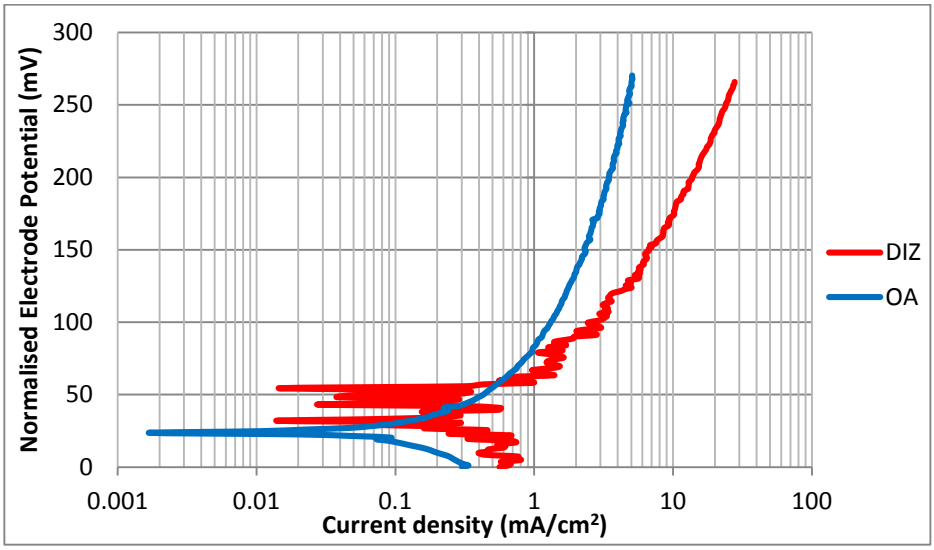

Figure 4.5 Anodic polarisation scans of the segmented specimen of medium carbon steel UNS G10400 under solid/liquid impingement

Figure 4.6 shows the anodic polarisation scans on the full specimen (38mm diameter) of a stainless steel and a medium carbon steel. The electrode potentials are again normalised to facilitate more effective comparison. The current density fluctuations of the stainless steel indicate that the passivity was periodically disrupted by the mechanical impact of the solids in the slurry. On the other hand, the medium carbon steel experienced active corrosion behaviour during impingement.

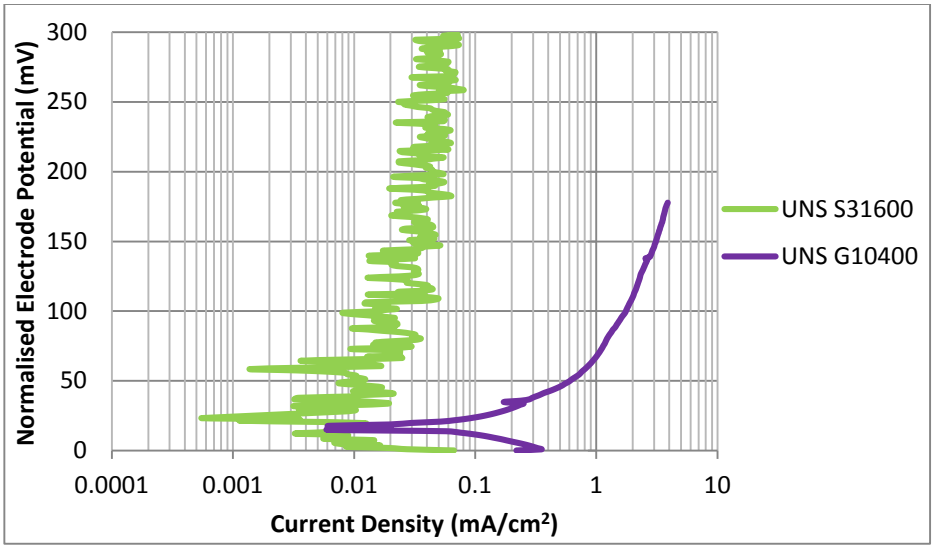

Figure 4.6 Full specimen anodic polarisation scans of the tested materials under solid/liquid impingement.

Table 4.2 displays the E_{corr} values of the segmented and full specimens along with the corrosion current densities (i_{corr}), obtained by Tafel extrapolation involving plotting a straight line from the average of the oscillating currents back to E_{corr}. Hence, the corrosion current densities were converted to mass losses by applying Faraday's law (see Section 2.3.7.2). Apparently, there is little or no difference between the sum of the mass losses due to corrosion measured by the segmented specimens and the full specimen. This provides a high level of confidence for a successful segmentation of the specimen.

Table 4.2 Comparison of free erosion-corrosion potentials (E_{corr}) the current densities and mass losses due to corrosion on the segmented and the full specimens.

Properties	E_{corr} (mV) (Ag/AgCl)		Corrosion Current Density i_{corr} (mA/cm^2)		Mass loss (mg)	
	UNS S31600	UNS G10400	UNS S31600	UNS G10400	UNS S31600	UNS G10400
DIZ (Area = 0.2 cm^2)	-547	-574	0.200	0.50	0.04	0.1
OA (Area = 11.0 cm^2)	-337	-524	0.003	0.35	0.03	4.0
Full specimen	-442	-557	0.070	0.35	0.08	4.1

4.7.3 Surface topography

4.7.3.1 Surface Profile scans

To evaluate the behaviour of these two alloys in the zone directly under the impinging jet (wear scar), surface profile scans were performed via surface topography (see Section 3.4.2), on post-test specimens. Figures 4.7 and 4.8 show examples of U-shaped wear scar profiles of the stainless steel and the carbon steel, respectively, after tests in free erosion-corrosion condition and also after implementation of cathodic protection. It should be mentioned that the wear scar diameter (3.5mm) corresponds approximately to the diameter of the nozzle (3mm) used in this study.

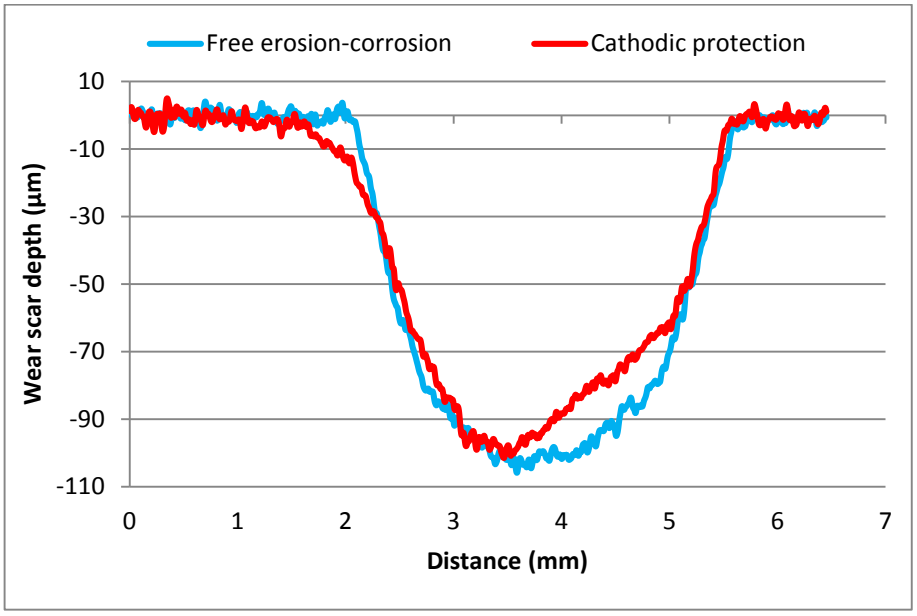

Figure 4.7 Surface profile scans of the wear scar of the stainless steel UNS S31600 after free erosion-corrosion (blue) and cathodic protection (red) under solid/liquid impingement.

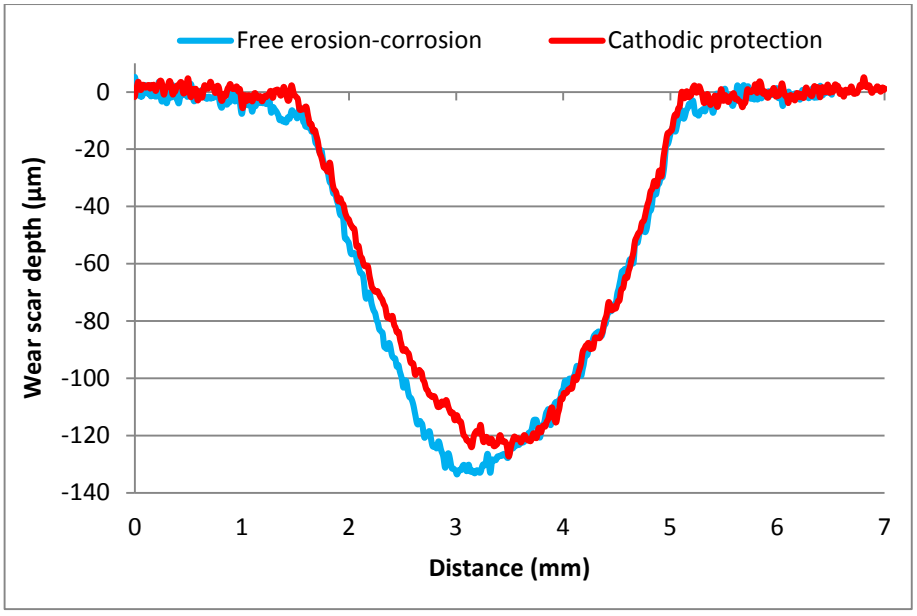

Figure 4.8 Surface profile scans of the wear scar of the medium carbon steel UNS G10400 after free erosion-corrosion (blue) and cathodic protection (red) under solid/liquid impingement.

Figure 4.9 shows the wear scar depths of replicate specimens of the two steels with and without cathodic protection. There is a clear correlation between the mass losses and the wear scar depths, as the UNS G10400 exhibited deeper wear scars than the UNS S31600. It is also evident, that the application of CP has not generally resulted in a significant reduction in wear scar depth on either material.

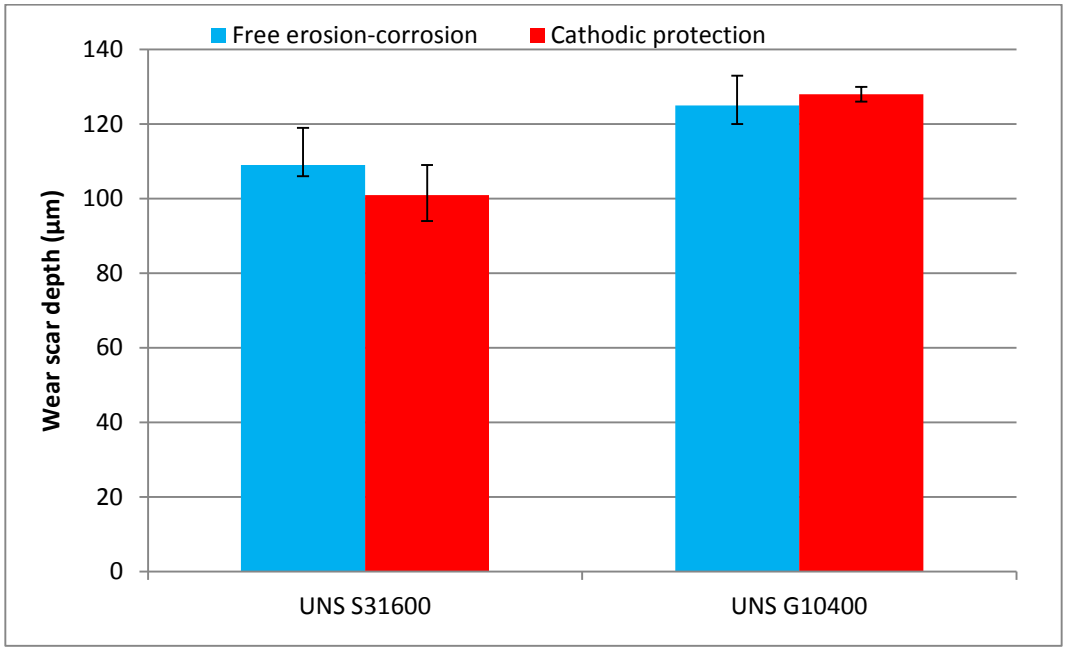

Figure 4.9 Wear scar depths of the two steels under solid/liquid impingement with free erosion-corrosion and cathodic protection conditions.

4.7.3.2 Volumetric analysis of the wear scars

Figure 4.10 shows the volume measurement of the directly impinged zone of a UNS S31600 specimen after test. The volumetric analysis was executed on the region inside the red ring, which represents the area under the jet, by following the surface topography method in Section 3.3.3.

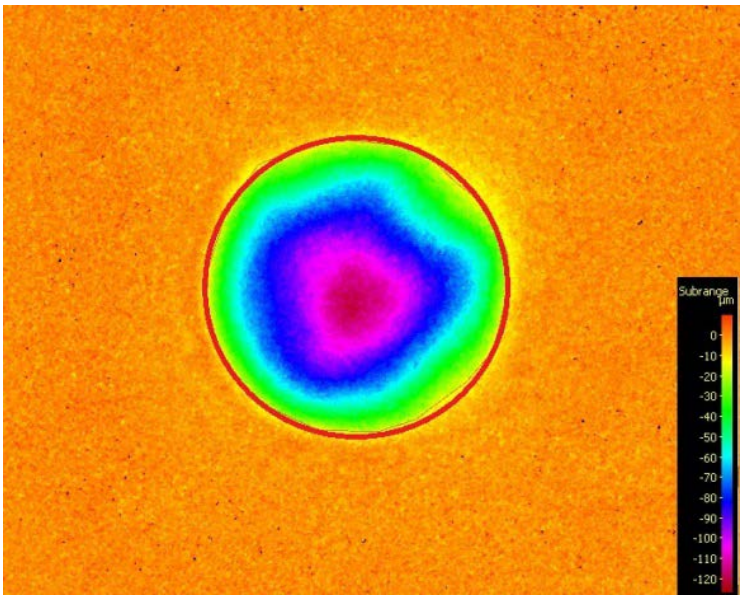

Figure 4.10 Volumetric analysis on the direct impinged zone of the UNS S31600 surface after solid/liquid impingement.

Figure 4.11 illustrates the volume losses within the wear scar during solid/liquid impingement with and without cathodic protection. The volume loss of the UNS G10400 steel was 20% higher than UNS S31600 in both conditions, which shows the benefit of the stainless steel over the medium carbon steel within the direct impinged zone. It is also evident that the volume losses of both steels remained unaffected when cathodic protection was applied to the specimens. This trend demonstrates that the volume loss on the direct impingement is predominantly associated with erosion damage.

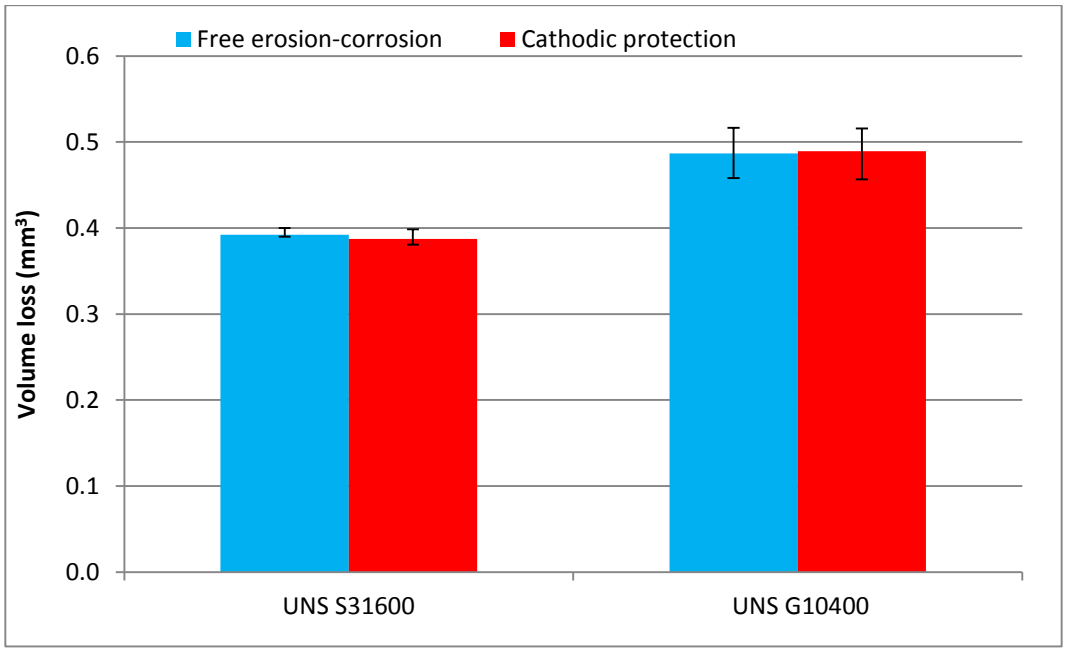

Figure 4.11 Comparison of the average wear scar volume losses of the UNS S31600 and UNS G10400 under solid/liquid impingement with free erosion-corrosion and cathodic protection conditions.

4.8 Discussion

4.8.1 Total Mass loss (TML) in free erosion-corrosion (FEC) conditions

The total mass losses were measured directly from the experiments, see Figure 4.3. The overall mass loss of the UNS S31600 was substantially lower than the UNS G10400 in free erosion corrosion conditions, which demonstrates the superiority of the stainless steels compared to carbon steels. Similar features of the poor erosion-corrosion performance of the carbon steel in comparison with stainless steels have been observed by other researchers in the past [4.4,4.18,4.44,4.45,4.47].

Discrimination of the total mass loss in DIZ and OA

The total mass loss is identified as the mass loss in the wear scar and the material loss beyond the direct impinged zone, as summarised in Equation 4.1.

$$TML(FEC) = ML[DIZ] + ML[OA] \qquad \textbf{Equation 4.1}$$

where, TML (FEC) is the total mass loss under free erosion-corrosion conditions and ML[DIZ] is the mass loss in the direct impinged zone (DIZ) which is calculated from the measured volume losses, through surface topography, and the material densities as follows;

UNS S31600: $ML[DIZ] = 0.39mm^3 \times 8.00g/\mathrm{cm}^3 = 3.1mg$

UNS G10400: $ML[DIZ] = 0.48mm^3 \times 7.85g/\mathrm{cm}^3 = 3.9mg$

ML [OA] represents the mass loss on the outer area (OA), which is quantified as follows;

$$ML[OA] = TML(FEC) - ML[DIZ]$$

UNS S31600: $ML[OA] = 5.9mg - 3.1mg = 2.8mg$

UNS G10400: $ML[OA] = 11.7mg - 3.9mg = 7.8mg$

Figure 4.12, demonstrates clearly that, for the UNS S31600 steel, the most substantive manifestation of damage caused by the submerged jet is the wear scar in the directly impinged zone. For the carbon steel, however, sliding abrasion/corrosion damage in the outer area is much more significant and this feature precludes simple correlation of material loss with target hardness.

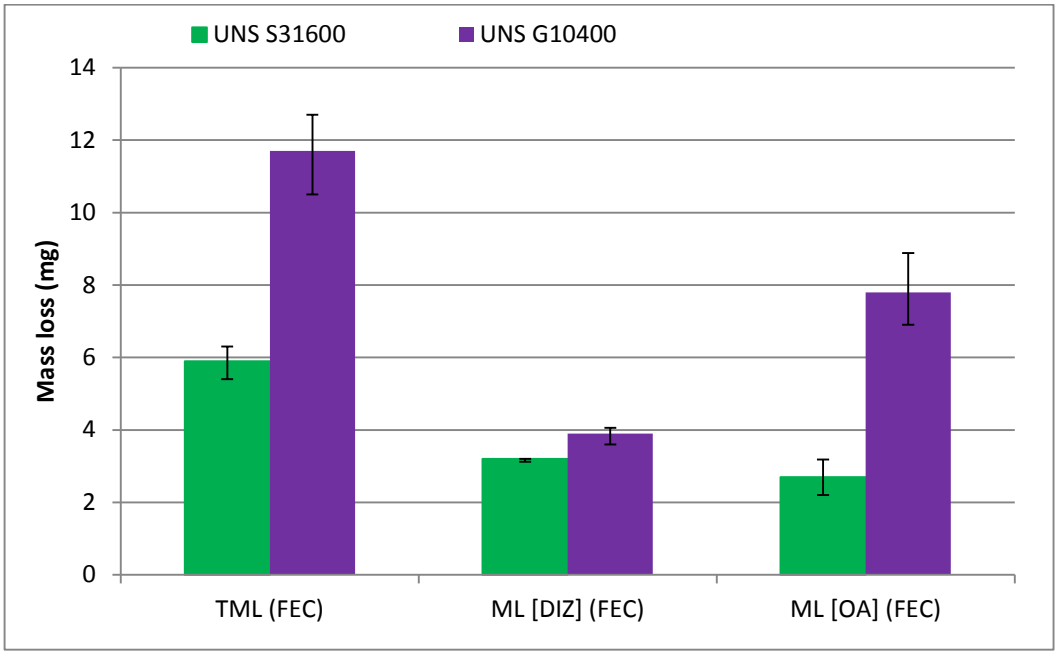

Figure 4.12 Breakdown of the total mass loss into the mass losses of the two regions under free erosion-corrosion

Consequently, separation of the mass losses in the two zones enhances the understanding of the fundamental mechanisms of deterioration of components subjected to a submerged jet. It also facilitates comparisons of materials' behaviour under two distinct erosion-corrosion situations (i.e. directly under the jet and on the outer area). The contributors to erosion-corrosion damage were shown in Equation 2.2 (see Section 2.1). This approach enables the computation of the magnitudes of damage due to the various components of erosion-corrosion within the two zones. The quantitative material losses, shown in Figure 4.13, are based on Equation 4.2 below, and they demonstrate the substantial benefits of the expanded assessment of erosion-corrosion testing.

$$TML(FEC) = E[DIZ] + C[DIZ] + S[DIZ] + SA[OA] + C[OA] + S[OA] \quad \textbf{Equation 4.2}$$

Where, E [DIZ] is the erosion damage inside the wear scar, C [DIZ] is the corrosion damage in the wear scar, S [DIZ] is the synergy effect in the wear scar, SA [OA] is the sliding abrasion (mechanical damage), C [OA] and S [OA] represent the corrosion and synergy in the outer area.

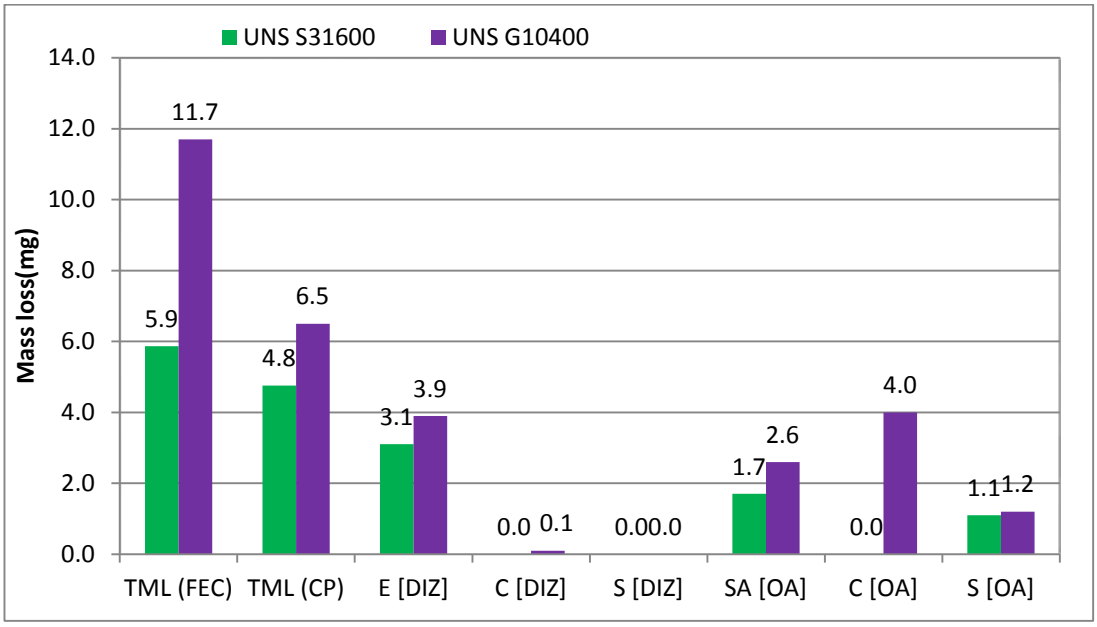

Figure 4.13 Distinction of the different material degradation processes on the UNS S31600 and UNS G10400 steels.

This assessment provides quantitative data applicable to the two extreme angles of impingement associated with the direct impinged zone and the outer area (near to 0°). It also demonstrates the differentiation between the mechanical deterioration mechanisms of erosion and sliding abrasion, showing that the latter process contributes significantly to the overall mechanical damage. In general, this procedure enables a wider appreciation to be obtained of the comparative performances, of different materials under solid/liquid impingement, than is acquired by a simple comparison of a single measured parameter (i.e. mass loss).

4.8.2 Total mass loss with cathodic protection (CP)

The total mass losses, with cathodic protection of the steels, were measured directly from the experiments (see Figure 4.3). Since the application of cathodic protection supresses any corrosion reaction, the total mass loss, TML (CP) represents the erosion damage inside the wear scar and the sliding abrasion which takes place outside the wear scar (Equation 4.3).

$$TML(CP) = E[DIZ] + SA[OA] \qquad \textbf{Equation 4.3}$$

The stainless steel exhibited higher resistance to mechanical damage than the carbon steel. In more detail, the application of CP reduced the overall mass loss of both

materials. It is clear that the mass loss on the UNS G10400 was decreased by 44.5%, whereas the UNS S31600 mass loss dropped by 18% with CP. Similar reductions of the mass losses of the carbon steels by the application of cathodic protection were also found in previous studies [4.18,4.44,4.47]. This signifies that the corrosion related component (C+S) is playing a more substantial role on the material degradation of the medium carbon steel and it influences insignificantly the stainless steels.

4.8.3 Erosion damage on the direct impinged zone (DIZ)

The mechanical damage occurred in the direct impinged zone (DIZ), was measured through the volume loss measurements on the cathodically protected tested coupons. Table 4.3 illustrates the mass loss due to the mechanical damage on the wear scar.

Table 4.3 Mass loss calculated from the volumetric analysis of the wear scar for cathodically protected specimens.

Materials	Measured volume loss (mm^3)	Density (g/cm^3)	Mass loss (mg)
UNS S31600 (CP) [DIZ]	0.39	8.00	3.1
UNS G10400 (CP) [DIZ]	0.49	7.85	3.9

The UNS G10400 steel exhibited significantly higher erosion deterioration than UNS S31600. Alike trends, where the impingement erosion damage of the carbon steel was higher than the austenitic stainless steel have been observed in past studies of the author [4.47] and Uhbi and Hodgkiess [4.18] only in terms of wear scar depths, which still represents effectively the mass loss in the direct impinged zone.

By taking into account the comparable hardness of the two steel alloys (Table 4.1), the above results comprise evidence of the relative insensitivity of impingement erosion to target hardness. Although it is generally accepted that material hardness is an important parameter in terms of damage by abrasive wear, for other types of wear (e.g. impingement erosion), however, such a relationship, with hardness alone, is less appropriate. The elastic modulus is considered to be another important property with a high value of the ratio of hardness to elastic modulus being desirable [4.50]. In any case, for a high velocity impinging jet, attempted correlations with conventional mechanical properties may be less relevant

than the incorporation of mechanical properties determined under high-strain-conditions [4.51].

4.8.4 Corrosion and synergy on the direct impinged zone (DIZ)

According to Figure 4.11, for both materials, the wear scar volume losses, with and without the application of CP, were similar in the testing conditions employed herein. The material loss in the direct impinged region is purely by mechanical action and in the material/testing conditions in this study, the corrosion related component was found to be negligible. This feature has also been verified by the estimation of the mass loss due to corrosion from anodic polarisation scans on the segmented coupons as shown in Table 4.2. This erosion domination is likely to have been associated with the erodent properties (size/shape/concentration) and the jet velocities.

4.8.5 Sliding abrasion on the outer area (OA)

The mechanical sliding abrasion damage of both steels was determined by re-arranging Equation 4.3.

$$SA[OA] = TML(CP) - E[DIZ]$$

Using the data in Figure 4.3 and Table 4.3;

Stainless steel: $SA[OA] = 4.8mg - 3.1mg = 1.7mg$

Medium Carbon steel: $SA[OA] = 6.5mg - 3.9mg = 2.6mg$

Given that the sliding abrasion damage is often said to be related to the target material hardness [4.50], this difference in performance of the two steels is unexpected. However, the sliding abrasion results agree with previous studies which reported that the mechanical resistance of the carbon steel in low angle impacts (i.e. effectively sliding abrasion) can be either similar to or lower than the stainless steel depending on the erosive conditions [4.4,4.46].

4.8.6 Corrosion on the outer area (OA)

The anodic polarisation scans on the segmented specimen (Figures 4.5 and 4.6), provided an indication of the corrosion damage occurring on the outer areas for both steels. From

the Tafel extrapolations, the mass loss due to corrosion was estimated to be 0.03mg and 4.0mg for stainless steel and medium carbon steel, respectively. The stainless steel suffered less corrosion, apparently, because of the lower tendency for the passive film to break down as opposed to the situation in the direct impinged zone. On the other hand, the carbon steel was not protected by any passive film and for this reason it exhibited higher mass loss. Similar poor corrosion behaviour of the carbon steel has been reported from past researchers [4.18,4.46,4.48].

4.8.7 Synergy on the outer area (OA)

The interaction of erosion with corrosion, known as synergy, on the outermost area was calculated by the subtraction of the sliding abrasion damage and the corrosion damage from the calculated overall mass loss on the outer area, as shown below:

$$S[OA] = ML[OA] - SA[OA] - C[OA]$$

Stainless steel: $S[OA] = 2.7mg - 1.6mg - 0.03mg = 1.1mg$

Medium Carbon steel: $S[OA] = 7.8mg - 2.6mg - 4.0mg = 1.2mg$

The synergy of the medium carbon steel is comparable with that of the stainless steel. In terms of the synergy on the stainless steels, Matsumura et al [4.52] suggested that the elimination of the work hardened layer by corrosion attack is likely to increase the mechanical abrasion damage of the steel. On the other hand, synergy on carbon steels can be associated with their low pitting corrosion resistance, as the corrosion pits are likely to cause local turbulence and therefore enhance the erosion damage.

4.9 Conclusions

An extended evaluation procedure has been presented that:

- Contributes to the understanding of the fundamental mechanisms of erosion-corrosion on a component subjected to a locally-impinging, solid/liquid stream.
- Enhances the assessment of the performance of different materials or surface engineering treatments in various erosion-corrosion environments.

The study has, perhaps not unexpectedly, demonstrated the superiority of the UNS S31600 stainless steel over the medium carbon steel (UNS G10400) under erosion-corrosion conditions in agreement with others. It has also facilitated comparisons related to some of the detailed degradation processes as summarised below:

1. UNS S31600 has been shown to exhibit greater erosion-corrosion performance at both angles of impingement (90^o and also at the glancing angle close to 0^o).
2. The superior performance of stainless steel (UNS S31600) in comparison with carbon steel (UNS G10400) has been shown to involve benefits in respect of pure mechanical damage (in the wear scar and outer area) and also in terms of corrosion related phenomena.
3. The application of cathodic protection decreased the mass loss of the steels substantially (i.e. 18.6% on the stainless steel and 44.5% on the carbon steel). This significant reduction occurred in the outer area, since the wear scar was erosion dominated.
4. The experimental results have illustrated that there are some limitations in simple correlation of erosion-corrosion damage with target hardness.

4.10 References

[4.1] R.J.K. Wood, J.C. Walker, T.J. Harvey, S. Wang, S.S. Rajahram, Influence of microstructure on the erosion and erosion-corrosion characteristics of 316 stainless steel, Wear. 306 (2013) 254–262.

[4.2] G.R. Desale, B.K. Gandhi, S.C. Jain, Slurry erosion of ductile materials under normal impact condition, Wear. 264 (2008) 322–330.

[4.3] G.D. Nelson, G.L.F. Powell, V.M. Linton, Investigation of the Wear Resistance of High Chromium White Irons, (2010).

[4.4] S.S. Rajahram, T.J. Harvey, R.J.K. Wood, Erosion–corrosion resistance of engineering materials in various test conditions, Wear. 267 (2009) 244–254.

[4.5] M.M. Stack, J.S. James, Q. Lu, Erosion–corrosion of chromium steel in a rotating cylinder electrode system: some comments on particle size effects, Wear. 256

(2004) 557–564.

[4.6] M. Bjordal, E. Bardal, T. Rogne, T.G. Eggen, Erosion and corrosion properties of WC coatings and duplex stainless steel in sand-containing synthetic sea water, Wear. 186-187 (1995) 508–514.

[4.7] S.W. Watson, B.W. Madsen, S.D. Cramer, Wear-corrosion study of white cast irons, Wear. 181-183 (1995) 469–475.

[4.8] H.H. Tian, G.R. Addie, E.P. Barsh, A new impact erosion testing setup through Coriolis approach, Wear. 263 (2007) 289–294.

[4.9] H.H. Tian, G.R. Addie, R.J. Visintainer, Erosion-corrosion performance of high-Cr cast iron alloys in flowing liquid-solid slurries, Wear. 267 (2009) 2039–2047.

[4.10] R.J. Llewellyn, S.K. Yick, K.F. Dolman, Scouring erosion resistance of metallic materials used in slurry pump service, Wear. 256 (2004) 592–599.

[4.11] M. Reyes, A. Neville, Mechanisms of Erosion-Corrosion on a Cobalt-Base Alloy and Stainless-Steel UNS S17400 in Aggressive Slurries, J. Mater. Eng. Perform. 10 (2001) 723–730.

[4.12] N. Andrews, L. Giourntas, A.M. Galloway, A. Pearson, Effect of impact angle on the slurry erosion-corrosion of Stellite 6 and SS316, Wear. 320 (2014) 143–151.

[4.13] J.I. Ukpai, R. Barker, X. Hu, A. Neville, Determination of particle impacts and impact energy in the erosion of X65 carbon steel using acoustic emission technique, Tribol. Int. 65 (2013) 161–170.

[4.14] D. Lopez, N.A. Falleiros, A.P. Tschiptschin, Effect of nitrogen on the corrosion-erosion synergism in an austenitic stainless steel, Tribol. Int. 44 (2011) 610–616.

[4.15] S. Shrestha, T. Hodgkiess, A. Neville, Erosion–corrosion behaviour of high-velocity oxy-fuel Ni–Cr–Mo–Si–B coatings under high-velocity seawater jet impingement, Wear. 259 (2005) 208–218.

[4.16] A. Neville, X. Hu, Mechanical and electrochemical interactions during liquid–solid impingement on high-alloy stainless steels, Wear. 251 (2001) 1284–1294.

[4.17] T. Hodgkiess, A. Neville, S. Shrestha, Electrochemical and mechanical interactions during erosion-corrosion of a high-velocity oxy-fuel coating and a stainless steel, Wear. 233-235 (1999) 623–634.

[4.18] A. Uhbi, T. Hodgkiess, The erosion-corrosion behaviour and performance of engineering steels, Unpublished work, University of Glasgow, 2009.

[4.19] A. Gnanavelu, N. Kapur, A. Neville, J.F. Flores, An integrated methodology for predicting material wear rates due to erosion, Wear. 267 (2009) 1935–1944.

[4.20] A. López, W. Nicholls, M.T. Stickland, W.M. Dempster, CFD study of Jet Impingement Test erosion using Ansys Fluent® and OpenFOAM®, Comput. Phys. Commun. 197 (2015) 88–95.

[4.21] D.A. López, J.P. Congote, J.R. Cano, A. Toro, A.P. Tschiptschin, Effect of particle velocity and impact angle on the corrosion–erosion of AISI 304 and AISI 420 stainless steels, Wear. 259 (2005) 118–124.

[4.22] M. Vite-Torres, J.R. Laguna-Camacho, R.E. Baldenebro-Castillo, E.A. Gallardo-Hernández, E.E. Vera-Cárdenas, J. Vite-Torres, Study of solid particle erosion on AISI 420 stainless steel using angular silicon carbide and steel round grit particles, Wear. 301 (2013) 383–389.

[4.23] J.M. Perry, A. Neville, V.A. Wilson, T. Hodgkiess, Assessment of the corrosion rates and mechanisms of a WC-Co-Cr HVOF coating in static and liquid-solid impingement saline environments, Surf. Coatings Technol. 137 (2001) 43–51.

[4.24] V. Stoica, R. Ahmed, T. Itsukaichi, Influence of heat-treatment on the sliding wear of thermal spray cermet coatings, Surf. Coatings Technol. 199 (2005) 7–21.

[4.25] J.M.U. Guilemany, J.M. Miguel, S. Vizcaino, F. Climent, Role of three-body abrasion wear in the sliding wear behaviour of WC-Co coatings obtained by thermal spraying,

Analysis. (2001) 141–146.

[4.26] R. Ahmed, O. Ali, N.H. Faisal, N.M. Al-Anazi, S. Al-Mutairi, F.L. Toma, et al., Sliding wear investigation of suspension sprayed WC–Co nanocomposite coatings, Wear. 322-323 (2015) 133–150.

[4.27] Q.B. Nguyen, C.Y.H. Lim, V.B. Nguyen, Y.M. Wan, B. Nai, Y.W. Zhang, et al., Slurry erosion characteristics and erosion mechanisms of stainless steel, Tribol. Int. 79 (2014) 1–7.

[4.28] V.B. Nguyen, Q.B. Nguyen, Z.G. Liu, S. Wan, C.Y.H. Lim, Y.W. Zhang, A combined numerical–experimental study on the effect of surface evolution on the water–sand multiphase flow characteristics and the material erosion behavior, Wear. 319 (2014) 96–109.

[4.29] H.M. Hawthorne, B. Arsenault, J.P. Immarigeon, J.G. Legoux, V.R. Parameswaran, Comparison of slurry and dry erosion behaviour of some HVOF thermal sprayed coatings, Wear. 225-229 (1999) 825–834.

[4.30] V.A. De Souza, A. Neville, Corrosion and erosion damage mechanisms during erosion–corrosion of WC–Co–Cr cermet coatings, Wear. 255 (2003) 146–156.

[4.31] Z. Kamdi, P.H. Shipway, K.T. Voisey, A.J. Sturgeon, Abrasive wear behaviour of conventional and large-particle tungsten carbide-based cermet coatings as a function of abrasive size and type, Wear. 271 (2011) 1264–1272.

[4.32] M. Salasi, G.B. Stachowiak, G.W. Stachowiak, Three-body tribocorrosion of high-chromium cast irons in neutral and alkaline environments, Wear. 271 (2011) 1385–1396.

[4.33] T.A. Adler, Ö.N. Doğan, Damage by indentation and single impact of hard particles on a high chromium white cast iron, Wear. 203-204 (1997) 257–266.

[4.34] H.M. Clark, H.M. Hawthorne, Y. Xie, Wear rates and specific energies of some ceramic, cermet and metallic coatings determined in the Coriolis erosion tester,

Wear. 233-235 (1999) 319–327.

[4.35] H.J. Rack, U.J. DeSouza, A. Wang, Impact deformation and damage in austenitic high chromium white cast iron by spherical projectiles at normal incidence, Wear. 159 (1992) 121–126.

[4.36] D. Matzavinos, Durability studies relevant to marine equipment, Ph.D. Thesis, University of Glasgow, 2001.

[4.37] R.B. Cook, N.R. Shearwood-Porter, J.M. Latham, R.J.K. Wood, Volumetric assessment of material loss from retrieved cemented metal hip replacement stems, Tribol. Int. 89 (2015) 1–4.

[4.38] M. Lindroos, V. Ratia, M. Apostol, K. Valtonen, A. Laukkanen, W. Molnar, K. Holmberg, V.T. Kuokkala The effect of impact conditions on the wear and deformation behavior of wear resistant steels, Wear. 328-329 (2015) 197–205.

[4.39] K. Van Acker, D. Vanhoyweghen, R. Persoons, J. Vangrunderbeek, Influence of tungsten carbide particle size and distribution on the wear resistance of laser clad WC/Ni coatings, Wear. 258 (2005) 194–202.

[4.40] G. Bolelli, V. Cannillo, L. Lusvarghi, T. Manfredini, Wear behaviour of thermally sprayed ceramic oxide coatings, Wear. 261 (2006) 1298–1315.

[4.41] H. Engqvist, N. Axén, S. Hogmark, Tribological properties of a binderless carbide, Wear. 232 (1999) 157–162.

[4.42] M.A. Islam, Z.N. Farhat, Effect of impact angle and velocity on erosion of API X42 pipeline steel under high abrasive feed rate, Wear. 311 (2014) 180–190.

[4.43] R.J. Barker, Erosion-Corrosion of Carbon Steel Pipework on an Offshore Oil and Gas Facility, Ph.D. thesis, University of Leeds, 2012.

[4.44] A. Neville, C. Wang, Erosion–corrosion of engineering steels—Can it be managed by use of chemicals?, Wear. 267 (2009) 2018–2026.

[4.45] G. Karafyllias, T. Hodgkiess, A. Galloway, The Influence of Acidic Conditions in Erosion-Corrosion Behavior of Medium Carbon Steel (UNS G10400) and Superduplex Stainless Steel (UNS S32760), in: Dep. Def. -Allied Nations Tech. Corros. Conf. Pittsburgh, 2015.

[4.46] A.V. Levy, G. Hickey, Liquid-solid particle slurry erosion of steels, Wear. 117 (1987) 129–146.

[4.47] L. Giourntas, T. Hodgkiess, A.M. Galloway, Comparative study of erosion–corrosion performance on a range of stainless steels, Wear. 332-333 (2015) 1051–1058.

[4.48] A. Neville, T. Hodgkiess, J.T. Dallas, A study of the erosion-corrosion behaviour of engineering steels for marine pumping applications, Wear. 186-187 (1995) 497–507.

[4.49] X. Hu, A. Neville, The electrochemical response of stainless steels in liquid-solid impingement, Wear. 258 (2005) 641–648.

[4.50] A. Matthews, A. Leyland, Materials related aspects of nanostructured tribological coatings, 51st SVC TechCon. (2008).

[4.51] G. Sundararajan, The solid particle erosion of metallic materials: The rationalization of the influence of material variables, Wear. 186-187 (1995) 129–144.

[4.52] M. Matsumura, Y. Oka, H. Hiura, M. Yano, The role of passivating film in preventing slurry erosion– corrosion of austenitic stainless steel, ISIJ Int. 31 (1991) 168–176.

Chapter 5

Erosion-corrosion study on white cast irons and stainless steels

5.1 Introduction

Weir Minerals have dedicated considerable research and development effort in developing the metallurgy of the white cast irons to fit a range of industrial wear conditions. The Group is aware that the operational behaviour of the different cast irons is crucially dependant on the degree of damage associated with mechanical, corrosion and interaction mechanisms. As part of the alloy development, they have devoted much attention to means of increasing the wear resistance by variations of the casting technology and the incorporation of the harder carbides into the white chromium cast iron structure. Another aspect of their research philosophy is to modify the metallic matrix of the white cast iron in order to mimic the corrosion properties of stainless steels. In pursuance of these objectives, it was decided to focus on two of the currently used white cast irons; one of which exhibits relatively good wear resistance but lacks of corrosion resistance (martensitic metallic phase) and the other demonstrating good corrosion performance via its austenitic metallic phase but relatively lower wear resistance in neutral pH environments. To facilitate an enhanced correlation between microstructure and erosion-corrosion mechanisms, it was deemed useful to include a martensitic and an austenitic stainless steel in the testing program.

5.2 Literature review on white cast irons

The high chromium cast irons comprise three key elements; iron, chromium and carbon. The carbon is present primarily in the form of carbides, as the chromium has high affinity for carbon then high-hardness, chromium carbides are precipitated. The presence of chromium is also important in enhancement of the corrosion resistance of the metallic phase. There are three fundamentally different microstructures that can be obtained in high-chromium cast irons by varying the carbon content. These three possible types are designated, according to the level of carbon from low to high, as follows; hypoeutectic, eutectic, and hypereutectic alloys. Another major difference between these types of alloys is their solidification path. The eutectic alloys solidify at a single temperature and this occurs at a unique carbon level known as the eutectic composition. On the other hand, in the case of the hypoeutectic cast irons, the ferrous phase is nucleated primarily followed by the formation of eutectic structure with carbides and the ferrous matrix. On the other hand, the solidification of the hypereutectic starts with the nucleation and growth of the primary carbides, often M_7C_3 type, followed by the precipitation of the eutectic mixture of carbides and the ferrous phase. The development

of the wear-resistant, high-chromium cast irons is focused on the carbide refinement, ferrous matrix modification and different manufacturing processes.

5.2.1 Effect of carbide volume fraction (CVF)

By increasing the carbon content, the volume fraction of carbides is considerably raised, reducing, though, the cast iron's toughness. The greater volume fraction of carbides provides an improvement in the abrasive wear resistance of the cast irons, as it raises their bulk hardness and it leads to lower inter-carbide spacing that is also an important factor of the cast iron durability under abrasive wear [5.1–5.3].

Fulcher et al [5.1] reported that the 30% CVF showed greater abrasion resistance against the 45% CVF when silica particles were used in the rubber wheel abrasion tester. However, the white cast iron with 45%CVF showed superior abrasion resistance compared to the 30% CVF cast iron in the same abrasion tester with alumina. Similar trends were found in the work by Gahr and Eldis [5.4], who discovered that an increase of the carbide volume fraction beyond 30% can result in higher abrasive wear loss in a rubber wheel tester. However, in their pin-on-disk abrasion tests, the abrasion resistance of the cast irons was linearly increased by the increase of the volume fraction of carbides. This is attributed to the different wear mechanisms that take place in these two completely different testing techniques.

In terms of erosion and erosion-corrosion behaviour of white cast irons, a review of the literature [5.5,5.6] does not reveal any consistent relationships between CVF and erosion-corrosion rate. It appears that such relationships are influenced by a number of environmental factors such as type of fluid (i.e. air or liquid), flow velocity and sand characteristics. Walker and Robbie [5.7] also showed that there is no simple correlation of the carbide volume fraction with the wear resistance, by assessing two white cast irons in four different testing techniques. For instance, the dry sand rubber wheel tester and the slurry jet erosion tester at 20^{o} angle of impingement showed that the near eutectic 27%Cr white cast iron exhibited greater wear resistance than the 37%Cr hypereutectic white iron. On the other hand, the Corriolis tester and the fresh water slurry jet tester at 30^{o} demonstrated the superiority of the 37%Cr hypereutectic over the 27%Cr white iron. The reason of this lack of agreement between the testing results is associated with differences in the testing conditions of each testing apparatus (i.e. stand-off distance, wear mechanisms).

An additional feature of Walker and Robbie [5.7] work was the change in the relative wear rates of two cast irons by utilising different types of erodent particles under jet test conditions. The 37%Cr hypereutectic showed 1.2 times higher mass loss than the 27%Cr hypoeutectic under jet test with silica carbide, whereas the performance of the 37%Cr hypereutectic exhibited 0.76 times lower mass loss with silica sand in the jet test. Gates et al [5.8], reviewed the wear rates of three white cast irons in seven different testing devices and their conclusions were that there are formidable challenges in developing white cast irons for service in erosion-corrosion situations.

5.2.2 Advancements through addition of elements with high affinity for carbon and different manufacturing processes

The incorporation of elements with relatively high affinity for carbon yields advantages in the wear resistance of the white cast irons. In fact, chromium is one of the nine elements in the periodic table of elements which possess strong thermodynamic tendency to form carbides. Table 5.1 shows the nine elements which exhibit this high affinity for carbon.

Table 5.1 Elements with high affinity with carbon extracted from the Periodic Table

Ti	V	Cr
Zr	Nb	Mo
Hf	Ta	W

Elements like zirconium, hafnium and tantalum are rare metals and are present in small quantities as minerals in the Earth, which makes them extremely difficult and expensive to be included to casting melts in foundries [5.9]. The other elements, though, are readily available in nature and they are added to achieve either refined microstructure with finer carbides or even harder carbides which would enhance the bulk hardness of the white cast iron.

Addition of chromium up to 32% and molybdenum up to 9% in hypoeutectic, eutectic and hypereutectic cast irons showed benefits on their sliding wear resistance in the pin-on-disc tribometer [5.10]. The molybdenum addition enhanced the hardness of the cast irons and reduced the volume fraction of the ferrous phase due to the formation of the Mo-rich

carbides. Arikan et al [5.11] investigated the benefits of 0.38% titanium addition to a 15Cr/3Mo white cast iron as an increase of the dry abrasion resistance was detected, especially on the as-quenched coupons where the matrix was martensitic. A more in-depth study of the effect of titanium was attempted by Chung et al, who investigated a hypereutectic Fe-25%Cr-4%C alloy with 2%Ti addition [5.12]. The hypereutectic white cast iron was transformed to a hypoeutectic cast iron due to the addition of titanium that caused depletion of the carbon to form titanium carbides. The microstructural refinement by titanium addition resulted in reduction of the volume fraction of the coarse carbides with increasing the bulk hardness of the eutectic structure and enhancing sliding abrasion resistance of the white cast irons.

The scope of the previous work [5.12] was subsequently expanded by considering the influence of other carbide-forming elements (V, Nb, Mo, B) on the solidification process, bulk hardness and wear behaviour of the hypereutectic Fe-25%Cr-4%C alloy [5.13]. The optimum element addition percentages, in terms of dry sliding resistance in a pin-on disk tester, were 4.5% for vanadium, 7.5% for niobium, 10-13% for boron and 13-16% for molybdenum in a cast iron of 3.72% carbon content. The improved wear resistance was closely related to the refinement of the microstructure by transforming the hypereutectic to a eutectic and hypoeutectic cast iron as the carbon is depleted to form carbides other than chromium rich carbides. The Nb_4C_3 exhibited the highest hardness (~2,220HV) of the carbides formed in this study by exhibiting almost double hardness value from the Cr_7C_3 (~1200HV).

The research outcomes of the work conducted by Chen et al [5.14], also verify the benefits of niobium addition on dry sliding wear resistance of a 15%Cr white cast iron . The niobium forms carbides of about 2,400HV hardness and since it shifts the eutectic point to the right, by gradually changing the eutectic structure into a hypoeutectic with primary austenite. Another interesting characteristic within this work [5.14] is the morphology of the hook-like NbC which strengthens the bonds between the matrix and the carbides. Their results field tests were in agreement with their sliding abrasion tests as the Nb addition increased the service life of the pump components up to 67%.

Wang et al [5.15] investigated the dry sliding wear performance of cast alloys that contain high affinity elements such titanium, vanadium, tungsten and molybdenum with concentration range from 5% to 35%, and they showed remarkably greater dry sliding behaviour compared to the base cast iron (Fe-20%Cr-5%C). The advantage of this concept is

that it enables modification of the white cast iron by forming different types of hard carbides such as M_7C_3, MC and M_6C. Each carbide type was enriched with different elements (MC with Ti and V, M_7C_3 with Fe and Cr, and M_6C with W and Mo). The high entropy alloys performed better than the base alloy on the dry pin on disk tester because of three fundamental reasons;

i) the newly formed carbides are harder than the Cr carbides,
ii) the MC and M_6C type carbides were smaller in size and hence less prone to cracking than the rod type M_7C_3 and
iii) the refined carbides showed higher density of interphase boundaries that can block dislocation movement and prevent cracking more effectively.

The same research group followed up their idea and they assessed a Fe-27Cr-2.5C-0.8Si white cast iron with small additions of B, B-V, B-Nb, B-W and also an ingot of Fe-27Cr-2.5C-0.8Si-1B-2V-067Nb-3.3W [5.16]. On a pin-on-disc tribometer, the sliding wear volume losses of the modified cast irons were lower than the base alloy due to their higher hardness. However, on the air blast erosion apparatus, the erosion rates at the normal incidence showed that the hybrid cast irons performed poorer than the base cast iron and at the 45^o of attack the behaviour of all the cast irons were comparable. This feature was attributed to the number of carbides that were fracturing at the 90^o impingement.

5.2.3 Potential improvements via modified manufacturing processes

Further advancement of the white cast irons' erosion resistance has been observed on the basis of different manufacturing processes. Llewellyn et al [5.17] reported that chill casting of hypereutectic chrome white irons increased the relative erosion resistance by a factor of 4.5 times compared to the sand cast material. The reasoning for this behaviour is the fact that the fast cooling and solidification during chill casting had resulted to the formation of more rounded primary carbides, compared with the coarse and elongated carbides, leaving the bulk hardness unaffected. Similar advantages of rapid cooling were found by Nelson et al [5.18], who compared an as-cast hypereutectic iron with a weld overlay iron with similar composition on a steel substrate. The slurry pot results showed the superiority of the weld overlay hypereutectic iron is associated with the higher bulk hardness and the finer carbides which minimised the inter-carbide spacing of the M_7C_3 that did not allow the abrasive particles to impinge onto the matrix.

Matsuo et al [5.19] found that the sliding abrasion resistance and the hardness of white cast irons deposited by a spraying process was greater than that of the as-cast alloys with the same chemical composition. The sprayed white irons showed refined carbides which were distributed homogeneously in the matrix. The material loss of the sprayed form white irons pins was lower than the as-cast pins on an 11%Cr martensitic stainless steel (VC 131) discs. Heat treatment of the as-sprayed pins can provide an additional improvement to the high velocity oxy fuel sprayed multi-component white cast irons coatings as reported by Maranho et al [5.20]. The heat treatment acts as sintering, where pores can be partially eliminated and transformation of austenite into martensite can be achieved.

5.2.4 Role of electrochemical deterioration mechanisms on the erosion-corrosion resistance of white cast irons

The electrochemical degradation cannot be omitted from the overall degradation equation (Equation 2.2), since the mining environments do contain slurries of different levels of corrosivity. Watson et al [5.21], have studied the individual phases of the white cast iron in order to broaden the understanding of the deterioration processes occurring on each of the cast iron elements. They isolated the carbides and the matrix by hot pressing and hot isostatic pressing techniques. Through a modified rotating cylinder apparatus, in which electrochemical monitoring system was embedded, the sliding wear, the pure corrosion and the synergy of these two mechanisms were determined for each carbide and matrix component. Their novel research outcomes showed that the Fe-14Cr-2.6C white iron is exhibiting a higher synergy effect than the isolated metallic phase as a result of the vulnerability of the M_7C_3 carbides to synergy effects. Although, the detailed mechanisms of synergy on isolated carbides were not discussed. Another important feature was the fact that the high synergy effect was associated with extremely low rates of pure corrosion damage of the white cast iron.

Zhang et al, have also studied the corrosion aspects of the interaction between the metallic and ceramic phases of white chromium cast irons of different chromium contents in flowing acidic conditions with silica sand in a rotating cylinder-type erosion-corrosion tester [5.22]. The segregation of the carbides from the matrix was completed by an etching procedure, whereas the matrix was prepared by inductive melting according to the composition specifications of the cast irons. The open circuit potentials (OCP) of the white cast irons were always between the OCP values of the carbides and the matrix. The carbides

exhibited more positive OCPs than the cast iron and the matrix, which indicates their high level of resistance to corrosion. This potential difference between the matrix and the carbides initiates a galvanic or inter-phase corrosion which leads to carbide protrusion and pre-fracture as the matrix plays the role of the anode and corrodes selectively.

On the other hand, Salasi et al [5.23] showed that when a white cast iron is exposed to high alkalinity environments (over pH=12), the carbides of a white cast iron can be removed faster than the ferrous phase, as it corrodes in a higher rate. This is another example of the effect of composition of the aqueous fluid (i.e. acidic or alkaline) in the different phases of the cast irons, which highlights the complexity of the erosion-corrosion phenomena.

From the above reports, it is evident that the chromium content in the matrix is the controlling factor of the corrosion resistance of the cast irons. Neville et al [5.24], demonstrated the importance of the chromium in the matrix by assessing the corrosion behaviour of three white cast irons under static conditions. The ratio of the chromium concentration in the carbides and matrix ($Cr_{carbides}$/ Cr_{matrix}) is responsible for the corrosion resistance of the high chromium white cast irons. The lower the $Cr_{carbides}$/ Cr_{matrix} ratio, the better corrosion resistance would be obtained.

The same research group [5.25] also investigated the effect of solids in the corrosion performance of the same white cast irons, where the obtained corrosion rates were higher than the ones under liquid impingement, but the relative corrosion behaviour of the three white irons was maintained as the $Cr_{carbides}$/ Cr_{matrix} ratio governed the corrosion resistance of each cast iron even under solid/liquid conditions.

Tian and Taylor [5.26], reported higher corrosion rates on a 30%Cr ferritic white cast iron at from pH 2.5 to pH 1.5. Other useful work from Tian et al [5.27], comprised an erosion-corrosion assessment of a near eutectic (25%Cr) and two hypoeutectic cast irons (30%Cr and 40%Cr) content in Corriolis apparatus. They determined that the 40%Cr hypoeutectic cast iron exhibited superior erosion-corrosion resistance compared to the other two alloys in all environments (with pH levels at 7, 4 and 1.5) under 10μm size solid impingement. However, when the particle size was increased to 148μm, the 40%Cr hypoeutectic cast iron exhibited poorer erosion-corrosion resistance than the other two cast alloys. This attribute should be associated with the difference in the erosivity level of the flowing slurry, as the larger the sand particles, the more predominant the erosion mechanism.

Tang et al [5.28], also reviewed the effect of pH on a white cast iron with 45%Cr content and variable carbon content from 1% to 6% on a slurry pot erosion tester. The chromium in the matrix was decreased as the carbon content was increased, due to the depletion of chromium in forming chromium carbides. For this reason, the polarisation resistances of the 1%C alloys (hypoeutectic) were significantly higher than those alloys with 6%C content alloys (hypereutectic) in all pH environments in static conditions. However, the Fe-45Cr-4C alloy exhibited the greatest erosion-corrosion resistance out of these six white cast irons as it exhibited the second higher total carbide volume fraction with the highest eutectic carbide fraction (18%) and 17% Cr content in the matrix.

These results agree with the research outcomes of Lu et al [5.3], who screened twelve white cast irons on a dry sand rubber wheel tester along with static corrosion tests and they concluded that the optimum wear resistance of a white cast iron is achieved when the chromium content of the matrix and the volume fraction of the carbides are higher than 12% and 28%, respectively. A detailed wear/corrosion performance map, shown in Figure 5.1, was created for prediction of the corrosion-abrasion resistance of the white cast irons.

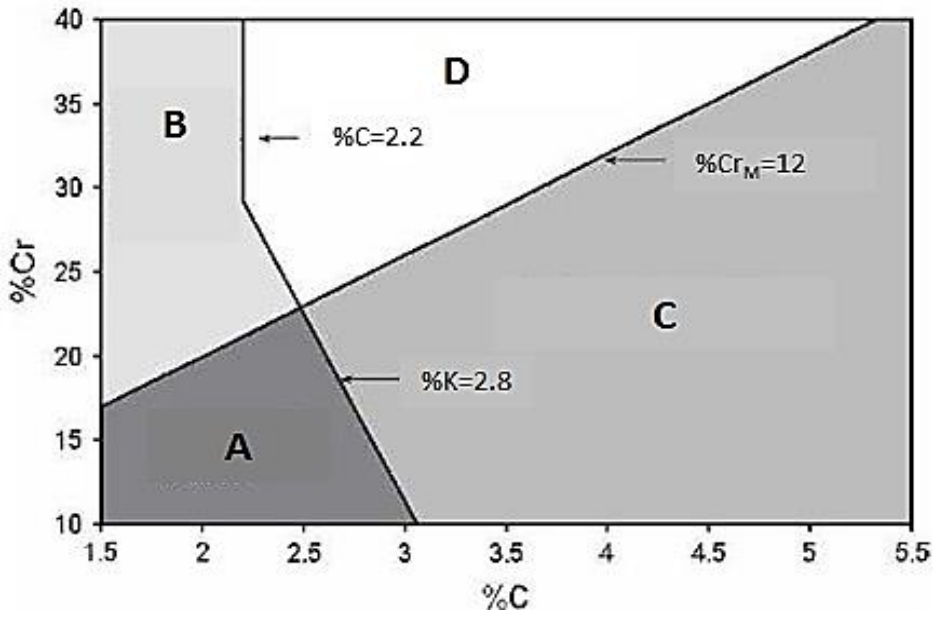

Figure 5.1 Wear/corrosion maps for the white cast irons (A- Poor wear & corrosion resistance, B – Poor wear resistance but good corrosion resistance, C – Good wear resistance but poor corrosion resistance, D – Good wear & corrosion resistance). [5.3]

5.2.5 Comparative studies of white cast irons with other materials

Over the past years, many researchers have assessed different types of white cast irons with other materials to form wear prediction tools by understanding the deterioration mechanisms. Stevenson and Hutchings [5.29], investigated the effect of impact angles on three hypereutectic weld deposited hard facing white irons, one Fe-27Cr-3C white cast iron ingot and a mild steel in an air blast erosion tester. At low angles (less than 60^o) the erosion rate of the white cast irons was considerably lower than the mild steel, highlighting the factor of hardness on the low angle abrasion. At the normal incidence, however, the mild steel behaved better than the white cast irons, revealing the brittle response of the white cast irons. This brittle response of the white cast irons was also observed in the slurry erosion (fresh water with silica sand) work of Al-Bukhaiti et al [5.30], where the erosion rate of the white cast iron was gradually raised as the impingement angle was increased from 15^o to 90^o. The maximum erosion rate of the UNS G10170 carbon steel was observed at 45^o of impingement. It should be mentioned, that the erosion rates of the white cast irons were significantly lower than the steel even at 90^o impingement.

Gore and Gates [5.31] reported also the superiority of the white cast irons over mild steel and an austenitic stainless steel. The volume loss of the carbon steel and stainless steel was around 12 and 5 times higher than the white irons, respectively, on a dry sand rubber wheel tester. According to their results the wear resistance on the conventional dry sand rotational wheel tester increases with the bulk hardness of the material. Parent and Li [5.32], also obtained the benefits of the white cast iron against a high strength martensitic stainless steel under 15^o slurry impingement (fresh water with 10wt% silica sand), as the volume loss of the stainless steel was 20 times higher than the cast iron.

Llewellyn et al [5.17] had a similar view point, by detecting the advantages of the hard white cast irons compared with corrosion resistant duplex stainless steels and UNS G10200 carbon steel on a Corriolis tester with fresh water and 10wt% silica sand circulated. The erosion resistance of the hard white cast iron (64.4 HRC) and the lower hardeness white cast iron (45HRC) was about 21 times and three times higher than that of the stainless steels (24-26HRC), respectively. Similarities on the relative performance of the stainless steels and the white cast irons were found in the work of Xie et al [5.33], where the Corriolis test results with slurry of fresh water and 10wt% silica sand, showed that the wear rates of the martensitic stainless steel were 22 times higher than those of the near eutectic cast iron (Fe-

27Cr-3C). Their additional slurry erosion, free-jet tests at 90^{o} with fresh water and 10wt% silica sand showed that the martensitic stainless steel exhibited about nine times higher volume loss than the eutectic cast iron. The excellent erosion performance of the white cast iron against the stainless steel was highlighted further when the angle of impingement changed from 90^{o} to 45^{o} and 20^{o}, where the volume loss difference between these two materials was accelerated to 14 and 22 times, respectively.

Jones and Llewellyn [5.34] have assessed the static corrosion rates of an austenitic stainless steel with a near eutectic and hypereutectic cast iron, resulting in exceptional behaviour of the stainless steel compared with both cast irons. In more detail, the polarisation resistance of the near eutectic and hypereutectic cast irons exhibited 29 times and 40 times lower polarisation resistances than the stainless steel under static liquid with 3.5%NaCl and pH 6.5. However, the slurry jet impingement tests at 45^{o} angle with sand size of 50-70 mesh showed the superiority of the white cast irons against the stainless steel exhibiting five times (near eutectic) and 11 times (hypereutectic) lower volume loss.

The same research group employed their newly developed slurry pot, which enables the embedment of electrochemical equipment, to investigate the erosion-corrosion phenomena of one austenitic stainless steel and three different types of white cast irons (hypereutectic, near eutectic and hypoeutectic with duplex structure) [5.35]. Their comprehensive study comprised free erosion-corrosion experiments, cathodic protection application and electrochemical monitoring. The UNS S31603 stainless steel exhibited the poorest erosion-corrosion resistance, while the hypereutectic white cast iron showed slightly better erosion-corrosion performance with high synergy that contributed up to 66% on its total mass loss. The near eutectic cast iron behaved similarly with the hypoeutectic white iron, in terms of total mass loss, with the former alloy being superior at the pure mechanical damage and the latter exhibiting greater corrosion resistance. In fact, the hypoeutectic white iron exhibited negligible corrosion damage, comparable to that of the austenitic stainless steel, due to its high chromium content (40%wt).

Neville and Reza [5.25] studied the erosion-corrosion of three different white cast irons with similar Cr/C ratio on a solid/liquid (1,000ppm of NaCl, pH 8.5, 5wt% solid loading) impingement recirculating rig, including an austenitic stainless steel (UNS S31603) as a reference. They showed that the erosion-corrosion performance can be altered when the fine silica sand is replaced with coarse silica sand. They observed a change of the relative

performance of the materials, as the stainless steel performed better than the white cast irons under coarse particles impingement, but the stainless steel exhibited higher mass loss than the cast irons when fine particles were utilised. These results demonstrated the complexity of the erosion-corrosion phenomena and the numerous variables that need to be considered.

In the recent study of Karafyllias et al [5.36], the erosion-corrosion impingement resistance of four materials; a hypoeutectic cast iron with martensitic matrix, a hypoeutectic white cast iron with austenitic matrix, and a martensitic (UNS S42000) and austenitic stainless steel (UNS S31600) was evaluated. The angle of solid/liquid impingement was kept at 90^{o} and the slurry comprised of 3.5%NaCl and 500 mg/L solid concentration. Their results illustrated the superior behaviour (lower volume loss) of the near eutectic cast iron and the hypoeutectic cast iron compared to the two stainless steels. This attribute was observed in both free erosion-corrosion and erosion conditions (i.e. application of cathodic protection). The austenitic based alloys were clearly better than the martensitic based alloys in terms of corrosion resistance.

5.3 Experimental work objectives

The objective of the present work was to investigate the deterioration mechanisms that occur within two hypoeutectic high chromium white cast irons with different %C and %Cr contents. Properties like the CVF factor, bulk hardness and the Cr/C ratio were investigated through impingement tests. The corrosion component, based on the $Cr_{matrix}/Cr_{carbides}$ ratio of each white cast iron was also evaluated, through electrochemical monitoring techniques. In addition to the cast irons, an austenitic and a martensitic stainless steel were also considered; the purpose being to consider the presence of the chromium carbides within each of the stainless steel-like structures. The application of the newly developed technique, described in Chapter 4, facilitated the quantification of the impingement erosion, sliding abrasion, corrosion and the synergistical effects of the electrochemical degradation to mechanical deterioration mechanisms of the white cast irons. This extensive analysis is highly novel as these cast irons have not been previously assessed as intensively as herein.

5.4 Materials and Methodology

The alloys that were selected for this study are listed below:

- Austenitic stainless steel (UNS S31600), which exhibits good corrosion resistance in various corrosive environments.
- Martensitic stainless steel (UNS S4200), which has moderate corrosion performance in saline conditions.
- Hypoeutectic chromium cast iron Fe-27Cr-2.9C alloy, referred to as 27%Cr cast iron herein, which possesses good wear resistance and low corrosion resistance through a eutectic structure derived from hard M_7C_3 type carbides and high hardness martensitic matrix.
- The hypoeutectic cast iron, named as 37%Cr cast iron herein, yields improved corrosion resistance by reducing the amount of chromium carbides and maintaining more chromium in the matrix, transforming to austenite, to attain 300 series austenitic stainless steels corrosion resistance with improved wear resistance.

Table 5.2 illustrates the nominal compositions of the stainless steels and cast irons (limited to carbon/chromium contents due to confidentiality), provided by the suppliers. Table 5.3 demonstrates the materials' densities along with their measured hardness.

Table 5.2 Nominal composition (wt%) of the stainless steels and cast irons.

Material	C	Cr	Ni	Mo	S	Mn	Si	N	P	Fe
UNS S31600	≤0.08	16-18	10-14	2.0-3.0	≤0.03	≤2.0	≤0.75	≤0.1	0.045	Bal.
UNS S42000	<0.15	12-14			<0.03	<1	<1		<0.04	Bal.
27%Cr cast iron	3.0	27								
37%Cr cast iron	1.8	37								

Table 5.3 Nominal densities and measured hardness of the stainless steels and cast irons

Material	Density (g/cm^3)	Hardness (HV-5kgf)
UNS S31600	8.00	200
UNS S42000	7.85	280
27%Cr cast iron	7.50	765
37%Cr cast iron	7.65	365

Figures 5.2 and 5.3 demonstrate the microstructure of the 27%Cr and 37%Cr cast irons through their cross sections, as described in Section 3.2.3. The 27%Cr cast iron has apparent eutectic rod-type chromium carbides (white) with eutectic martensite (light brown) and primary martensite (dark brown). On the other hand, 37%Cr cast iron consists of austenitic dendrites and eutectic structure of austenite and small size (around 1-2µm) chromium carbides.

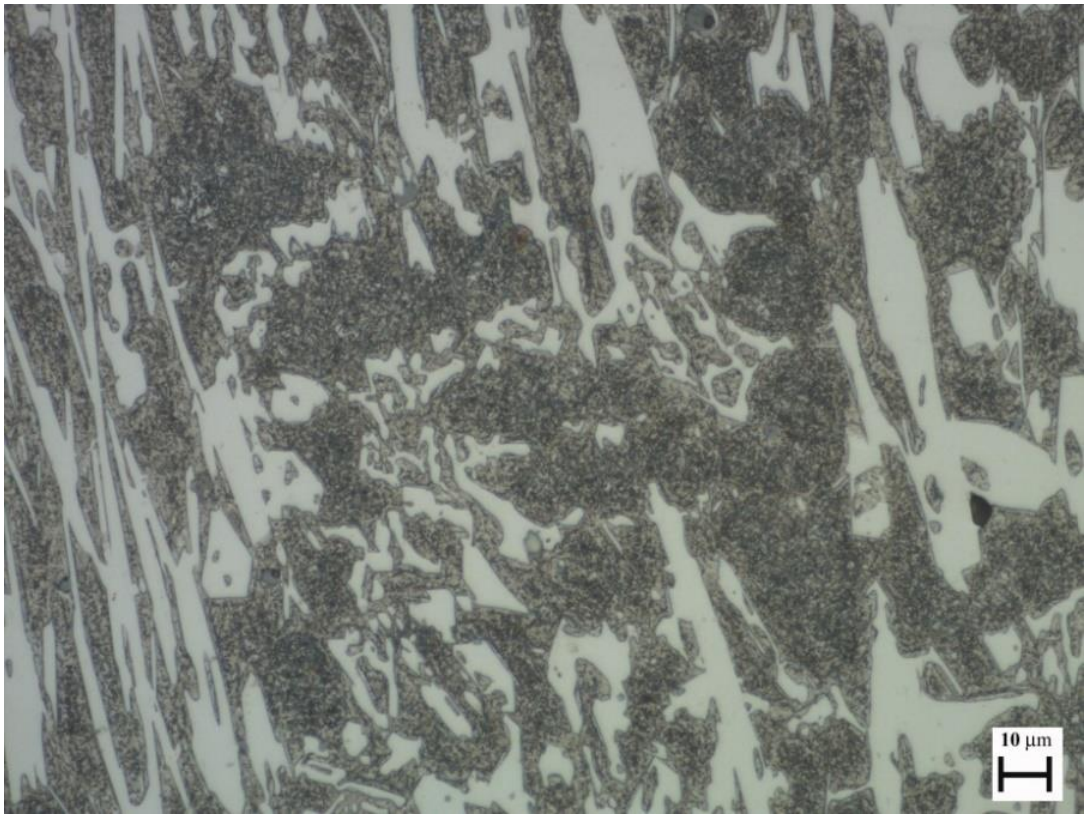

Figure 5.2 The microstructure of the 27%Cr cast iron with the large size eutectic carbides and eutectic and primary martensite.

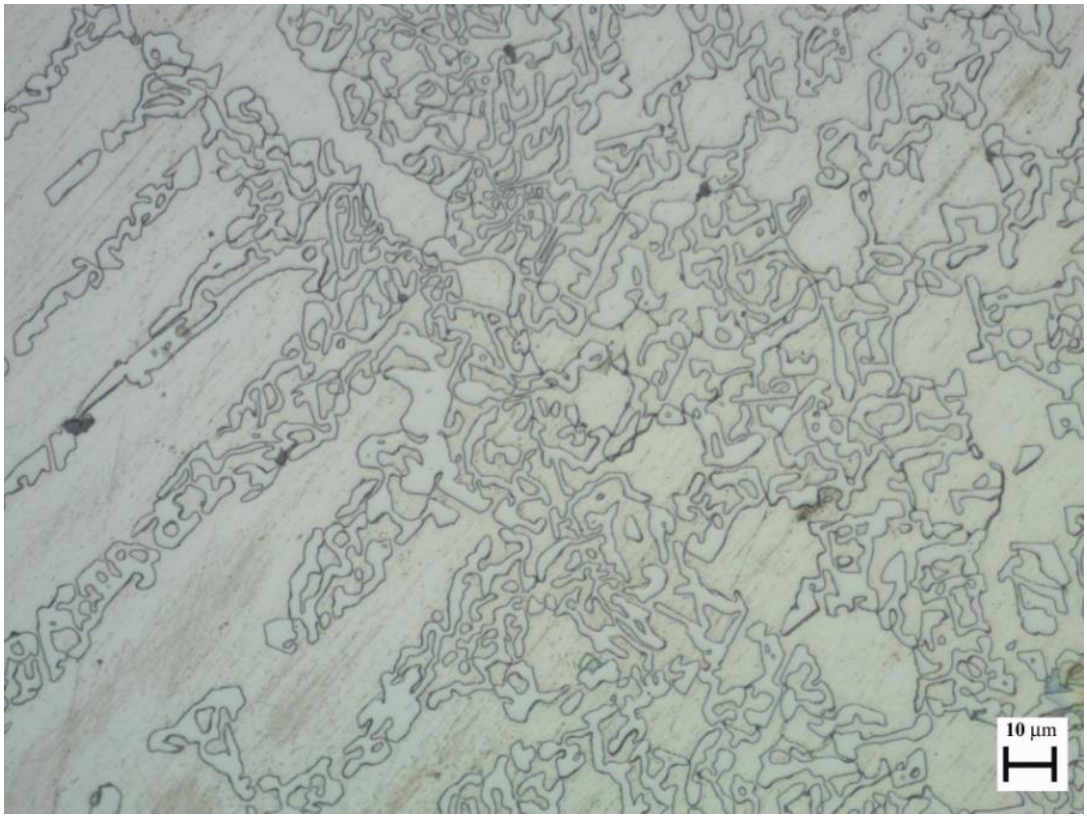

Figure 5.3 The microstructure of the 37%Cr cast iron with the eutectic structure and austenite dendrites.

The erosion-corrosion experiments were carried out using a submerged jet impingement rig described in Section 3.3.1. The testing duration was 2h. The nozzle diameter was 4 mm. The slurry contained aqueous solution with 3.5% NaCl and sand particles at 39±1^{o}C, impinged at 17 m/s velocity perpendicular to the specimen surface. The angular silica sand particles used in this study exhibits hardness of about 1160HV. The sand concentration was 200±20 mg/L. After the free erosion-corrosion experiments, the martensitic stainless steel (UNS S42000) and the 27%Cr cast iron were immersed briefly in an inhibited acid solution (Clark's solution) in order to remove the apparent corrosion products on their surface prior to weighing. On the other hand, the austenitic stainless steel and the 37%Cr cast iron exhibited negligible corrosion product on their post-test surface.

5.5 Results

5.5.1 Static corrosion experiments

Static corrosion experiments in a beaker of aqueous solution which contained 3.5% of NaCl were undertaken on a small selection of the cast irons. The aim of this typical corrosion test was to initially compare (prior to further testing) the relative corrosion resistance of the cast irons. For this reason, polished specimens of 27%Cr and 37%Cr cast irons were immersed in saline water. Figure 5.4, illustrates the two specimens after four weeks of immersion. It is clear that the 27%Cr cast iron specimen exhibits extensive general corrosion, while 37%Cr cast iron surface is passive.

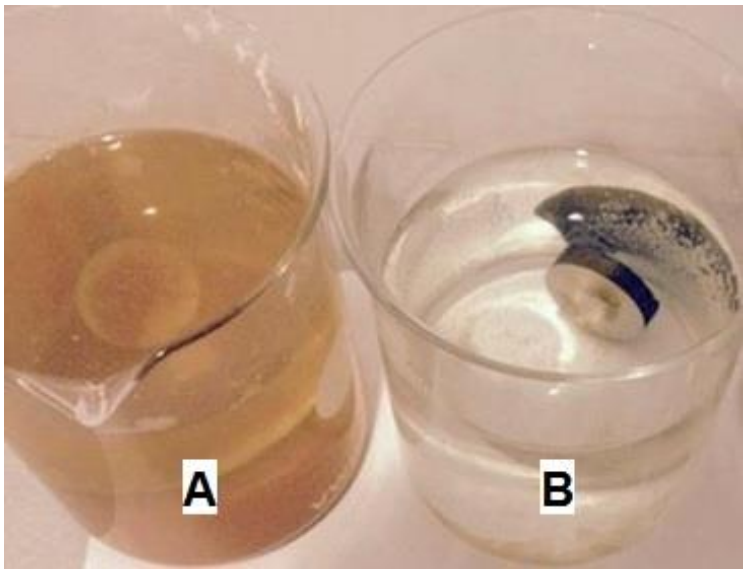

Figure 5.4 Surface condition and solution colour after four weeks submersion of the three polished specimens (A- 27%Cr cast iron and B- 37%Cr cast iron)

5.5.2 Wavelength dispersive spectroscopy (WDS)

Wavelength dispersive spectroscopy was utilised, as described in Section 3.2.4.1, to quantify the %Cr content in the matrix and the carbides of the two white irons. The 27%Cr cast iron consist of a mixture of martensitic matrix and M_7C_3 rod type carbides, and the 37% cast iron is comprised of austenitic matrix and $M_{23}C_6$ [5.9]. The average size of the chromium carbides in 27%Cr cast iron is bigger compared to the chromium carbides in 37%Cr cast iron, as a result of their different solidification paths.

Table 5.4 shows the average values of measured chromium contents of the metallic matrix and the chromium carbides out of three replicates and the ±1 represents their scatter.

The obtained chromium contents of the matrix distinguish clearly the martensitic structure of the 27%Cr cast iron and the austenitic structure of the 37% cast iron. The $Cr_{carbides}/Cr_{matrix}$ ratio has also been calculated as it determines the corrosion resistance of the white cast irons.

Table 5.4 Chemical point analysis of the two white cast irons

Alloy	Cr_{matrix}	$Cr_{carbides}$	$Cr_{carbides}$ / Cr_{matrix}
27%Cr cast iron	14.6 ± 1	52.1 ± 1	3.6
37%Cr cast iron	23.5 ± 1	60.7 ± 1	2.6

5.5.3 Volume fraction and micro-hardness measurements of the cast irons

Table 5.5 illustrates the volume fraction (VF) of the three different constituents of each cast iron, which were determined by Image J analysis of the materials' cross sections, as described in Section 3.2.6.

Table 5.5 Volume fraction of the different phases of the composite-like microstructure of cast irons.

27%Cr cast iron	Average VF (%)	37%Cr cast iron	Average VF (%)
Primary martensite	39	Austenite Dendrites	57
Eutectic Martensite	34	Eutectic austenite	27
Eutectic Carbides	27	Eutectic Carbides	16
Total	100	Total	100

The above volume fractions assist in verification of the acquired values of chromium content within the metallic phase of both white cast irons through the model of Lu et al [5.3]. Their model [5.3] suggests that the chromium concentration of the matrix can be calculated by the Equation 5.1 below, considering the carbide volume fraction and the overall chromium content of the white cast iron:

$$\%Cr_{matrix} = \frac{CVF}{\left(1 + 0.032 \times \%Cr_{cast\_iron}\right)} \qquad \textbf{Equation 5.1}$$

Taking into consideration the overall chromium content on Table 5.2 and the CVF values of Table 5.5, the measured $\%Cr_{matrix}$ (14.5 and 24.5for the 27%Cr cast iron and 37%Cr cast iron respectively) agree with the WDS measured values shown in Table 5.4.

The micro-hardness test technique also enhances the understanding of the erosion mechanisms that take place on each cast iron, as it is well known that the carbides are wear resistant in comparison with the metallic matrix which is likely to erode preferentially under slurry. Hence, an average of ten micro-hardness measurements, which followed the micro-hardness testing procedure described in Section 3.2.5, were conducted on the primary solidification phase, eutectic structure, and the 27%Cr cast iron chromium carbides (example given in Figure 5.5) and they are illustrated in Table 5.6.

Table 5.6 Measured micro-hardness values of the different phases of the composite-like microstructure of the 27%Cr and 37% cast irons.

Material	Primary solidification phase (50gf)	Eutectic Structure (200gf)	Eutectic Carbides (50gf)
27%Cr cast iron	640 HV	733 HV	1114 HV
37%Cr cast iron	251 HV	459 HV	

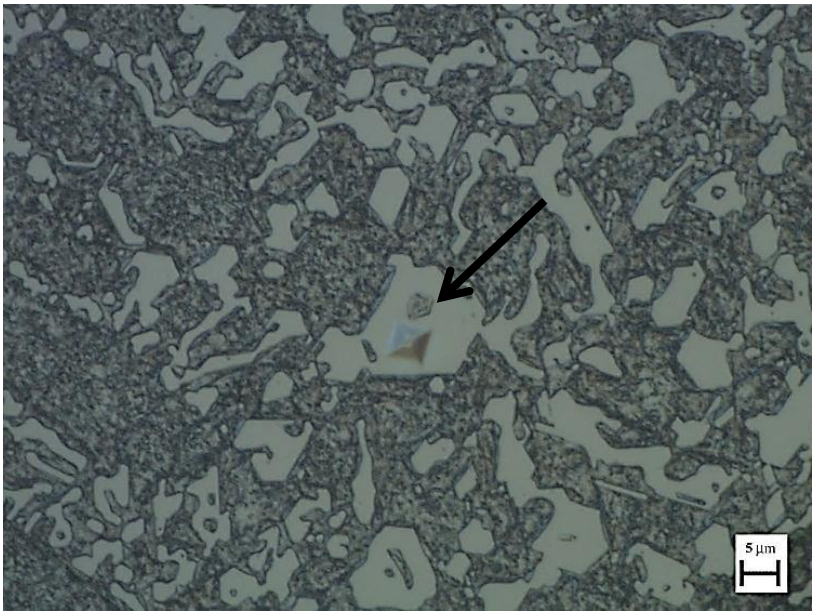

Figure 5.5 Hardness indentation on the M_7C_3-type eutectic carbide of the 27%Cr cast iron.

It is clear that the 37%Cr cast iron's austenitic dendrites possess half the hardness of the martensitic matrix of 27%Cr cast iron which will inevitably make the former cast iron more susceptible to erosion than the latter cast iron. The 37%Cr cast iron eutectic structure exhibited lower hardness than the 27%Cr cast iron as a result of its austenitic matrix and the lower hardness carbides. Due to the small size of the eutectic carbides of the 37%Cr cast iron, their micro-hardness could not be measured directly. Taking into consideration the rule of mixtures [5.37] though, which suggests that the overall hardness of a multi-phase material is determined by the sum of the volume average of the material's phases' hardness, the hardness values of Cr_7C_3 (present in 27%Cr cast iron) and $Cr_{23}C_6$ (present in 37%Cr cast iron) can be determined using the Equation 5.2 below.

$$H_{Total} = \left(H_{Metallic\_matrix} \times VF_{Metallic\_matrix}\right) + \left(H_{Carbides} \times VF_{Carbides}\right) \Rightarrow \quad \textbf{Equation 5.2}$$

$$H_{Carbides} = \frac{H_{Total} - \left(H_{Metallic\_matrix} \times VF_{Metallic\_matrix}\right)}{\left(VF_{Carbides}\right)}$$

For 27%Cr cast iron,

$$H_{Cr_7C_3} = \frac{767 - \left(640 \times 0.73\right)}{\left(0.27\right)} = 1111HV$$

For 37%Cr cast iron,

$$H_{Cr_{23}C_6} = \frac{365 - \left(251 \times 0.84\right)}{\left(0.16\right)} = 968HV$$

The above calculated hardness values of the chromium carbides are in agreement with the literature, where the H_{Cr7C3} is approximately 1200HV [5.6] and the H_{Cr23C6} is about 976HV [5.38].

5.5.4 Volume loss measurements

The measured mass losses of individual specimens illustrated in Table 5.7, were converted to volume losses by using the nominal density of the alloys (Table 5.3) to facilitate a more accurate comparison between the white cast irons and the stainless steels. Figure 5.6 illustrate the average volume losses of the comparative materials with error bars representing the scatter band from three replicates under free erosion-corrosion (FEC) and

also with the application of cathodic protection (CP). It is evident that the performance of all materials under free erosion corrosion conditions was similar. According to the cathodic protection results, the 27%Cr cast iron exhibits superior erosion performance compared to the other comparative materials. The martensitic stainless steel follows the 27%Cr cast iron erosion behaviour and the SS316 steel is comparable to the 37%Cr cast iron.

Table 5.7 Average mass loss of the stainless steels and cast irons in free erosion corrosion and with cathodic protection.

Material	Average Mass loss (mg)	
	Free erosion-corrosion	Cathodic protection
UNS S31600	9.7	9.2
UNS S42000	10.1	7.3
27%Cr cast iron	10.0	6.1
37%Cr cast iron	10.3	8.5

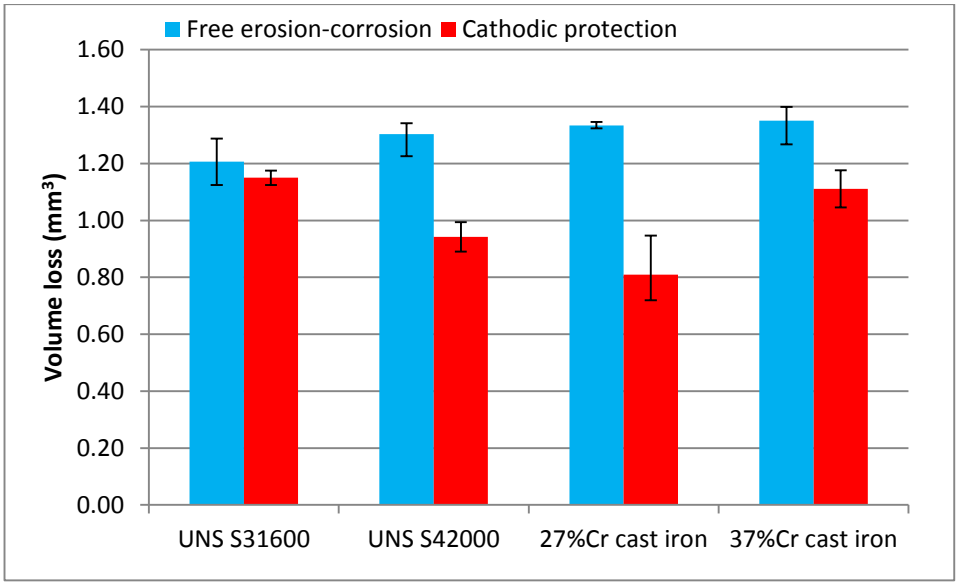

Figure 5.6 Volume losses of the stainless steels and cast irons in free erosion corrosion and with cathodic protection without the porous cast irons' results.

5.5.5 Electrochemical monitoring

5.5.5.1 Linear polarisation scans

Figures 5.7 – 5.10 show the linear polarisation scans, as described in Section 3.3.4, on the direct impinged zone (DIZ) of each segmented specimen, which are generated according to

Section 3.3.3. The high current fluctuations in the linear polarisation scans are associated with the high concentration of solids that caused extensive de-passivation of the Cr-rich film in the direct impinged zone of each material. The current fluctuations of the UNS S31600 and 37%Cr cast iron are narrower compared to that of UNS S42000 and 27%Cr cast iron due to their greater corrosion resistance and effectively greater re-passivation rates. The linear polarisation scans of each material within the different exposure times coincide, which indicates that the corrosion rates remain constant during the 2h impingement test.

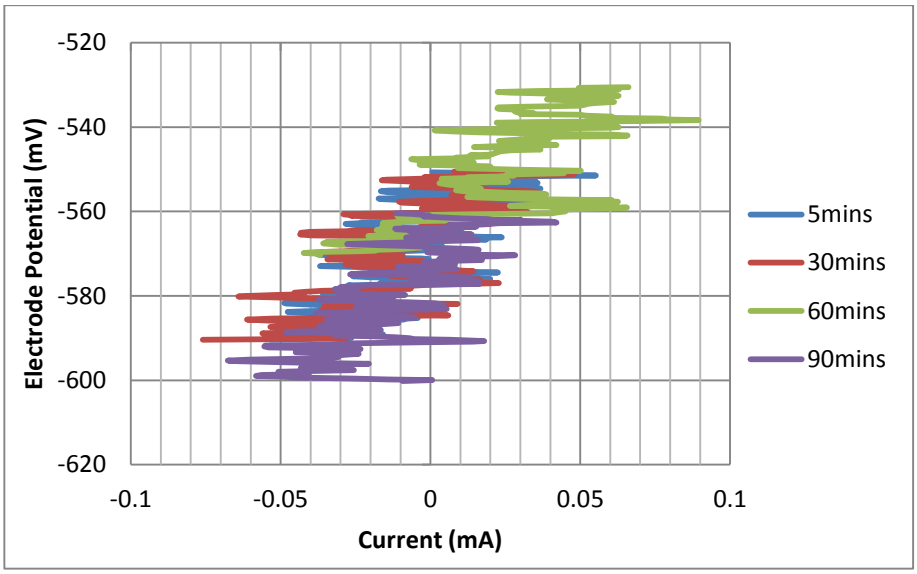

Figure 5.7 Linear polarisation scans on the direct impinged zone of the UNS S31600 in solid/liquid impingement.

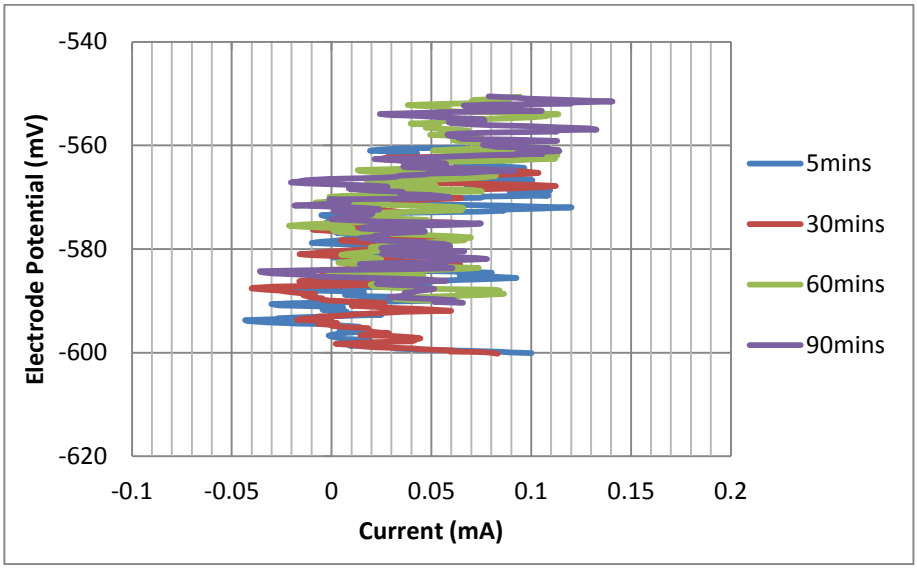

Figure 5.8 Linear polarisation scans on the direct impinged zone of the UNS S42000 in solid/liquid impingement.

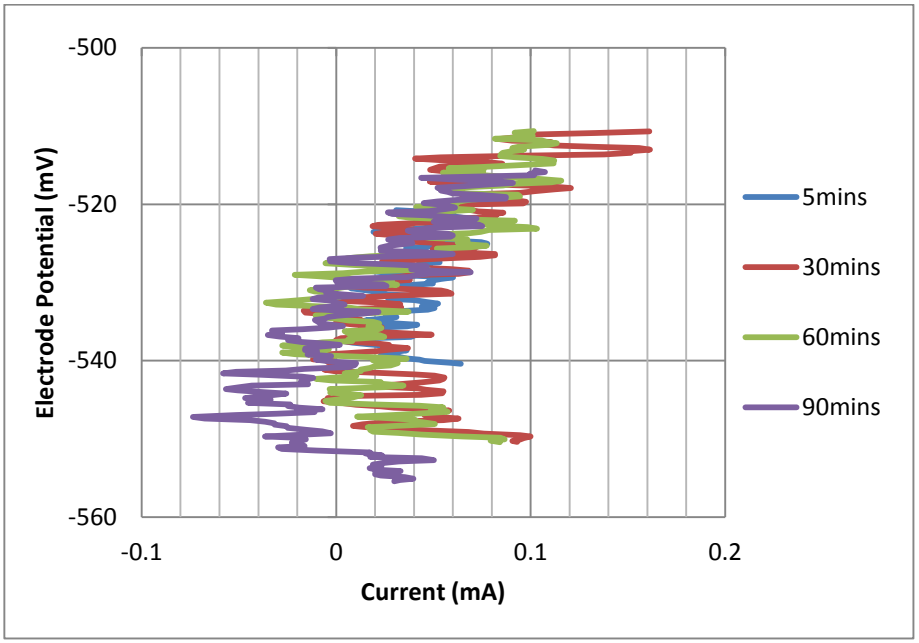

Figure 5.9 Linear polarisation scans on the direct impinged zone of the 27%Cr cast iron in solid/liquid impingement.

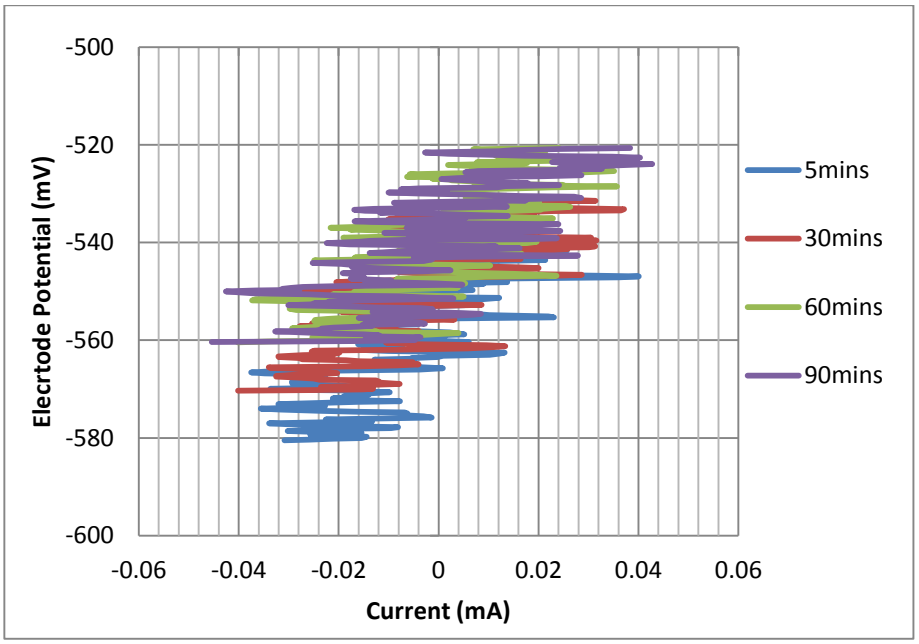

Figure 5.10 Linear polarisation scans on the direct impinged zone of the 37%Cr cast iron in solid/liquid impingement.

Figure 5.11 – 5.14 display the linear polarisation scans on the outer area (OA) of the specimen. Considering the polarisation resistance, the corrosion rate on the outer area is lower than on the direct impinged zone, as tabulated in Table 5.8. It is evident that the current fluctuations on the outer area are significantly smaller than on the direct impinged zone. This common feature emanates by the fact that in the outer area lower velocities and

oblique angles of impingement take place. This implies that the passive film is likely to be more stable. During the first 5 minutes of each linear polarisation, the gradient is slightly higher but the polarisation resistance stabilises at a certain value after the first 30 minutes.

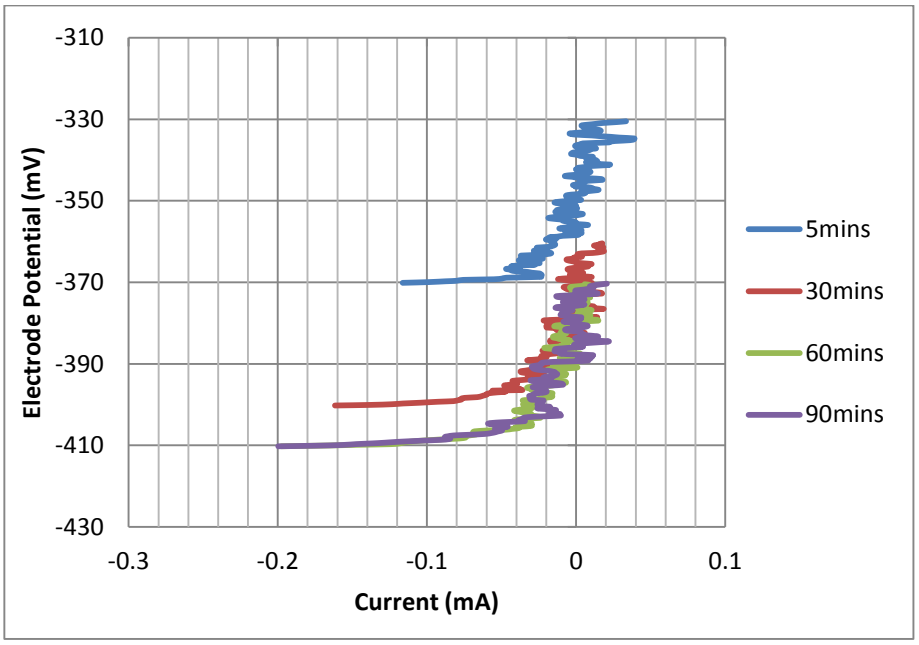

Figure 5.11 Linear polarisation scans on the outer area of the UNS S31600 in solid/liquid impingement.

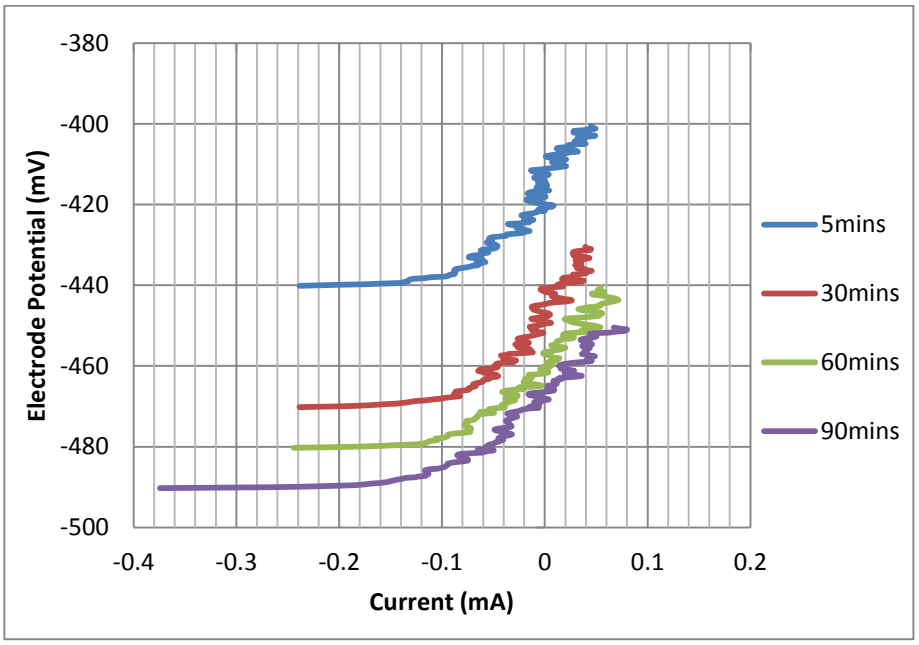

Figure 5.12 Linear polarisation scans on the outer area of the UNS S42000 in solid/liquid impingement.

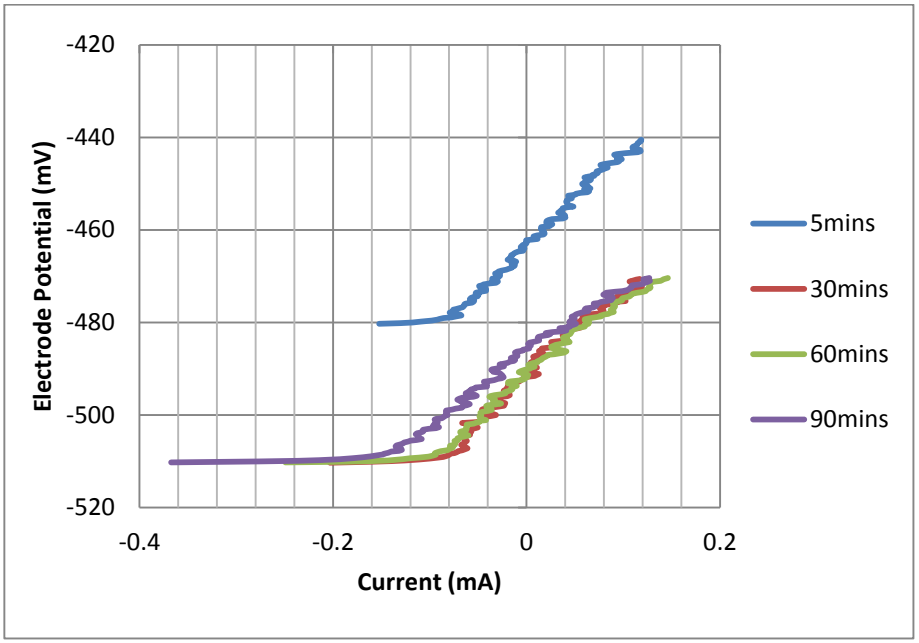

Figure 5.13 Linear polarisation scans on the outer area of the 27%Cr cast iron in solid/liquid impingement.

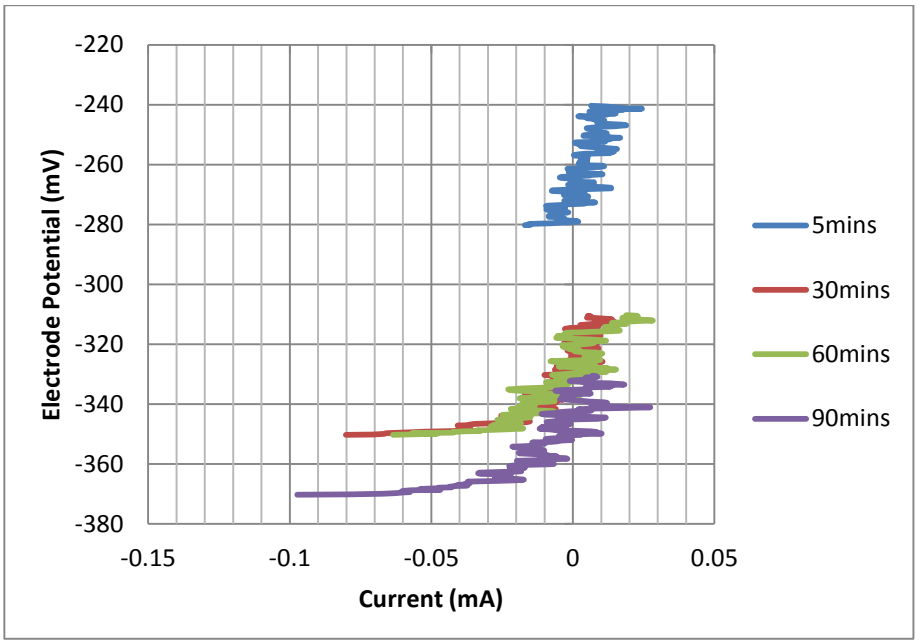

Figure 5.14 Linear polarisation scans on the outer area of the 37%Cr cast iron in solid/liquid impingement.

To compare the linear polarisation results for the two zones, their surface areas have to be taken into account. Table 5.8 shows the normalised polarisation resistances in terms of unit surface area, of both scanned regions of each segmented specimen. Since the polarisation resistance is inversely proportional to the corrosion current, it is evident that the

direct impinged zone is suffering from a high corrosion rate, whereas the outer area is subjected to much lower corrosion rates. The austenitic based materials (UNS S31600 and 37%Cr cast iron) show their superiority in both areas compared to martensitic based alloys (UNS S4200 and 27%Cr cast iron). This feature is associated with the formation of a passive film on the former group that even it is breaking down consistently in the direct impinged zone, their good corrosion resistance is maintained.

Table 5.8 Polarisation resistances by taking into account the surface areas of the segments of each comparative material.

Material	**Polarisation resistance R_p (Ω*cm^2)**	
	DIZ (Area = 0.2 cm^2)	**OA (A = 11.00 cm^2)**
UNS S31600	148	8800
UNS S42000	66	2926
27%Cr cast iron	44	1628
37%Cr cast iron	285	17600

5.5.5.2 Potentiodynamic scans

The anodic polarisation scans on the direct impinged zone (DIZ) and outer area (OA) of the segmented specimen were performed after the linear polarisation monitoring at 90mins. Figures 5.15 – 5.18 show the anodic polarisation of each comparative material on the direct impinged zone and on the outer area. The normalised potential represents the electrode potential of at least 25mV more negative to E_{corr} and it has been utilised for a more effective comparison, since the E_{corr} are different between the two specimen regions. The current fluctuations in UNS S31600 and 37%Cr cast iron scans are indicative of de-passivation/re-passivation of a passive film. These fluctuations are largely absent for the UNS S42000 and 27%Cr cast iron which, together with the exhibited high currents, implies the lack of a passive film.

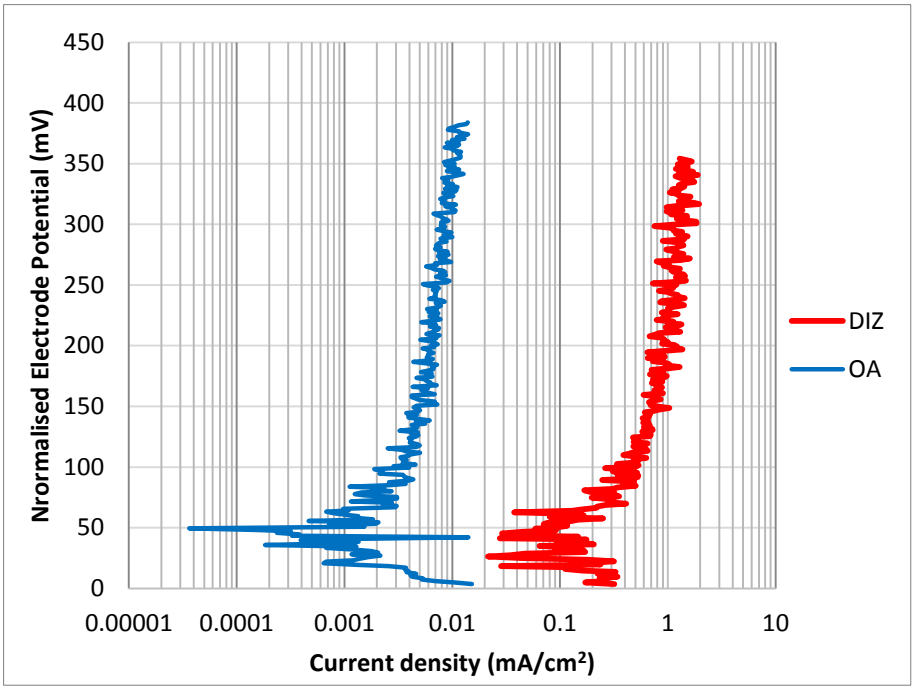

Figure 5.15 Anodic polarisation scans on both segments of UNS S31600 in solid/liquid impingement.

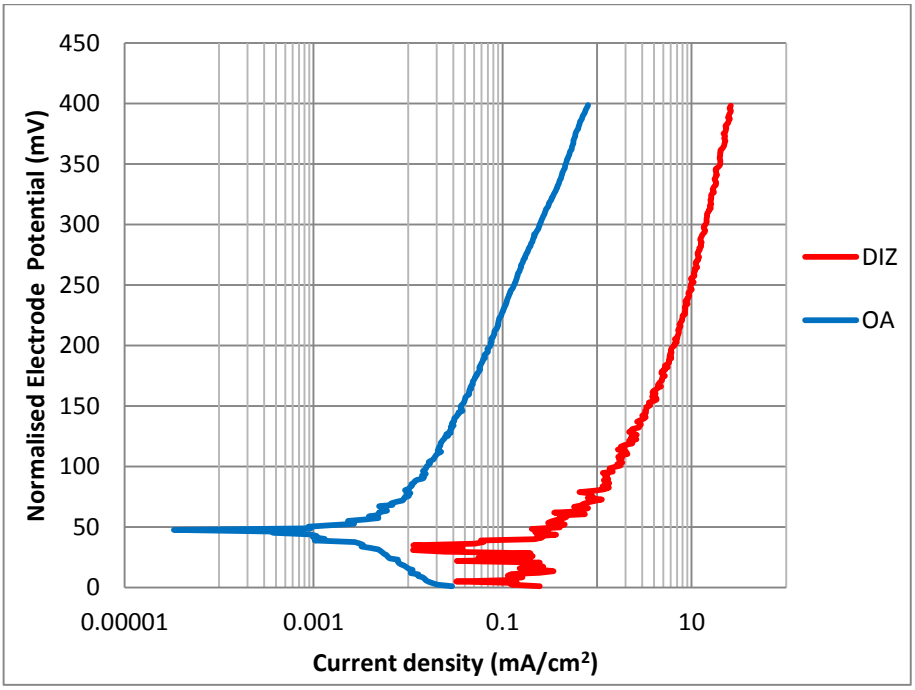

Figure 5.16 Anodic polarisation scans on both segments of UNS S42000 in solid/liquid impingement.

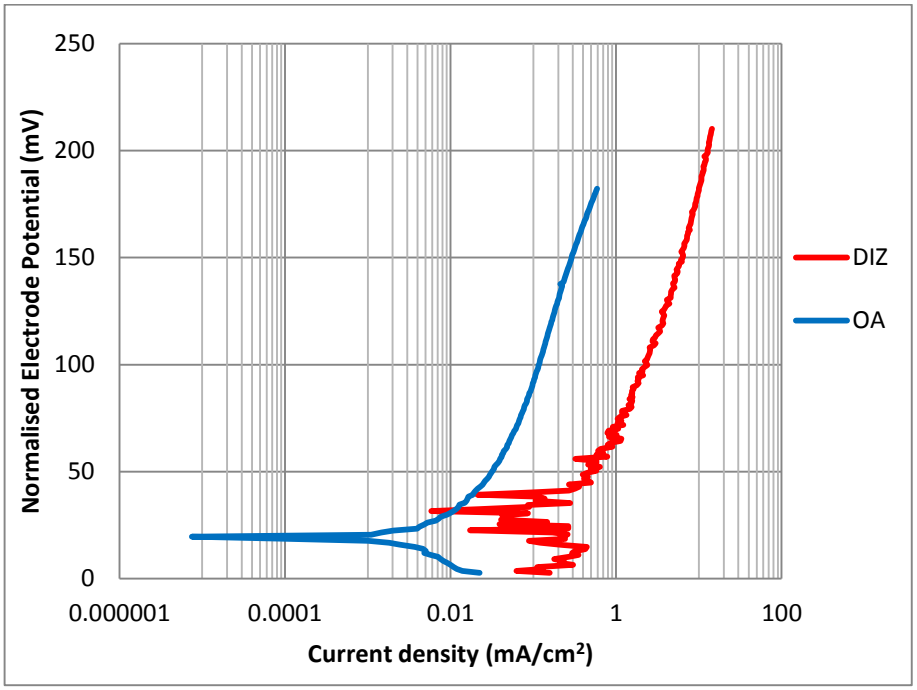

Figure 5.17 Anodic polarisation scans on both segments of 27%Cr cast iron in solid/liquid impingement.

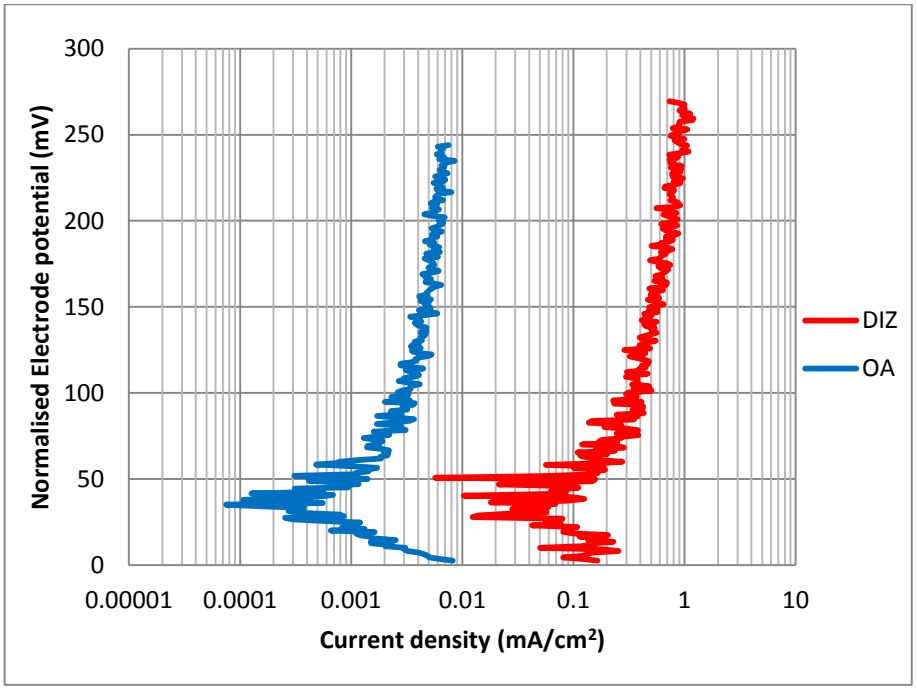

Figure 5.18 Anodic polarisation scans on both segments of 37%Cr cast iron in solid/liquid impingement.

Table 5.9 lists the corrosion current densities along with the E_{corr} of each region through Tafel extrapolation by plotting a straight line from the average of the oscillating currents. The mass losses were calculated by using the Faraday's law (see section 2.3.7.2). A common attribute of all tested materials was the corrosion current density on their direct impinged zone which was higher than that of their outer area.

Comparison of the tested materials shows that the 37%Cr cast iron exhibited the lowest corrosion rate in the direct impinged zone, with the UNS S31600 exhibiting slightly higher rate and the two martensitic alloys corroding at substantially higher rates. In the outer area, there was a distinct difference between the austenitic structured alloys (with corrosion rates at least five times lower) than the martensitic-base materials. The 27%Cr cast iron displayed by far the highest corrosion rate in the outer area.

Table 5.9 Free corrosion potentials (E_{corr}), corrosion rates and calculated mass losses due to corrosion on both areas of the segmented electrodes.

Material	DIZ (Area = 0.2 cm^2)			OA (A = 11.00 cm^2)		
	E_{corr} (mV)	Corrosion Current density (mA/cm^2)	Mass loss due to corrosion (mg)	E_{corr} (mV)	Corrosion Current density (mA/cm^2)	Mass loss due to corrosion (mg)
UNS S31600	-553	0.25	0.10	-369	0.002	0.04
UNS S42000	-563	0.50	0.20	-452	0.010	0.20
27%Cr cast iron	-529	0.50	0.20	-482	0.020	0.44
37%Cr cast iron	-531	0.20	0.06	-343	0.001	0.02

Figure 5.19 shows the anodic polarisation scans on the full specimen (38mm diameter) after 30 minutes of impingement, as the corrosion rates were steady after this period. The normalised potential represents the electrode potential of at least 25mV more negative to E_{corr} and it has been employed for better comparison, since the E_{corr} are different between the materials. It is apparent that there are two groups of materials; the low

corrosion resistant materials (27%Cr cast iron and UNS S42000) and more corrosion resistant materials (UNS S31600 and 37%Cr cast iron).

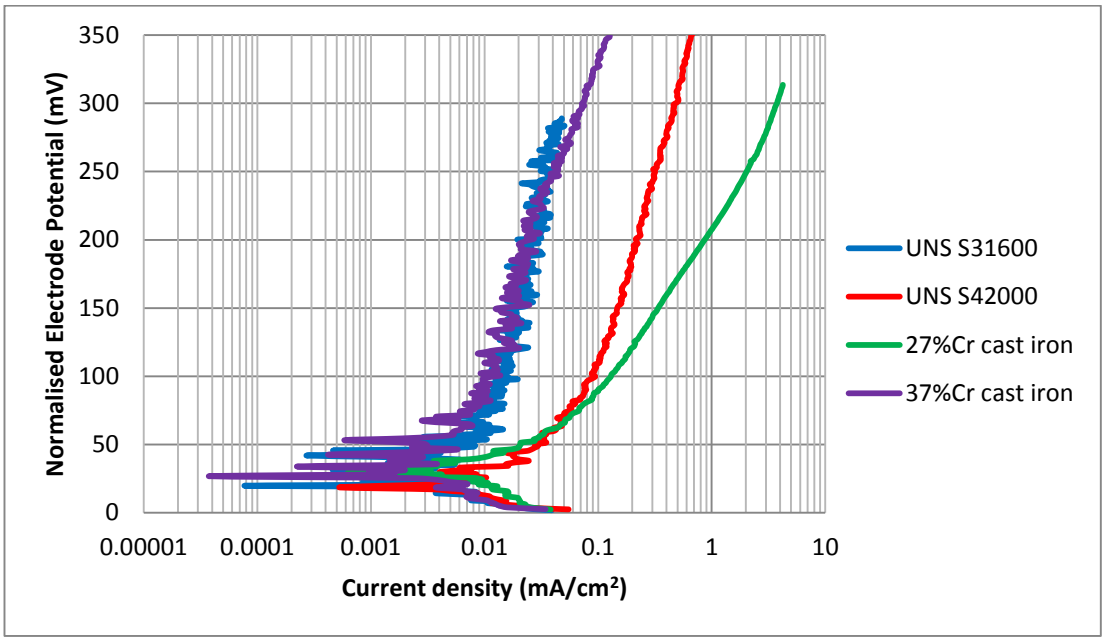

Figure 5.19 Anodic polarisation scans on the full specimen of each comparator material in solid/liquid impingement.

Table 5.10 shows the generated current densities from the Tafel extrapolations for the full specimen of each comparative material along with their E_{corr} and the calculated mass losses via Faraday's law. The ranking of the corrosion rates of the full specimen of the materials is in agreement with that of the segmented specimens as the austenitic based alloys are exhibiting better corrosion resistance than the martensitic based alloys.

Table 5.10 Free corrosion potentials (E_{corr}), corrosion rates and calculated mass losses due to corrosion of the full specimen of each material.

Material	E_{corr} (mV)	Corrosion current density (mA)	Mass loss due to corrosion (mg)
UNS S31600	-440	0.008	0.17
UNS S42000	-491	0.026	0.62
27%Cr cast iron	-471	0.035	0.80
37%Cr cast iron	-381	0.004	0.08

5.5.6 Surface topography

5.5.6.1 Macro-views observations

Figure 5.20 shows the post-test surface directly after the two hours free erosion-corrosion. It is apparent that the UNS S31600 and 37%Cr cast iron surfaces do not exhibit any corrosion products, which reveals their superior corrosion resistance. However, UNS S42000 and 27%Cr cast iron are experiencing high corrosion rate by developing a ring shaped corrosion products adjacent to the wear scar.

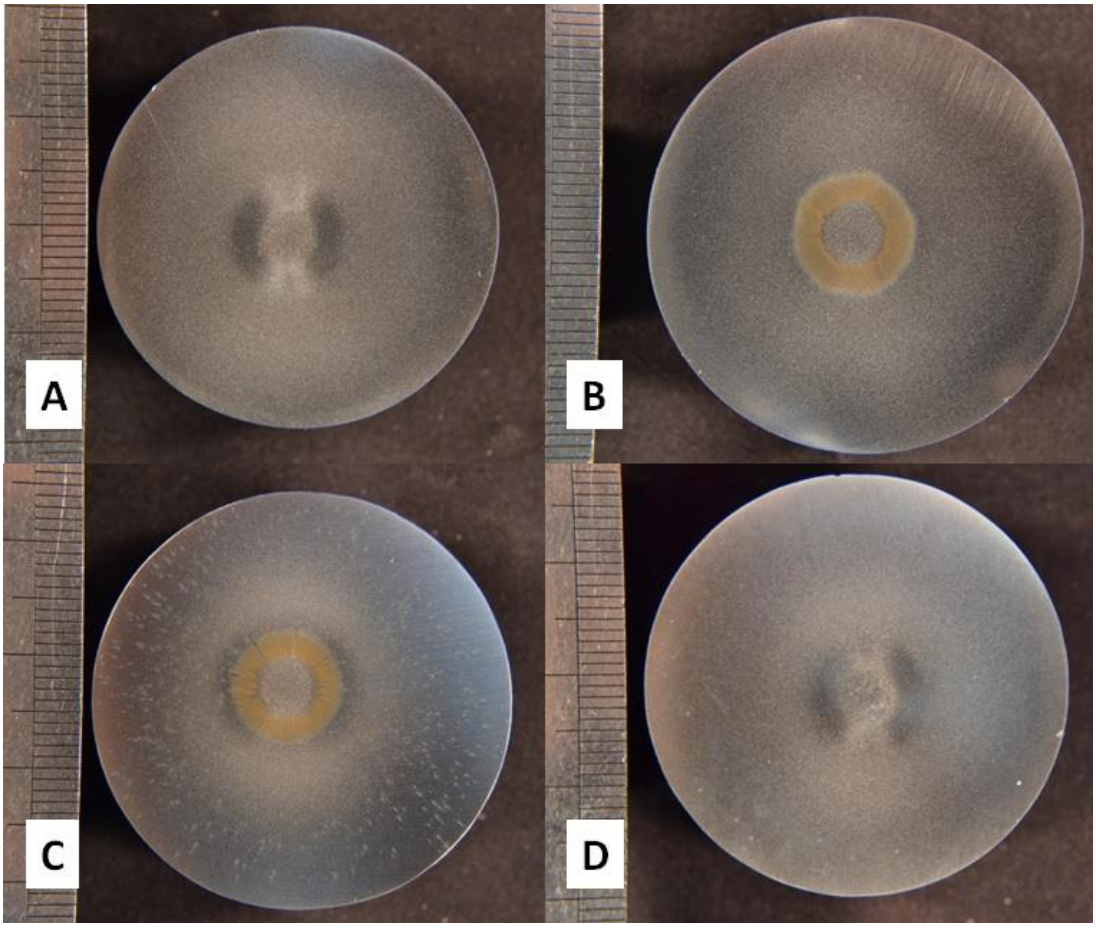

Figure 5.20 Post-test surface of the materials after 2h solid/liquid impingement: UNS S31600 (A); UNS S42000 (B); 27%Cr cast iron (C) and 37%Cr cast iron (D).

5.5.6.2 Wear mechanisms under the jet

The deterioration mechanisms occurring inside the wear scars were determined via cross sections of the post-tested stainless steel specimens and as post-tested SEM views of the cast irons. The UNS S31600 stainless steel exhibited different wear mechanisms than the high chromium cast irons, as the former shows work hardening effects by the constant impact of

the solid particles and the latter demonstrate micro-cracking on their chromium carbides. The UNS S42000 did not exhibit any visible surface hardening within its wear scar and for this reason was excluded from this assessment. The surface hardening and the carbide micro-cracking are discussed in the sections below:

UNS S31600

Figure 5.21 shows the cross section of the UNS S31600 stainless steel wear scar. It is evident that erosion-related deformation has taken place within the subsurface regions. The thickness of the UNS S31600 hardened layer is about 30μm. This conforms to the typical stress and strain curve of a ductile material, where it has a broader plastic deformation region than a less ductile material for a certain stress. Such distorted surface structure was not evident in the region outside the wear scar of the austenitic stainless steel.

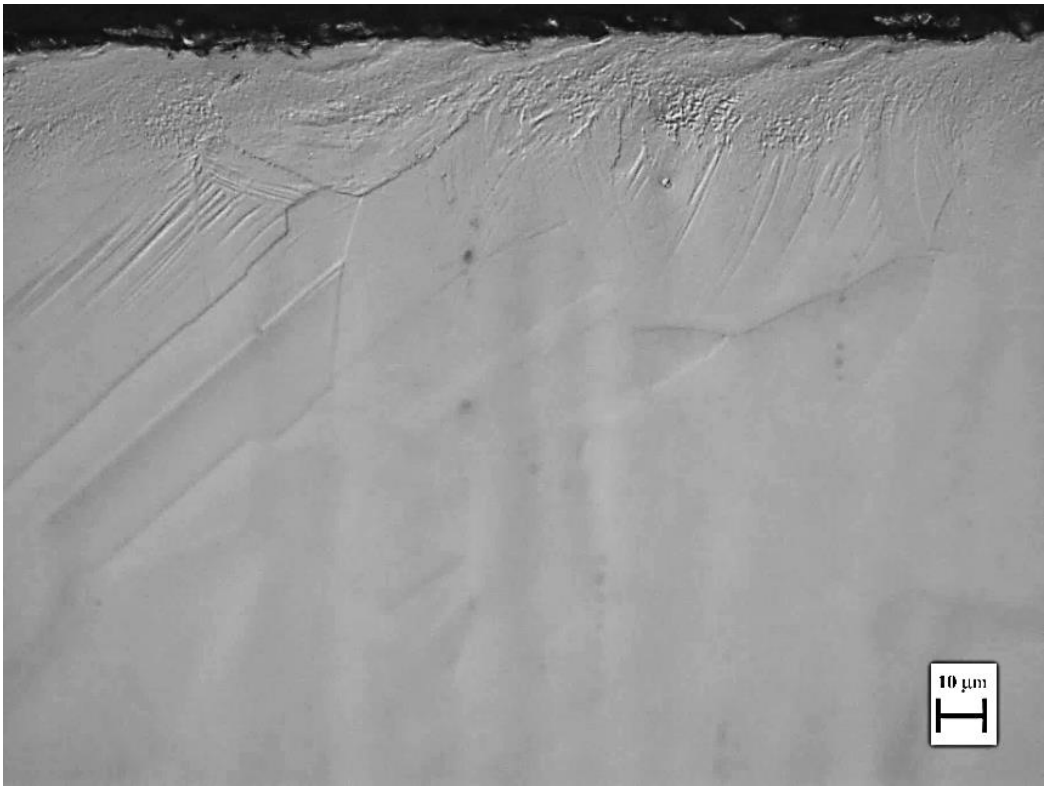

Figure 5.21 Hardened layer on the UNS S31600 wear scar.

Many researchers [5.39–5.41] in the past have seen the strain hardening effect, but they had not attempted to measure the hardness of the surface hardening layer. Singh et al [5.42], found in fact that the surface hardening of the UNS S316000 was substantial, as the hardness was increased from $160HV_{50}$ to $430HV_{50}$ during air blast erosion at normal incidence. In this study therefore, Knoop hardness testing (see Section 3.4.3) was employed

to assess the intensity of hardness near the surface due to the impact stresses of the sand particles. This assessment focused on the austenitic stainless steel, as the hardened layer on the martensitic wear scar was too thin to be indented. Table 5.11 illustrates ten indentations beneath the wear scar and 10 indentations at the core of the stainless steel. It is evident that the surface hardness has been increased by almost 100HK by the impact effect of the particles.

Table 5.11 Hardness measurements on the hardened layer and the core material of the UNS S31600.

Indentation No.	Hardened layer (HK)	Core material (HK)
1	244	156
2	243	143
3	256	134
4	264	144
5	248	144
6	253	143
7	251	147
8	235	149
9	230	157
10	251	149
Average	*248±10*	*147±7*

High chromium cast irons

Figure 5.22 shows the heavily degraded microstructure of the 27%Cr cast iron inside its wear scar after solid/liquid impingement. Extensive micro-cracking of the chromium carbides with some spalling events, are apparent in the wear scar, as a result of the impact stresses of the striking erodent that cause fracture of the Cr_7C_3 rod like carbides. On the other hand, the martensite, which surrounds the carbides, has been widely deformed.

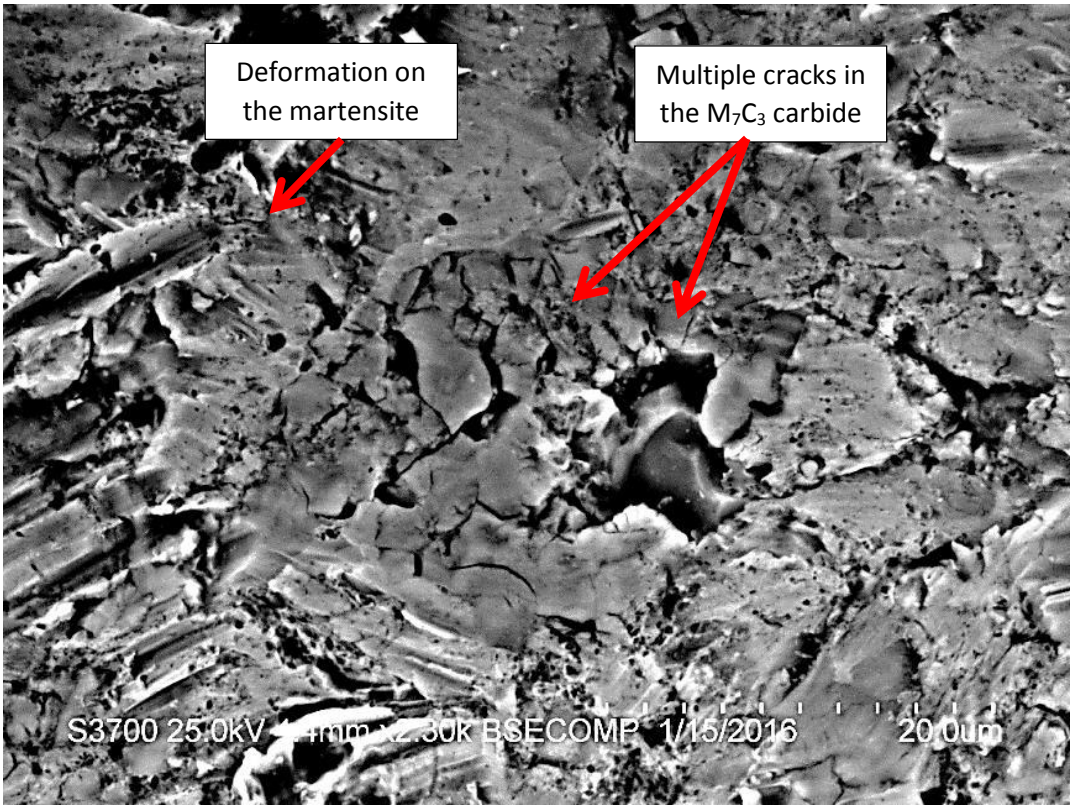

Figure 5.22 Carbide cracking and spalling sites inside the wear scar of the 27%Cr cast iron.

Figure 5.23 and 5.24 illustrates the cross section of the 27%Cr wear scar, where subsurface cracking is evident for at least 20µm below the surface. This feature demonstrates that the impact stresses of the abrasives have also been transmitted to the carbides and martensite, causing multiple cracks on the former while the latter deforms. The fracture of the carbides below the surface would lead to easier spalling on the next erodent impact.

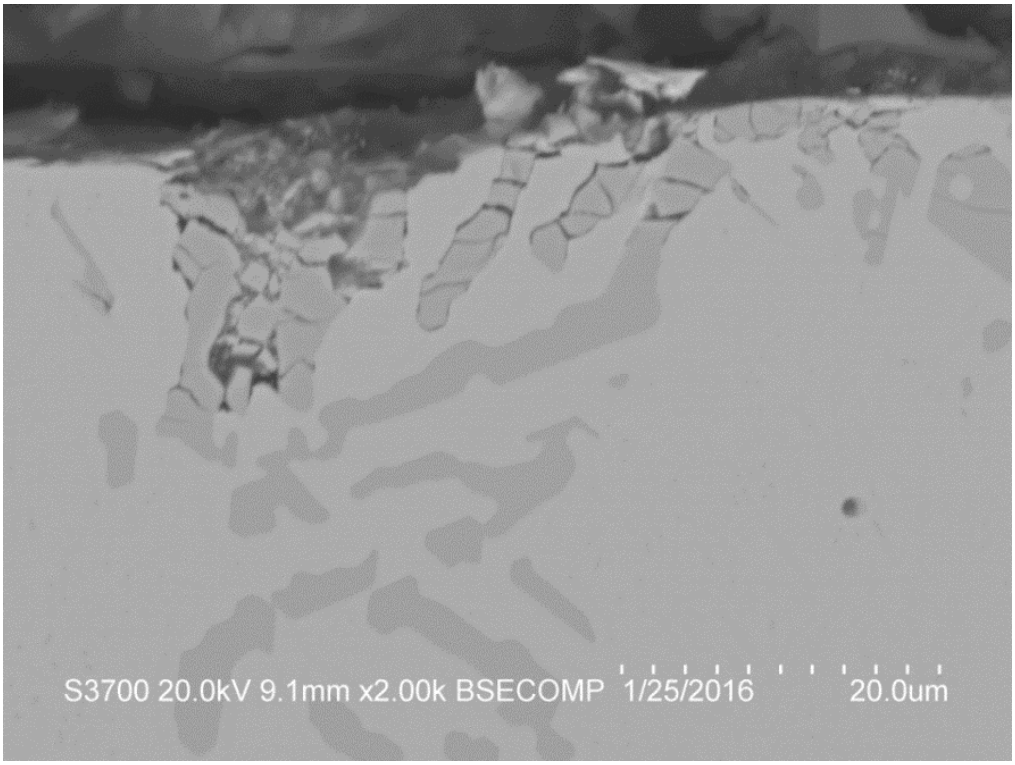

Figure 5.23 Cross section of the 27%Cr wear scar with heavily cracked chromium carbides and carbide removal.

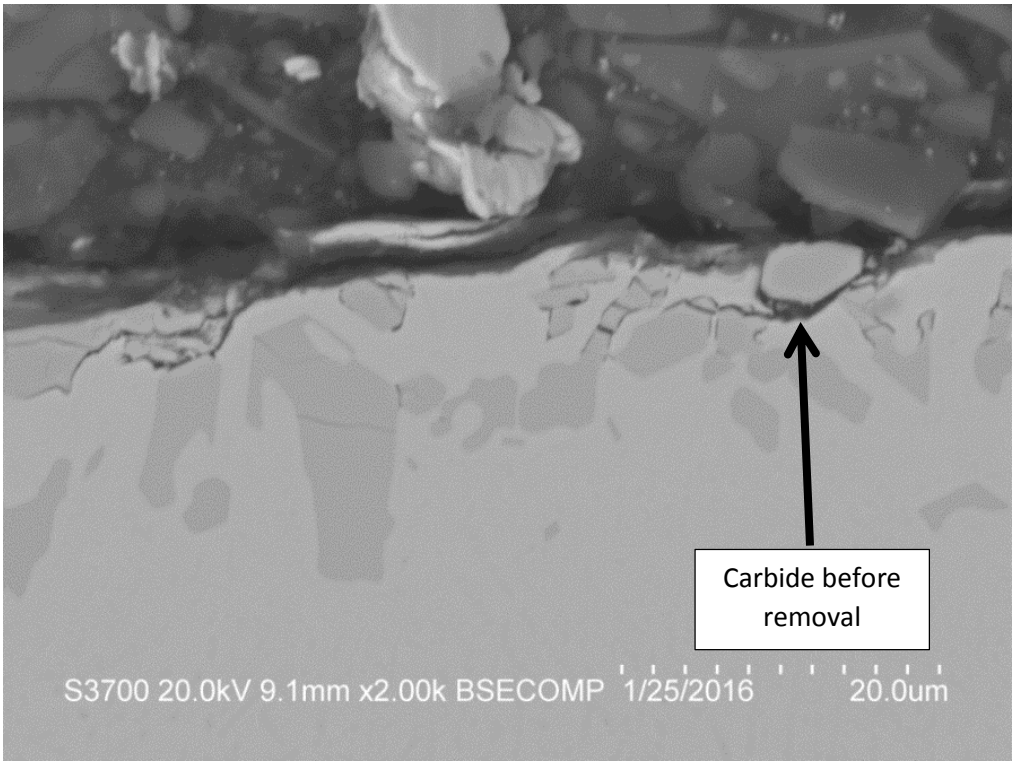

Figure 5.24 Cross section of the 27%Cr wear scar with apparent cracks well below the top surface and carbide-ready to be removed.

Figure 5.25 illustrates the cracked eutectic carbides in the wear scar of the 37%Cr cast iron after solid/liquid impingement. Figures 5.26 and 5.27 show the cross section of 37%Cr cast iron's wear scar, where also extensive subsurface cracking had taken place for at least 30µm below the top surface. This trait triggers the detachment of lumps of the cast irons which would include both austenite and eutectic carbides. It should be noted that the sub-surface cracking was not observed in regions of the cross sections outside the wear scar of both cast irons.

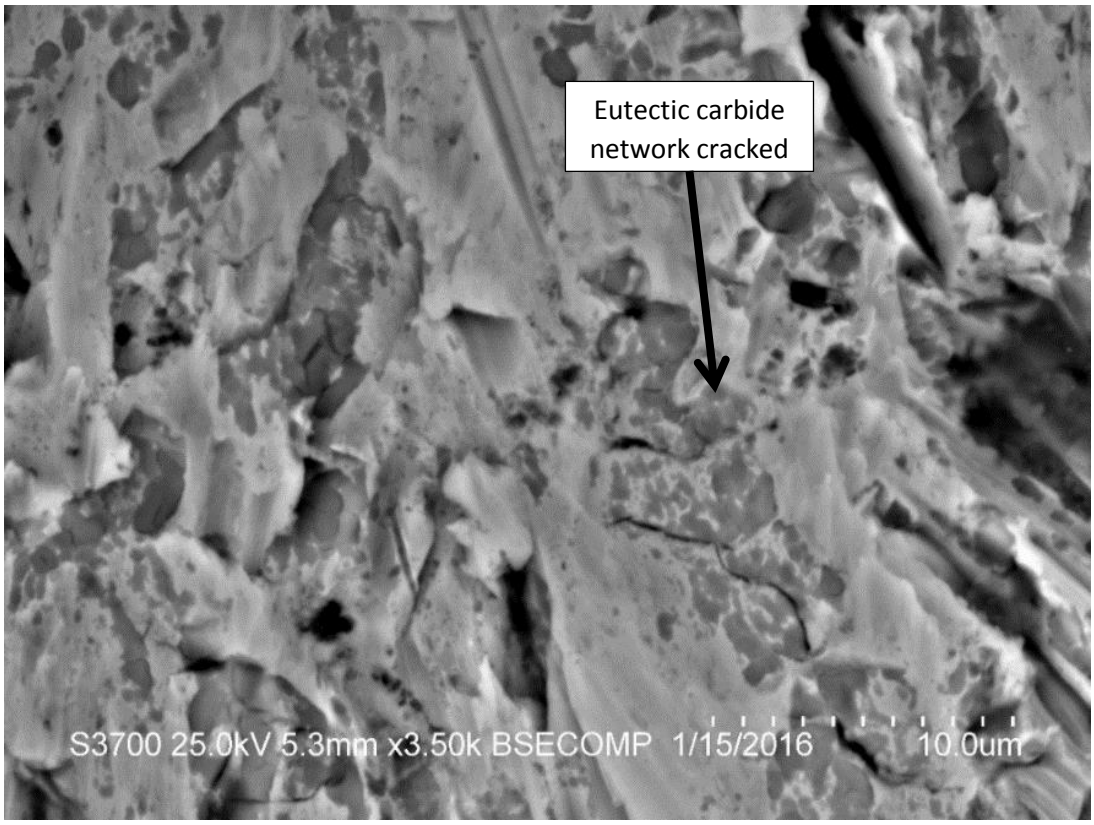

Figure 5.25 Extensive cracking on the eutectic carbide network inside the wear scar of the 37%Cr cast iron.

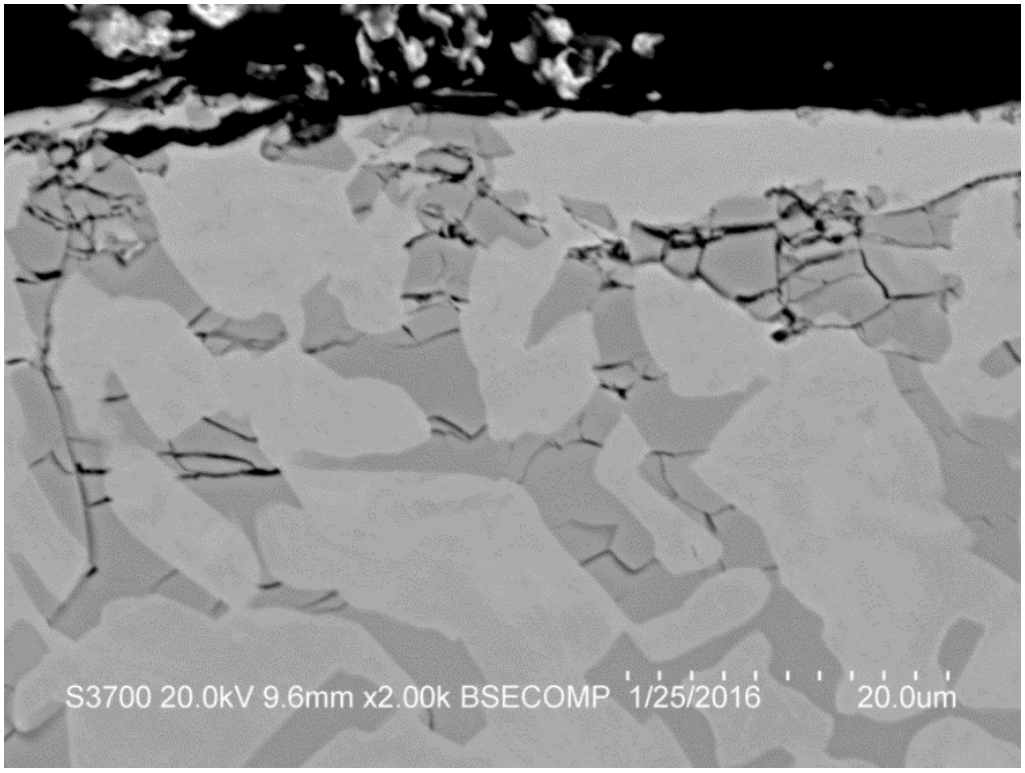

Figure 5.26 Vertical and perpendicular cracking on the eutectic carbides.

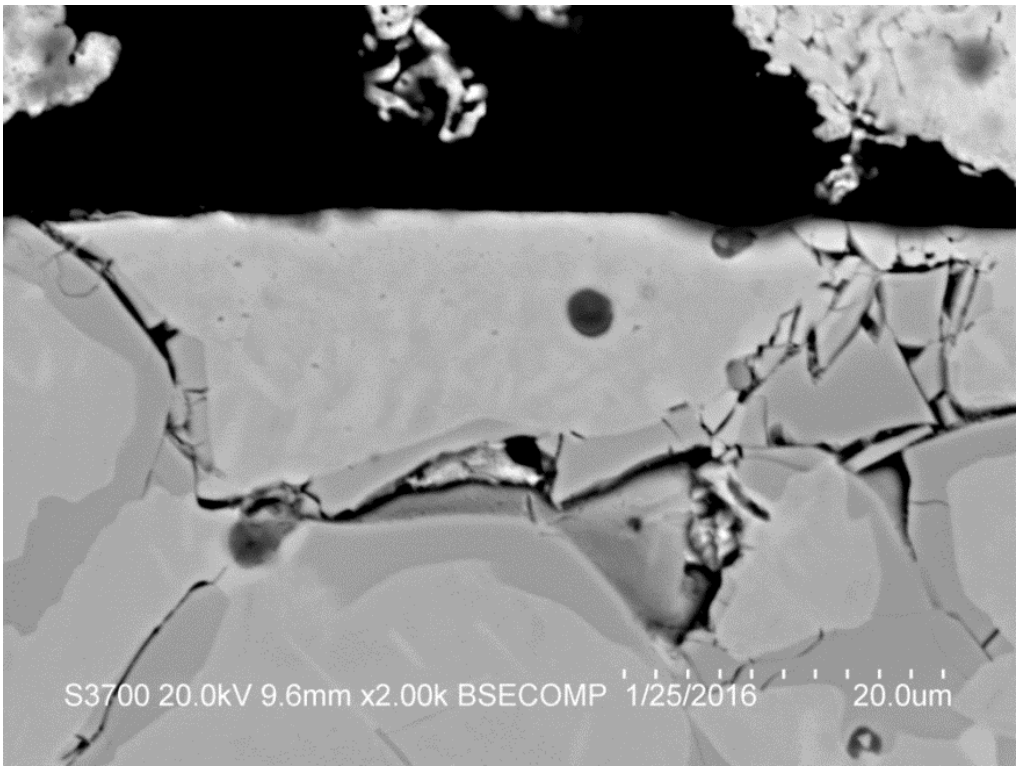

Figure 5.27 Continuous cracking on chromium carbides below a segment of austenite.

5.5.6.3 Wear scar depths

Surface profile scans were performed, via surface topography (see Section 3.4.2), on the wear scar of each specimen to broaden the evaluation of the deterioration mechanisms occurring in the zone directly under the impinging jet. Figure 5.28 shows an example of the wear scar profile scans of the UNS S31600 under free erosion-corrosion conditions and cathodic protection conditions, respectively. It is clear that there is no significant difference in the two depths, which indicates that the dominant degradation mechanism occurring in the UNS S31600 wear scar is erosion.

Figure 5.29 and 5.30 illustrate examples of the wear of the martensitic stainless steel (UNS S42000) and 27%Cr cast iron under free erosion-corrosion conditions and cathodic protection. The effect of corrosion related damage is apparent on the wear scar profile scans on both martensitic-structured materials.

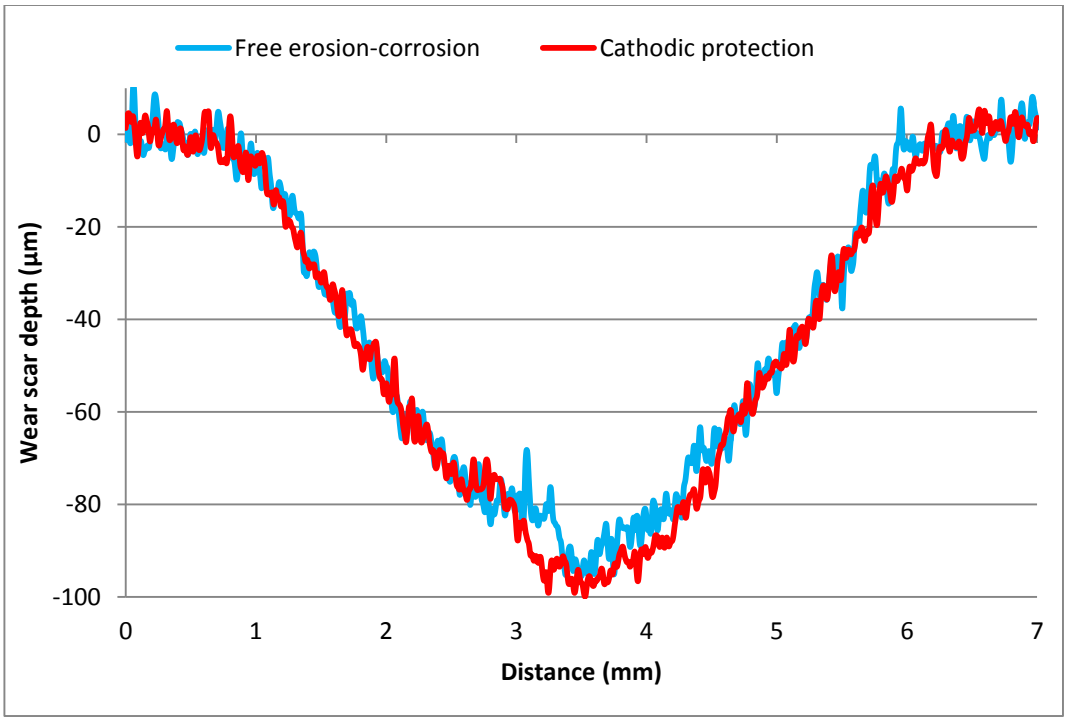

Figure 5.28 Surface profile scan of the wear scar of the stainless steel UNS S31600 under solid/liquid impingement in free erosion-corrosion and cathodic protection.

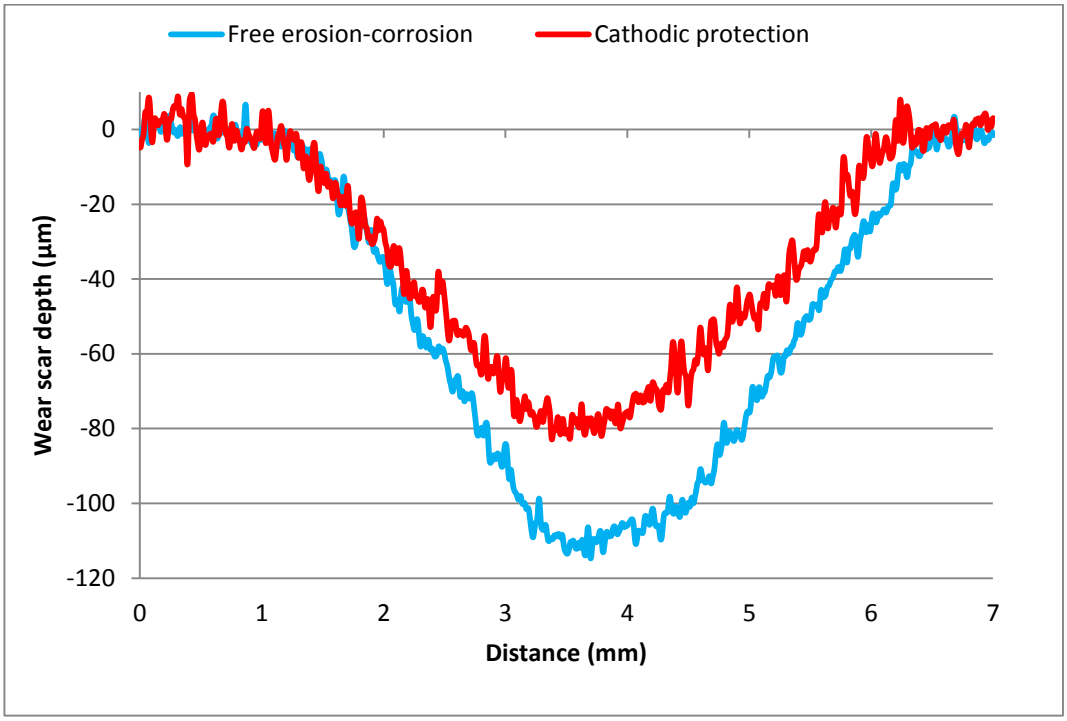

Figure 5.29 Surface profile scan of the wear scar of the stainless steel UNS S42000 under solid/liquid impingement in free erosion-corrosion and cathodic protection.

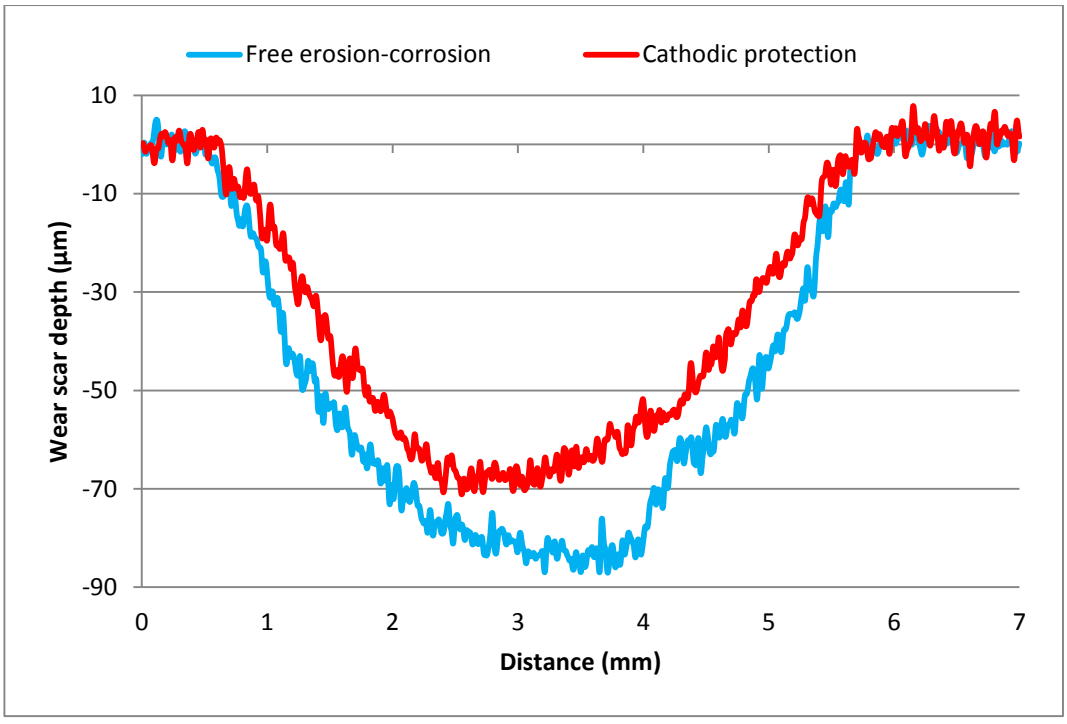

Figure 5.30 Surface profile scan of the wear scar of the 27%Cr cast iron under solid/liquid impingement in free erosion-corrosion and cathodic protection.

Figure 5.31 shows the wear scar profile scans of the 37%Cr cast iron under free erosion-corrosion conditions and cathodic protection. There is a clear difference in the wear scar depths under free erosion-corrosion conditions compared to the pure erosion conditions as observed on the martensitic-based alloys above, but the most interesting feature out of the profile scan examination is the uneven shape of the wear scar in both conditions which indicates that the mechanical effect of sand particles have impacted differently the microstructure of the 37%Cr cast iron.

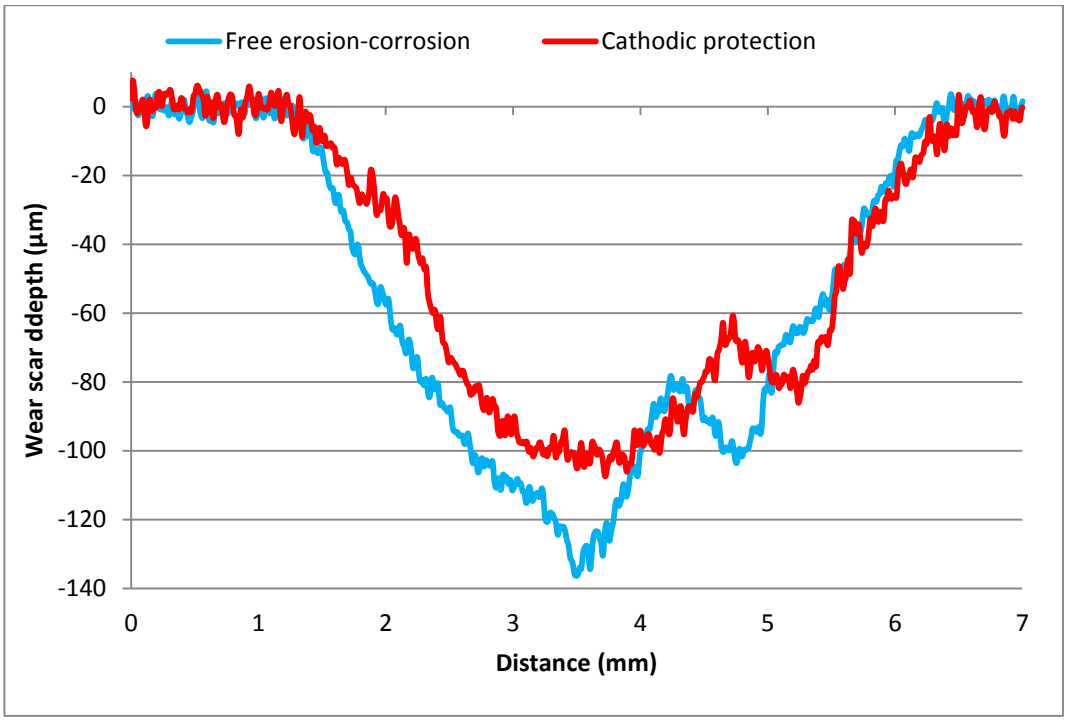

Figure 5.31 Surface profile scan of the wear scar of the 37%Cr cast iron under solid/liquid impingement in free erosion-corrosion and cathodic protection.

Figure 5.32 illustrates the wear scar depths of all comparative materials with and without cathodic protection for at least two replicate experiments. The wear scar depths agree with the total volume losses in Figure 5.6, as the application of cathodic protection resulted in a significant reduction of the total volume loss of the two cast irons and UNS S42000 and less effective on UNS S31600.

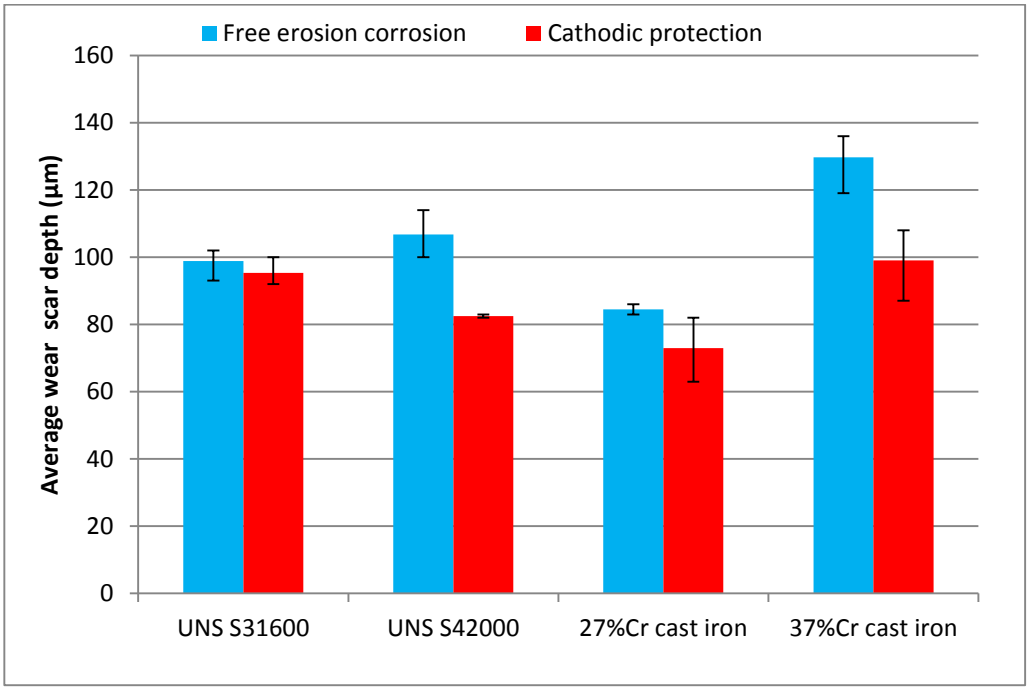

Figure 5.32 Average wear scar depths of the studied materials under solid/liquid impingement in free erosion-corrosion and cathodic protection.

5.5.6.4 Volumetric analysis of the wear scars

Figure 5.33 shows a 3D profile of the 27%Cr cast iron wear scar, which is typical of the stainless steels as well.

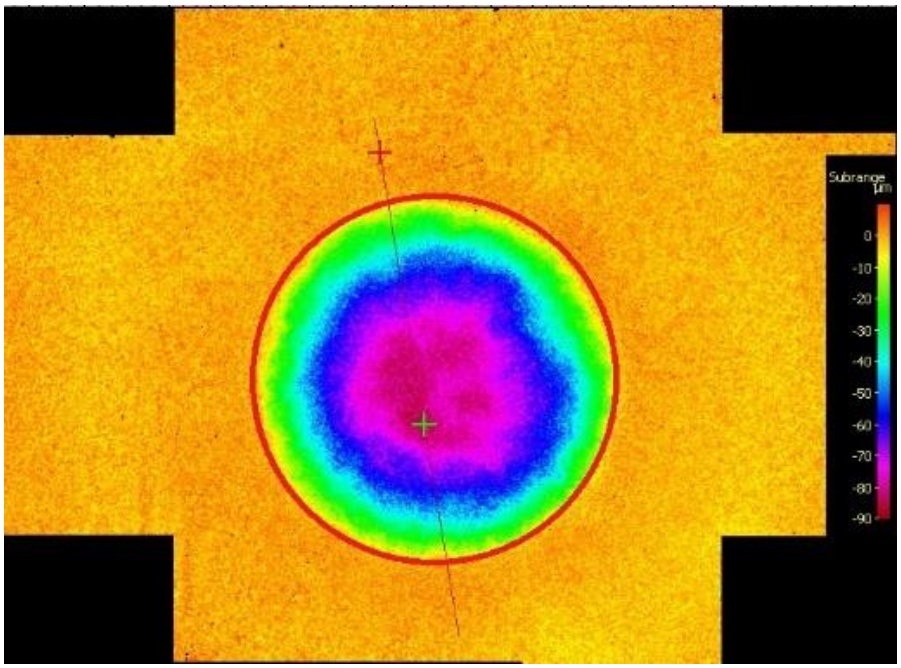

Figure 5.33 Volumetric analysis on the direct impinged zone of the 27%Cr cast iron surface after solid/liquid impingement.

An exception was observed at the 37%Cr cast iron wear scar morphology, as illustrated in Figure 5.34, as it exhibits an irregular shape with peaks and valleys in all impingement conditions (i.e. free erosion-corrosion and cathodic protection). This feature is a result of the distinct hardness difference between the matrix (251HV) and the eutectic structure (457HV) and the extensive cracking of the eutectic carbides shown in Figures 5.26 & 5.27.

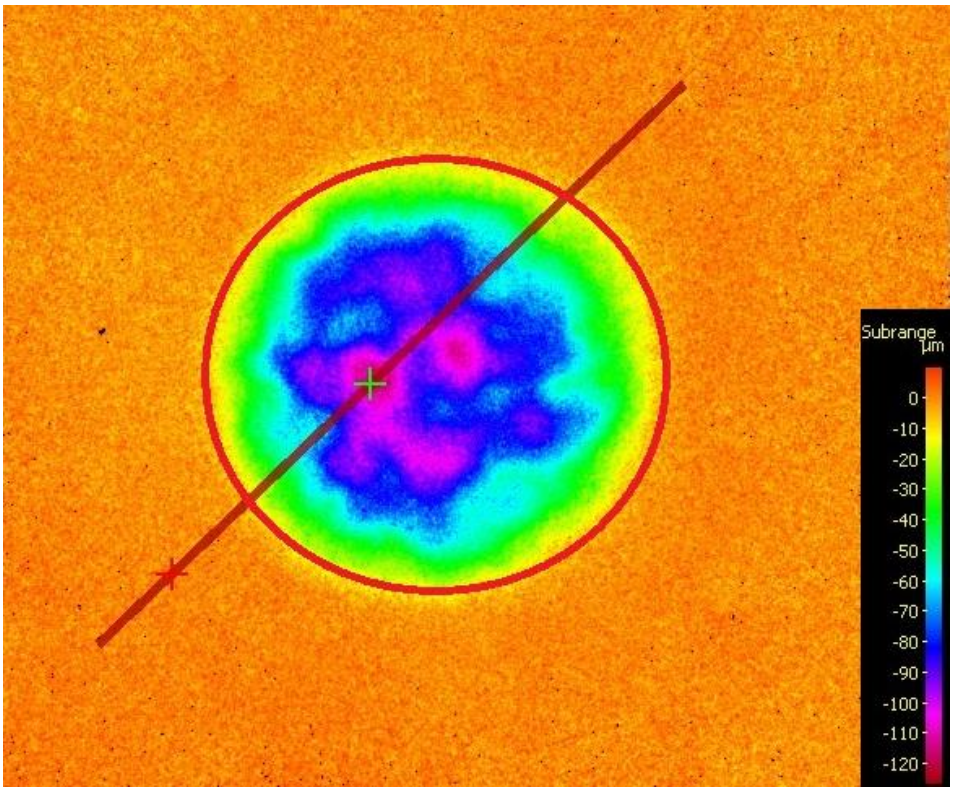

Figure 5.34 Volumetric analysis on the direct impinged zone of the 37%Cr cast iron surface after solid/liquid impingement.

Figure 5.35 illustrates the volume losses of the comparative materials within the direct impinged zone during solid/liquid impingement with and without cathodic protection. The volume losses, when the cathodic protection was applied, were reduced. The UNS S31600 had about 5% reduction on the wear scar volume, whereas the UNS S4200 and both cast irons exhibited about 30% which shows the benefit of cathodic protection on those materials.

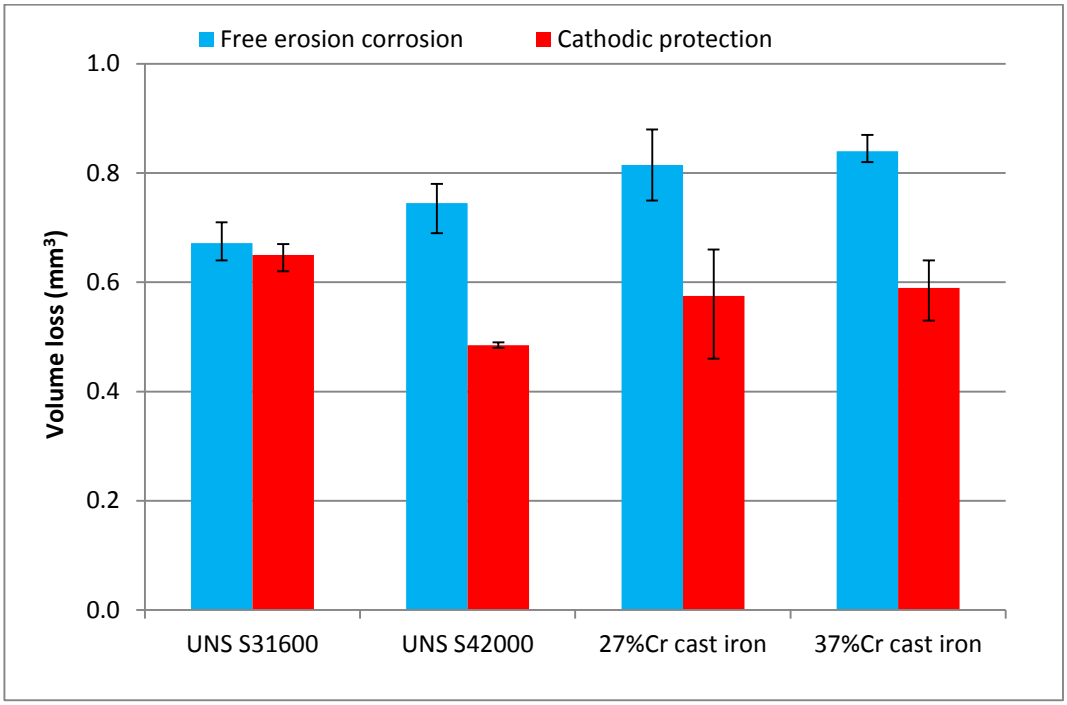

Figure 5.35 Comparison of the average volume losses within the wear scar of the two stainless steels and the two cast irons under solid/liquid impingement in free erosion-corrosion and cathodic protection.

5.6 Discussion

5.6.1 Total Volume loss (TVL) in free erosion corrosion (FEC) conditions

The total volume losses were measured directly from the experiments, see Figure 5.6. The overall volume losses of all the comparative materials were similar under free erosion-corrosion conditions. These results are not in accord with previous studies, which have reported that the erosion-corrosion resistance of white cast irons is superior to that of stainless steels [5.17,5.31–5.35]. However, these tests [5.17,5.31–5.35] involved either three-body dry abrasion or low angle of impingement with much higher solid loadings. Moreover, a recent solid/liquid impingement study examined the effect of increasing the erosivity of the slurry by involving higher velocity and sand loading and indeed demonstrated the superiority of the cast irons over stainless steels. This again indicates how the material performance under erosion-corrosion conditions are crucially dependent on the balance between mechanical and electrochemical severity [5.25,5.36].

Discrimination of the total volume loss in DIZ and OA

Figure 5.36 illustrates the discrimination of the total volume loss to the volume loss of the wear scar and the material loss on the outmost area that enhances the understanding and quantification of the corrosive wear mechanisms that occur during the experiments. It is difficult to distinguish the best performing material, as the volume losses of the four materials are comparable in both direct impinged zone (DIZ) and outer area (OA). However, an interesting feature of this distribution is the fact that if the surface area of the direct impinged zone (~0.2cm^2) and outer area (~11.0 cm^2) are considered, the volume losses per unit area on the outer zone is substantially smaller than that of the direct impinged zone. This demonstrates that the material loss is critically affected by the erosion conditions a) high solid loading and extremely high velocities (DIZ) which results in high volume loss and b) low sand loading and velocities (OA) that cause low volume loss.

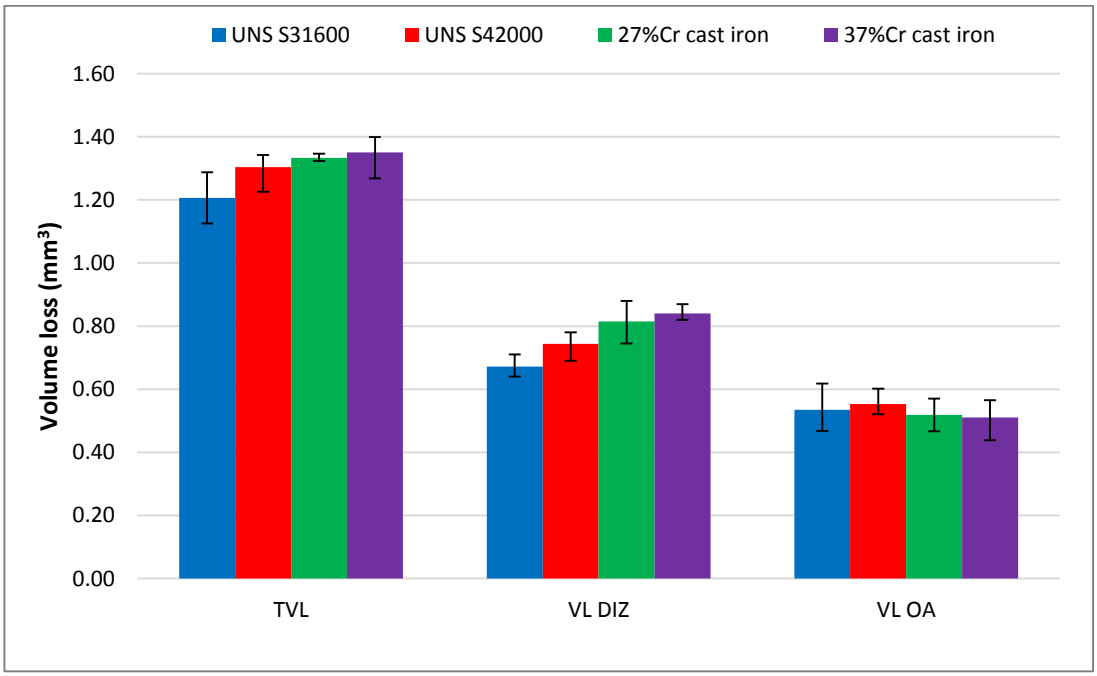

Figure 5.36 Proportions of volume loss damage in the direct impingement zone and in the outer area of the comparative materials.

Figure 5.36 is indicative of the overall damage on each specimen region but further discrimination of the erosion-corrosion degradations processes will add value to this evaluation. It is known that the volume loss in the direct impinged zone represents the pure erosion, pure corrosion and the synergy within the wear scar. The volume loss on the outer area signifies the sliding abrasion (mechanical), the pure corrosion and the synergy that take place outside the wear scar. The quantitative volume losses, shown in Figure 5.37, are

measured in accordance to Section 4.8 in Chapter 4, and demonstrate the substantial benefits of the expanded assessment of erosion-corrosion testing that forms the basis of this thesis.

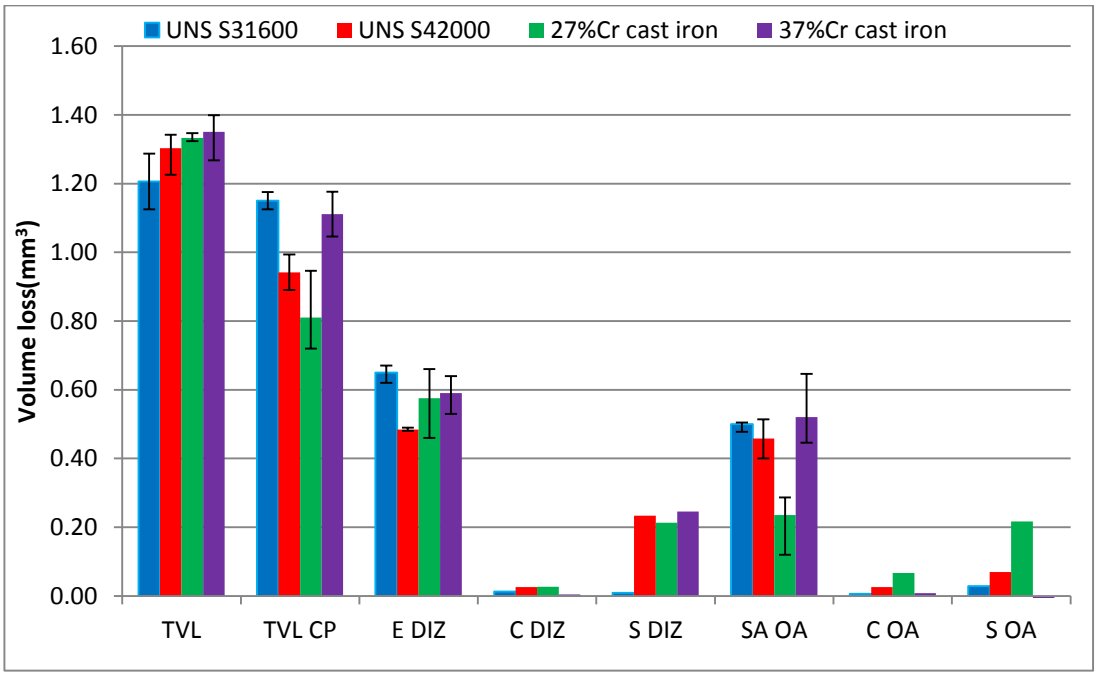

Figure 5.37 Distinction of the different material degradation processes on the two stainless steels and the two cast irons.

5.6.2 Total volume loss with cathodic protection (CP)

The total volume losses with the cathodic protection were measured directly from the experiments as shown in Figure 5.6. The application of CP assisted in the distinction of the comparative materials, since the martensitic based alloys exhibited superior erosion resistance compared with the austenitic based materials. Similar changes in the relative ranking of white cast irons and stainless steels were observed in past studies [5.25,5.36] through alteration of the environmental conditions.

The employment of CP reduced the overall material loss of all materials. It is noteworthy, though, to mention that 27%Cr cast iron benefited the most by the application of CP, as its total volume loss was decreased by 39%. The UNS S42000 and 37%Cr cast iron also benefited from CP as their volume loss dropped by about 28% and 18%, respectively. On the other hand, the UNS S31600 volume loss fell by just 5%. This demonstrates that the corrosion related component, had most substantial effect on the 27%Cr cast iron and the

UNS S42000 and lower impact on the 37%Cr cast iron and the austenitic stainless steel. Similar traits of the significant reduction of the martensitic based alloys have been observed in previous studies [5.22,5.35,5.36]. The same group of studies [5.22,5.35,5.36], have found that the material loss of the austenitic based alloys is less affected as the chromium content in their matrix is higher than the martensitic based alloys.

In terms of mechanical damage, the difference between the two stainless steels may be linked to their different hardness, even if the UNS S31600 was work hardened by the continuous solid particle impact as shown in Figure 5.21. The relative behaviour of the two cast iron alloys may be associated with their Cr/C ratio. The 37%Cr cast iron exhibits a Cr/C ratio of 20.6 which is more than two times of the Cr/C ratio of the 27%Cr cast iron (9.0). Since it is suggested that the lower the Cr/C ratio is, the higher the wear resistance [5.35,5.43], the above results agree with the literature.

5.6.3 Erosion damage on the direct impinged zone (DIZ)

The material deterioration by erosion mechanisms that takes place inside the wear scar was determined by the volume loss analysis of the cathodically protected wear scars. The UNS S42000 showed the lowest erosion damage within the direct impinged zone. The two cast irons showed higher volume loss than the martensitic stainless steel and this is attributed with the heavy cracking of their hard chromium carbides by the impinging particles, as observed in Figures 5.22 - 5.27. Nevertheless, both cast irons exhibited better erosion resistance in their wear scar than the austenitic stainless steel, which was the most vulnerable material under direct impingement erosion. According to the literature [5.5–5.7,5.25], the hardness of a material cannot determine the erosion resistance of the material as a single factor, especially when the target exhibits a composite-like structure. Other mechanical properties (e.g. elastic modulus) should also be taken into account to obtain improved correlations with the erosion rates.

At this point, it should be mentioned that the 37%Cr cast iron wear scar depths in cathodic protection are about the same as with the UNS S31600 but the total wear scar volume loss is quite different. This also suggests that the wear scar depth, as a single parameter, cannot represent the level of the mechanical damage as the morphology of the wear scar was asymmetrical and not a perfect U-shape as on the other three materials. It is

evident that the soft austenitic dendrites of the 37%Cr cast iron, that comprise about 57% volume fraction of the overall structure, are selectively eroded and the protruding chromium carbides are susceptible to cracking and consequently spalling. Another interesting feature, though, was apparent on the cross sections of the 37%Cr cast iron wear scar (See Figures 5.26 and 5.27) where the cracking propagation on the eutectic carbides follows the eutectic structure that encloses the austenitic dendrites, resulting in spalling of carbides along with the large dendrites. This attribute has caused the uneven shape of the 37%Cr wear scar. On the other hand, the 27%Cr cast iron showed a different erosion mechanism as the rod like carbides experienced cracking but the hard martensitic matrix was not eroded preferentially to the carbides; as a result the mechanical support to the carbides was maintained.

5.6.4 Corrosion on the direct impinged zone (DIZ)

Although the volume loss due to corrosion within the wear scar (DIZ), as calculated through Faraday's Law, was a small proportion of the overall damage for all comparative materials in this study, there were some differences in the corrosion rates. The 27%Cr cast iron showed poor corrosion resistance in the initial static corrosion tests with saline water. On the other hand, the 37%Cr cast iron performed better in the same environment. Under the solid/liquid impingement conditions, the in-situ corrosion rates in Table 5.11 showed that the 27%Cr cast iron and the UNS S42000 corrosion rates were almost double that of the UNS S31600 and three times greater than the 37%Cr cast iron. It is apparent that the chromium content on the matrix of the cast iron dictates their corrosion resistance, as suggested in the literature [5.24–5.26,5.28,5.35].

5.6.5 Synergy on the direct impinged zone (DIZ)

The enhancement of erosion by the corrosion mechanisms on the direct impinged zone was determined by the subtraction of the corrosion and erosion damage from the total volume loss in the direct impinged zone. Synergy was a key factor of the material loss inside the wear scar of the two cast irons and the UNS S42000. In fact, synergy (S) was more predominant than pure corrosion (C) in the direct impinged zone. The synergy values of the cast irons and the martensitic stainless steel were about eight times bigger than the UNS S31600. Toro et al [5.44] have suggested that intergranular corrosion along with uniform corrosion of the metallic matrix are the main mechanisms that enhance the mechanical removal of the martensitic stainless steel. It is considered that the synergy of the two cast irons has been accentuated due to the following factors below, as suggested by the literature [5.21–5.26]:

- By micro-galvanic corrosion between the metallic and ceramic phases. Since the chromium content of each phase is controlling its electrode potential, the $Cr_{carbides}$ /Cr_{matrix} ratio of the chromium cast irons is important.
- By corrosion attack at the phase interfaces weakening the interphase bond and facilitating additional material loss by mechanical action.
- Crevice corrosion caused by the corrosion of the metallic phase.

5.6.6 Sliding abrasion on the outer area (OA)

In the experimental set up utilised in this research, the abrasion damage is, in a sense, an impingement at oblique angle. According to Finnie [5.45], the most vulnerable materials in low angle impingement are the soft metals. In other words, the abrasion resistance of a material is dependant of the target material hardness. Thus, the two low hardness stainless steels were prone to sliding abrasion damage. On the other hand, the 27%Cr cast iron as a brittle cast iron with high volume fraction of rod-shape large chromium carbides and a hard martensitic matrix exhibited superior sliding abrasion resistance. This links with the notion that high CVF often provides good durability to abrasion [5.1,5.4,5.35]. The hypoeutectic 37%Cr cast iron exhibited similar sliding abrasion resistance as the stainless steels, which should be associated with the low carbide volume fraction with small size eutectic chromium carbides (100 times smaller than the erodent) and also their soft austenitic dendrites. These microstructural features of the 37%Cr cast iron contributed to the relatively lower sliding abrasion resistant than the 27%Cr cast iron.

5.6.7 Corrosion on the outer area (OA)

Similar corrosion performance trends with the direct impinged zone were observed also on the outer area. It should be noted, though, that the relative ranking was more distinct in the outer area as the 37%Cr cast iron was two times better than the UNS S31600, and the UNS S42000 was two times better than the 27%Cr cast iron, as shown in Table 5.9. This attribute is important as it demonstrates that the austenitic-based alloys maintain their good static corrosion resistance (Figure 5.4) also in the less aggressive conditions outwith the direct impinged zone. However, similar to the corrosion on the direct impinged zone, the corrosion contribution to the overall damage obtained in the outer area was negligible.

5.6.8 Synergy on the outer area (OA)

The synergistical effect of corrosion with erosion on the outer area would take place with similar mechanisms as on the direct impinged zone. However, the synergy was decreased in the outer area compared to the direct impinged zone for the 37%Cr cast iron and UNS S42000. This characteristic is apparent due to the decreased corrosion component, which is related to the synergy. For instance, the volume loss of the 37%Cr cast iron due to synergy on the outer area was negligible, since its corrosion rate was insignificant within this region. The UNS S42000 had the same trait with the 37%Cr cast iron as its volume loss was reduced from the direct impinged zone to the outer area. The 27%Cr cast iron showed similar volume loss due to synergy in both areas, as its corrosion rate was slightly reduced. The UNS S31600 synergy was slightly increased in the outer area compared to the direct impinged zone even though, its corrosion rate was substantially reduced and it might be due to the great susceptibility to the erosion.

5.7 Conclusions

1. The application of the newly developed method of analysing the material loss yielded the discrimination of the various degradation mechanisms that take place under impingement and, thereby, provided a better understanding the erosion-corrosion behaviour of the materials than that of the obtained from a consideration of the total volume loss alone. For example, the superiority of the 27%Cr cast iron under pure mechanical conditions is related with its outstanding sliding abrasion resistance and not with its direct impingement erosion. This feature would not be perceptible by only considering the total volume loss under cathodic protection experiments.
2. The cathodic protection was extremely effective on the martensitic structured alloys (27%Cr cast iron, UNS S42000), since they exhibited a volume reduction of 39% and 28%, respectively. The UNS S31600 and 37%Cr cast iron showed superior corrosion resistance and for this reason the cathodic protection did not have a substantial effect.
3. The suppression of the corrosion component changed the relative performance of the comparative materials as the martensitic structured alloys demonstrated greater erosion resistance against the austenitic based alloys.

4. The 27%Cr and UNS S42000 alloys exhibited similar overall erosion-corrosion behaviour. However, the 27%Cr showed greater mechanical performance in pure erosion conditions (i.e. with CP) compared to UNS S42000.
    - The UNS S4200 demonstrated better behaviour under direct impingement in contrast with the 27%Cr cast iron as the chromium carbides of the 27%Cr cast iron were heavily cracked and consequently large volumes of material were removed.
    - The presence of chromium carbides within the hard martensitic matrix of the 27%Cr cast iron provided superior resistance to sliding abrasion.
    - Despite these facts, their high volume loss in free erosion-corrosion conditions was directly associated with the large corrosion component of their martensitic structure, with clear disadvantage of the 27%Cr cast iron as its composite-like structure provoked more synergy effects.
5. Comparing the 37%Cr cast iron with the SS316; they showed only a small difference under free erosion-corrosion conditions.
    - The addition of chromium carbides in the austenitic matrix of 37%Cr cast iron has slightly enhanced its erosion resistance.
    - The corrosion related component of the 37%Cr cast iron is higher than UNS S31600 in the direct impinged zone due to the interaction of the metallic matrix with the carbides. On the other hand, the 37%Cr cast iron exhibited superior corrosion resistance in the outer area as the corrosion related component was negligible compared to that of UNS S31600. The 37%Cr cast iron has higher Cr content than the UNS S31600 and this could be the reason why its behaviour is better in corrosive environments.
6. Comparing the two cast irons, it is evident that the 27%Cr cast iron has superior erosion resistance compared to 37%Cr cast iron. In terms of corrosion though, the 37%Cr cast iron outperforms in every corrosive environment (static and solid liquid impingement) with also smaller synergy effects. This is in line with industrial experience; that suggests the 27%Cr cast iron for neutral/less acidic environments and 37%Cr cast iron for field applications, where the pH is highly acidic (corrosion dominated conditions).

5.8 References

[5.1] J.K. Fulcher, T.H. Kosel, N.F. Fiore, The effect of carbide volume fraction on the low stress abrasion resistance of high Cr-Mo white cast irons, Wear. 84 (1983) 313–325.

[5.2] G. Pintaude, A.P. Tschiptschin, D.K. Tanaka, A. Sinatora, The particle size effect on abrasive wear of high-chromium white cast iron mill balls, Wear. 250 (2001) 66–70.

[5.3] B. Lu, J. Luo, S. Chiovelli, Corrosion and wear resistance of chrome white irons—A correlation to their composition and microstructure, Metall. Mater. Trans. A. 37 (2006) 3029–3038.

[5.4] Z.U.M. Gahr, G.T. Eldis, Abrasive wear of white cast irons, Wear. 64 (1980) 175–194.

[5.5] S.G. Sapate, A.V. Ramarao, Effect of carbide volume fraction on erosive wear behaviour of hardfacing cast irons, Wear. 256 (2004) 774–786.

[5.6] R.J. Chung, X. Tang, D.Y. Li, B. Hinckley, K. Dolman, Abnormal erosion-slurry velocity relationship of high chromium cast iron with high carbon concentrations, Wear. 271 (2011) 1454–1461.

[5.7] C.I. Walker, P. Robbie, Comparison of some laboratory wear tests and field wear in slurry pumps, Wear. 302 (2013) 1026–1034.

[5.8] J.D. Gates, G.J. Gore, M.J.P. Hermand, M.J.P. Guerineau, P.B. Martin, J. Saad, The meaning of high stress abrasion and its application in white cast irons, Wear. 263 (2007) 6–35.

[5.9] Private communication with Kevin Dolman, Materials Research & Development Manager, WEIR Minerals, Sydney, Australia, 2015.

[5.10] C. Scandian, C. Boher, J.D.B. de Mello, F. Rézaï-Aria, Effect of molybdenum and chromium contents in sliding wear of high-chromium white cast iron: The relationship between microstructure and wear, Wear. 267 (2009) 401–408.

[5.11] M.M. Arikan, H. Çimeno, E.S. Kayali, The effect of titanium on the abrasion resistance

of 15Cr – 3Mo white cast iron, Wear. 247 (2001) 231–235.

[5.12] R.J. Chung, X. Tang, D.Y. Li, B. Hinckley, K. Dolman, Effects of titanium addition on microstructure and wear resistance of hypereutectic high chromium cast iron Fe-25wt.%Cr-4wt.%C, Wear. 267 (2009) 356–361.

[5.13] R.J. Chung, X. Tang, D.Y. Li, B. Hinckley, K. Dolman, Microstructure refinement of hypereutectic high Cr cast irons using hard carbide-forming elements for improved wear resistance, Wear. 301 (2013) 695–706.

[5.14] H.X. Chen, Z.C. Chang, J. C. Lu, H.T. Lin, Effect of niobium on wear resistance of 15 % Cr white cast iron, Wear. 166 (1993) 197–201.

[5.15] Y.P. Wang, D.Y. Li, L. Parent, H. Tian, Improving the wear resistance of white cast iron using a new concept - High-entropy microstructure, Wear. 271 (2011) 1623–1628.

[5.16] Y.P. Wang, D.Y. Li, L. Parent, H. Tian, Performances of hybrid high-entropy high-Cr cast irons during sliding wear and air-jet solid-particle erosion, Wear. 301 (2013) 390–397.

[5.17] R.J. Llewellyn, S.K. Yick, K.F. Dolman, Scouring erosion resistance of metallic materials used in slurry pump service, Wear. 256 (2004) 592–599.

[5.18] G.D. Nelson, G.L.F. Powell, V.M. Linton, Investigation of the Wear Resistance of High Chromium White Irons, (2010).

[5.19] T.T. Matsuo, C.S. Kiminami, W.J.B. Fo, C. Bolfarini, Sliding wear of spray-formed high-chromium white cast iron alloys, Wear. 259 (2005) 445–452.

[5.20] O. Maranho, D. Rodrigues, M. Boccalini, A. Sinatora, Mass loss and wear mechanisms of HVOF-sprayed multi-component white cast iron coatings, Wear. 274-275 (2012) 162–167.

[5.21] S.W. Watson, B.W. Madsen, S.D. Cramer, Wear-corrosion study of white cast irons, Wear. 181-183 (1995) 469–475.

[5.22] A.F. Zhang, J.D. Xing, L. Fang, J.Y. Su, Inter-phase corrosion of chromium white cast irons in dynamic state, Wear. 257 (2004) 198–204.

[5.23] M. Salasi, G.B. Stachowiak, G.W. Stachowiak, Three-body tribocorrosion of high-chromium cast irons in neutral and alkaline environments, Wear. 271 (2011) 1385–1396.

[5.24] A. Neville, F. Reza, S. Chiovelli, T. Revega, Characterization and corrosion behavior of high-chromium white cast irons, Metall. Mater. Trans. A Phys. Metall. Mater. Sci. 37 (2006) 2339–2347.

[5.25] A. Neville, F. Reza, Erosion-corrosion of cast white irons for application in the oilsand industry, in: Nace Int. Corros. 2007 Conf. Expo, 2007: pp. 1–13.

[5.26] H.H. Tian, P.A. Taylor, Corrosion study on high alloyed white cast irons in acidic and chloride containing solutions, in: Nace Int. Corros. 2011 Conf. Expo, 2011: pp. 1–14.

[5.27] H.H. Tian, G.R. Addie, R.J. Visintainer, Erosion-corrosion performance of high-Cr cast iron alloys in flowing liquid-solid slurries, Wear. 267 (2009) 2039–2047.

[5.28] X.H. Tang, R. Chung, C.J. Pang, D.Y. Li, B. Hinckley, K. Dolman, Microstructure of high (45wt.%) chromium cast irons and their resistances to wear and corrosion, Wear. 271 (2011) 1426–1431.

[5.29] A.N.J. Stevenson, I.M. Hutchings, Wear of hardfacing white cast irons by solid particle erosion, Wear. 186-187 (1995) 150–158.

[5.30] M.A. Al-Bukhaiti, S.M. Ahmed, F.M.F. Badran, K.M. Emara, Effect of impingement angle on slurry erosion behaviour and mechanisms of 1017 steel and high-chromium white cast iron, Wear. 262 (2007) 1187–1198.

[5.31] G.J. Gore, J.D. Gates, Effect of hardness on three very different forms of wear, Wear. 203-204 (1997) 544–563.

[5.32] L.L. Parent, D.Y. Li, Wear of hydrotransport lines in Athabasca oil sands, Wear. 301

(2013) 477–482.

[5.33] Y. Xie, J.J. Jiang, K.Y. Tufa, S. Yick, Wear resistance of materials used for slurry transport, Wear. (2015) 1–7.

[5.34] M. Jones, R.J. Llewellyn, Assessing the Erosion Corrosion Properties of Materials for Slurry transportation and processing in the oil sands industry, in: Nace Int. Corros. 2007 Conf. Expo, 2007: pp. 1–15.

[5.35] M. Jones, R.J. Llewellyn, Erosion-corrosion assessment of materials for use in the resources industry, Wear. 267 (2009) 2003–2009.

[5.36] G. Karafyllias, L. Giourntas, T. Hodgkiess, A.M. Galloway, Relative performance of two cast irons and two stainless steels under erosion-corrosion conditions, Accepted for publication, in: NACE Int. Corros. 2016 Conf. Expo, 2016.

[5.37] V.D. Krstic, On the fracture of brittle-matrix/ductile-particle composites, Philos. Mag. 48 (1983) 695–708.

[5.38] R. Chattopadhyay, Surface Wear, Analysis, Treatment and Prevention, 2001.

[5.39] I.M. Hutchings, Tribology: Friction and Wear of Engineering Materials . 1992, London, 1992.

[5.40] R.J.K. Wood, J.C. Walker, T.J. Harvey, S. Wang, S.S. Rajahram, Influence of microstructure on the erosion and erosion-corrosion characteristics of 316 stainless steel, Wear. 306 (2013) 254–262.

[5.41] T.A. Adler, Ö.N. Doğan, Damage by indentation and single impact of hard particles on a high chromium white cast iron, Wear. 203-204 (1997) 257–266.

[5.42] T. Singh, S.N. Tiwari, G. Sundararajan, Room temperature erosion behaviour of 304, 316 and 410 stainless steels, Wear. 145 (1991) 77–100.

[5.43] C. Çetinkaya, An investigation of the wear behaviours of white cast irons under

different compositions, Mater. Des. 27 (2006) 437–445.

[5.44] A. Toro, A. Sinatora, D.K. Tanaka, A.P. Tschiptschin, Corrosion–erosion of nitrogen bearing martensitic stainless steels in seawater–quartz slurry, Wear. 251 (2001) 1257–1264.

[5.45] I. Finnie, The mechanism of erosion of ductile metals, in: Proced. 3rd U.S. Congr. Appl. Mechnanics., 1958.

Chapter 6

Manufacturing process effect on the erosion-corrosion behaviour of cermets

6.1 Introduction

The Oil and Gas and Power sectors of Weir Group widely use cermet materials in both high velocity oxy fuel (HVOF) spray coatings and sintered forms. Nowadays, HVOF WC based coatings have replaced Stellite coatings for sea water injection pumps on Oil and Gas rigs, as they provide excellent abrasion resistance [6.1]. Sintered WC-based cermets are also employed in crude oil pumps, bearings and wear rings, in which the erosion-corrosion conditions are aggressive and HVOF coatings cannot be employed [6.1]. The Group has proposed to expand the applications of these types of cermets to enhance the life expectancy of Weir products. To achieve this target, though, extensive research is required to unravel the various micro-mechanisms that occur during erosion, corrosion and erosion-corrosion by assessing both the manufacturing process and the effect of the binder type and composition.

Two high velocity oxy fuel coatings (HVOF) WC-12Co and WC-10Ni, their substrate UNS S31600 and two sintered WC based cermets (WC-11Co & WC-6Ni) were utilised in this study. The technique, described in Chapter 4, enabled the assessment of the mechanical damage, the electrochemical response and the synergistical effects of these five materials. This study aims to understand the effect of the metallic binder on the erosion-corrosion behaviour of a spray coating under impingement. In addition to that, cermets in sintered form with similar composition have also been investigated to identify the impact of the manufacturing process on the performance of these cermets.

6.2 Literature Review of the cermet materials

6.2.1 Comparison of HVOF cermet coatings with sintered cermets

The high-velocity oxygen-fuel (HVOF) thermal spraying process comprises a combustion chamber in which a mixture of fuel (e.g. propylene, hydrogen or kerosene) and material powder are burned with oxygen and passed through a nozzle in a molten or semi-molten state at supersonic velocities. The HVOF process is characterised by its high flame velocity, up to 2000 m/s, which results in the formation of spray particle stream with relatively high velocity of the particles (400–800 m/s) [6.2]. The advantage of the HVOF process over conventional thermal spraying processes is the relatively low temperature (1600-2200^{o}C) that reduce the possibility of decomposition or oxidation of the carbide particles compared

with other thermal spraying processes, such as plasma spraying [6.3]. The materials deposited in HVOF deposition can be metallic, polymeric, and cermets. The WC-based cermet powders are commonly employed on account of their good wear and corrosion resistance depending on their metallic binder.

An alternative manufacturing process that is followed to engineer the WC based cermets is vacuum sintering, where a treated powder of WC and metallic binder is heated at 1350-1500^{o}C with 60 bar Argon pressure to ensure a low porosity level after the densification of the liquid phase [6.4]. A small portion of other types of carbides (i.e. Cr_3C_2 and VC) may also be employed to prevent any grain growth during sintering. During sintering, substantial amounts of WC dissolve in the metallic binder and precipitate during cooling, mainly along the periphery of existing WC grains and as finely dispersed particles in the binder which results in a strong bond between the carbide and the metallic binder [6.5].

Hardly any comparative studies of the wear resistance of the sintered and thermally sprayed cermets appear to have been carried out in the past. A sintered form of WC-12Co was compared with a HVOF sprayed coating of the same composition by Clark et al [6.6]. Their Corriolis results showed that the sintered WC-12Co performed better than the HVOF sprayed WC-12Co in fresh water slurry of 10wt% alumina concentration. On the other hand, the slurry impingement tests with fresh water and 9.1wt% alumina showed opposite attributes as the coating exhibited better erosion resistance in contrast to the sintered form at both 90^{o} and 20^{o} impingement angle.

Wayne and Sampath [6.7], also compared the abrasion and erosion resistance of sintered and thermally sprayed coatings (WC-12Co and WC-17Co) under air/sand jet impingement conditions. According to their findings, the sintered cermets showed two times better resistance than that of the HVOF cermet coatings of the same composition mainly due to the non-uniform fracture toughness of the HVOF coatings.

Two studies have compared sintered WC-based cermets and a coating produced by the detonation gun (D-Gun) process. The latter is another high-velocity thermal spray method, but employs a repetitive “splat-plug” induced detonation process to impact energy to the coating powder. Wood et al [6.8], studied the erosion resistance of sintered WC-7.2Ni-6.2Co-1.6Cr and D-gun sprayed 86WC-10Co-4Cr by using an erosion rig with fresh water and abrasive sand of 2.1wt% concentration at normal incidence. Their testing

programme comprised low energy impacts and high energy impacts by using 60μm size sand with 18m/s velocity (LEI) and 235μm size sand with 28m/s (HEI), respectively, with the aim of finding a relationship between the erosion rate and the kinetic energy of the particles. The sprayed and sintered forms of cermets showed similar erosion rates under low energy impacts but the sintered cermet outperformed, by four times, the sprayed material under high energy impacts.

An abrasion study by Thakare et al [6.5], showed that the wet abrasion behaviour of the WC-5.7Co-0.3Cr sintered cermet and WC-10Co-4Cr D-gun sprayed coating showed the superiority of the sintered cermet compared to the D-gun coating in a modified ASTM G65 wheel abrasion tester with alkaline fluid feed (pH 11) and SiC particles (4.5μm, 17μm and 180μm). In more detail, the sintered cermet exhibited 100 times better abrasion resistance than the D-Gun coating when small particles were used, but this relative performance was decreased substantially (10 times better) in abrasive conditions where 180μm abrasives were involved.

It is concluded that insufficient work has been reported to facilitate general comparisons of the wear behaviour of the two forms of cermets. Moreover, these appears to have no effort to investigate the influence of corrosion (via tests in saline water) on the erosion/abrasion process.

6.2.2 Potential defects in HVOF cermet coatings in comparison with the sintered form cermets.

The wear resistance of sprayed cermets is likely to be affected by the defects associated with the spray coatings process. These flaws are described below:

6.2.2.1 Decarburisation

This phenomenon causes embrittlement of the matrix through dissolution of the WC, which leads to formation of mixed compounds of type $M_xW_xC_z$ and decomposition of the WC to secondary phases, brittle W_2C, and metallic W [6.9]. Magnani et al [6.10], have suggested that the secondary phases occur by the decarburisation reactions below:

$$2WC \rightarrow W_2C + C$$

$$W_2C \rightarrow 2W + C$$

$$2C + O_2 \rightarrow 2CO$$

And

$$2WC + O_2 \rightarrow 2W + 2CO$$

$$4WC + O_2 \rightarrow 2W_2C + 2CO$$

These decarbusation products can be observed in X-Ray diffraction scans, where an increase in the intensity of the background spectra at 2θ between 35 and 45^o is observed, and this particular region is often called the amorphous nano-crystallisation region because the amorphous mixed compounds of type $M_xW_xC_z$ are detected within this region [6.10].

Wood et al [6.8], reported that decarburisation would steer changes in the coating microstructure and as a result it would not correspond to that of the nominal composition of the powder. Marple et al [6.11], have also demonstrated the importance of the spraying conditions by assessing three different HVOF gun fuel combinations and their effect on the extent of decarburisation process. Tu et al [6.12], reported that the vacuum plasma spray process of WC-17%Co coating was more efficient in terms of wear and impact resistance than are air plasma coatings. This performance feature was associated with the presence of the secondary phases (W_2C and W) that were provoked by the reaction of the powder with the oxygen during air plasma spraying.

The vacuum sintered products are less likely to exhibit decomposition products in their microstructure [6.4,6.8]. This is a potential advantage of the sintered cermets against the HVOF sprayed coatings.

6.2.2.2 Microporosity and coating cracking

The porosity of the HVOF sprayed coating is usually lower than 2% according to the majority of HVOF spray suppliers. Cho et al, have measured the porosity levels of four different coatings (WC-Co, WC-Co-Cr, WC-CrC-Ni, WC-Ni) with almost similar spraying conditions and they found that the porosity does not exceed 1.2% [6.13]. The spray conditions should be carefully considered to ensure good quality coating, otherwise, the porosity can reach higher values (about 6%) that may also interconnect [6.14–6.16] and microcracks [6.2] may also appear which would lead to corrosion attack of the substrate and hence accelerated erosion that would result on coating removal.

In the work produced by Marple et al [6.11], the particle temperature was found to affect the porosity level of the HVOF WC-12Co nano-structured coating. They discovered that the hydrogen and propylene fuel and low particle temperature (<1800^{o}C) resulted in 3-4% porosity of the WC-12Co coatings, which is higher than that obtained on the coatings sprayed at higher spray temperatures (> 1,900^{o}C). The highest porosity level has been observed on the study of Perry et al [6.17], where the measured porosity of WC-CoCr coating was about 3-6% by image analysis.

Mahdipoor et al [6.18], investigated the water droplet erosion behaviour of two WC based HVOF sprayed coatings with identical feedstock powder composition. Despite their same chemical composition, one HVOF coating exhibited two to three times better erosion resistance than the other. The main reason for this different behaviour of the two HVOF coatings was the imprecisely controlled spraying conditions that led to defects such as increased porosity and high decomposition of the WC grains during spraying. Mahdipoor et al work [6.18] shows the effect of spraying conditions on the microstructure of the coating and its performance characteristics. Figure 6.1, represents an extreme example of a poor quality HVOF cermet coating (WC-NiCrSiB). The macrocracks have been initiated due to the lack of spray process control.

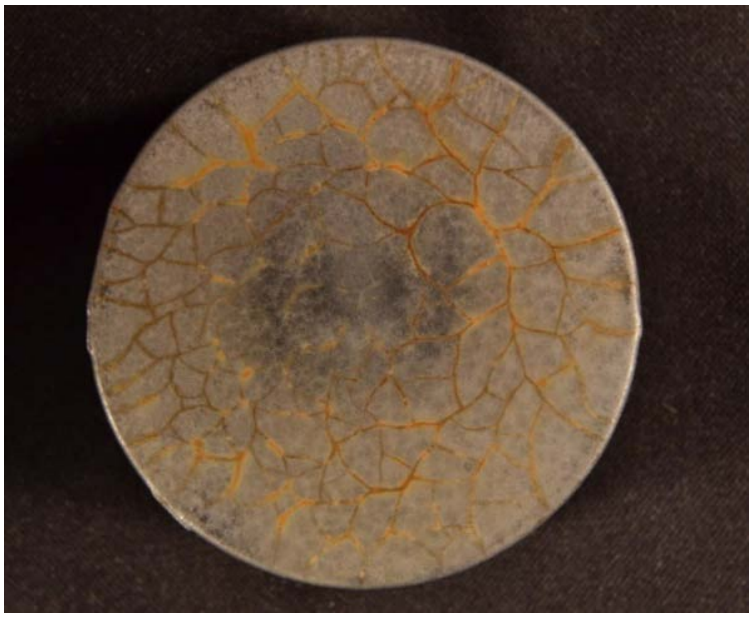

Figure 6.1 Post-test surface of the WC-NiCrSiB (38mm diameter) on a carbon steel substrate after erosion-corrosion impingement for 2h.

Such material flaws are likely to be less present after the vacuum sintering process as the manufacturing conditions are well controlled [6.4]. It has been demonstrated that the porosity levels of the sintered TiC base hard metals are around 0.1 to 0.2vol% [6.19,6.20]. The composition of the TiC based cermets is totally different than the WC based cermets but their manufacturing process is the same (i.e. vacuum sintering). The fact that researchers who focus on the sintered forms of cermets do not mention any porosity level may be an indicator of the low porosity.

6.2.2.3 Anisotropic microstructure

Thermal spray coatings also differ from sintered products in their microstructure, as it is anisotropic by the build-up of splats by the deposition of individual molten droplets during the thermal spray process [6.8]. Such effects will lead to anisotropic wear resistance and also crack growth behaviour. Vacuum sintering results in a good distribution of the material phases, and thus the sintered cermets exhibit no anisotropic behaviour. The critical effect of the anisotropic microstructure on the wear resistance of the HVOF coatings was evident in Wayne and Sampath work [6.7], where the HVOF WC-Co cermet coatings exhibited double abrasion and erosion rates than the sintered cermets of the same chemical composition due to their non-uniform fracture toughness.

6.2.3 Effect of binder concentration

The selection of the concentration of the metallic binder is important for both HVOF cermet coatings and sintered cermets. For this reason, this section will discuss further the binder characteristics and its effect on erosion, abrasion and mechanical properties of the cermets. The influence of corrosive action does not appear to have received any attention in terms of binder concentration.

Pirso et al [6.21], studied the dry sliding abrasion performance of five sintered WC-Co with different binder content (6%wt, 8%wt, 11%wt, 15%wt, 20%wt). The block-on-ring tests revealed that, the higher Co content of the WC based cermets, the higher the volume loss that occurred on the cermets. These performance characteristics were directly related with the hardness of the cermets, which was reduced as the metallic binder content was increased. The same dry abrasion apparatus was utilised by Antonov et al [6.22], to investigate the influence of the binder content along with the size of the WC grains on sintered WC-Co cermets. The medium (1.0μm-2.0μm) WC grain size with the lowest Co

binder content (6%wt) showed better abrasion performance than those with either small (0.2µm-1.0µm) or coarse (2.0µm-10.0µm) WC grains for all Co binder concentrations. This work added the factor of the WC grain size on the abrasion resistance of cermets which is in addition to the influence of the Co binder content.

Similar performance trends were found in wet abrasion tests in the work of Gant and Gee [6.23], who evaluated the effect of binder concentration in a modified ASTM G65 abrasion tester. The WC-Co cermets with the lowest binder concentration (<9.94wt%) exhibited superior performance against the higher binder content (>19.55wt%) WC-Co cermets. This feature was a result of the different wear mechanisms that governed the wear rate of these two groups of hardmetals. The wear rate of the low-cobalt cermets was dictated by simultaneous wear of the hard phase with the extrusion of the cobalt binder, whereas the deterioration of the high-cobalt cermet occurred by ploughing of the abrasive through the cobalt binder together with the fracture of the carbide grains. These results highlight the fact that the hardness and the WC inter-particle spacing are major parameters in determining the abrasion resistance.

Kulu et al [6.24], have summarised the impact of the hard phase concentration on the abrasion resistance, hardness and fracture toughness of a material. Figure 6.2, demonstrates clearly that the harder phase content on a material will enhance its abrasive wear resistance and hardness but it will reduce substantially its fracture toughness.

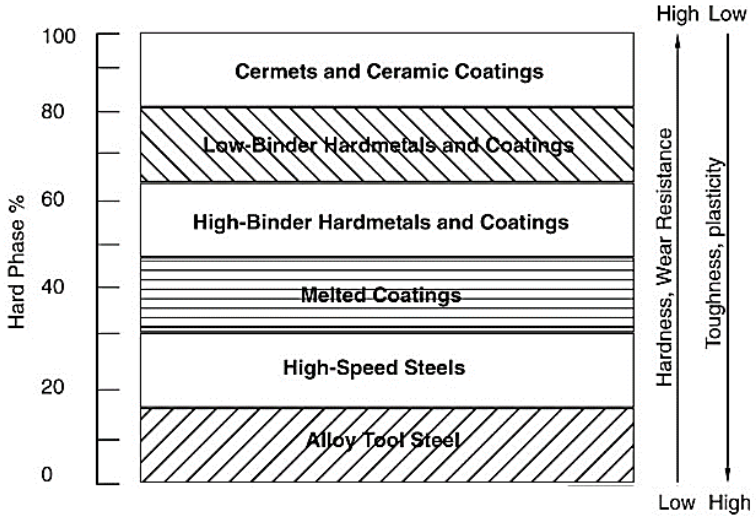

Figure 6.2 Effect of hard phase content on materials' properties.[6.24]

In terms of dry erosion, Ninham and Levy [6.25], investigated the effect of the binder content (10%wt, 20%wt, 25%wt) on sintered WC-Co cermets in air blast impingement at 60m/s velocity with quartz abrasives at a range of impingement angles. They found that the higher the tungsten carbide volume fraction, the lower the erosion rates of the cermets. The WC-10Co cermet performed two times and three times better than the WC-20Co and WC-25Co cermet, respectively, at all impingement angles (30^o, 60^o, 90^o). The researchers suggested that the control of erosion behaviour is transferred from the binder to the carbide skeleton for cermets with 80% volume of carbides, as on WC-10Co, and this was the main reason for the better erosion resistance.

Comparable outcomes were observed in the study of Reshetnyak and Kuybarsepp [6.19], where the dry erosive wear resistance of WC-10Co was greater than that of the WC-20Co and, whilst this appears to correlate with the higher hardness of the former coating, the authors were of the view that such a simple correlation between wear resistance and hardness is inappropriate. They considered that other mechanical properties; such as transverse rupture strength, compressive strength, proof stress and ultimate plastic strain of the cermet may play a role in determining the erosive behaviour of the cermets.

It is evident that the remarkable erosion and abrasion performance of the WC-based cermet with low binder concentration is not attributed to a single parameter. Hardness plays a key role on the abrasion resistance of the cermet but also the grain size of the WC along with the inter-carbide spacing are also important factors. Additional mechanical properties, may also determine the behaviour of cermets under erosive wear.

6.2.4 Influence of binder type

The metallic binder is likely to influence the erosion/abrasion resistance and also the corrosion behaviour of the cermets. The metallic binder can be either cobalt or nickel or compounds (i.e. CoCr, NiCrSiB). Since the focus of this thesis is on the pure cobalt and nickel binders, their compounds will not be reviewed in the sections below.

A sintered WC-12Co and WC-10Ni in both Corriolis tests and slurry jet impingement were evaluated by Clark et al [6.6]. The Corriolis tests showed that the sintered WC-12Co exhibited two times better wear resistance than the sintered WC-10Ni under fresh water slurry with 10wt% alumina sand concentration. The slurry jet impingement tests with fresh water slurry and alumina sand at 90^o and 20^o impingement angles showed different trends

on the relative erosion resistance of these two cermets, as the sintered WC-10Ni cermet showed greater erosion resistance than the WC-12Co type at both angles, with more prominent improvement of the WC-10Ni resistance at 20^{o} angle.

Engqvist et al [6.26], evaluated the tribological properties of sintered cermets WC-6Co and WC-6Ni under abrasion conditions, using the crater grinding test with silica (15μm) and diamond (6μm) abrasives, and also under sliding wear by utilising ball-on-disc wheel tests with alumina balls in air, water and acidic water (pH=0.5). The abrasion tests showed that the wear rate of the two sintered cermets were similar under all abrasion conditions. In the ball-on-disc tests the cermets with cobalt binder suffered less attack that of the Ni binder in dry sliding and wet grinding conditions. However, in acidic lubrication conditions, the WC-6Ni cermet was superior to the WC-6Co material.

Wetzel and Allen [6.27], investigated the effect of impact angle on erosion-corrosion resistance of WC-6Co and WC-6Ni sintered cermets under free jet tests with fresh water and 7%wt silica sand of 500μm size at 6.5m/s. The erosion-corrosion rate of the WC-6Co hardmetal was steadily lower than the WC-6Ni at all impingement angles (45^{o}, 60^{o}, 75^{o}, 90^{o}). According to the authors, the higher hardness of the cobalt promoted the erosion-corrosion resistance of the WC-6Co against the WC-6Ni.

The same researchers [6.28] also examined also the effects of the binder type and content on the slurry erosion-corrosion performance of WC-based hardmetals under saline water solutions (SWS) and tap water solutions (TWS) with 6.3wt% silica sand concentration of 500μm size, 7m/s flow velocity at 75^{o} impingement angle. They focused on an impingement angle of 75^{o}, since the maximum damage of the cermets had been observed at this angle in their previous study [6.27]. Both WC-10Co and WC-6Co performed better than the WC-6Ni cermet under saline and tap water aqueous slurries. The slurry tests on the isolated metallic phase in tap water showed no distinct difference between the pure metallic samples (i.e. Co and Ni), but in saline slurries the Ni binder showed its superiority. The slurry tests on the metallic samples highlighted that when corrosion is predominant, there is no simple relationship of the slurry erosion resistance of hardmetals with hardness.

The static corrosion resistance of two HVOF WC based cermet coatings (WC-17Co & WC-17Ni) in a saline solution (3wt% of NaCl) was investigated by the work produced by Aw et al [6.29]. The WC-17Ni coating exhibited better corrosion resistance than the coating

with Co binder in all the electrochemical techniques (Open circuit potential, Impedance measurements and potentiodynamic scans). Their results underline the significance of the corrosion properties of the binder when the WC based coatings are exposed to saline aqueous solutions.

Cho et al [6.13], assessed the corrosion behaviour of two HVOF coatings (WC-10Ni and WC-12Co) in a strong acidic aerated environment with 5wt%H_2SO_4. The corrosion current density of the WC-10Ni coating was about 10 times smaller than the WC-12Co under the both testing conditions. Some evidence of micro-galvanic corrosion was also observed between WC particles and the metallic binder, which enhanced the overall corrosion of the binder.

6.2.5 Comparison of cermets with metallic alloys

Comparative studies between cermets and other types of alloys have been completed over the past years with the aim of estimating the relative resistance to erosion and/or corrosion of the cermets and also to demonstrate the effectiveness of the HVOF spray coatings against the substrate.

In the recent publication of Kamdi et al [6.30], the abrasion resistance of a HVOF sprayed coating WC-17Co was assessed on a block-on-ball apparatus, which is a micro-scale abrasion tester with abrasive slurry dripping on the rotating ball with either 17.2%wt alumina or 30%wt silica of similar size (2-10µm). A mild steel was used as a reference and the tests shown that the coating performed about 8 and 125 times better than the mild steel with alumina slurries and silica slurries, respectively. Their work involved also a dry sand rotating wheel (DSRW), where the alumina size was between 212µm to 300µm and the silica sand size was in a range of 180µm -250µm, and it demonstrated similar attributes to the block on ball tests. In more detail, the DSRW results showed that the HVOF coating outperformed the mild steel by a factor of 38 times with alumina and 9 times with silica sand slurry, respectively.

A dry abrasion study on a WC-12Co HVOF sprayed coating with different HVOF spraying parameters compared with their substrate (UNS A97050 alluminium alloy) on a rubber wheel tester equipment was performed Magnani et al [6.10]. The abrasive wear rates of the WC-12Co HVOF sprayed coatings were consistently nine times lower than the

aluminium substrate, highlighting the excellent protection of the coating over the substrate.

Gant and Gee [6.23], investigated the fresh water wet abrasion resistance of five different sintered WC cermets with various concentrations of Co binder (6%wt, 9.4%wt, 9.5%wt, 20%wt, 24%wt) manufactured by three different suppliers. They focused on the effect of load, wheel speed and total sliding distance of a modified rubber rimmed steel wheel on wet abrasion of cermets and three high-speed steels. The sintered cermets with lower than 9.5%wt Co binder concentration were superior compared to the other comparative materials in all wet abrasion conditions. The performance of cermets compared with the high speed steels was variable depending on the abrasive conditions.

Karimi et al [6.9], evaluated two HVOF cermet coatings (i.e. WC-12Co and WC-12Ni) in a fresh water slurry erosion tester, that simulates low angle of impingement, with varying flow velocity from 20m/s to 145m/s and 0.3%wt silica sand concentration of 120µm average size. They found that the relative wear resistance of WC-12Co coating was six times higher than the UNS K91470 stainless steel under low flowing conditions (20m/s) and 78 times higher at flowing velocity of 145m/s. For the WC-12Ni sprayed coating, the relative wear resistances were three times better than the UNS K91470 stainless steel at 20m/s ad 59 times at 145m/s velocity.

Two HVOF sprayed coatings (WC-12Co and WC-10Ni) were studied in terms of their dry and fresh water slurry erosion behaviour under free-jet conditions at two angles of impingement (90^o and 20^o) by Hawthorne et al [6.31]. The dry erosion tests with 50µm alumina sand showed similar erosion rates between the two sprayed coatings and the UNS S31600 stainless steel at 90^o, but the coatings exhibited two times better erosion resistance at 20^o. The slurry erosion tests with 35µm and 200µm alumina sand demonstrated the superiority of the two sprayed coatings in comparison with the UNS S31600 stainless steel at both angles of attack.

Feng and Ball [6.32], reported that WC-7Co hardmetal performed better than UNS S30400 under air-blast erosion of 45m/s velocity and 180µm -250µm size silica sand at all impingement angles (i.e. 30^o, 60^o and 90^o). When silicon carbides with 180µm -250µm average size were utilised, the UNS S30400 exhibited better behaviour than WC-7%Co at impingement angles below 40^o but was inferior at higher angles of impingement.

The static corrosion and erosion-corrosion mechanisms of a thermal spray Detonation Gun WC-10Co-4Cr coating and two stainless steels (UNS S31603 and UNS S32760) were assessed by Souza and Neville [6.33]. The static corrosion tests demonstrated that the corrosion current density of the superduplex stainless steel was lower than that of the austenitic stainless steel and the coating with the coating exhibiting a rapid increase of current density during the first 150 mV potential scan above E_{corr} that indicated its lack of passivity. The total volume losses of the WC-Co-Cr coating, after the solid/liquid impingements (3.5%NaCl, 17m/s, 180µm-250µm size silica sand, 18^{o}C), were half of these of the two stainless steels at both solid loadings (200mg/l and 500mg/l) showing the excellent erosion-corrosion resistance of the coating.

Hodgkiess et al [6.34], evaluated the erosion-corrosion of an HVOF WC-Ni-Cr-Si-C coating and an austenitic stainless steel (UNS S31603) under solid/liquid and solid-free liquid impingements of 17m/s flow velocity. The solid-free liquid impingement demonstrated the lower erosion-corrosion resistance of the HVOF coating compared to the austenitic stainless steel. When cathodic protection was applied, the weight losses of these two materials were comparable due to the high corrosion related component of the attack on the HVOF coating. With the introduction of 800ppm silica sand, of mean size of 180µm-250µm, at 18^{o}C -20^{o}C, the relative performances of the two materials changed as the coating exhibited only about 50% of the weight loss of the stainless steel. The superior erosion-corrosion behaviour of the coating was associated with the great erosion resistance of the hard coating.

Bjordal et al [6.35], assessed the performance of a HVOF WC-17Co coating and a duplex stainless steel (UNS S31803) under erosion-corrosion conditions in a rotating disk apparatus. This circulated a slurry comprised of synthetic sea water and 0.25%wt silica sand of 200µm size at pH 8.2 with 20 ± 3^{o}C temperature and flow velocities of 14m/s to 29m/s. At all flowing velocities the corrosion current density of the coating was 0.1 mA/cm^2, whereas the corrosion current density of the duplex stainless steel was increased from 0.0002 to 0.01 mA/cm^2 as the flow velocity increased from 14m/s to 29m/s. In terms of total volume losses of the coating due to erosion-corrosion, the coating exhibited greater resistance than that of the duplex stainless steel. The UNS SS31803 stainless steel had erosion dominated damage in comparison with the WC-17Co coating in which the sum of corrosion and synergy contributions were substantial (more than 50%).

6.3 Experimental work objectives

As it is evident, from the above literature review, that there have been only limited research investigations that compare the erosion-corrosion performance of vacuum sintered WC based cermets and HVOF sprayed coatings of similar composition. Hence, one major aim of research, described in this chapter, has been to investigate the influence of the manufacturing processes on erosion-corrosion of WC based cermets. The influence of the metallic binder was also assessed, since the somewhat inconclusive findings in relation to the Co and Ni binder, from previous studies (section 6.2.2) are likely to be associated with the detailed erosion-corrosion mechanisms in different experimental investigations. Thus, it is considered that the erosion-corrosion assessment techniques, utilised in this project, would enable more affirmative understanding to be reached on the influence of cobalt and nickel binders. The addition of the austenitic stainless steel substrate in this study enabled a measurement of the level of the erosion-corrosion protection provided by the WC-coatings. The application of the novel technique, described in Chapter 4, facilitated a quantification of the deterioration mechanisms taking place on the cermet under direct impingement erosion-corrosion and corrosion-abrasion and has contributed to an improved understanding of this rather complex phenomenon.

6.4 Materials and Methodology

Two HVOF sprayed coatings (WC-12Co & WC-10Ni) were purchased from a well-known commercial supplier. The thickness of both coatings was 500μm, as shown in Figure 6.3. The sintered WC cermets were also obtained from a major producer. They were manufactured by vacuum sintering at 1350 °C to 1500°C with a temperature up ramping in dependency of the size of the parts. A 60 bar Argon was utilised to decrease the level of porosity to 0.02% of the total material volume with the pore size lower than 10μm after the full densification. The vanadium carbides and the chromium carbides in the sintered WC-11Co and WC-6Ni, respectively, act as grain growth inhibitors during the sintering process.

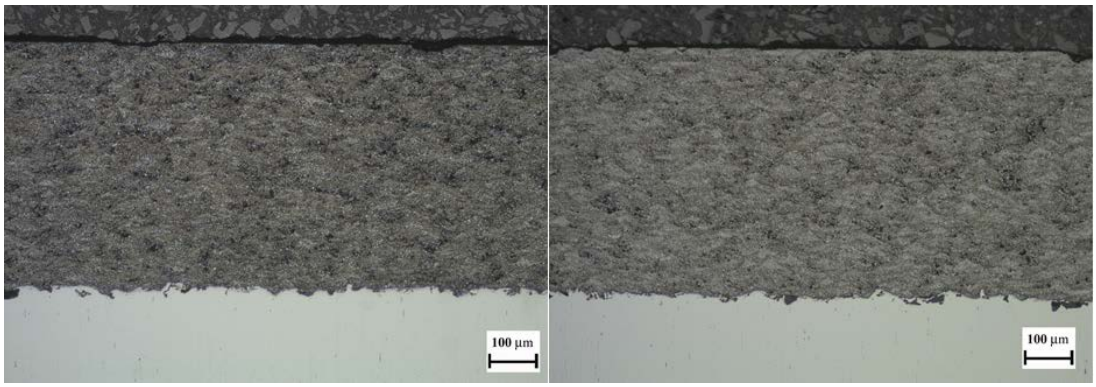

Figure 6.3 Microscopic views of the two 500µm thick HVOF coatings; HVOF WC-12Co (left) and HVOF WC-10Ni (right).

Table 6.1 illustrates the nominal chemical composition of the HVOF sprayed cermets and the sintered cermets. Stainless steel type UNS S31600 was employed as a reference material within this work and Table 6.2 below gives its nominal composition. The densities values, obtained by the suppliers, and the measured hardness values of each material are presented in Table 6.3.

Table 6.1 Nominal chemical composition (wt%) of the HVOF sprayed and sintered cermets.

Cermets	WC	Co	Ni	VC	Cr_3C_2
Sin WC-11Co	88.85	11		0.15	
Sin WC-6Ni	93.5		6		0.5
HVOF WC-12Co	88	12			
HVOF WC-10Ni	90		10		

Table 6.2 Nominal chemical composition (wt%) of UNS S31600

Material	C	Cr	Ni	Mo	S	Mn	Si	N	P	Fe
UNS S31600	≤0.08	16-18	10-14	2.0-3.0	≤ 0.03	≤2.0	≤ 0.75	≤ 0.1	0.045	Bal.

Table 6.3 Nominal density and measured hardness values of the comparative materials.

Material	Density (g/cm^3)	Hardness (HV)
Sin WC-11Co	14.40	1420±50
Sin WC-6Ni	14.85	1605±50
HVOF WC-12Co	14.82	965±50
HVOF WC-10Ni	14.96	1061±50
UNS S31600	8.00	200±20

The erosion-corrosion experiments were carried out using the submerged jet impingement rig described in Section 3.3.1. The testing duration was 2h. The nozzle diameter was 4 mm. The slurry comprised an aqueous solution with 3.5% NaCl at 39±1^{o}C and sand particles that were impinging at 17 m/s velocity perpendicular to the specimen surface. The angular silica sand particles possess hardness of about 1160HV. The sand concentration was 200±20 mg/L. The 38mm diameter HVOF sprayed coated and sintered cermets' specimens were diamond polished by the suppliers.

In order to facilitate corrosion monitoring of the separate direct impinged and outer region, segmented specimens were manufactured, as described in section 3.3.3. Figure 6.4 illustrates the good adherence of the HVOF WC-12Co coating at the inner coupon of the segmented specimen. This indicates that the water jet cutting tool has not affected the quality of the coating during segmentation. Figure 6.5 shows the encapsulated segmented specimen of the WC-6Ni sintered cermet which includes also the travel line of the wire.

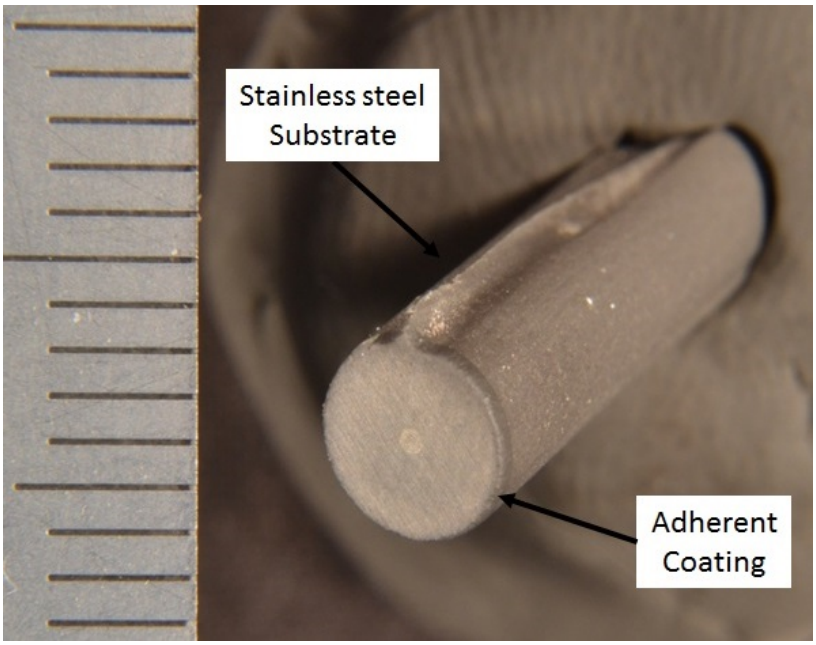

Figure 6.4 The inner HVOF WC-Co specimen after the segmentation from the outer specimen with a water jet cutting tool.

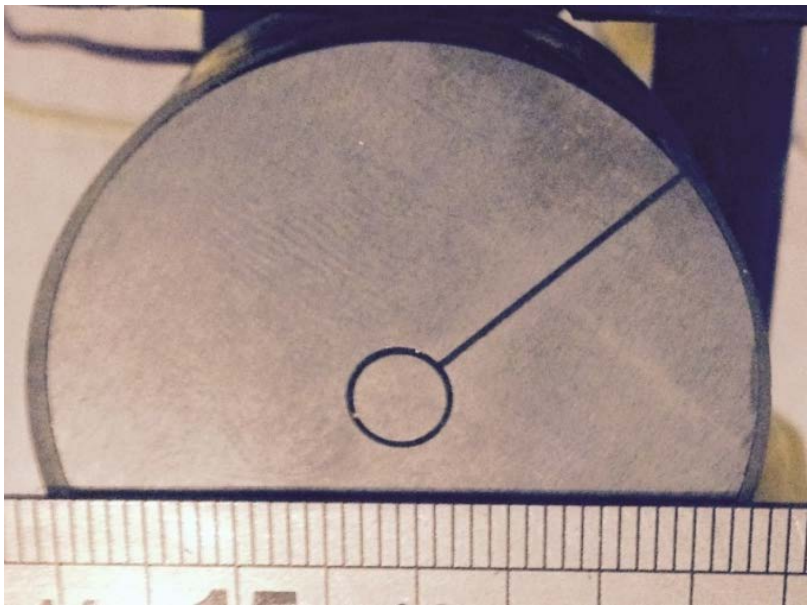

Figure 6.5 The two segments of the WC-12Co sintered cermet coupon encapsulated in epoxy resin.

6.5 Results

6.5.1 Material characterisation

6.5.1.1 Microstructure of the cermets

Figures 6.6 and 6.7 show the cross sections of the sintered WC-11Co and WC-6Ni, respectively. It is evident that the WC-11Co cermet exhibit higher binder content than the WC-6Ni cermet, as Figure 6.7 shows a structure that is rich in WC grains with minimum amount of binder. Figures 6.8 and 6.9 illustrate the microstructure of the HVOF WC-12Co and HVOF WC-10Ni coatings, respectively through their cross sections. The HVOF WC-12Co coating seems to be porous but this feature may be attributed to the preparation process of the cross section. It should be stated, though, that the WC grains and the binder are uniformly distributed. The size of the WC grains is between 1.5μm to 6μm.

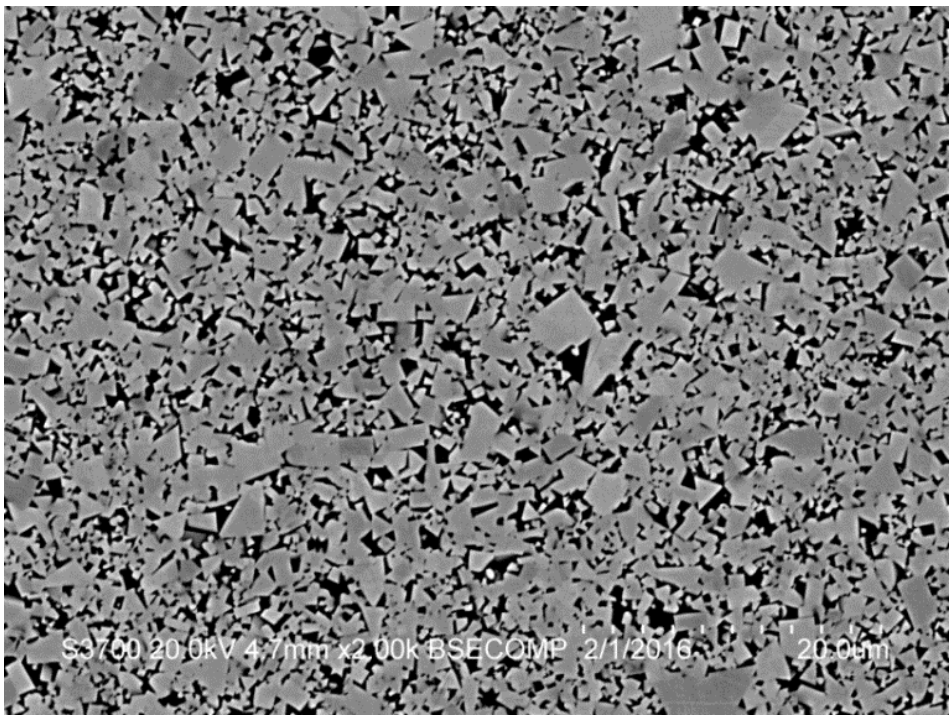

Figure 6.6 Microstructure of the WC-11Co sintered cermet.

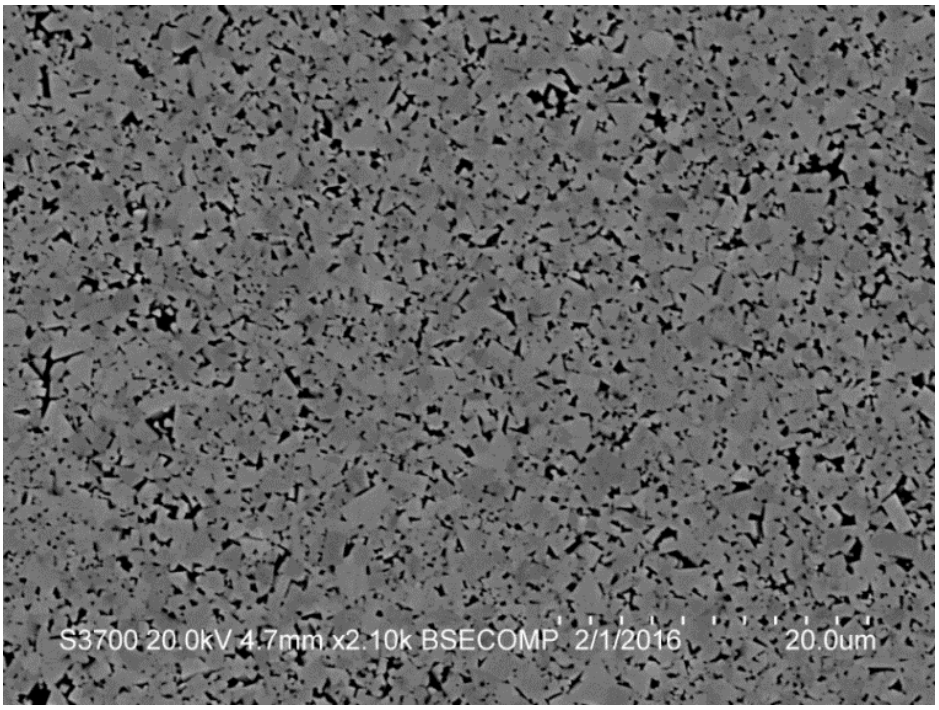

Figure 6.7 Microstructure of the WC-6Ni sintered cermet.

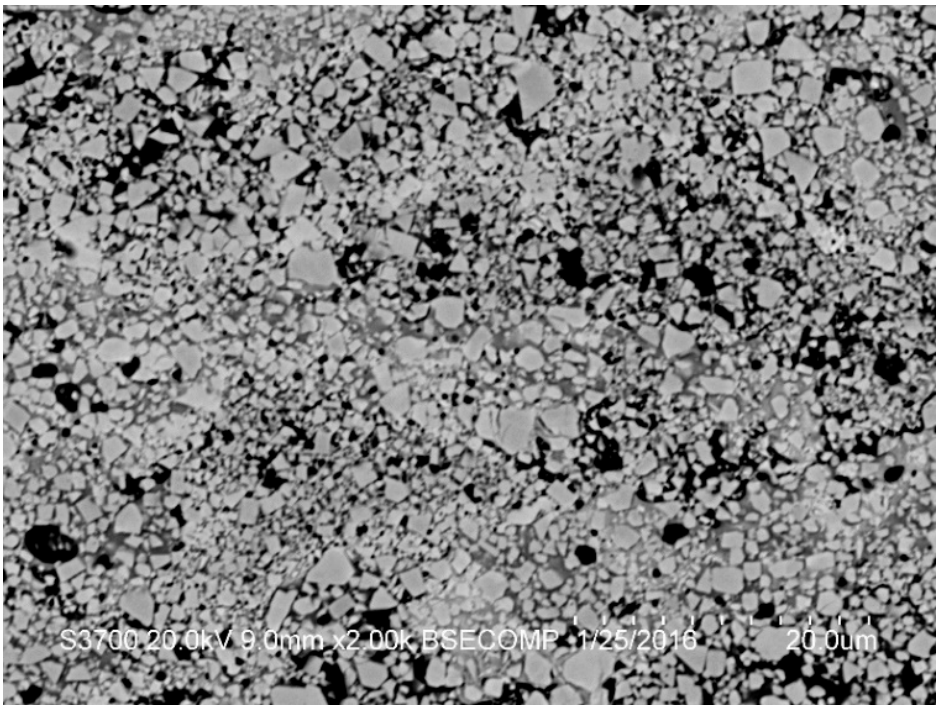

Figure 6.8 Microstructure of the HVOF sprayed WC-12Co.

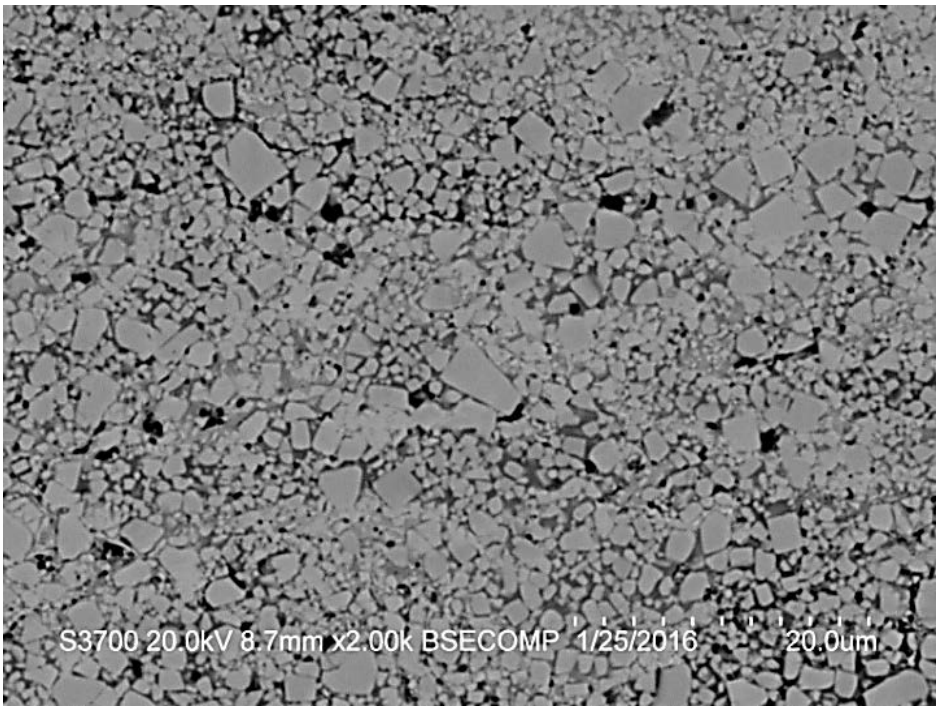

Figure 6.9 Microstructure of the HVOF sprayed WC-10Ni.

6.5.1.2 Wavelength-dispersive X-ray spectroscopy (WDS)

The WDS analysis was utilised, as described in Section 3.2.4.1, to confirm the concentration of the metallic binder in the studied cermets. Table 6.4 shows the Co and Ni binder content, as an average of three replicates, for both sintered cermets and HVOF cermet coatings. It is evident that the Co and Ni contents of the sintered cermets are in agreement with the supplier's specifications. However, the metallic binder content of the HVOF coatings is slightly higher than the specifications of the spray supplier. This difference is not significant but it should be stated that the measured values of the metallic binders have been considered for the electrochemical monitoring calculations later in this chapter.

Table 6.4 Average metallic binder content (wt%) of the cermets via WDS analysis

Material	Co	Ni
Sin WC-11Co	11.0	
Sin WC-6Ni		6.5
HVOF WC-12Co	13.5	
HVOF WC-11Ni		13.0

6.5.1.3 XRD analysis of the cermets

The XRD analysis was performed, as described in Section 3.2.4.2, to determine the different ceramic and metallic phases. Overall, the cermets were identical with the provided specifications of the suppliers. Figure 6.10 and 6.11 shows the XRD scans of the two Co binder cermets and the two Ni binder cermets, respectively. An interesting feature in relation to the sprayed cermets and the sintered cermets was observed between 2θ angles of 37° and 46°, where the presence of the W_2C is evident on the HVOF spayed coating. According to Bartuli et al [6.36], the extent of decarburisation in deposited coatings can be quantified by the index of carbide retention, which is a factor that is calculated through the relative intensities of the most intense peak of the main phases, as shown in Equation 6.1.

$$I_{ret.W} = \frac{I_{WC}}{\left(I_{WC} + I_{W_2C} + I_W\right)} \qquad \textbf{Equation 6.1}$$

Where I_{WC} is the intensity of the WC peak at 2θ = 35.7°;

I_{W2C} is the intensity of the W_2C peak at 2θ = 39.8°, and

I_W is the intensity of the W peak at 2θ = 40.5°.

The index is 0.79 and 0.81 for the HVOF sprayed WC-12Co and HVOF sprayed WC-10Ni. Bartulli [6.36] suggests that a typical index of carbide retention of HVOF sprayed WC base coatings is declared to be about 0.85. Thus, the WC grains of the HVOF WC-10NI had more tendency to dissolve into the matrix compared to the HVOF WC-12Co. The decarburisation results in a loss of the hard phase and embrittlement of the ductile binder, which are unfavourable properties for erosion-corrosion resistance.

On the other hand, it should be mentioned that no apparent decarburisation on a coating would indicate insufficient particle heating, resulting in defective coatings with low inter-lamellar cohesion [6.37]. It is evident that the sintered cermets lack any decarburisation products. This feature would potentially become an advantage of the cermets compared with the HVOF coatings under erosion-corrosion conditions.

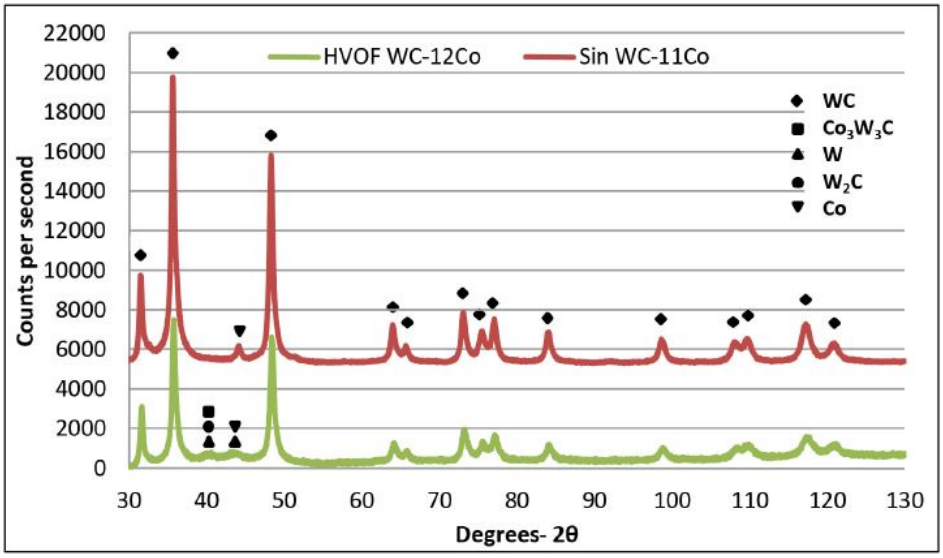

Figure 6.10 XRD patterns of the HVOF sprayed WC-12Co coating and the WC-11Co sintered cermet.

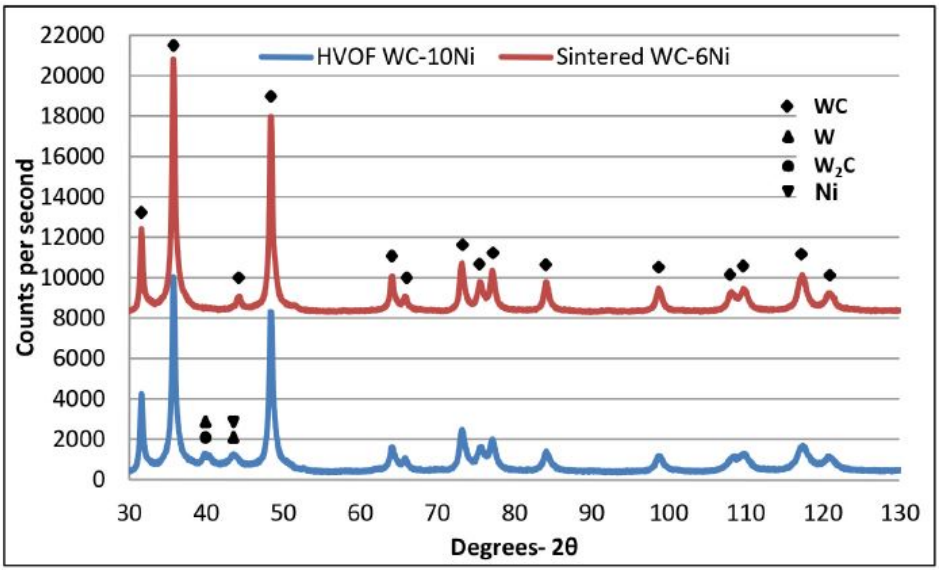

Figure 6.11 XRD patterns of the HVOF sprayed WC-10Ni coating and the WC-6Ni sintered cermet.

6.5.2 Volume loss measurements

Figure 6.12 shows the volume losses of the tested materials under free erosion-corrosion conditions and also application of cathodic protection. These were converted from the measured mass losses (Table 6.5) with the use of the nominal density values in Table 6.3. The error bars represent the scatter of the three replicates. Similar volume losses in free erosion-corrosion and cathodic protection conditions were observed for the UNS S31600 and the sintered WC-6Ni. This indicates that erosion domination has taken place for these

two materials. On the other hand, the sintered WC- 11Co along with the two HVOF sprayed coatings showed a substantial difference in volume loss when cathodic protection was applied. This feature suggests that these three materials suffer from an extensive corrosion-related attack.

Table 6.5 Average mass loss of the stainless steels and cast irons in free erosion corrosion and with cathodic protection.

Material	Average Mass loss (mg)	
	Free erosion-corrosion	Cathodic protection
UNS S31600	9.0	9.2
Sin WC-11Co	16.7	2.1
Sin WC-6Ni	2.6	2.3
HVOF WC-12Co	27.6	2.8
HVOF WC-10Ni	14.0	5.0

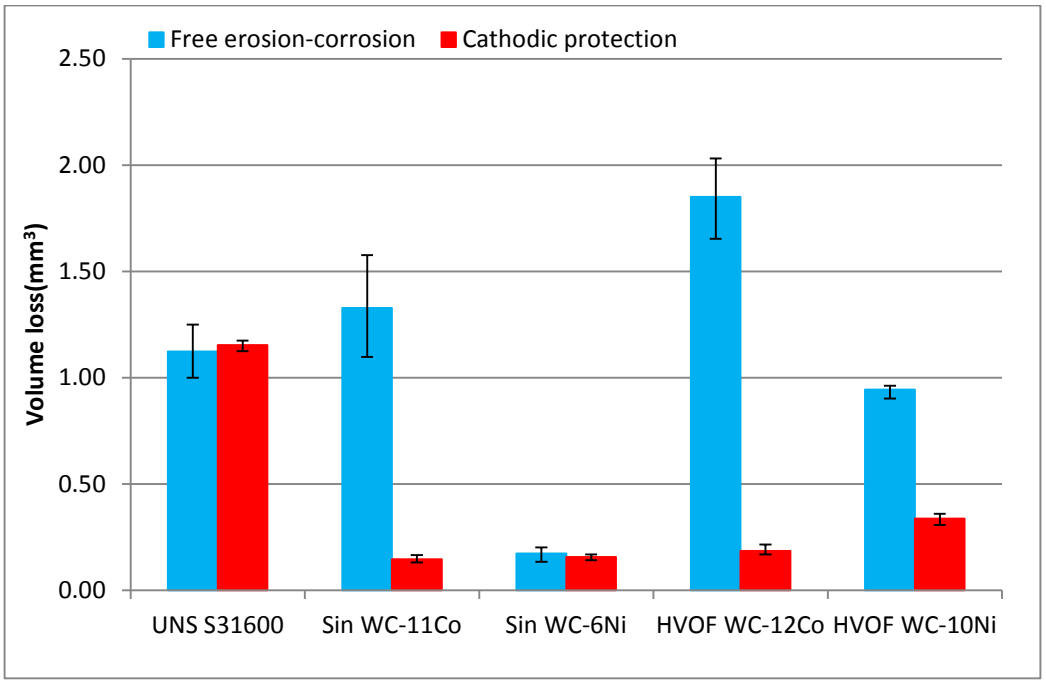

Figure 6.12 Volume losses of the five tested materials under solid/liquid impingement in free erosion-corrosion and cathodic protection conditions.

6.5.3 Electrochemical monitoring

Table 6.6 illustrates the surface area of the metallic binders according to the volume fraction of the binder on each cermet. The surface areas used to calculate the polarisation resistances (Table 6.7) and the current densities of the studied materials (Table 6.8) in the following sections were considered as the volume concentration of the metallic binder, as the corrosion resistance of the thermal spray coatings, and the sintered hard metals, is determined by the corrosion behaviour of the metallic binder [6.15,6.33]. Monticelli et al [6.15] and Bjordal et al [6.35], have also applied this electrochemical monitoring methodology in their studies on coatings.

Table 6.6 Surface area of the metallic binder on the material specimen and the two segments.

Material	Surface area of the metallic binder (cm^2)		
	Full specimen	**Direct impingement zone**	**Outer area**
UNS S31600	11.34	0.200	11.00
Sintered WC-11Co	2.02	0.036	1.96
Sintered WC-6Ni	1.15	0.020	1.11
HVOF WC-12Co	2.47	0.044	2.40
HVOF WC-10Ni	2.34	0.041	2.27

6.4.3.1 Linear polarisation scans

Figures 6.13 – 6.17 display the linear polarisation scans on the direct impinged zone (DIZ) of each segmented specimen. Figure 6.13 and Figure 6.15 show high current fluctuations that are related to the high concentration of solids that trigger great de-passivation of the passive surface film of the UNS S31600 and WC-6Ni sintered cermet in the direct impinged zone. The re-passivation rates of the WC-6Ni sintered cermet though, are greater compared to that of the stainless steel. Figures 6.14, 6.16 and 6.17 demonstrate a clearly lower tendency, of the two sprayed coatings and the sintered WC-11Co, to form any passive film. There is a common characteristic between these linear polarisation figures, as the 5mins scan is displaced from these of the other time-interval scans. This implies that the electrode potential is not stabilised within the first 5mins of the scan. In contrast, the scans at times of 30mins and later were similar for each tested material. Hence, the corrosion rates are considered to be constant during the 2 h of the impingement tests.

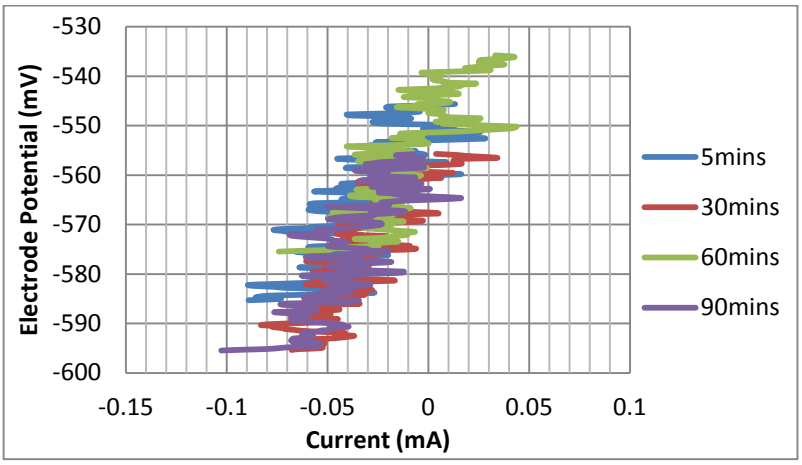

Figure 6.13 Linear polarisation scans on the direct impinged zone of the UNS S31600 in solid/liquid impingement.

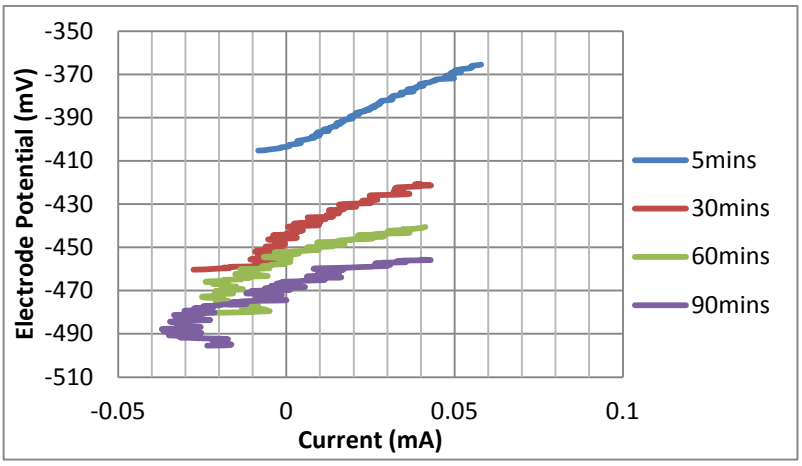

Figure 6.14 Linear polarisation scans on the direct impinged zone of the sin WC-11Co in solid/liquid impingement.

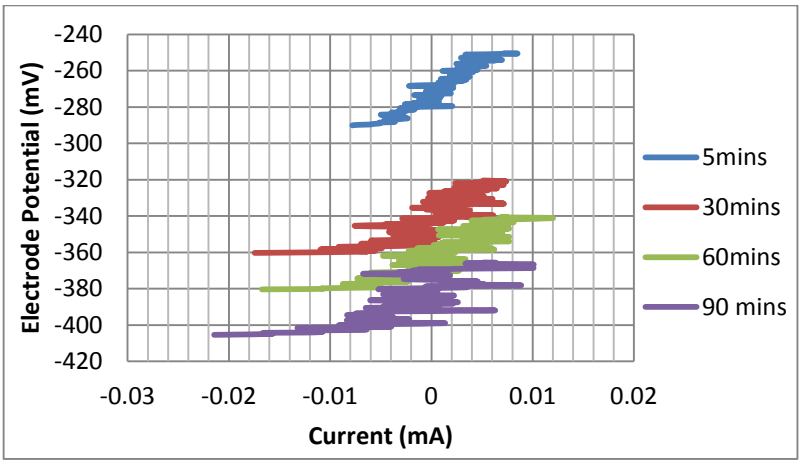

Figure 6.15 Linear polarisation scans on the direct impinged zone of the sin WC-6Ni in solid/liquid impingement.

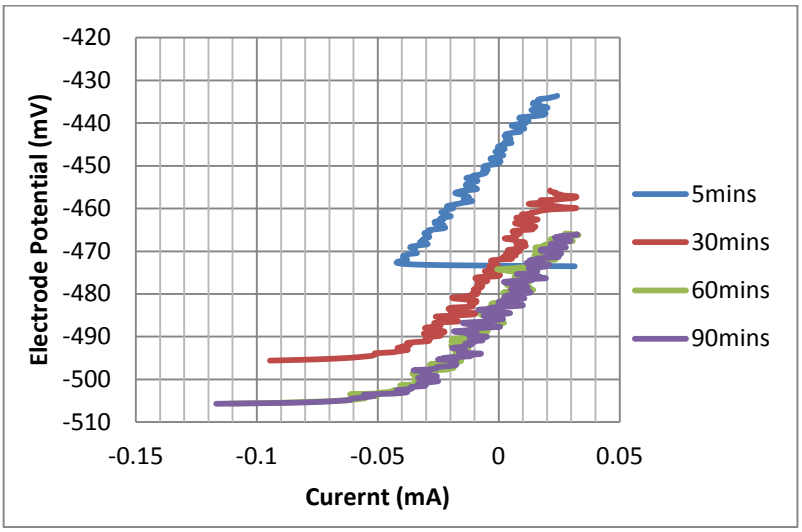

Figure 6.16 Linear polarisation scans on the direct impinged zone of the HVOF sprayed WC-12Co in solid/liquid impingement.

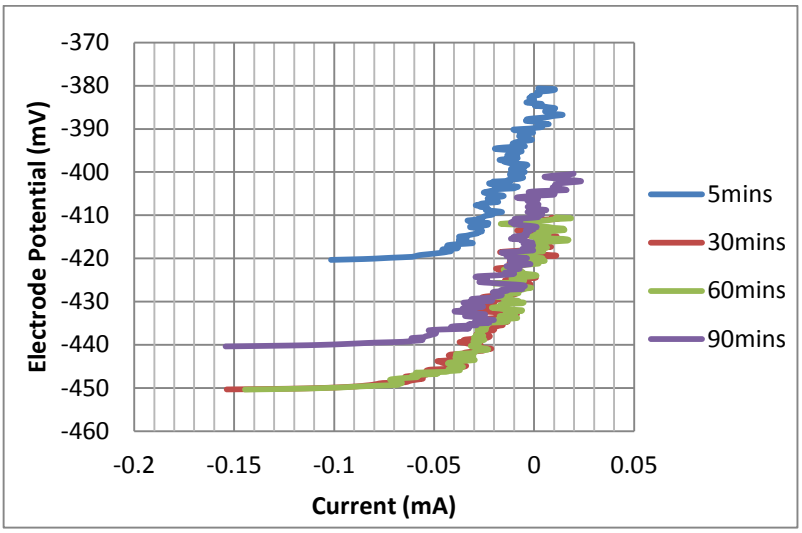

Figure 6.17 Linear polarisation scans on the direct impinged zone of the HVOF sprayed WC-10Ni in solid/liquid impingement.

Figure 6.18 – 6.22 illustrate the linear polarisation scans in the outer area (OA) of the specimen. The polarisation resistance is higher, which indicates a lower corrosion rate, due to the lower severity of the slurry in this region compared with the direct impinged zone. The fluctuations in the currents are evidence of attempts of the UNS S31600 and sintered WC-6Ni cermet to form passive films. On the other hand, the two HVOF sprayed coatings and the sintered WC-11Co appear to maintain active behaviour also in the outer zone.

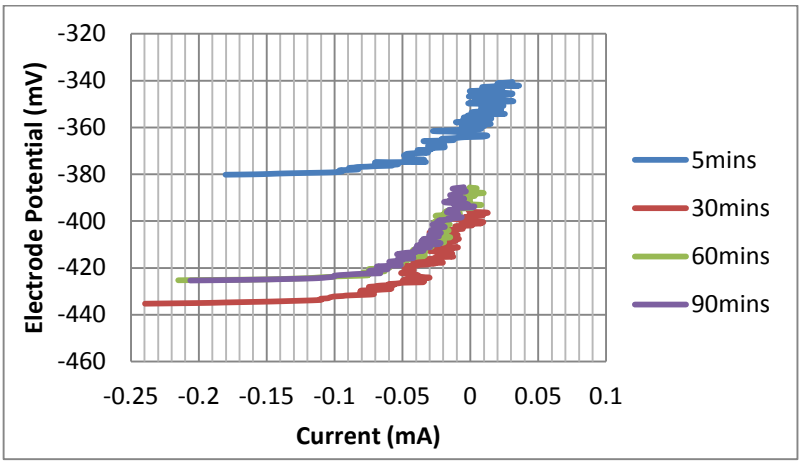

Figure 6.18 Linear polarisation scans on the outer area zone of the UNS S31600 in solid/liquid impingement.

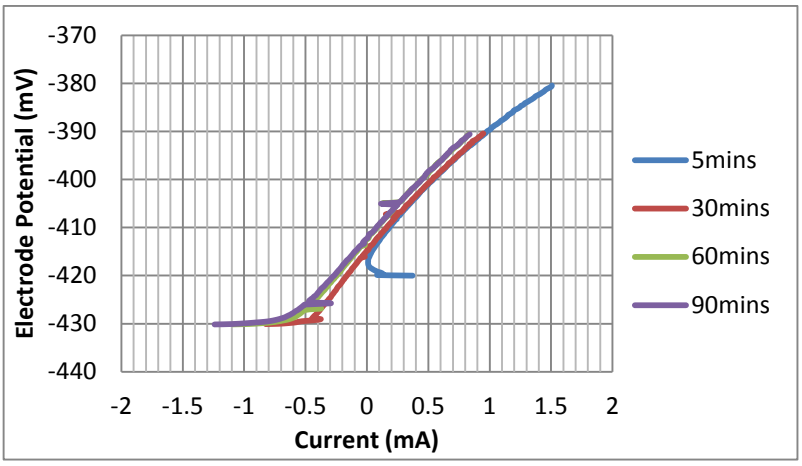

Figure 6.19 Linear polarisation scans on the outer area of the WC-11Co sintered in solid/liquid impingement.

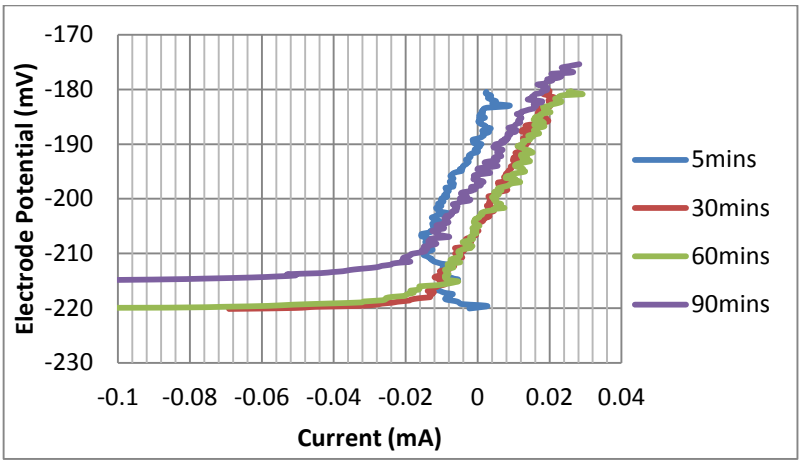

Figure 6.20 Linear polarisation scans on the outer area of the WC-6Ni in solid/liquid impingement.

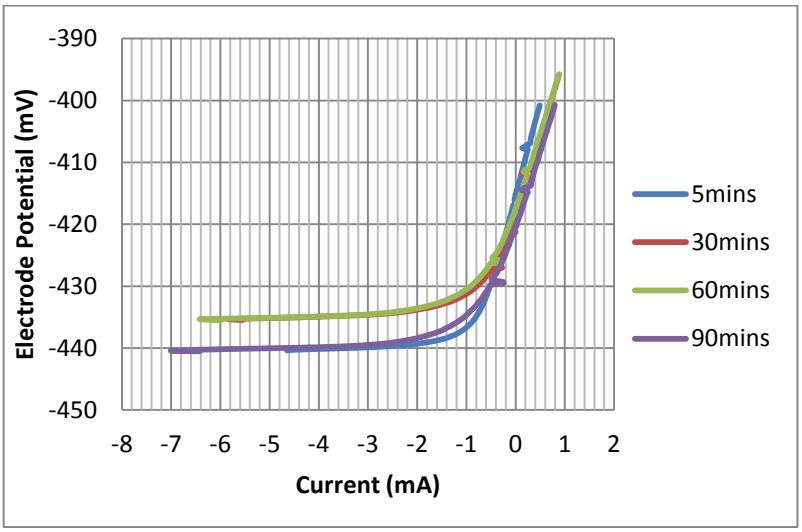

Figure 6.21 Linear polarisation scans on outer area of the HVOF sprayed WC-12Co in solid/liquid impingement.

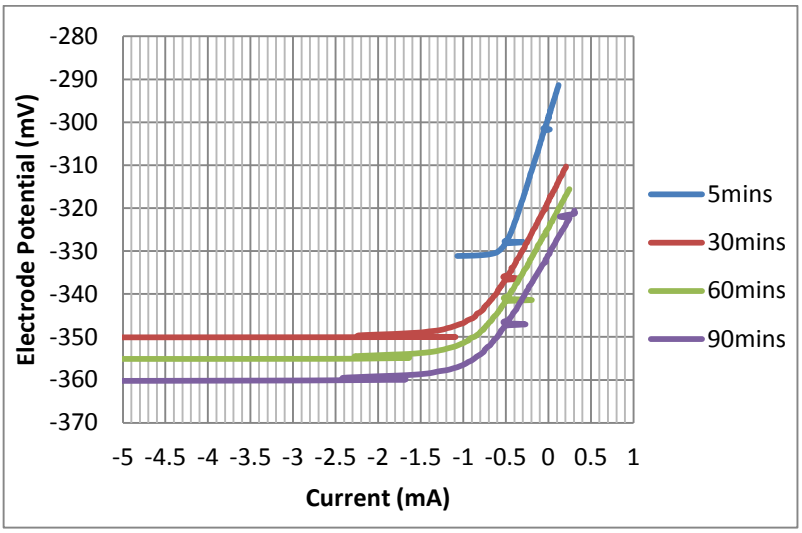

Figure 6.22 Linear polarisation scans on the outer area of the HVOF sprayed WC-10Ni in solid/liquid impingement.

Table 6.7 illustrates the normalised polarisation resistances in the form of unit surface area of both scanned regions of the segmented specimen, as illustrated in Table 6.6. Since the polarisation resistance is inversely proportional to the corrosion current, it is apparent that the direct impinged zone is experiencing a high corrosion rate, whereas the outer area is subjected to a much lower corrosion rate. Two groups of materials are evident; the WC-6Ni and UNS S31600 which display good corrosion resistance and the two HVOF sprayed coatings with the WC-11Co sintered cermet which exhibit relatively poor corrosion resistance.

Table 6.7 Polarisation resistances according to the surface areas of the segments of the comparative materials.

Material	Polarisation Resistance R_p (Ω*cm^2)	
	Direct Impinged Zone	**Outer Area**
UNS S31600	101	5500
Sin WC-11Co	12	52
Sin WC-6Ni	98	798
HVOF WC-12Co	29	45
HVOF WC-10Ni	32	68

6.5.3.2 Potentiodynamic scans

Figures 6.23 – 6.27 illustrate the anodic polarisation of each comparative material on the direct impinged zone and on the outer area, considering the surface areas illustrated in Table 6.6. The normalised potential represents the electrode potential of at least 25mV more negative to E_{corr} and it has been utilised for a more effective comparison, since the E_{corr} values are different between the two specimen regions.

The current density fluctuations on UNS S31600 and WC-6Ni follow the same trend as shown at the linear polarisations scans in both regions. Conversely, the two sprayed coatings and the sintered WC-11Co sintered cermet corrode actively in both regions with limited evidence of current density fluctuation. A notable feature is the very similar plots in the two zones of the two HVOF coatings.

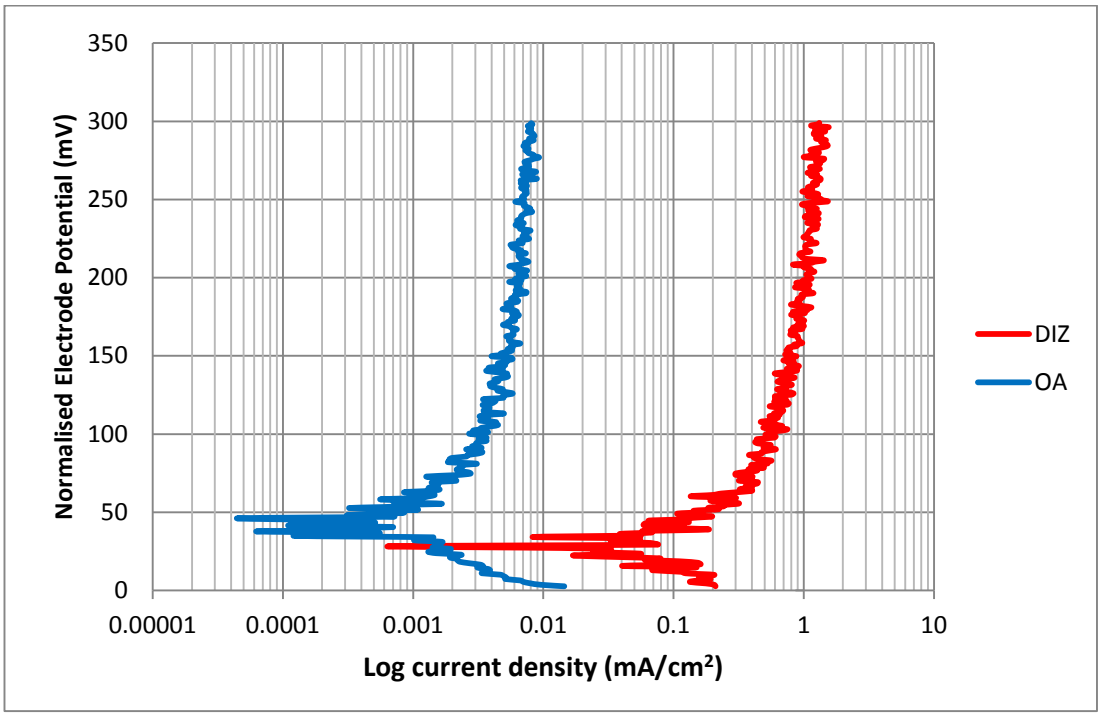

Figure 6.23 Anodic polarisation scans on both segments of UNS S31600 in solid/liquid impingement.

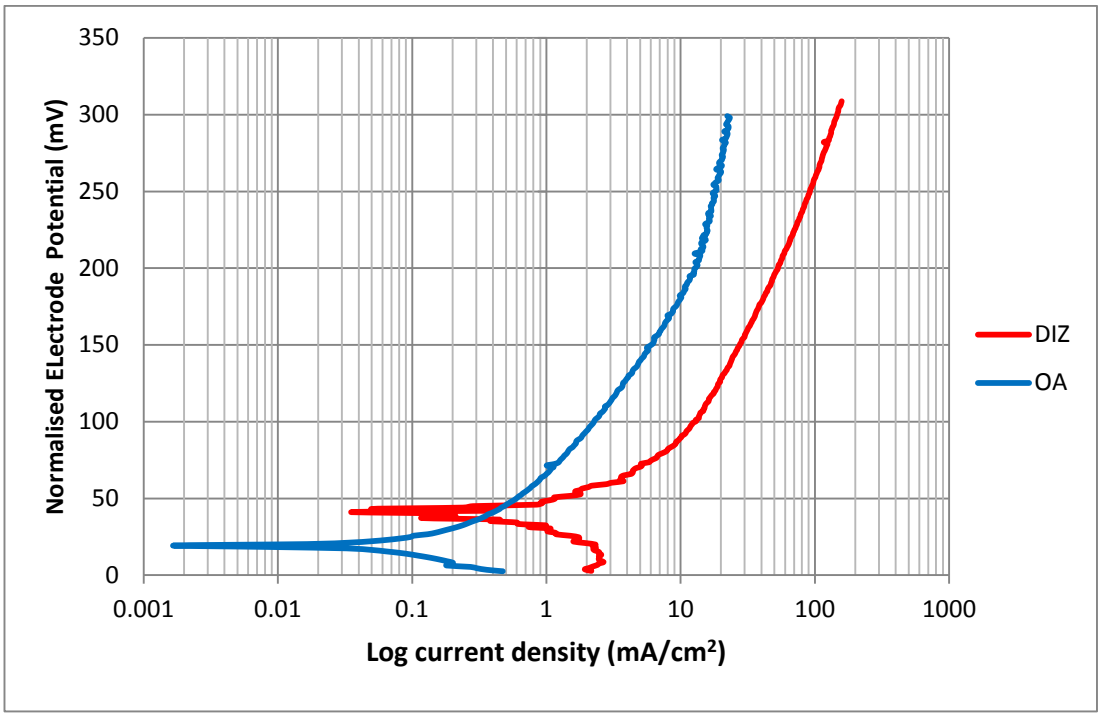

Figure 6.24 Anodic polarisation scans on both segments of WC-11Co sintered cermet in solid/liquid impingement.

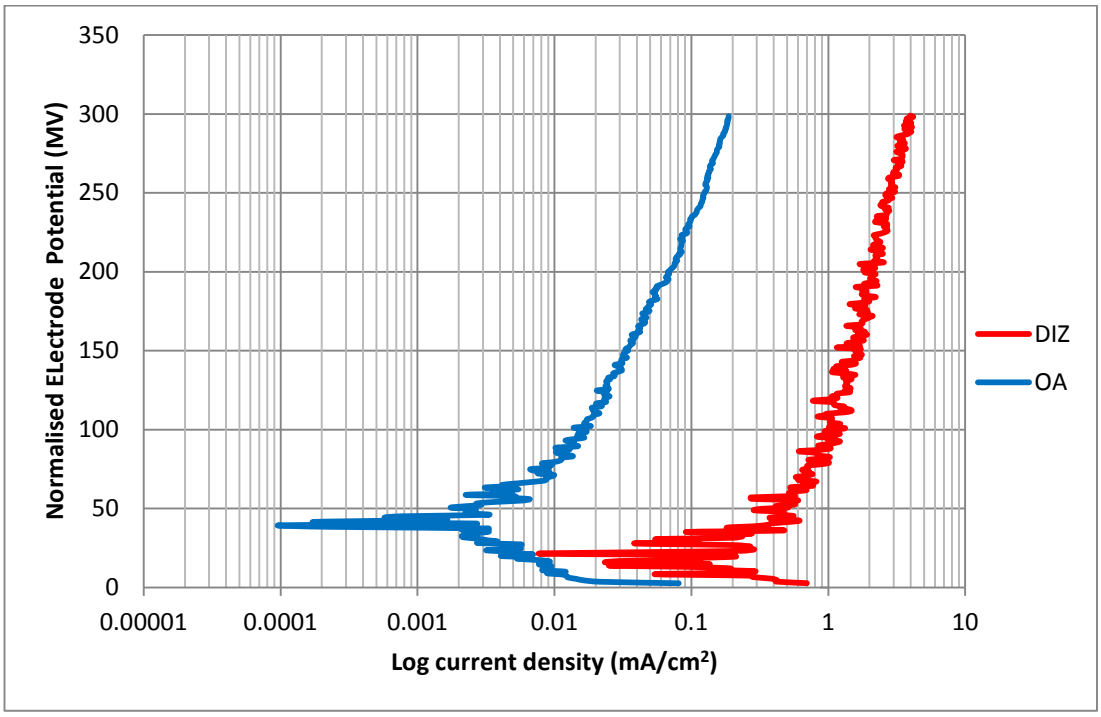

Figure 6.25 Anodic polarisation scans on both segments of the WC-6Ni sintered cermet in solid/liquid impingement.

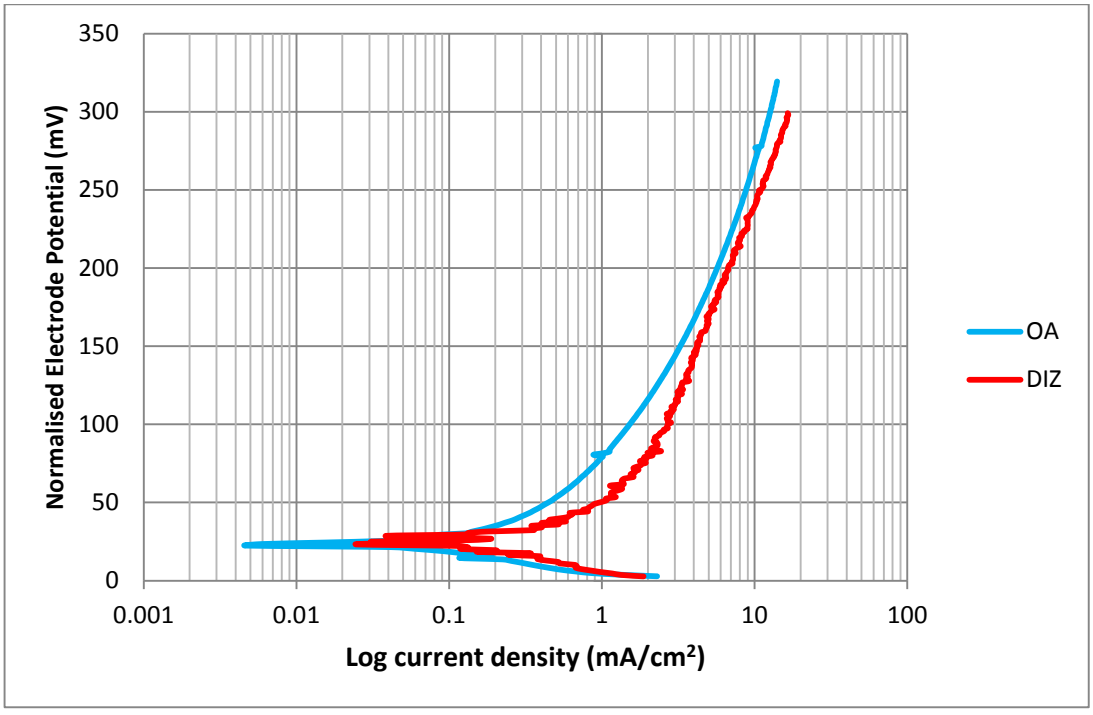

Figure 6.26 Anodic polarisation scans on both segments of HVOF sprayed WC-12Co in solid/liquid impingement.

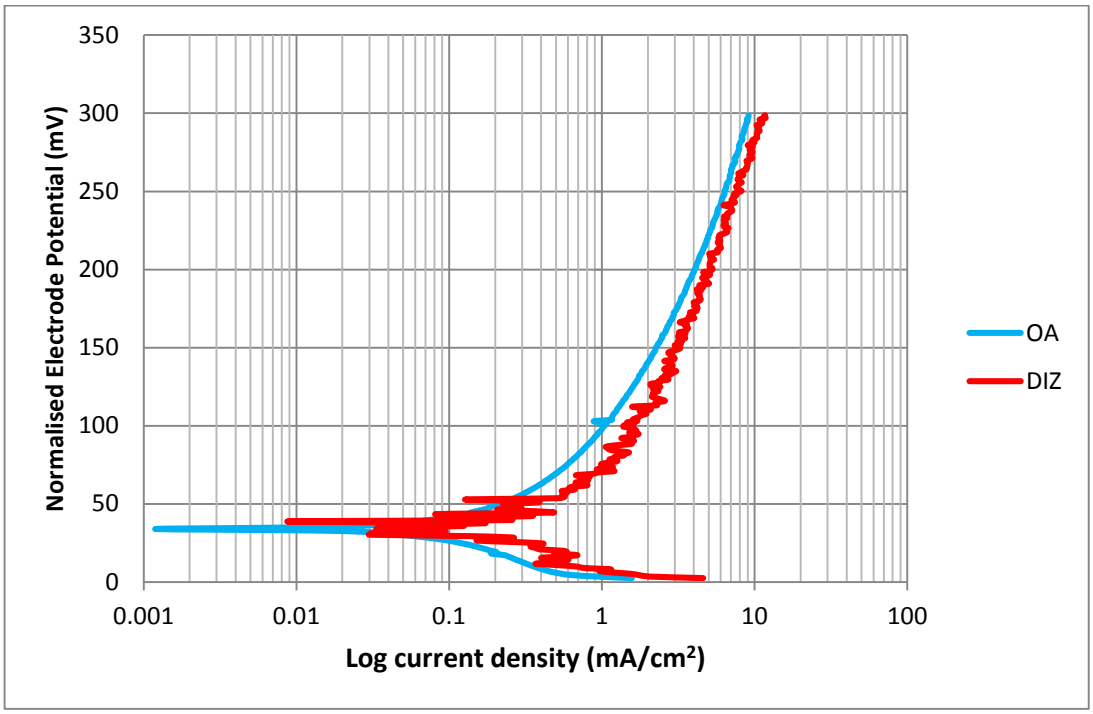

Figure 6.27 Anodic polarisation scans on both segments of HVOF sprayed WC-10Ni in solid/liquid impingement.

Table 6.8 shows free erosion-corrosion potentials (E_{corr}) and the measured corrosion current densities of each region, by taking into consideration the different surface areas of each material, through Tafel extrapolation by plotting a straight line from the average of the oscillating currents. The mass losses due to corrosion were also calculated with the use of Faraday's law (See 2.3.7.2). Similar trends to those observed with the polarisation resistances, were evident in respect of corrosion current densities in both the direct impinged zone and the outer area. In more detail, the UNS S31600 and the WC-6Ni sintered cermet displayed superior corrosion resistance compared with the two sprayed coatings and the sintered WC-11Co cermet.

Figure 6.28 illustrates the anodic polarisation scans on the full specimen (38mm diameter) after 30 minutes of impingement, as the corrosion rates were steady after this period. Again the normalised electrode potential represents the value of at least 25mV more negative to E_{corr}. There are two distinct groups of materials; the high corrosion resistant materials (WC-6Ni sintered cermet and UNS S31600) and the low corrosion resistance materials (HVOF sprayed coatings and WC-11Co sintered cermet). Table 6.9 shows the free erosion-corrosion potentials (E_{corr}), the generated corrosion current densities by the Tafel extrapolations estimations and the surface areas shown in Table 6.6,

along with the mass loss due to corrosion for the full specimen of each comparative material.

Table 6.8 E_{corr} values and corrosion rates on both areas of the segmented electrodes.

Material	Direct impingement area			Outer area		
	E_{corr} (mV)	Corrosion Current density (mA/cm²)	Mass loss due to corrosion (mg)	E_{corr} (mV)	Corrosion Current density (mA/cm²)	Mass loss due to corrosion (mg)
UNS S31600	-546	0.3	0.12	-374	0.002	0.04
Sin WC-11Co	-471	4.9	0.4	-413	0.397	1.72
Sin WC-6Ni	-384	0.3	0.01	-139	0.003	0.01
HVOF WC-12Co	-482	1.4	0.13	-423	0.621	3.30
HVOF WC-10Ni	-409	0.7	0.07	-337	0.318	1.58

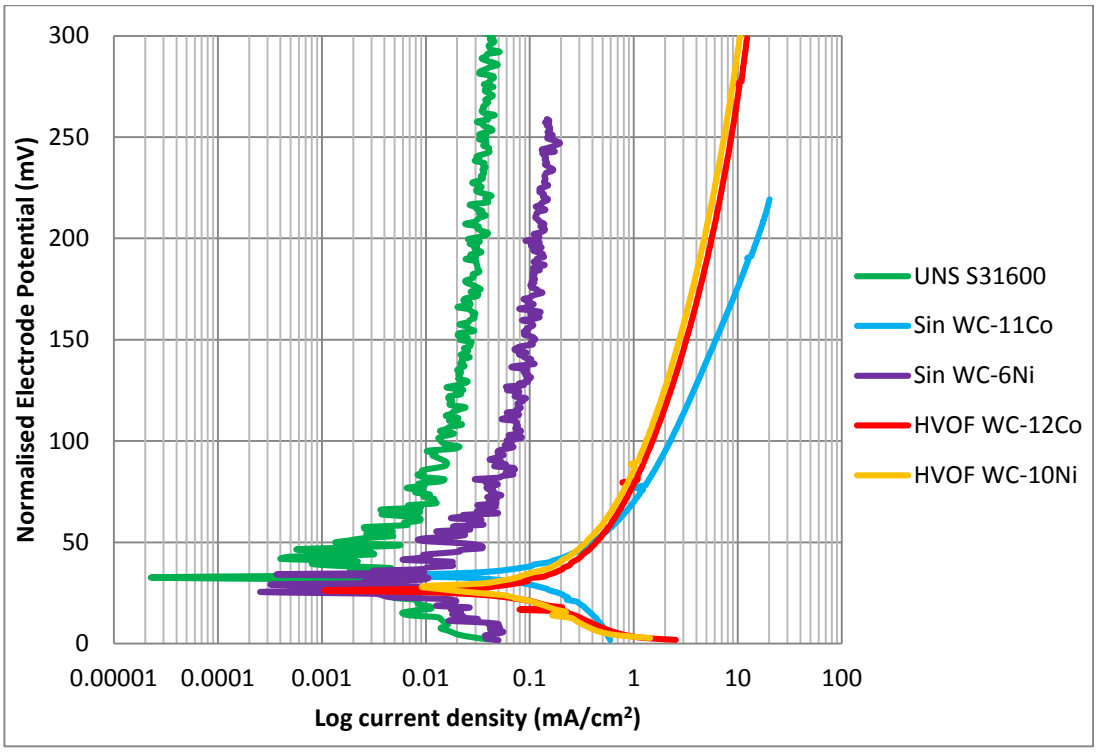

Figure 6.28 Anodic polarisation scans on the full specimen of each comparative material in solid/liquid impingement.

Table 6.9 E_{corr} values and corrosion rates of the full specimen of each material.

Material	E_{corr} (mV)	Corrosion current density (mA/cm^2)	Mass loss due to corrosion (mg)
UNS S31600	-464	0.01	0.24
Sin WC-11Co	-410	0.50	2.21
Sin WC-6Ni	-225	0.03	0.08
HVOF WC-12Co	-424	0.44	2.41
HVOF WC-10Ni	-344	0.40	2.05

6.5.4 Post-test examination

6.5.4.1 Visual examination

Figures 6.29 – 6.33 show the surface of each tested material under free erosion-corrosion and cathodic protection conditions. It is evident that the UNS S31600, the sintered WC-6Ni and the HVOF WC-10Ni materials possessed superior corrosion resistance, as there are no signs of corrosion products. On the other hand, the sintered WC-11Co, as well as the sprayed WC-12Co, experienced extensive corrosion-related attack during free erosion-corrosion, as their post-test surface was heavily degraded. Under cathodic protection conditions though, the diamond polishing marks are still apparent on their post-test surface adjacent to the wear scar.

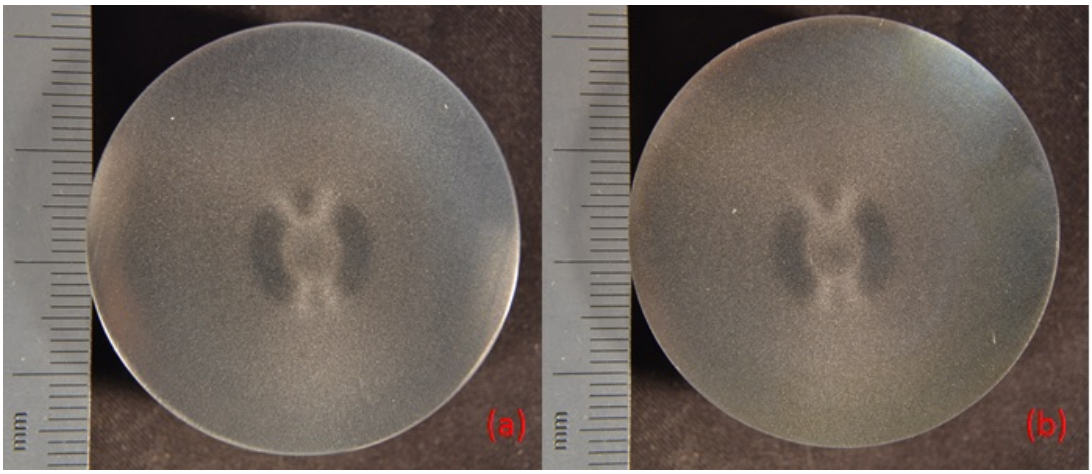

Figure 6.29 Surface of the UNS S31600 after 2h solid/liquid impingement a) under free erosion-corrosion conditions, b) cathodically protected.

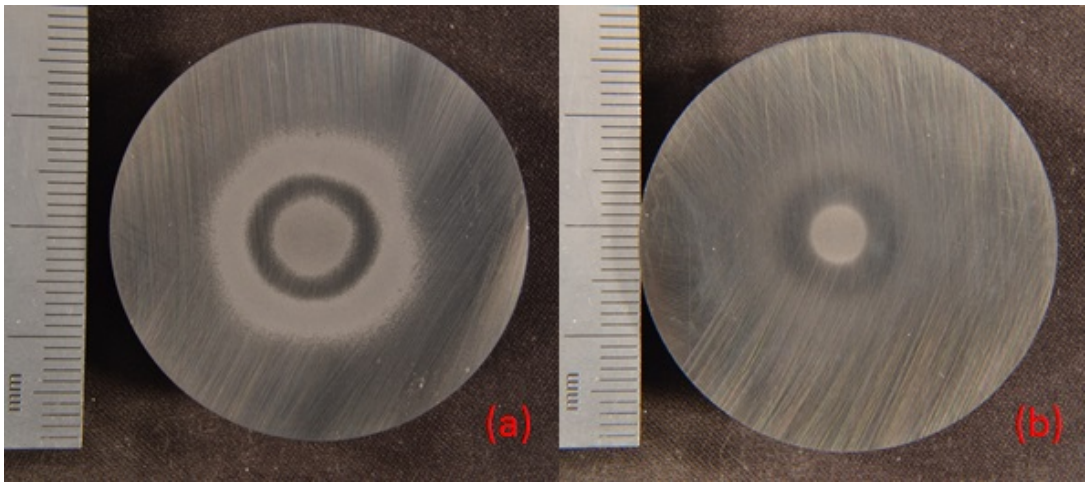

Figure 6.30 Surface of the WC-12Co sintered after 2h solid/liquid impingement a) under free erosion-corrosion conditions, b) cathodically protected.

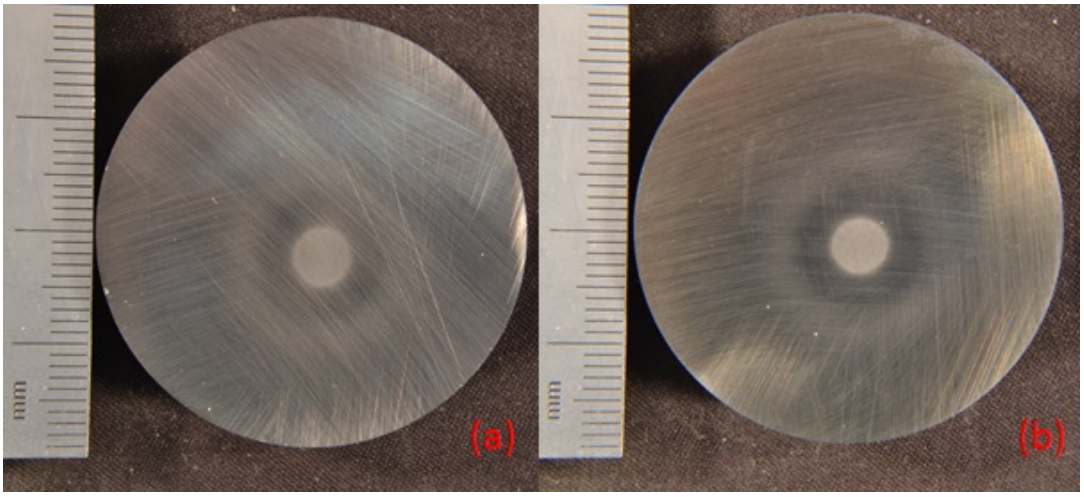

Figure 6.31 Surface of the WC-6Ni sintered after 2h solid/liquid impingement a) under free erosion-corrosion conditions, b) cathodically protected.

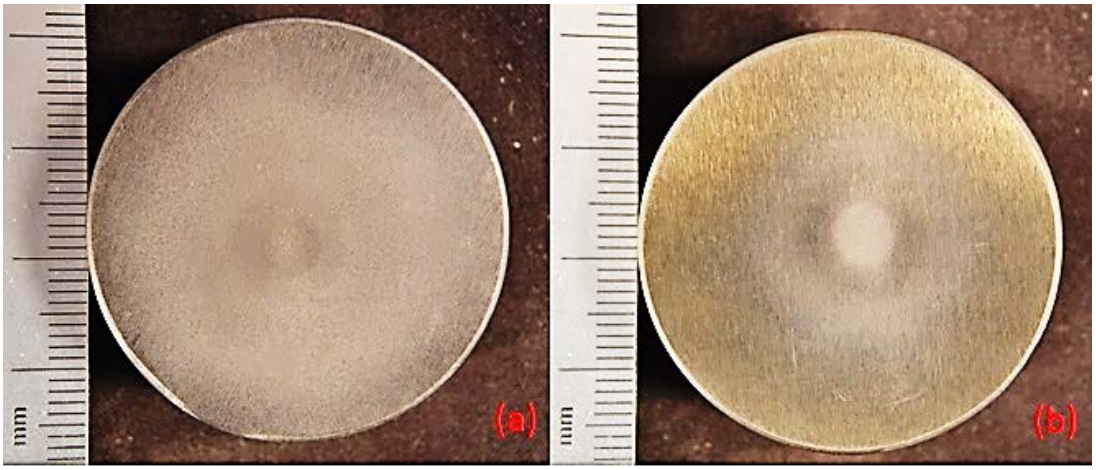

Figure 6.32 Surface of the HVOF sprayed WC-12Co after 2h solid/liquid impingement a) under free erosion-corrosion conditions, b) cathodically protected.

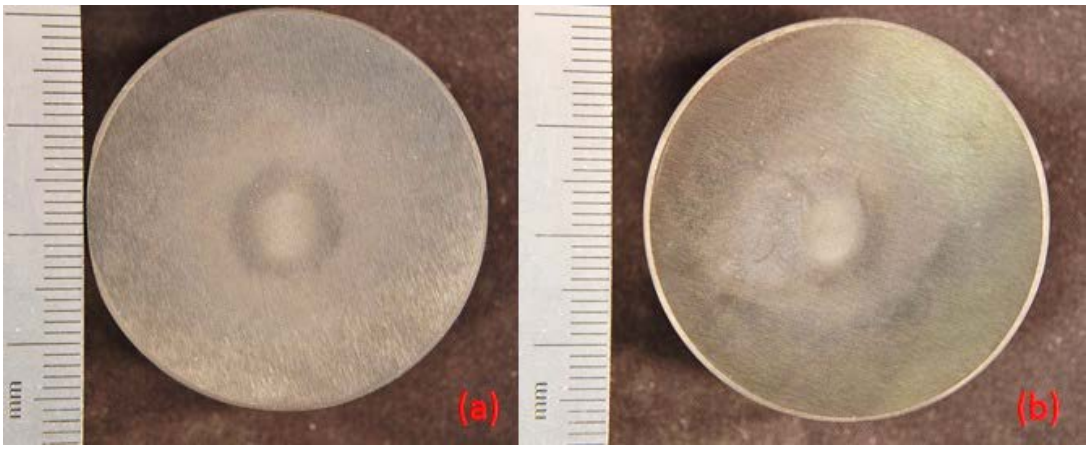

Figure 6.33 Surface of the HVOF sprayed WC-10Ni after 2h solid/liquid impingement a) under free erosion-corrosion conditions, b) cathodically protected.

6.5.4.2 Scanning Electron Microscope (SEM) Imaging in cermets

Figures 6.34 – 6.41 show SEM images of the direct impinged zone and the outer area with and without cathodic protection for the tested cermets. There is a common feature in the direct impinged zone as the WC grains experience cracking in all tested samples. This characteristic is likely to be associated with the size of the impinging particles, which is 100 times higher than the WC grains, and their extremely high kinetic energy under the jet that exceeded the tensile strength of the carbides.

Under free erosion-corrosion conditions, preferential corrosion of the binder was apparent, which resulted in the loss of the mechanical support on the carbides. Thereafter, the carbides were standing proud, being more susceptible to cracking and subsequent removal. Similar features were evident in the outer area, especially for the Co-binder cermets, but with less to negligible cracking of carbides. The sintered WC-6Ni was exempted of this attribute as it showed negligible corrosion related damage in both direct impinged zone and outer area. The application of the cathodic protection protected substantially the microstructure in both areas and more significant in the outer area, where the diamond polishing marks were still apparent after solid/liquid impingement.

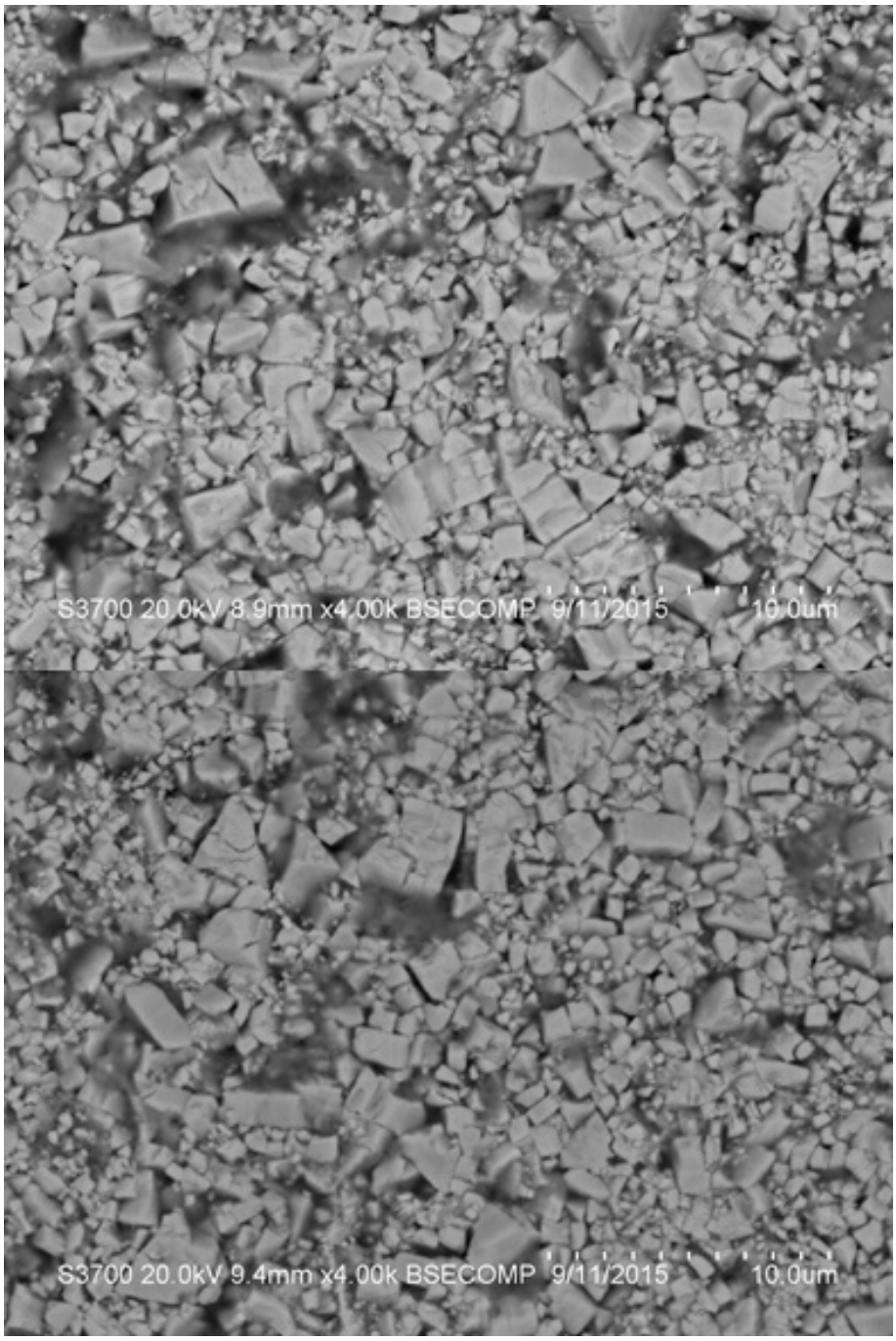

Figure 6.34 SEM images of the post- test structure of sintered WC-11Co; direct impinged zone under free erosion corrosion (top) and with cathodic protection (bottom).

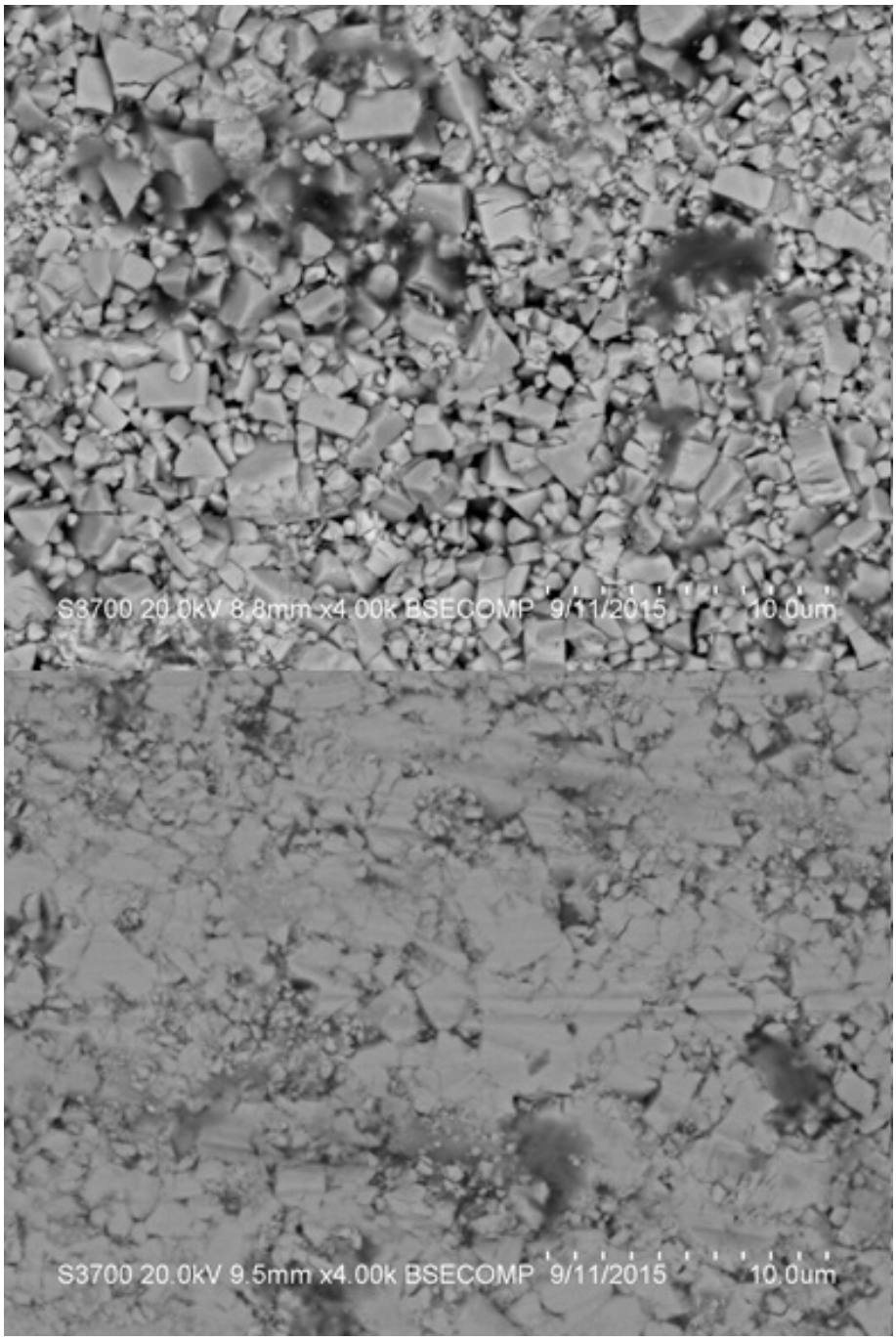

Figure 6.35 SEM images of the post- test structure of sintered WC-11Co; outer area under free erosion corrosion (top) and outer area with cathodic protection (bottom).

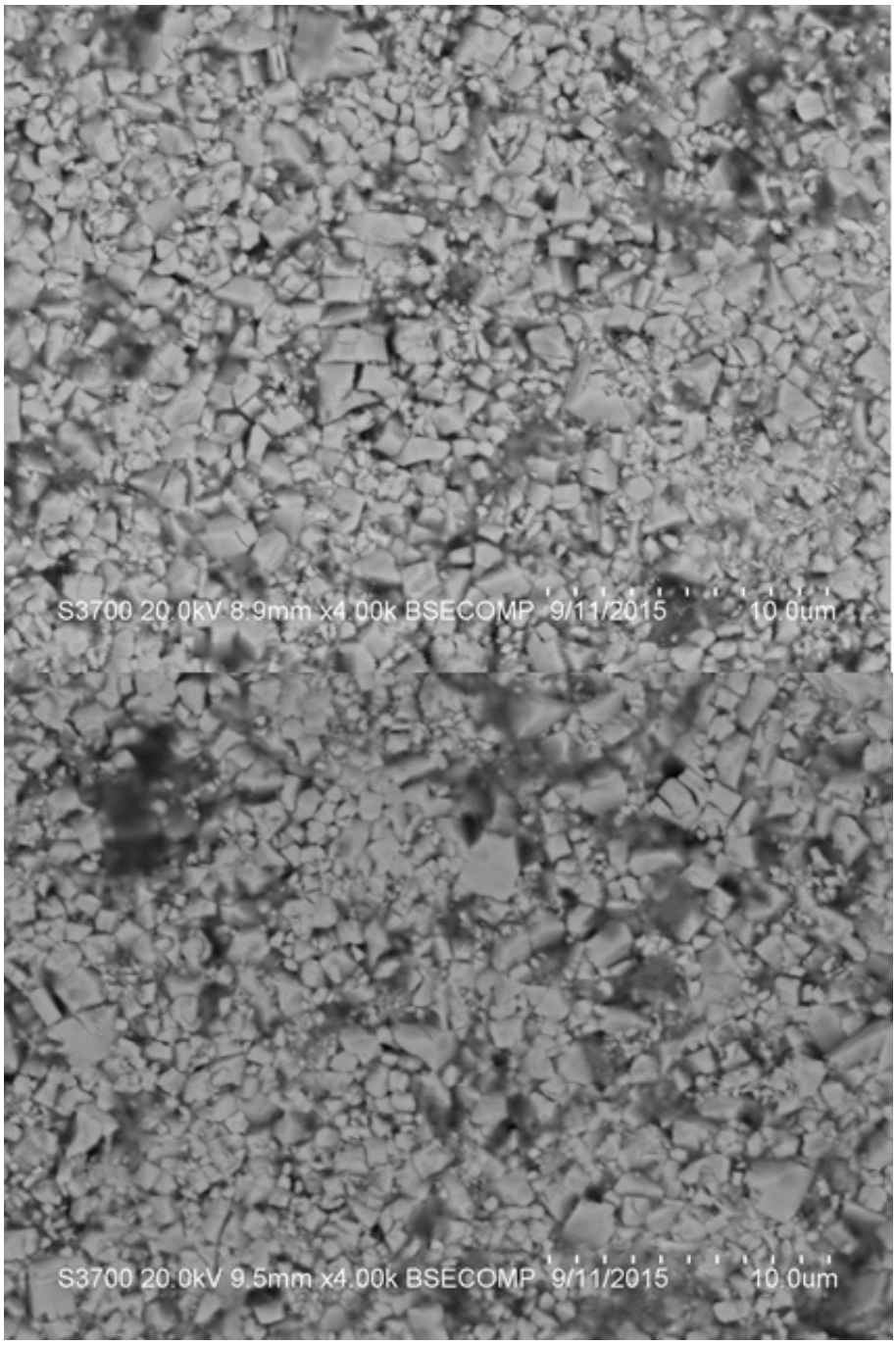

Figure 6.36 SEM images of the post- test structure of sintered WC-6Ni; direct impinged zone under free erosion corrosion (top) and with cathodic protection (bottom).

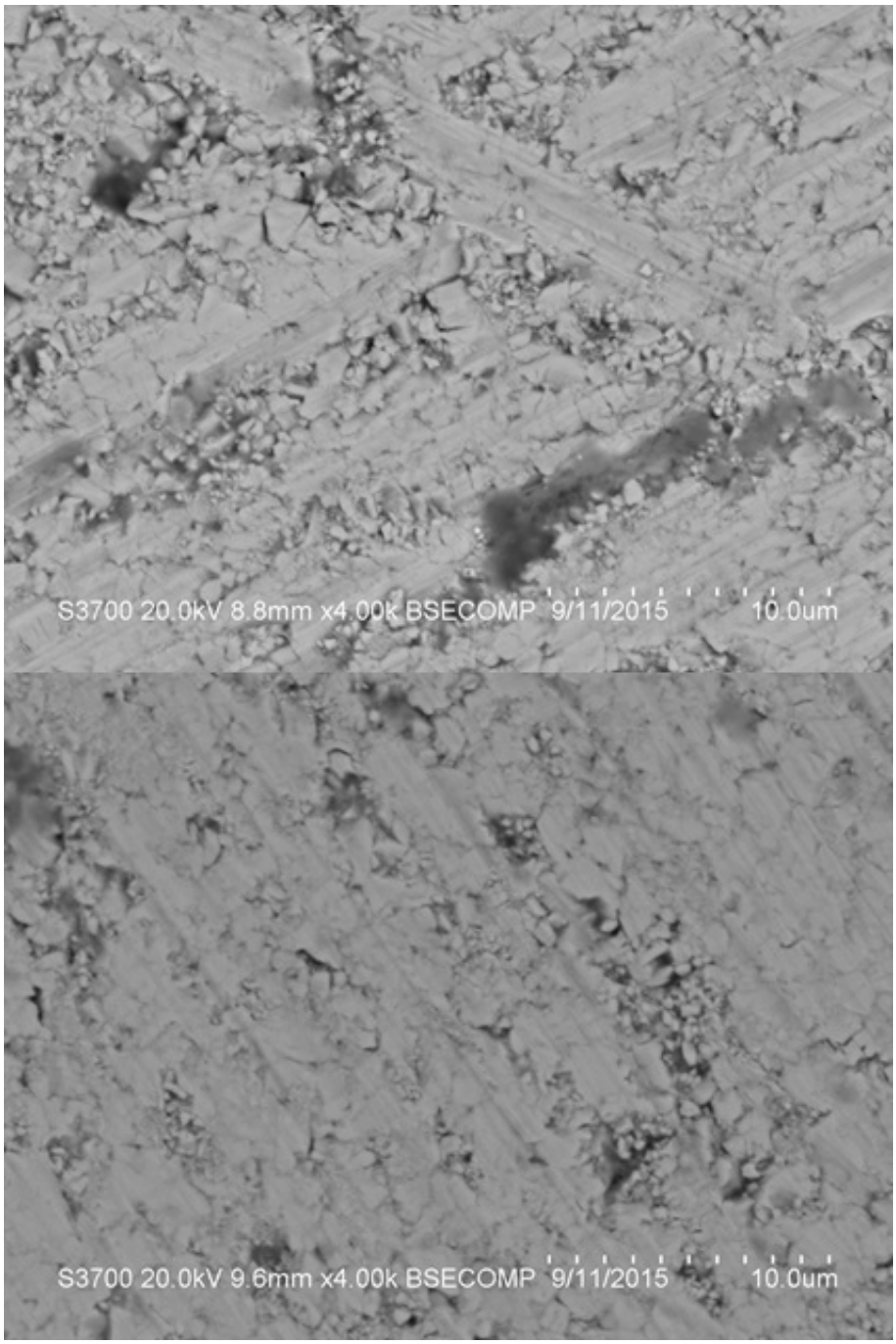

Figure 6.37 SEM images of the post- test structure of sintered WC-6Ni; outer area under free erosion corrosion (top) and outer area with cathodic protection (bottom).

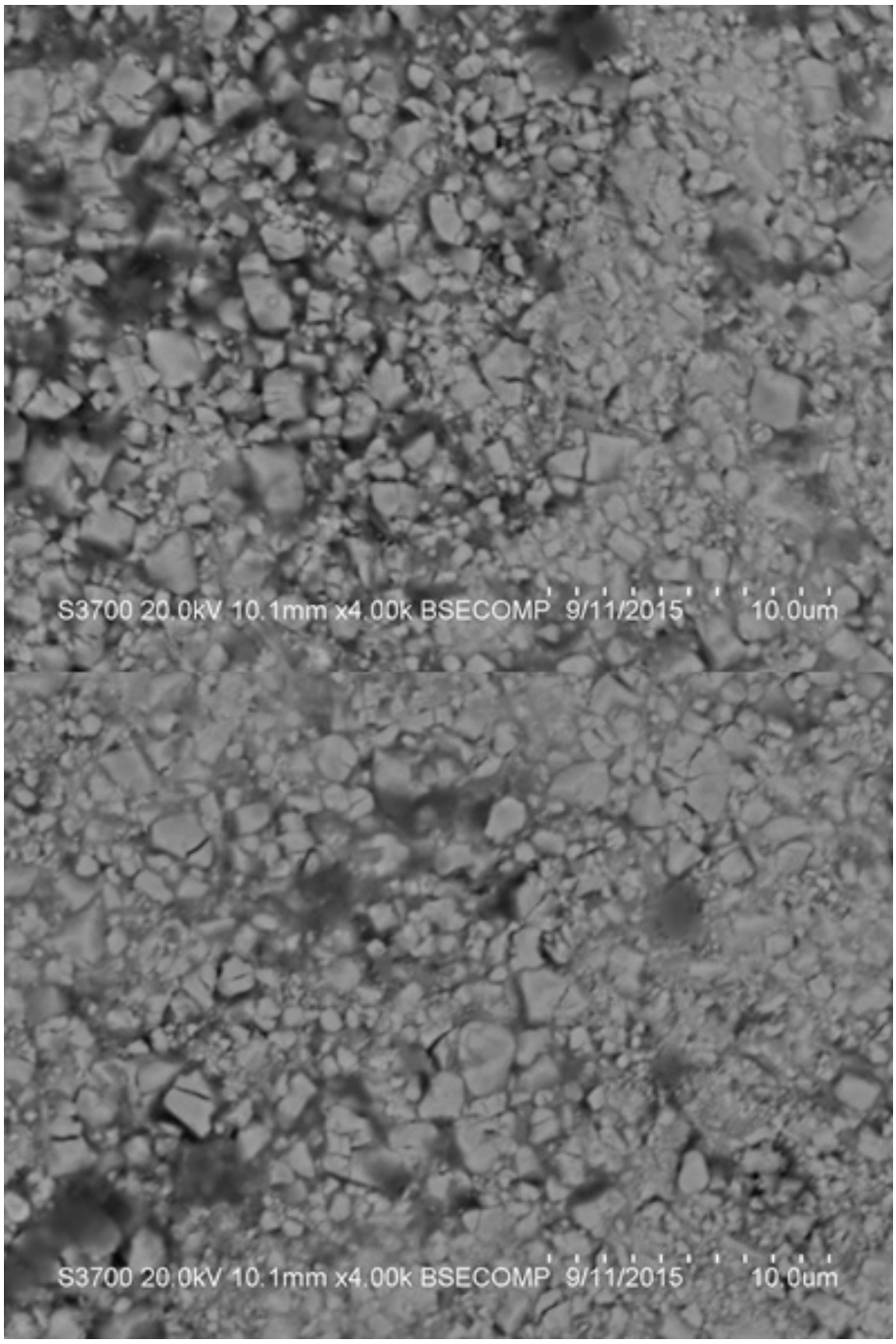

Figure 6.38 SEM images of the post- test structure of HVOF WC-12Co; direct impinged zone under free erosion corrosion (top) and with cathodic protection (bottom).

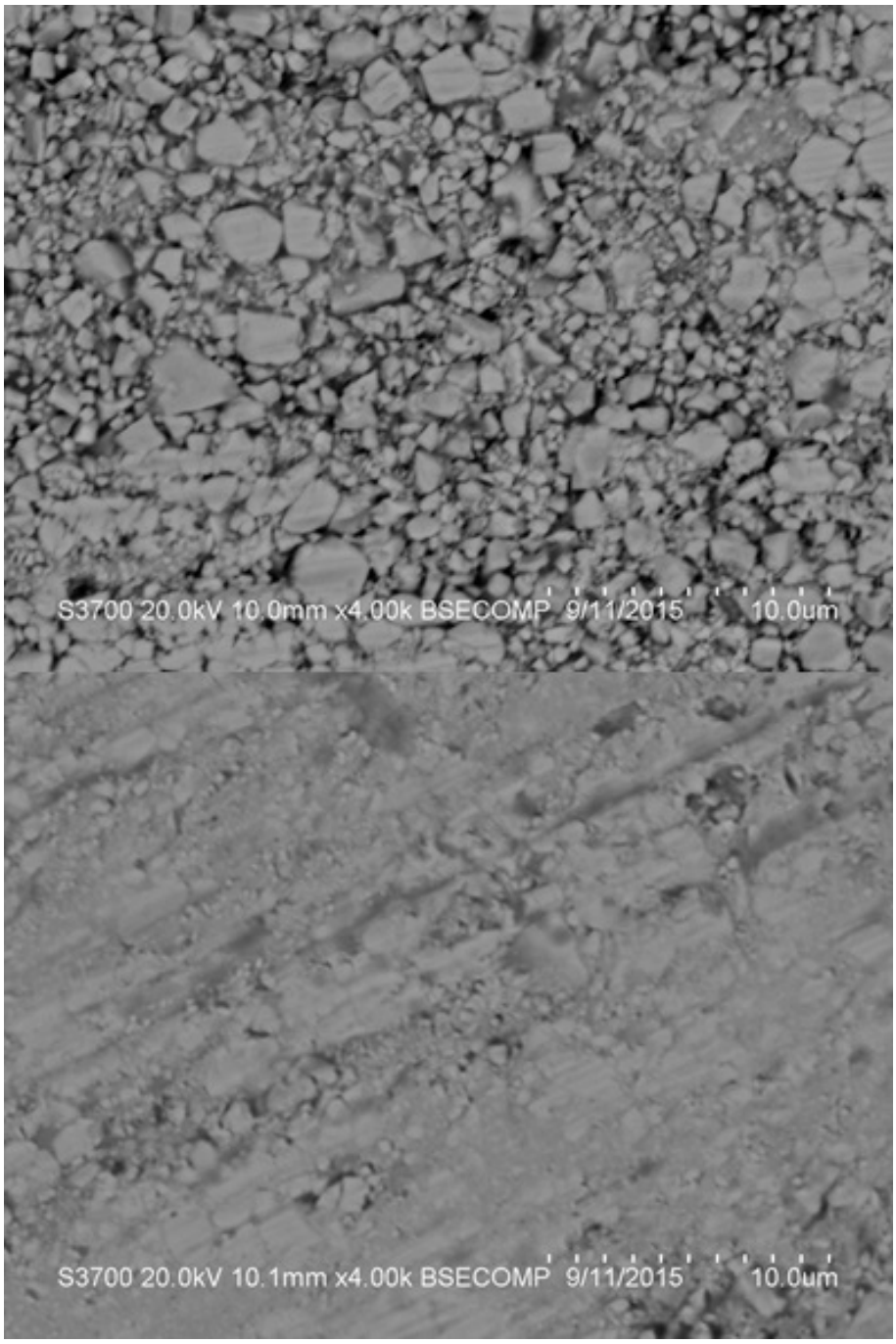

Figure 6.39 SEM images of the post- test structure of HVOF WC-12Co; outer area under free erosion corrosion (top) and with cathodic protection (bottom).

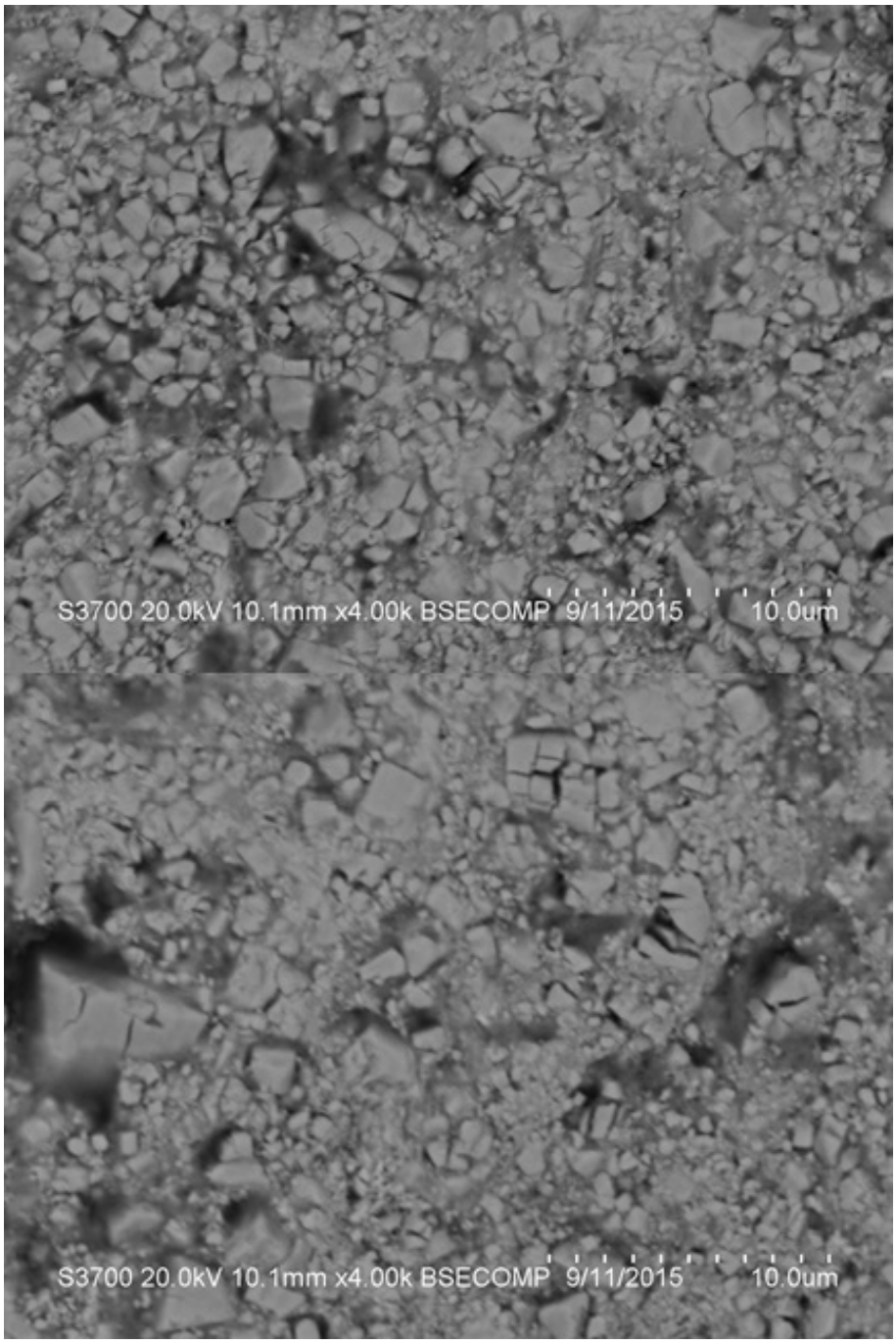

Figure 6.40 SEM images of the post- test structure of HVOF WC-10Ni; A) direct impinged zone under free erosion corrosion (top) and with cathodic protection (bottom).

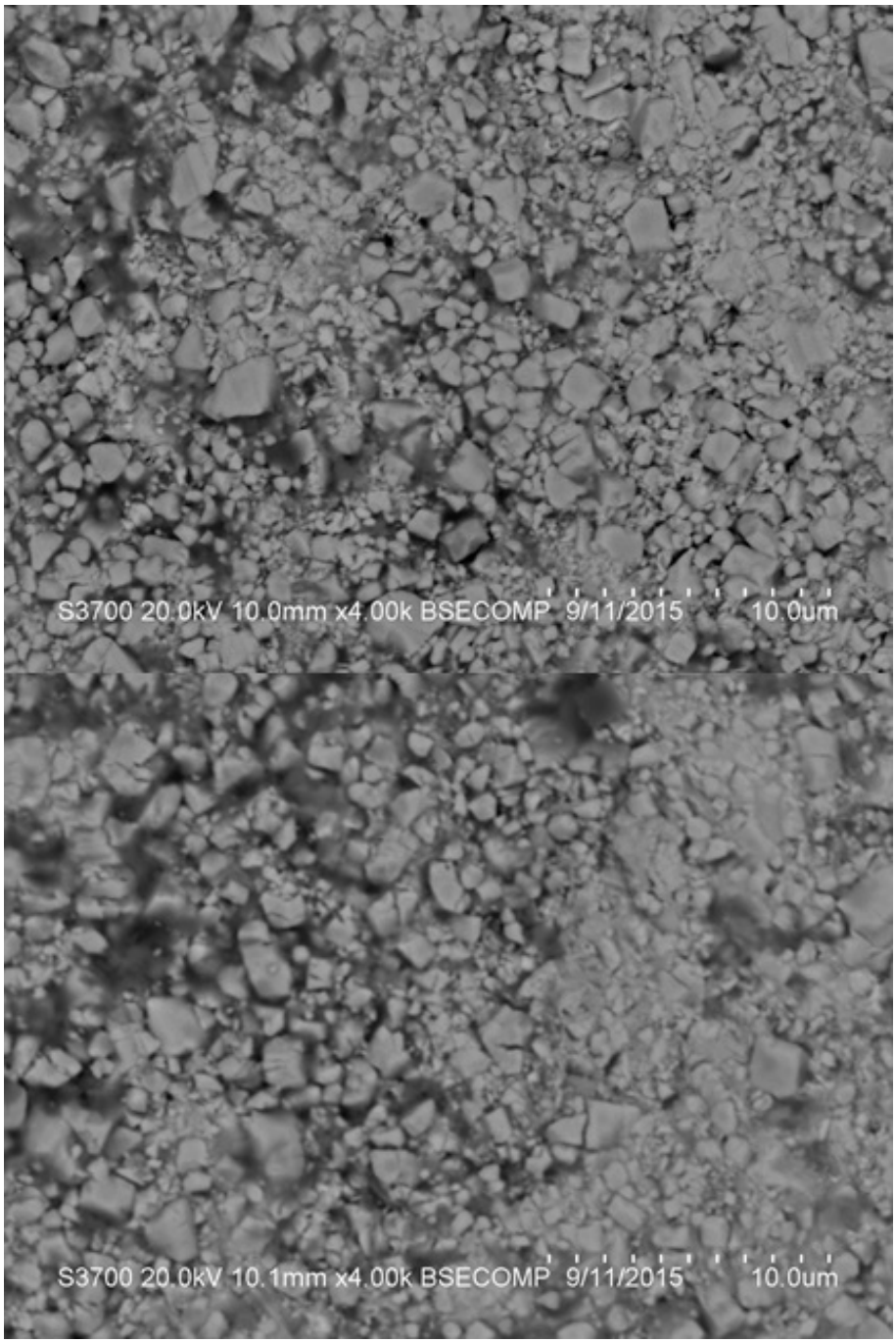

Figure 6.41 SEM images of the post- test structure of HVOF WC-10Ni; outer area under free erosion corrosion (top) and with cathodic protection (bottom).

6.5.4.3 Surface roughness

Surface roughness measurements were undertaken to reveal the effect of erosion corrosion in different surface regions. The areas of interest are shown in Figure 6.42.

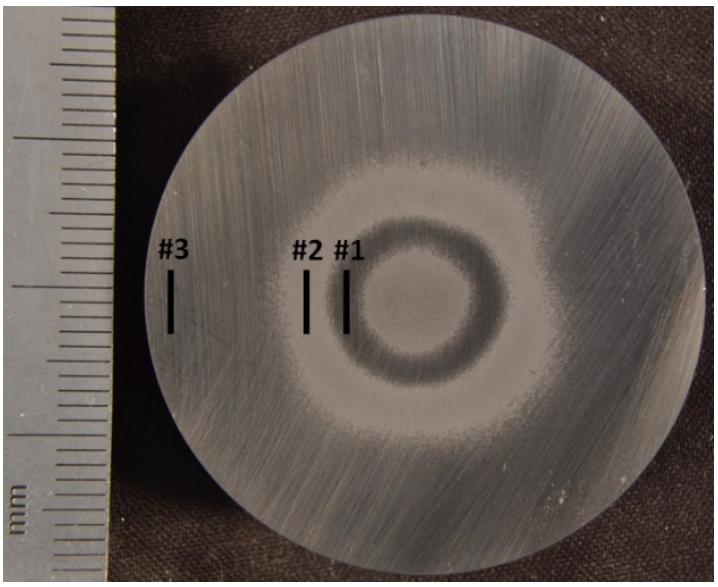

Figure 6.42 Representation of the line roughness scans in the three different regions of the post-test outer area of the sintered WC-11Co cermet. (#1- Area adjacent to the wear scar, #2- Outermost area, #3- Near the edge)

Figure 6.43 illustrates an effective way to investigate any difference in the surface morphology when erosion-corrosion or pure erosion is apparent. The UNS S31600 stainless steel was worn (roughened) adjacent to the wear scar and the outermost area in both free erosion-corrosion and cathodic protection conditions. The minor change in roughness values of the UNS S31600 in the near edge region was due to the fact that less abrasive particles would scratch the stainless steel surface as the kinetic energy becomes lower. The WC-11Co sintered cermet had substantially high surface roughness on the outermost area, as also shown in Figure 6.42. This is associated with the corrosion-related component because the cathodically protected specimens show similar roughness as that in the as-received state. The HVOF WC-12Co coating experienced similar traits with the sintered WC-11Co cermet, however, the area adjacent to the wear scar (i.e. Area #1) was also deteriorated by the corrosion-related component under free erosion-corrosion conditions. On the other hand, the Ni binder cermets displayed low discrepancies in roughness between the as-received state and the post-test surface.

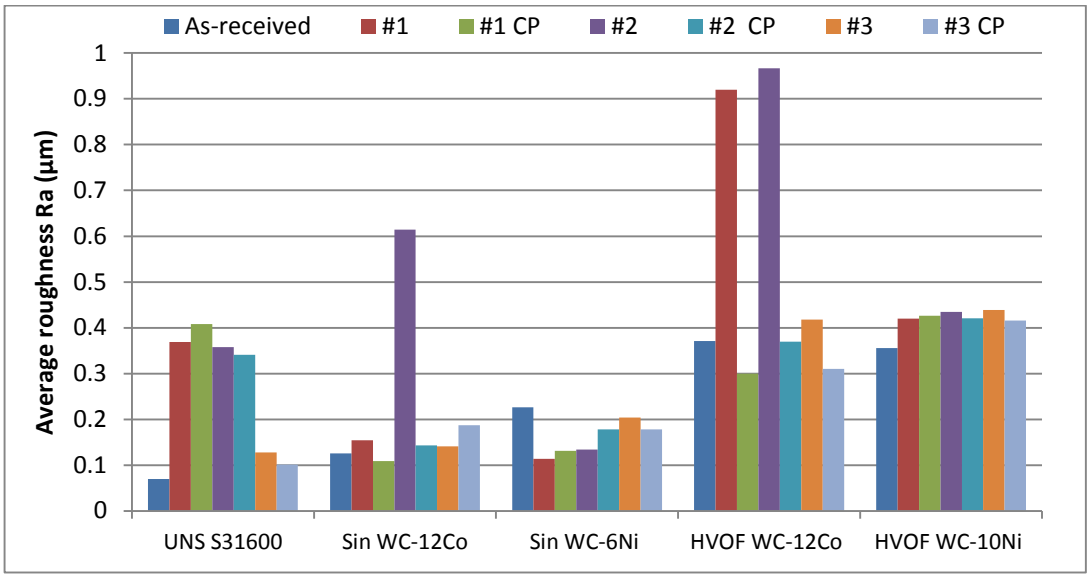

Figure 6.43 Ra values at different areas of the tested coupons of each material. (#1- Area adjacent to the wear scar, #2- Outermost area, #3- Near the edge**)**

6.5.4.4 Surface profile scans

Surface profile scans were performed on the wear scar of each specimen to broaden the evaluation of the deterioration mechanisms occurring in the zone directly under the impinging jet. Figure 6.44 shows an example of the wear scar profile scans of the UNS S31600 stainless steel under free erosion-corrosion and cathodic protection. It is evident, that there is erosion domination on the wear scar of the stainless steel.

Figure 6.45 shows the most interesting feature from the wear scar profile scans' exercise as the application of cathodic protection on the sintered WC-11Co has reduced the wear scar depth by more than half and has also decreased the diameter of the wear scar from almost 7mm to 4mm, which is in effect the diameter of the nozzle. This trait demonstrates that the deterioration of the area under the jet involves a substantial corrosion related component. Figure 6.46 illustrates the wear scar depths of the sintered WC-6Ni cermet that are not experiencing any change even with the application of the cathodic protection which indicates that erosion domination takes place inside the wear scar. Figures 6.47 and 6.48 are examples of the wear scar profile scans of the HVOF sprayed coatings under free erosion-corrosion conditions and pure erosion conditions. It is clear that there is some significant difference in the two wear scar depths which implies that the erosion is not the dominant degradation mechanism as corrosion and synergy possess high

proportion of the overall material degradation. The wear scar depth trends are tabulated in Figure 6.49.

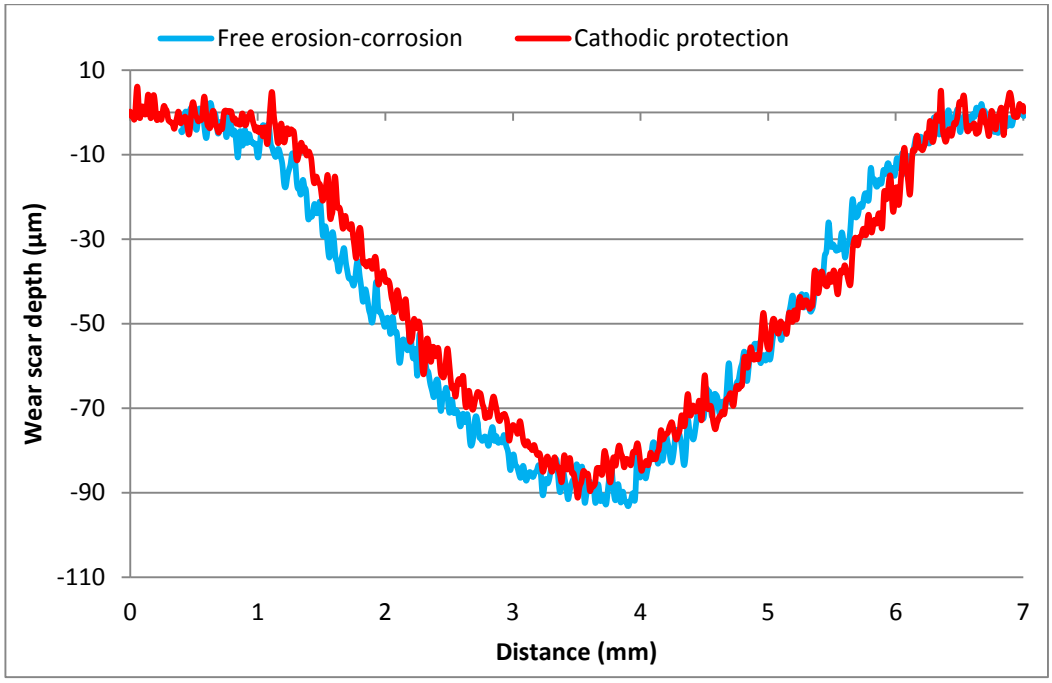

Figure 6.44 Surface profile scans of the wear scars of the UNS S31600 stainless steel under solid/liquid impingement in free erosion-corrosion and cathodic protection.

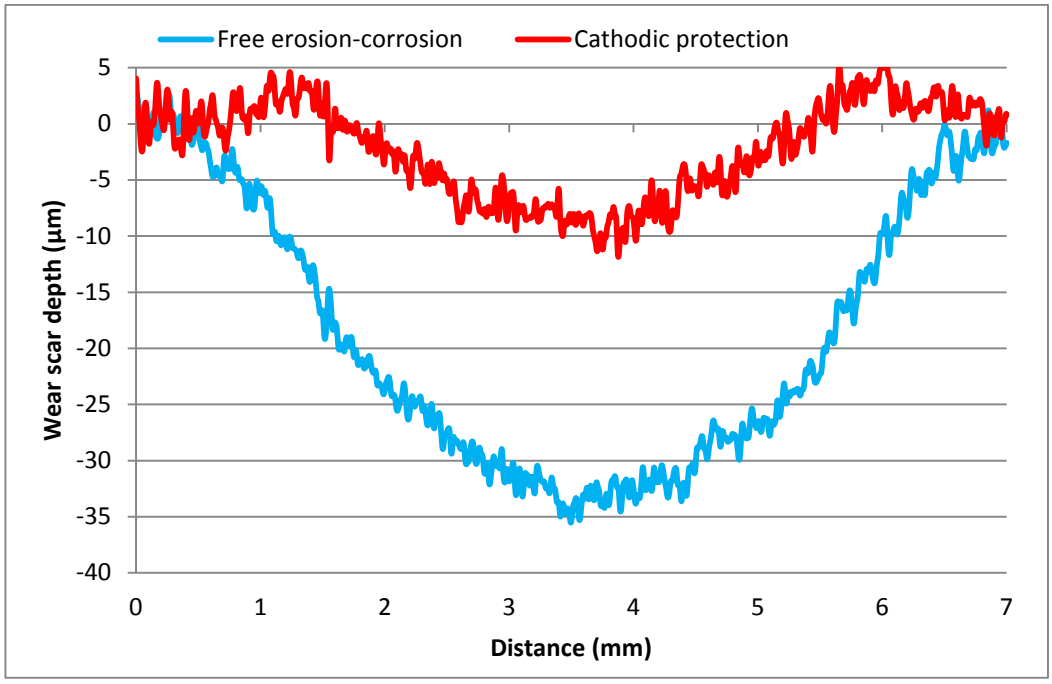

Figure 6.45 Surface profile scans of the wear scars of the sintered WC-11Co cermet under solid/liquid impingement in free erosion-corrosion and cathodic protection.

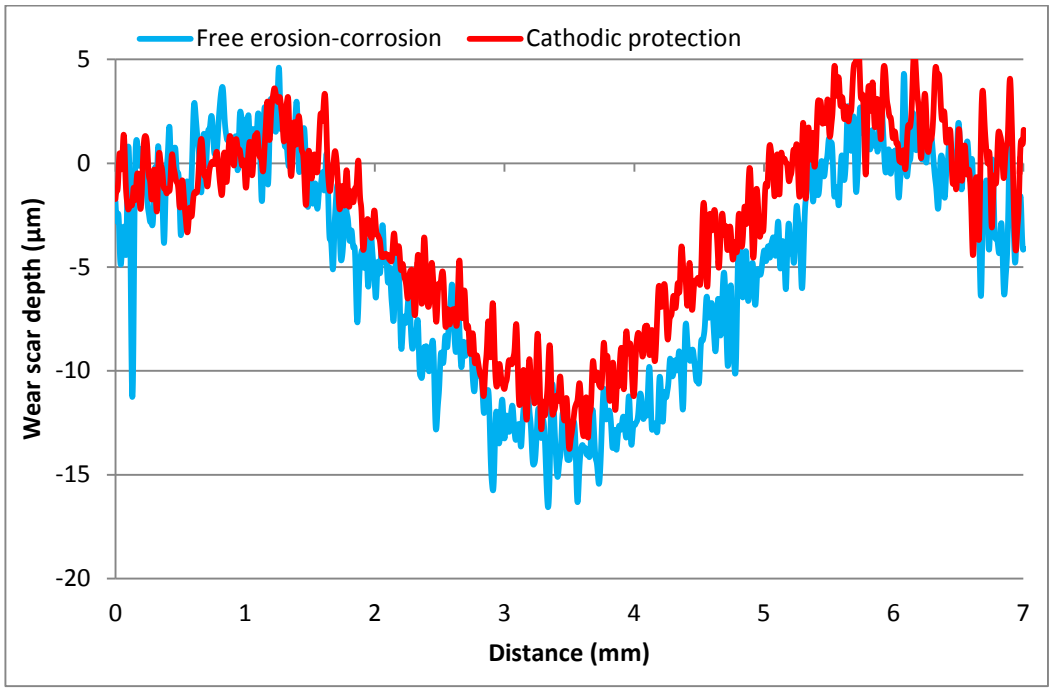

Figure 6.46 Surface profile scans of the wear scars of the sintered WC-6Ni cermet under solid/liquid impingement in free erosion-corrosion and cathodic protection.

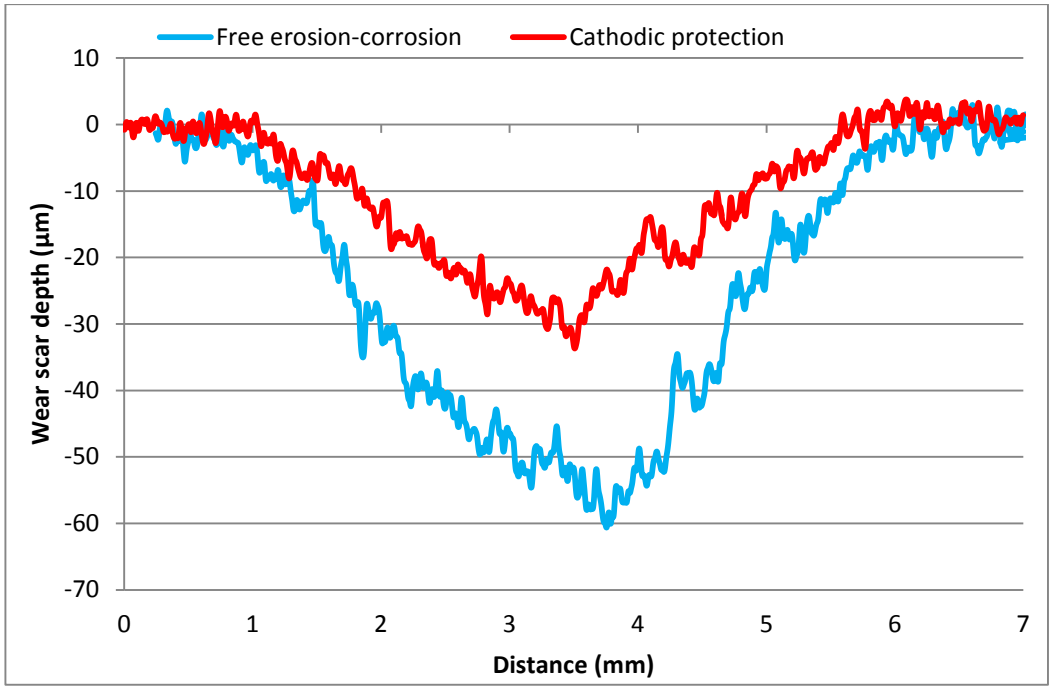

Figure 6.47 Surface profile scans of the wear scars of the HVOF WC-12Co coating under solid/liquid impingement in free erosion-corrosion and cathodic protection.

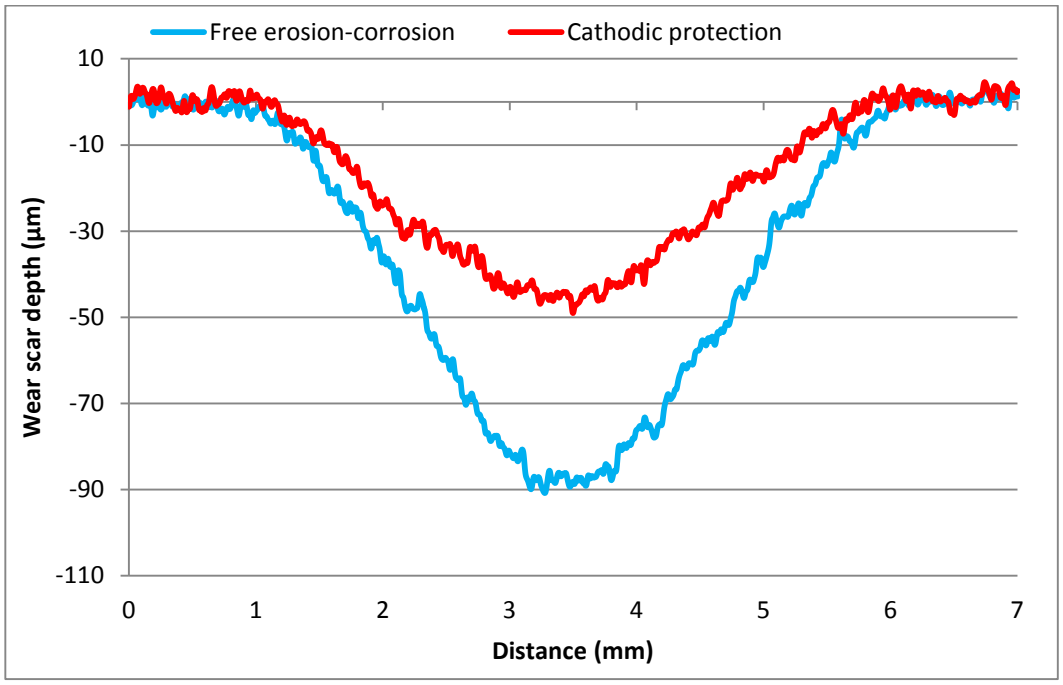

Figure 6.48 Surface profile scans of the wear scars of the HVOF WC-10Ni coating under solid/liquid impingement in free erosion-corrosion and cathodic protection.

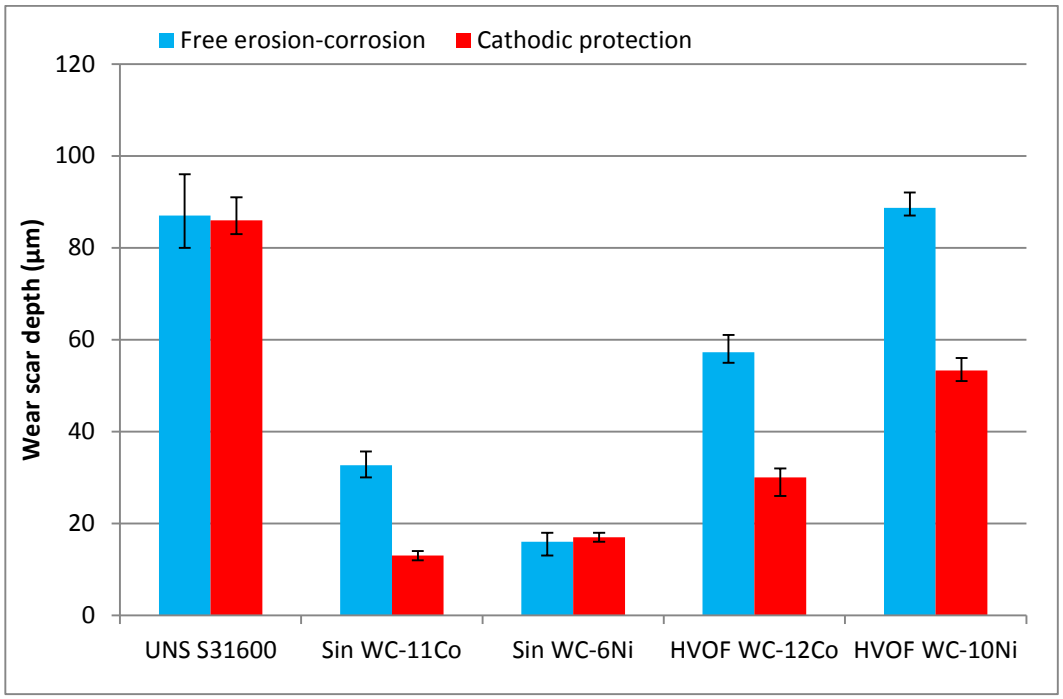

Figure 6.49 Wear scar depths of the materials under solid/liquid impingement in free erosion-corrosion and cathodic protection.

6.5.4.5 Volumetric analysis of the wear scars

Figure 6.50 is an illustrative example of the wear scar volume measurement. Figure 6.51, as expected, replicates the findings of the two-dimension measurements (Figure 6.49) as it demonstrates that the contribution of the corrosion related processes to the overall material damage inside the wear scar is significant for the sintered WC-1Co and the two HVOF coatings.

Figure 6.50 Volumetric analysis on the direct impinged zone of the WC-11Co sintered cermet surface after 2 hours solid/liquid impingement with cathodic protection.

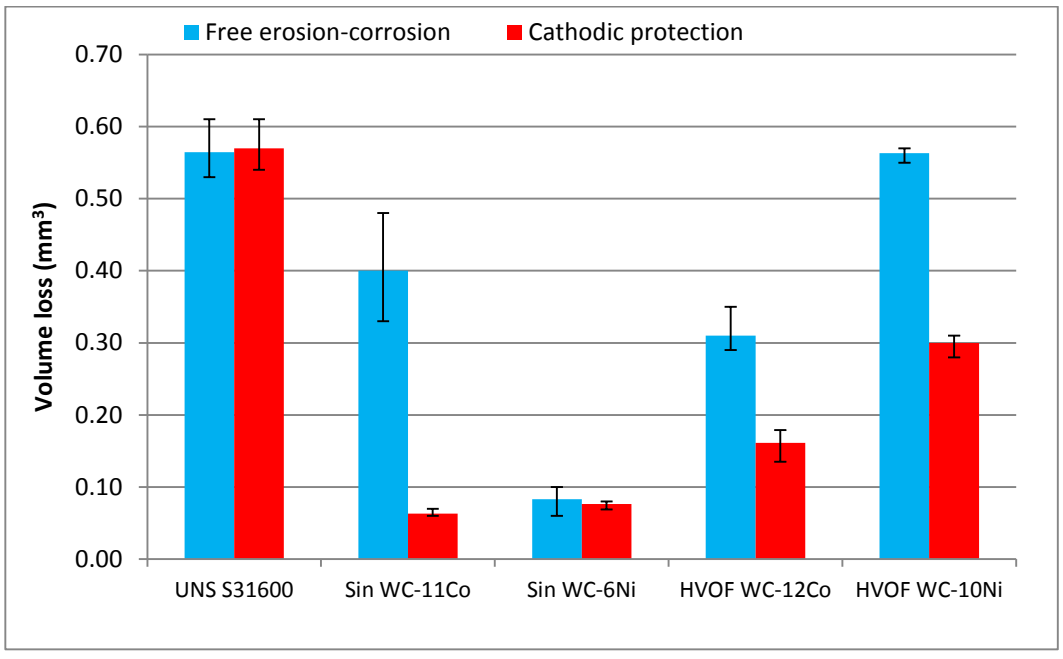

Figure 6.51 Comparison of the average volume losses within the wear scar of the comparative materials with and without cathodic protection.

6.6 Discussion

6.6.1 Total Volume loss (TVL) in free erosion corrosion (FEC) conditions

According to Figure 6.12, there is a clear discrimination of the volume loss of the cermets with the Co binder and the Ni binder, as the latter performs better under solid/liquid impingement. The sintered form of the cermets exhibits superior behaviour compared to the HVOF coated cermets. This feature is probably associated with the inevitable defects in the HVOF sprayed coatings (i.e. porosity, anisotropy etc). The HVOF sprayed WC-12Co exhibits the poorest overall erosion-corrosion behaviour, even inferior to the austenitic stainless steel. The sintered WC-11Co and the austenitic stainless steel showed similar total volume losses, which are slightly higher than that of the HVOF sprayed WC-10Ni. The WC-6Ni sintered cermet is superior to the other four tested materials.

Discrimination of the total volume loss in DIZ and OA

Figure 6.52 presents the overall volume losses and their separation into the losses occurred directly under the jet and the outer area. By taking into account the measured volume losses within the wear scar, the UNS S31600 has similar loss with the sprayed WC-10Ni. The two WC-Co cermets showed comparable performance with each other. The sintered WC-6Ni cermet exhibited the greatest resistance within this region.

The relative performance of the materials is considerably changed in the outer region. The WC-based cermets with the Co binder are no longer better than the austenitic stainless steel as in the direct impinged zone. In fact, they seem highly susceptible to corrosive abrasion, with the HVOF WC-12Co coating also exhibiting double the volume loss of the sintered WC-11Co cermet. The austenitic stainless steel possesses lower resistance than the Ni based WC cermets. The sintered WC-6Ni cermet maintains its excellent performance under the corrosive abrasion conditions. Figure 6.53 demonstrates how the overall erosion-corrosion volume loss is distributed into a number of deterioration mechanisms occurring under impingement.

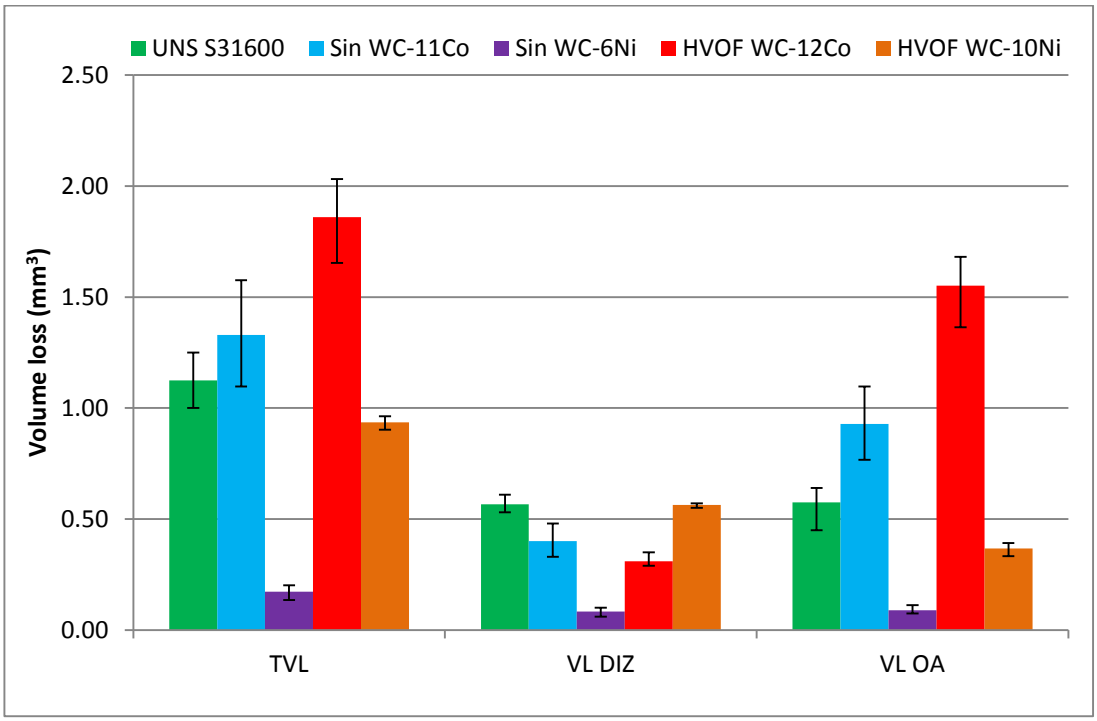

Figure 6.52 Proportions of volume loss damage in the direct impingement zone and in the outer area of the comparative materials in free erosion-corrosion conditions.

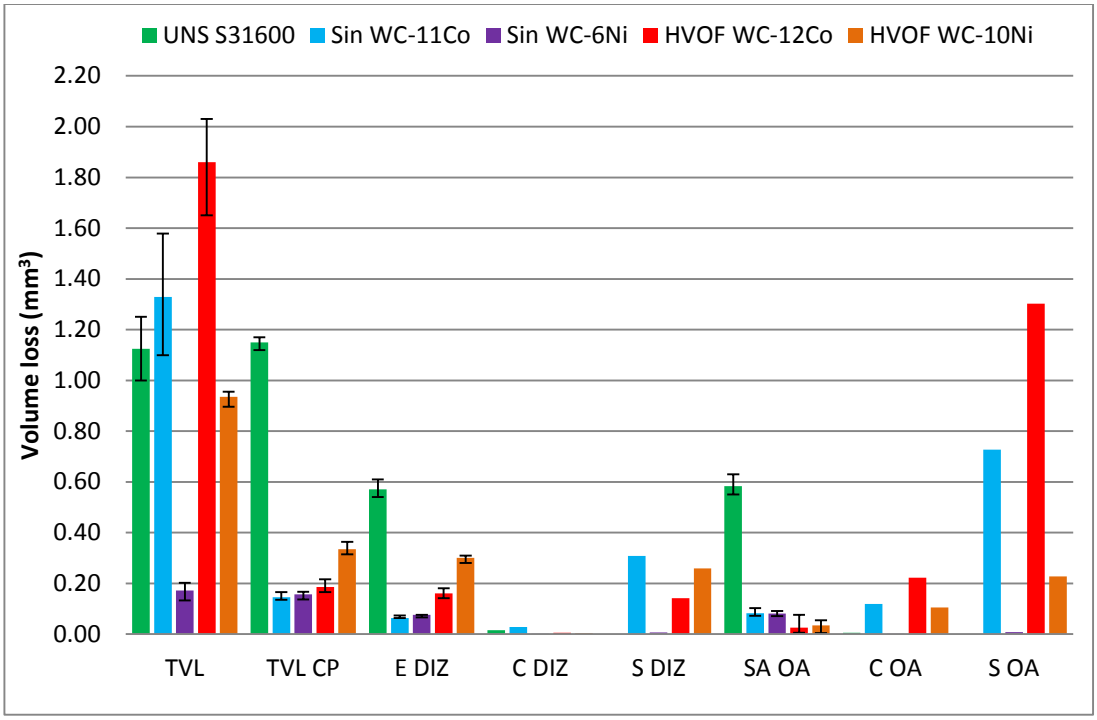

Figure 6.53 Discrimination of the different deterioration processes in volume loss terms of the comparative materials under solid/liquid impingement.

6.6.2 Total volume loss with cathodic protection (CP)

All the cermet materials exhibit substantially greater resistance to mechanical deterioration mechanisms than does the austenitic stainless steel. The somewhat greater amounts of material loss experienced by the sprayed coatings as opposed to the sintered forms of the cermets may be linked slightly to the higher hardness of the former but is more likely to be with the coatings defects (6.2.2). Clark et al [6.6], have found opposite trends in their slurry jet impingement tests as the HVOF WC-12Co coating exhibited greater resistance than the sintered WC-12Co. However, their testing apparatus involved free-jet slurry impingement, and hence the hydrodynamics of the slurry are completely different from the submerged jet impingement employed in this study.

The application of cathodic protection yields substantial benefits in reducing materials loss for three of the cermets but hardly changes the rate of attack for the austenitic stainless steel and the sintered WC-Ni. This feature demonstrates that the corrosion-related processed are of negligible effect on the overall behaviour of the stainless steel and the sintered WC-6Ni. This factor though, is set against the distinctly different resistance to pure mechanical erosion/abrasion mechanisms for these two materials. The extent of the reduced material loss obtained from the application of CP to other three cermets (see Table 6.10) leads to potential benefits in extending the good mechanical performance of especially WC-Co materials under erosion conditions.

Table 6.10 Effect of cathodic protection on the volume loss of the tested materials.

Material	Volume reduction by CP application (%)
UNS S31600	0
Sin WC-11Co	87
Sin WC-6Ni	9
HVOF WC-12Co	90
HVOF WC-10Ni	64

6.6.3 Erosion damage on the direct impinged zone (DIZ)

The microscopic examination revealed that the mechanical damage in the direct impinged zone involved selective erosion of the metallic binder followed by cracking of exposed

protruding WC grains. The relatively good performance of the WC-Co may be associated with a reportedly double micro-hardness of Co, compared to Ni binder [6.27]. However, this feature may have been counteracted in the case of the sintered WC-6Ni material by a lower binder content. The austenitic stainless steel, on the other hand, exhibited the poorest direct impingement erosion resistance of all tested materials. This feature may be an indication of the effect of hardness on materials that possess extremely lower hardness than the impinging particles, which is five times higher than the target in this case [6.38].

6.6.4 Corrosion damage on the direct impinged zone (DIZ)

It is clear, from Figure 6.53, that pure corrosion plays an extremely small direct role in the overall material loss in direct impinged zone. It is relevant to note that, in contrast with the stainless steel, the cermets have high concentration of noble tungsten carbides which would permit only the metallic binder to corrode. The Ni binder cermets showed their superiority in terms of corrosion resistance in comparison with the Co binder cermets. The greater static corrosion behaviour of the Ni binder than the Co binder was observed in previous studies [6.13,6.26,6.28,6.29]. The results in Table 6.8 demonstrate that the good corrosion resistance of the Ni binder can be maintained even in impingement conditions with the presence of solid particles.

6.6.5 Synergy damage on the direct impinged zone (DIZ)

Despite its extremely minor direct role, corrosion appears to initiate remarkable levels of synergistical mechanisms in enhancing erosion in some of the materials. Although, the WC-6Ni sintered and the stainless steel showed negligible synergy in the direct impinged zone, the other three materials exhibited a relatively high synergy effect. This is likely to have been provoked by two mechanisms; micro-crevices due to the preferential corrosion of the metallic binder [6.34] and micro-galvanic phenomena that prevail at the interfaces between the WC grains and the metallic binder [6.2,6.13,6.34] that both enhance the mechanical removal of the WC grains. In these respects, though, it is unclear as to why synergy displayed by the sintered WC-6Ni is so small, unless the lower binder content is the cause.

6.6.6 Sliding abrasion on the outer area (OA)

The cermets showed substantially less sliding abrasion damage than does the stainless steel, which has at least five times lower hardness than the cermets. This comparative behaviour is in line with the generally-accepted view that harder materials possess greater

reistance to abrasion damage. The sprayed cermets exhibited almost half abrasion damage than the sintered cermets and this can be explained by their roughness values, which are higher than the sintered cermets by 0.2µm Ra. The surface texture obstructs the sand particles from penetrating the coating as much as they would for the sintered cermets where the contact area between the solid particle and the target surface is larger. The roughness effect has also been found also in the work of Bolleli et al [6.39], where the abrasion resistance of the as-sprayed HVOF WC-17Co coating on a ball-on-ring apparatus with 100Cr6 ball was higher than the diamond polished specimens.

6.6.7 Corrosion on the outer area (OA)

The sintered WC-6Ni and the stainless steel suffered negligible corrosion damage. The Co-based cermets experienced higher corrosion rates than the Ni binder cermets. It is well known that the cobalt binder is more susceptible to corrosion than the Ni binder which explains the extensive damage of the Co based cermets [6.27–6.29]. The reason why the corrosion rates of the HVOF WC-12Co were higher than the sintered form of the WC-11Co is likely to be due to the microporosity of the HVOF WC-12Co, which could enhance corrosion by forming micro-crevices.

6.6.8 Synergy on the outer area (OA)

Perhaps the most remarkable aspect of the synergy damage on the outer area is that, as inspection of Figure 6.53 illustrates, for the WC-Co cermets, synergy represents a large proportion of their total volume losses. This feature highlights the advantages of the overall examination methodology adopted in this research in tunnelling into the various erosion-corrosion mechanisms occurring when a stream of fluid impinges locally on the surface of a relatively large component. Whilst it is fairly obvious to conclude that the relatively poor overall performance of the WC-Co cermets is related to their vulnerability to corrosion of this material, such a simple correlation does mask the potential roles of other features:

- The higher ratios of S: C for the WC-Co cermets as opposed to WC-Ni imply that rather different synergy deterioration mechanisms are occurring on WC-Co than on WC-Ni. This feature may be associated with the apparent mechanical removal of WC grains, which is more evident in WC-Co cermets, due to the lack of mechanical support (i.e. dissolution of the metallic binder) [6.18].

- The substantially different values of S between the two forms of WC-Co cermets (despite their similar binder contents) suggests than the binder content is not as critical as the manufacturing process for the degree of synergy damage.

6.7 Conclusions

1. Important distinctions between the cermet materials, in terms of their erosion-corrosion characteristics, have been identified and quantified by the extended protocol developed in this research. For instance, the HVOF WC-12Co cermet coating exhibited the highest total volume loss in free erosion-corrosion conditions. However, its direct impingement erosion (mechanical) and sliding abrasion performance was comparable with the other two superior cermets (i.e. WC-6Ni and WC-11Co sintered cermets) which signifies the role of the corrosion and synergy on the coating's degradation in both regions of the specimen. Further to that, the anodic polarisation scans at the two segmented regions (i.e. DIZ and OA) revealed that the material loss was dominated by synergy.
2. The sintered WC-6Ni cermet exhibited by far superior overall erosion-corrosion performance of all the comparative materials in this study.
3. The sintered cermets showed substantially greater erosion-corrosion resistance compared to the similar composition HVOF sprayed coatings. The effect of the spraying flaws was significant of the lower relative performance of the HVOF sprayed coatings.
4. The Ni binder cermets were superior under erosion-corrosion conditions compared with the Co binder cermets of equivalent manufacturing process. This indicates the vulnerability of the Co binder to corrosion and synergy. However, in the absence of corrosion, the relative performance of the Ni and the Co binder has changed.
5. The overall erosion-corrosion damage of the austenitic stainless steel was similar or even better than the Co based cermets. It was clear though, that this feature emanates from the poor resistance of the WC-Co cermets to corrosion related attack, since in terms of pure mechanical modes of damage, WC-Co cermets exhibited dramatically greater performance than the stainless steel. This suggests that the material selection process should be careful implemented as different erosion-corrosion conditions may result in unexpected results.

6. The material hardness played an important role on the erosion resistance as all the cermets behaved better than the austenitic stainless steel. The proportional relationship between hardness and erosion was highlighted in sliding abrasion rather in direct impingement erosion. However, in erosion-corrosion environments, hardness does not play a significant role in the prediction of the material deterioration
7. Due to the composite-like microstructure, the cermets exhibited high synergistical effects that contribute sometimes more than even pure erosion to the overall erosion-corrosion damage. An exception of this fact was the WC-6Ni, probably because of the low binder content/high WC content and inevitably low corrosion rate. The corrosion and synergy components should not be overlooked when the engineering component is exposed to any aqueous slurry.

6.8 References

[6.1] Private communication with Alastair Pearson , Chief Metallurgist, Weir Services, East Kilbride, Glasgow, Scotland, (2015).

[6.2] J.A. Picas, E. Rupérez, M. Punset, A. Forn, Influence of HVOF spraying parameters on the corrosion resistance of WC-CoCr coatings in strong acidic environment, Surf. Coatings Technol. 225 (2013) 47–57.

[6.3] V.A.D. Souza, A. Neville, Aspects of microstructure on the synergy and overall material loss of thermal spray coatings in erosion–corrosion environments, Wear. 263 (2007) 339–346.

[6.4] Private communication with Bernd Reis, Technical Manager, Element Six, Frankfurt, Germany, (2015).

[6.5] M.R. Thakare, J.A. Wharton, R.J.K. Wood, C. Menger, Effect of abrasive particle size and the influence of microstructure on the wear mechanisms in wear-resistant materials, Wear. 276-277 (2012) 16–28.

[6.6] H.M. Clark, H.M. Hawthorne, Y. Xie, Wear rates and specific energies of some

ceramic, cermet and metallic coatings determined in the Coriolis erosion tester, Wear. 233-235 (1999) 319–327.

[6.7] S.F. Wayne, S. Sampath, Structure/Property relationships in sintered and thermally sprayed WC-Co, J. Therm. Spray Technol. 1 (2014) 307–315.

[6.8] R.J.K. Wood, B.G. Mellor, M.L. Binfield, Sand erosion performance of detonation gun applied tungsten carbide/cobalt--cbxomium coatings, Wear. (1997) 70–83.

[6.9] A. Karimi, C. Verdon, J.L. Martin, R.K. Schmid, Slurry erosion behaviour of thermally sprayed WC-M coatings, Wear. 186-187 (1995) 480–486.

[6.10] M. Magnani, P.H. Suegama, N. Espallargas, S. Dosta, C.S. Fugivara, J.M. Guilemany, et al., Influence of HVOF parameters on the corrosion and wear resistance of WC-Co coatings sprayed on AA7050 T7, Surf. Coatings Technol. 202 (2008) 4746–4757.

[6.11] B.R. Marple, J. Voyer, J.F. Bisson, C. Moreau, Thermal spraying of nanostructured cermet coatings, J. Mater. Process. Technol. 117 (2001) 418–423.

[6.12] D. Tu, S. Chang, C. Chao, C. Lin, Tungsten carbide phase transformation during the plasma spray process, J. Vaccum Sci. Technol. A Vac. Surfaces Film. 3 (1985) 2479–2482.

[6.13] J.E. Cho, S.Y. Hwang, K.Y. Kim, Corrosion behavior of thermal sprayed WC cermet coatings having various metallic binders in strong acidic environment, Surf. Coatings Technol. 200 (2006) 2653–2662.

[6.14] S. Shrestha, T. Hodgkiess, A. Neville, Erosion–corrosion behaviour of high-velocity oxy-fuel Ni–Cr–Mo–Si–B coatings under high-velocity seawater jet impingement, Wear. 259 (2005) 208–218.

[6.15] C. Monticelli, A. Frignani, F. Zucchi, Investigation on the corrosion process of carbon steel coated by HVOF WC/Co cermets in neutral solution, Corros. Sci. 46 (2004) 1225–1237.

[6.16] J.M. Perry, A. Neville, V.A. Wilson, T. Hodgkiess, Assessment of the corrosion rates and mechanisms of a WC-Co-Cr HVOF coating in static and liquid-solid impingement saline environments, Surf. Coatings Technol. 137 (2001) 43–51.

[6.17] J.M. Perry, T. Hodgkiess, A. Neville, Some aspects of the erosion and corrosion behaviour of a WC-Co-Cr HVOF sprayed coating, Proc. Int. Therm. Spray Conf. ASM ITSC. (2000).

[6.18] M.S. Mahdipoor, F. Tarasi, C. Moreau, A. Dolatabadi, M. Medraj, HVOF sprayed coatings of nano-agglomerated tungsten-carbide/cobalt powders for water droplet erosion application, Wear. 330-331 (2015) 338–347.

[6.19] H. Reshetnyak, J. Kuybarsepp, Mechanical properties of hard metals and their erosive wear resistance, Wear. 177 (1994) 185–193.

[6.20] I. Hussainova, J. Kubarsepp, J. Pirso, Mechanical properties and features of erosion of cermets, Wear. 250-251 (2001) 818–825.

[6.21] J. Pirso, M. Viljus, S. Letunovitš, Friction and dry sliding wear behaviour of cermets, Wear. 260 (2006) 815–824.

[6.22] M. Antonov, R. Veinthal, D.-L. Yung, D. Katušin, I. Hussainova, Mapping of impact-abrasive wear performance of WC–Co cemented carbides, Wear. 332-333 (2015) 971–978.

[6.23] A.J. Gant, M.G. Gee, Wear of tungsten carbide–cobalt hardmetals and hot isostatically pressed high speed steels under dry abrasive conditions, Wear. 251 (2001) 908–915.

[6.24] P. Kulu, I. Hussainova, R. Veinthal, Solid particle erosion of thermal sprayed coatings, Wear. 258 (2005) 488–496.

[6.25] A.J. Ninham, A.V. Levy, The erosion of carbide-metal composites, Wear. 121 (1988) 347–361.

[6.26] H. Engqvist, N. Axén, S. Hogmark, Tribological properties of a binderless carbide, Wear. 232 (1999) 157–162.

[6.27] E.J. Wentzel, C. Allen, Erosion-corrosion resistance of tungsten carbide hard metals with different binder compositions, Wear. 181-183 (1995) 63–69.

[6.28] E.J. Wentzel, C. Allen, The erosion-corrosion resistance of tungsten-carbide hard metals, Int. J. Refract. Met. Hard Mater. 15 (1997) 81–87.

[6.29] P.K. Aw, A.L.K. Tan, T.P. Tan, J. Qiu, Corrosion resistance of tungsten carbide based cermet coatings deposited by High Velocity Oxy-Fuel spray process, Thin Solid Films. 516 (2008) 5710–5715.

[6.30] Z. Kamdi, P.H. Shipway, K.T. Voisey, A.J. Sturgeon, Abrasive wear behaviour of conventional and large-particle tungsten carbide-based cermet coatings as a function of abrasive size and type, Wear. 271 (2011) 1264–1272.

[6.31] H.M. Hawthorne, B. Arsenault, J.P. Immarigeon, J.G. Legoux, V.R. Parameswaran, Comparison of slurry and dry erosion behaviour of some HVOF thermal sprayed coatings, Wear. 225-229 (1999) 825–834.

[6.32] Z. Feng, A. Ball, The erosion of four materials using seven erodents - towards an understanding, Wear. 233-235 (1999) 674–684.

[6.33] V.A. De Souza, A. Neville, Corrosion and erosion damage mechanisms during erosion–corrosion of WC–Co–Cr cermet coatings, Wear. 255 (2003) 146–156.

[6.34] T. Hodgkiess, A. Neville, S. Shrestha, Electrochemical and mechanical interactions during erosion-corrosion of a high-velocity oxy-fuel coating and a stainless steel, Wear. 233-235 (1999) 623–634.

[6.35] M. Bjordal, E. Bardal, T. Rogne, T.G. Eggen, Erosion and corrosion properties of WC coatings and duplex stainless steel in sand-containing synthetic sea water, Wear. 186-187 (1995) 508–514.

[6.36] C. Bartuli, T. Valente, F. Cipri, E. Bemporad, M. Tului, Parametric Study of an HVOF Process for the Deposition of Nanostructured WC-Co Coatings, J. Therm. Spray Technol. 14 (2005) 187–195.

[6.37] Q. Yang, T. Senda, A. Ohmori, Effect of carbide grain size on microstructure and sliding wear behavior of HVOF-sprayed WC-12% Co coatings, Wear. 254 (2003) 23–34.

[6.38] I.M. Hutchings, Tribology: Friction and Wear of Engineering Materials . 1992, London, 1992.

[6.39] G. Bolelli, V. Cannillo, L. Lusvarghi, S. Riccò, Mechanical and tribological properties of electrolytic hard chrome and HVOF-sprayed coatings, Surf. Coatings Technol. 200 (2006) 2995–3009.

Chapter 7

Concluding remarks and recommendations for further work

7.1 Concluding remarks

7.1.1 Evaluation technique

A new quantitative technique has been developed to characterise the various material degradation processes that occur during impingement by combining the capabilities of the three dimensional surface topographical analysis with the common gravimetric analysis. This approach enables the discrimination of the direct impingement erosion from the sliding abrasion that occur simultaneously at the target material surface subjected to impingement. This feature comprises one of the key novelties of this thesis. Two examples of the importance of this approach to the assessment of jet impingement experiments are summarised below.

- Figure 5.37: There is a substantial difference between the 27%Cr cast iron and the 37%Cr cast iron indicated by the TVL measurements but this is not a result of mechanical damage in the DIZ but rather by substantially increased resistance to sliding abrasion of the 27%Cr cast iron.
- Figures 6.52 and 6.53: The TVL measurement alone indicates that HVOF WC-12Co is by far the most-vulnerable of the materials tested but the extended assessment reveals that, in terms of erosion-corrosion resistance in the directly-impinged zone, this material exhibits relatively good performance but a vulnerability to corrosion-assisted abrasion.

7.1.2 Material degradation mechanisms

In terms of the mechanical mechanisms, both direct impingement erosion and sliding abrasion were measured, with the latter property being unique as it had not been quantified before through the submerged impingement jet apparatus. A recurring finding from this work is that the behaviour under direct impingement erosion is not simply related to hardness. For instance, the austenitic stainless steel exhibited comparable volume losses with the hard cast irons and HVOF sprayed WC-10Ni. It is suggested that various mechanical properties determine the direct impingement erosion resistance; possibly hardness and elastic modulus and not a single factor. On the other hand, the sliding abrasion results indicated, in agreement with general opinion, that the higher the hardness, the better resistance of the material is observed. As a result, the hard cermets exhibited superior sliding abrasion compared with the other comparative materials. It should also be

recognised that, in erosion-corrosion conditions, the influence of the corrosion processes can override the mechanical damage that might be associated with hardness.

Along with the mechanical deterioration processes, the electrochemical damage was also assessed on a full specimen and also on the two distinct hydrodynamic regions of the specimens; directly impinged zone and outer area, through segmentation of the specimen. The corrosion resistance in the directly impinged zone was lower than that of the outer area, and this feature was common for all the comparative materials. The austenitic based alloys and the WC-6Ni sintered cermet exhibited superior corrosion performance in comparison with the other materials in both the direct impingement zone and the outer area. It should also be noted that although corrosion was responsible for a small proportion of the total volume loss of the materials studied, the predicted thickness loss per year are significant, as shown in Table 7.1.

Table 7.1 Thickness loss/year from pure corrosion for each comparative material

Material	Corrosion Current Density (μA/cm^2)	Thickness loss (μm/year)
UNS G10400	350	3424
UNS S31600	7	81
UNS S31600	7	81
UNS S42000	26	306
27%Cr cast iron	35	410
37%Cr cast iron	4	41
UNS S31600	10	115
Sin WC-11Co	500	5416
Sin WC-6Ni	30	323
HVOF WC-12Co	440	4802
HVOF WC-10Ni	400	4306

The presence of a small proportion of corrosion initiates a relatively high synergy effect that can sometimes be comparable to the pure mechanical erosion in terms of its contribution to the total volume loss. In this study, the synergy effects were governed by the microstructure of the material. The carbon steels and stainless steels exhibited relatively

low synergy effect due to their relatively uniform microstructure. The microstructure of the white cast irons and cermets is particularly complex with metallic and ceramic phases, which makes them vulnerable to synergy as these rather dissimilar elements interact significantly under saline aqueous solutions. For this reason, the white cast irons and the cermets depicted higher quantities of synergy than the metallic alloys. However, the sintered WC-6Ni showed superior erosion-corrosion resistance and especially negligible synergy effect, which was the exception of the cermet group.

The suppression of corrosion and synergy, via impressed current cathodic protection, resulted in a substantial reduction of the volume loss on the majority of the materials, as illustrated in Table 7.2. The assessment of the effect of cathodic protection, on the material losses in the entire specimen, was expanded to the two distinct regions; directly impinged zone (DIZ) and outer area (OA).

Table 7.2 Volume loss reduction via the application of cathodic protection on each material

Material	**Full specimen (mm^3)**			**DIZ (mm^3)**			**OA (mm^3)**		
	FEC	**CP**	**%**	**FEC**	**CP**	**%**	**FEC**	**CP**	**%**
UNS G10400	1.49	0.83	**44.3**	0.51	0.5	**2.0**	1	0.33	**67.0**
UNS S31600	0.73	0.6	**17.8**	0.39	0.39	**0.0**	0.35	0.21	**40.0**
UNS S31600	1.21	1.15	**5.0**	0.67	0.65	**3.0**	0.54	0.5	**7.4**
UNS S42000	1.3	0.94	**27.7**	0.74	0.48	**35.1**	0.55	0.46	**16.4**
27%Cr cast iron	1.33	0.81	**39.1**	0.82	0.58	**29.3**	0.52	0.23	**55.8**
37%Cr cast iron	1.35	1.11	**17.8**	0.84	0.59	**29.8**	0.51	0.52	**0.0**
UNS S31600	1.13	1.15	**0.0**	0.57	0.57	**0.0**	0.58	0.58	**0.0**
Sin WC-11Co	1.16	0.15	**87.1**	0.37	0.06	**83.8**	0.8	0.08	**90.0**
Sin WC-6Ni	0.17	0.16	**5.9**	0.08	0.08	**0.0**	0.09	0.08	**11.1**
HVOF WC-12Co	1.86	0.19	**89.8**	0.31	0.16	**48.4**	1.55	0.03	**98.1**
HVOF WC-10Ni	0.94	0.33	**64.9**	0.56	0.3	**46.4**	0.57	0.03	**94.7**

This rather novel feature contributed significantly on the understanding of the resistance to corrosion and synergy of each material under two clearly different slurry conditions; high flow velocities at normal impact and relatively lower flow velocities at oblique angles. For instance, the cathodic protection was less effective on the direct impinged zone of the HVOF WC-12Co cermet coating than on WC-11Co sintered variety, despite the fact that both materials exhibited similar total volume reductions by the application of cathodic protection on their full specimen.

7.1.3 Comparison of the materials

The material database, shown in Table 7.3, assesses the susceptibility of the different groups of materials to each degradation mechanism by comparing their volume losses with that of their reference austenitic stainless steel. This extended evaluation improves the material selection process by predicting the service life of the currently used materials. For example, one of the most valuable outcomes of this database is the clear distinction between the HVOF sprayed cermet coatings with the sintered cermets, where the latter exhibit substantially greater erosion-corrosion performance.

It has also provided guidance on erosion-corrosion protection techniques that have potential to extend the life of the engineering components. Some of the protection methodologies are listed below:

- Cathodic protection, as mentioned earlier, that would supress the electrochemical corrosion along with the considerable synergy reducing the volume loss of the material to substantial degree.
- Metallurgical modifications that would involve; a) heat treatments to increase the hardness and toughness, b) Change the chemical constituents of the multi-phase materials in order to avoid the initiation of a galvanic cell and also c) selection of different manufacturing processes that exhibit minimal defects.

Table 7.3 Material database based on the experimental findings.

Material	TVL	TVL CP	E (DIZ)	C (DIZ)	S (DIZ)	SA (OA)	C (OA)	S (OA)
UNS S31600	1.0	1.0	1.0	1.0	1.0	1.0	1.0	1.0
UNS G10400	2.0	1.4	1.3	10.2	1.0	1.6	407.6	1.1
UNS S42000	1.1	0.8	0.7	2.1	25.5	0.9	5.1	2.3
27%Cr cast iron	1.1	0.7	0.9	2.1	23.2	0.5	11.7	7.4
37%Cr cast iron	1.2	1.0	0.9	0.3	26.3	1.0	0.5	0.0
Sin WC-11Co	1.2	0.1	0.1	1.9	247.0	0.1	23.9	581.4
SinWC-6Ni	0.2	0.1	0.1	0.0	5.4	0.1	0.1	5.9
HVOF WC-12Co	1.7	0.2	0.3	0.6	111.7	0.0	44.5	1041.8
HVOF WC-10Ni	0.8	0.3	0.5	0.3	207	0.1	21.1	182.4
VL ratio < 0.8: Good, 0.8 ≤ VL ratio ≤ 1.2: Blue, VL ratio > 1.2: Poor								

7.2 Recommendations for further work

This section provides suggestions for further work ideas that could potentially enhance the value of this thesis and even structure new Ph.D. programmes that could possibly follow this initiative.

- In general, the application of the innovative methodology implemented in this thesis could be broadened by evaluating the entire spectrum of angle of impingement from 0^{o} to 90^{o}. Impingement angles of 60^{o}, 45^{o} and 20^{o} will provide relevant distinct insights of the material behaviour, in view of the fact that engineering components are exposed at all angles of impingements.

- Environmental parameters, like pH, velocity, sand concentration, could be assessed to determine their effect on erosion, corrosion and also the enhancement of erosion due to corrosion.
- The study of the efficiency of the corrosion protection of sacrificial anodes by comparing them with the impressed current cathodic protection and free erosion-corrosion tests. The effectiveness of the sacrificial anodes in aggressive erosion-corrosion conditions with normal incidence (region under the jet) and also moderate erosion-corrosion conditions with oblique angles of impingement (adjacent to the wear scar) would be beneficial for corrosion protection programmes.
- With regard to the cast irons, a study of a hyper-eutectic cast iron would be ideal addition to gain a better understanding of the effect of the cast iron type on erosion-corrosion resistance of the cast alloys. The investigation of the metallic phase (i.e. austenite or martensite) on the same type of cast iron would be also valuable as there is a clear impact of the metallic phase on both erosion and corrosion resistance, but more interestingly on the synergy of those two deterioration mechanisms. A more complicated route would be the assessment of different types of carbides (e.g. niobium carbides, vanadium carbides) which would definitely enhance the prediction studies through a review of the ceramic and metallic phase of the cast alloy. Also, alternative manufacturing processes of cast irons, such as centrifugal casting or even HVOF sprayed cast irons may be worthy for further study.
- In relation to the cermet study, more cermets, that would include also chromium in their metallic binder, would improve the benchmarking of the WC-based cermets. Investigation of the effect of the HVOF spraying parameters and the feedstock powder sizes on the coating's quality would also enhance this work.
- The investigation of more types of coatings, such as functionally graded coatings, plasma transferred arc (PTA) coatings or chemical vapour deposition (CVD) coatings, of the same chemical composition (i.e. WC-based with a metallic binder) which would extend the breadth of the understanding by focusing more on the manufacturing process effects.